Université de Liège
Faculté des Sciences Appliquées
Collège de doctorat en Électricité, Électronique et Informatique

# Investigation of passive magnetic shielding methods combining bulk superconductors and coated conductors

Doctoral dissertation presented by

**Sébastien Brialmont**

Submitted in partial fulfillment of the requirements for the degree of

*Doctor of Philosophy (PhD) in Engineering Sciences*

February 2024

# Thesis committee

Prof. Philippe Vanderbemden (Université de Liège), Advisor

Prof. Christophe Geuzaine (Université de Liège), President

Prof. Benoît Vanderheyden (Université de Liège)

Prof. Laura Gozzelino (Politecnico di Torino)

Prof. Timothy Coombs (University of Cambridge)

Dr. Eric Forton (Ion Beam Applications)

# Author contact information

**Sébastien Brialmont**

Sensors and Electrical Measurement Systems
Dept. of Electrical Engineering and Computer Science
Université de Liège

Montefiore Institute B28
Quartier Polytech 1
Allée de la Découverte 10
4000 Liège, Belgium

Email: s.brialmont@uliege.be

# Funding

S. Brialmont was recipient of a grant from the Fonds pour la Formation à la Recherche dans l'Industrie et l'Agriculture (FRIA).

# Acknowledgements

Back in 2017, a time during which the words ‘Electrical Measurement’ were almost meaningless to me, I remember knocking at that random door to meet a professor that I barely knew in order to talk about the design of a ‘torque magnetometer’ to measure magnetic properties of ‘bulk superconductors’. At that time, I could not even imagine that a bit more than six years later, I would knock at the same door to hand in the manuscript of my thesis to this same professor. And yet, here I am. ‘Du coup’, I would like to express my first and foremost gratitude to my advisor, Prof. Philippe Vanderbemden, for all the support and coaching during the last five years. In particular, I am incredibly grateful to him for introducing me to the fascinating world of Superconductivity, his world-class lectures, his exceptional availability as well as the passion and scientific rigor he brought me. The huge pedagogy he showed during these years as well as his ability to keep me positive and focus even when results would not show up were definitely priceless. I also thank him for his proof-reading and his countless feedbacks regarding all my results and manuscripts throughout this thesis.

I am also grateful to Prof. Benoît Vanderheyden for his deep knowledge in physics, engineering and science in general. Our discussions and interactions were most fruitful and stimulating. I thank Prof. Christophe Geuzaine for our interactions at the interface between numerical modeling and experimental work. I also thank him for accepting to be chairman during the defense. In addition, I want to thank Julien Dular for our exciting scientific collaborations as well as his great help regarding numerical modeling and Gabriel Digregorio for letting me use the 3D printer (a great tool by the way). I wish them a bright future.

I thank Prof. Tim Coombs and Dr. Eric Forton for accepting to be members of the jury. In particular, I want to thank Eric for his support and enthusiasm regarding this thesis and also for the short but exciting introduction to cyclotrons and particle accelerators industry.

In the scope of this thesis, I had the amazing opportunity to work in the framework of international scientific collaborations. I am grateful to Prof. Laura Gozzelino and Michela Fracasso for their warm welcome at Politecnico di Torino (Italy). In addition, I thank

Prof. Marian Ciszek for having me at the Institute of Low Temperature and Structure Research of Wrocław (Poland). I consider myself as incredibly fortunate for having this opportunity to exchange with him and benefit from his wide experience in the field of AC losses in superconductors. I would like to thank Prof. Frédéric Mazaleyrat for our fruitful discussions on ferromagnetic hysteresis. I also thank Prof. Seungyong Hahn, Dr. Anup Patel, Prof. Wanmin Yang and Dr. Pengtao Yang for providing us with the various superconducting samples, our regular contacts and their contribution to the papers published in the scope of this thesis. I thank Dr. Mark Rikel for our numerous discussions about coated conductors manufacturing.

Next, I thank the FRS-FNRS for awarding me with a FRIA grant in order to perform my research as well as the University of Liège for the nice, peaceful and comfortable work environment. I also thank the COST action for financing my work in Turin.

Then, my gratitude goes to my colleagues from the lab who set such a great ambiance in the team. I thank Jean-François Fagnard for all his help and advice in the lab as well as his (very) careful proof-reading of all my manuscripts, papers or presentations. Without him, no doubt this thesis would have been postponed a couple of years later... I also thank Pascal Harmeling for his precious experience to deal with any technical issue. I thank Michel, who was there since almost the beginning, Thor, Thibault, Philippe and Thomas. I wish them good luck for the upcoming years. I am also thankful to those who were by my side as teaching assistants. I thank Loïc who mentored me in this fascinating job, Clara and Nicolas.

Finally, I am grateful to my relatives and close friends for their support, their interest as well as their enthusiasm in having a ‘science guy’ around. They have always been a great source of motivation.

# Abstract

A lot of engineering applications require the development of electrical devices with high power densities and involve large magnetic fields. These devices are generally characterized by high values of stray flux densities potentially detrimental to their environment. In this context, it is necessary to screen these devices by means of effective magnetic shields. Large flux densities in the low frequency regime (typically $< 100$ Hz) cannot be efficiently shielded by conventional ferromagnetic or conducting materials and require the use of superconductors. The goal of this thesis is to investigate methods to combine the properties of bulk high-temperature superconductors and second generation coated conductors in order to design sizable passive magnetic shields.

In order to develop efficient magnetic shields, it is necessary to obtain information on the properties of the individual superconducting samples. Accordingly, the first part of this thesis consists in characterizing the electrical and magnetic properties of bulk samples and coated conductors. In addition to providing critical information to interpret experimental results, these properties can also be used to implement numerical models. In this work, bulk superconductors are characterized in terms of their critical current density and flux trapping ability. Some of the coated conductors are deposited on a slightly ferromagnetic substrate. An experimental set-up is thus developed to characterize the ferromagnetic properties of these substrates.

Then, hybrid magnetic shields (combining bulk superconductors and coated conductors) are investigated experimentally. The study is performed in configurations of increasing complexity both in terms of the uniformity of the applied magnetic field and in terms of the symmetry of the shield structure itself. In particular, a cylindrical shield made of coated conductor annuli stacked together is characterized under different configurations of external applied field. Methods to improve the efficiency of such a shield are also presented. Next, we demonstrate the ability to screen the stray flux density over a significant volume by using arrays of bulk superconducting samples. The influence of the non-superconducting joints between the different samples can be mitigated by combining these arrays with coated conductors in closed loop configuration.

Finally, an experimental prototype of hybrid magnetic screen is tested in the vicinity

of a large field superconducting magnet exhibiting a significant stray flux density. These conditions are commonly encountered in large scale engineering applications. This work is performed in the Department of Applied Science and Technology at Politecnico di Torino (Italy).

The various experimental results obtained throughout this study can be successfully reproduced by 2D and 3D numerical models. These models are useful to interpret the experimental data and estimate the influence of the superconducting parameters on the efficiency of the shield. Consequently, they allow for a deeper understanding of the shielding mechanisms. The results obtained in the framework of this thesis demonstrate the relevance of combining bulk superconductors and coated conductors for low frequency magnetic shielding. The intent is that these results can provide insights to design a variety of efficient magnetic shields combining both kinds of superconductors.

# Résumé

Un grand nombre d'applications d'ingénierie requièrent le développement d'appareillages électriques à haute densité de puissance basé sur des champs magnétiques intenses. Ces appareillages sont généralement caractérisés par des valeurs élevées d'induction magnétique de fuite, potentiellement néfaste pour l'environnement extérieur. Dans ce contexte, il est nécessaire d'écranter ces appareillages au moyen de blindages magnétiques performants. Des valeurs élevées d'induction magnétique dans le régime des basses fréquences (typiquement $< 100$ Hz) ne peuvent être blindées de manière efficace par des matériaux ferromagnétiques ou conducteurs conventionnels et nécessitent donc l'utilisation de supraconducteurs. Le but de cette thèse est d'investiguer des méthodes permettant de combiner les propriétés des supraconducteurs à haute température critique de type massifs (bulks) et les rubans supraconducteurs de seconde génération (coated conductors) de manière à concevoir des blindages magnétiques passifs de taille appréciable.

En vue de développer des blindages magnétiques efficaces, il est nécessaire d'obtenir des informations précises sur les propriétés des échantillons supraconducteurs individuels. Dès lors, la première partie cette thèse concerne la caractérisation des propriétés électriques et magnétiques des échantillons massifs et des rubans supraconducteurs utilisés. En plus de fournir des informations importantes permettant d'interpréter les résultats expérimentaux, ces propriétés peuvent aussi être utilisées pour l'implémentation de modèles numériques. Dans ce travail, les supraconducteurs massifs sont caractérisés en termes de leur densité de courant critique ainsi que de leur capacité de piégeage de flux. Certains rubans supraconducteurs sont déposés sur des substrats légèrement ferromagnétiques. Un système expérimental est donc développé en vue de caractériser les propriétés ferromagnétiques de ces substrats.

Ensuite, les blindages magnétiques hybrides (combinant matériaux massifs et rubans supraconducteurs) sont investigués expérimentalement. L'étude est effectuée dans des configurations de complexité croissante, à la fois en termes d'uniformité du champ magnétique appliqué et en termes de symétrie de la structure du blindage elle-même. En particulier, un blindage cylindrique composé d'un empilement de rubans supraconducteurs annulaires est caractérisé sous différentes configurations de champ appliqué externe. Des méthodes permettant d'améliorer l'efficacité de tels blindages sont également présentées. Par la suite, nous démontrons la capacité d'écranter l'induction de fuite sur un volume significatif grâce à des structures juxtaposant plusieurs échantillons supraconducteurs massifs. L'influence des interfaces non supraconductrices entre les différents échantillons peut être mitigée en combinant ces structures à des rubans supraconducteurs court-circuités sur eux-mêmes.

Finalement, un prototype expérimental d'écran magnétique hybride est testé au voisinage d'un aimant supraconducteur à haut champ, caractérisé par une induction de fuite significative. De telles conditions sont relativement fréquentes dans les applications d'ingénierie à large échelle. Ce travail est effectué au Département de Sciences Appliquées et Technologies de la Politecnico di Torino (Italie).

Les résultats expérimentaux obtenus tout au long de cette étude peuvent être reproduits de manière concluante grâce à des modèles numériques 2D et 3D. Ces modèles sont particulièrement utiles pour interpréter les données expérimentales ainsi que pour estimer l'influence des différents paramètres physiques sur l'efficacité des blindages. En conséquence, ils permettent une compréhension plus en profondeur des mécanismes de blindage. Les résultats obtenus dans le cadre de cette thèse démontrent la pertinence de combiner des matériaux massifs avec des rubans supraconducteurs pour le blindage magnétique à basse fréquence. Ces résultats pourront fournir des éléments d'information pour la conception de différents types de blindage magnétiques performants en combinant les deux types de matériaux supraconducteurs.

# Contents

# Introduction

## Context and motivation

A lot of engineering applications require the development of electrical devices with high power density involving large magnetic fields. Practical examples of such devices are electrical rotating machines. In these machines, the power density is limited by the maximal current density in the windings and by the magnetic flux density estimated when approaching the saturation state of the ferromagnetic core. Accordingly, increasing the power density in rotating machines requires the use of superconducting materials which are able, at low temperature, to carry high current density values without energy loss. This property paves the way towards partly or completely superconducting electrical rotating machines [1–8]. Nowadays, taking into account the challenge related to the cryogenics, it is well known that the use of superconductors brings advantages mainly for high power machines ($>$ 1 MW) [9].

High power density devices are generally accompanied by high values of stray magnetic field. As a result, it may be necessary to screen them by using a magnetic shield in order to protect the external environment. This is the so-called *emission problem*. Beside rotating machines, other electrical devices generating magnetic flux densities of several teslas require the use of a magnetic shield: let us mention MRI machines [10, 11] and cyclotron for cancer therapy [12–14] in the medical sector, but also accelerator magnets [15–17]. On the other hand, several electrical devices need to be operated at very low ambient magnetic fields. They require efficient shielding techniques to create an ultra low field environment. This is the *immunity problem*. An ultra low field background is desired in high-sensitivity devices like particle detectors [18], Superconducting Quantum Interference Devices (SQUIDs) [19] and various low-field magnetometers [20, 21]. Other areas of engineering also require a low-field environment like DC current transformers [22], biomedical applications [23–25] and space applications [26, 27].

In practice one can distinguish active from passive magnetic shields. Active magnetic shields basically rely on one or several windings supplied with a feedback controlled current that generate a magnetic field that ideally opposes the magnetic field to attenuate. Active magnetic shields are used to reduce the stray field from high power density devices (emission) [2] or to protect highly sensitive instruments operating in the low-frequency range (immunity) [28]. Passive magnetic shields are based on the intrinsic properties of the shield materials to generate their own compensating field or to modify the trajectory of the flux lines. Doing so, the volume enclosed by the shield is characterized by a considerably reduced field magnitude. In this thesis, only passive magnetic shields will be considered.

Passive magnetic shielding can be achieved by using ferromagnetic or conducting materials [29,30]. At high frequency, a good conductor can act as an efficient magnetic shield due to eddy currents induced in the material and opposing the magnetic flux variations. The resulting shielding behavior is thus efficient as long as the thickness of the shield is much larger than the skin depth $\delta$. The skin depth follows a $\delta \sim 1/\sqrt{f}$ dependence. Therefore, in the low-frequency regime ($f < 100$ Hz), conventional conductors become inoperable. In the DC or low-frequency regime, high-permeability ferromagnetic materials (e.g. mu-metal) can be used to provide low-reluctance paths and channel the stray magnetic flux lines. However, under high values of magnetic flux density (typically higher than 2 T), most of the ferromagnetic materials are saturated. Typical permalloys like mu-metal saturate around 0.7 T at room temperature [30,31].

Consequently, in applications involving high values of magnetic field in a low-frequency regime ($f < 100$ Hz), magnetic shields based on conventional ferromagnetic and conducting materials are inefficient. In this regime, superconductors can be used to design efficient passive magnetic shields. In addition to their ability to achieve an ultra-low field environment [26,32], one of the main advantages of superconducting shields over conventional ones is that they are not limited by the saturation magnetization inherent to ferromagnetic materials and can therefore operate at much higher flux densities.

Various superconducting materials can be used to develop passive magnetic shields in the quasi-DC or low frequency regime [33–35]. These are either low-temperature superconductors [36,37] or high-temperature superconductors (HTS). Among the latter, bulk superconductors exhibit constant progress in performance. At a temperature of 20 K, it has been demonstrated that one could shield efficiently a flux density up to 1.5 T using an $YBa_2Cu_3O_7$ (YBCO) tube [38] and up to 1.8 T using a $MgB_2$ cylinder [39,40]. $MgB_2$ has been shown to be very promising for shielding applications at low temperatures as Rabbers *et al.* obtained an efficient shielding up to 2 T at 4.2 K [41]. Fagnard *et al.* demonstrated the shielding ability of $Bi_2Sr_2CaCu_2O_8$ (Bi-2212) up to 1 T at 10 K [42]. If the magnetic shield is to be operated at liquid nitrogen temperature (77 K), melt-textured $(RE)Ba_2Cu_3O_7$ materials (where RE stands for rare earth) enable shielding at the highest fields [43]. One can currently achieve magnetic shielding up to 0.3-0.4 T in volumes of $\sim 1$ cm$^3$ [44,45] which is the current record at 77 K. Higher magnetic fields can be shielded but in tiny gaps of $\sim 1$ mm width [46]. More recently, the shielding properties of bulk bismuth-based cylinders have been studied by Hogan *et al.* in non-uniform magnetic fields [47–49]. Bulk HTS can also be used to design magnetic lenses which are based on the same mechanism than magnetic shielding (shielding currents expelling the magnetic flux) to concentrate flux lines and obtain locally flux densities of several teslas [50, 51]. A second category of interest includes shields made of second generation (2G) coated conductor tapes. Since the shielding process relies on persistent shielding currents, the shield geometry should allow for a closed superconducting path either across the width of the coated conductor [52–56] or using ‘eye-shaped’ closed loops [57–60]. 2G coated conductors were also used to increase the homogeneity of the field by shielding specific field components [61, 62]. The effect of frequency on magnetic shields made of coated conductors has been also widely investigated [25, 81–83]. It has been shown that a combination between superconductors and ferromagnetic materials can improve the shielding efficiency [63–67], sometimes without any flux line distortion (magnetic cloak) [68–71].

Over the last years, efforts have been made to increase the shielded volume, i.e. the volume over which a proper shielding efficiency can be obtained. Several authors report the increase in the size of magnetic shields by juxtaposing bulk materials together [72–74]. However such assemblies still remain problematic at the non-superconducting joints between the samples. Wéra *et al.* demonstrated the possibility to increase the shielded volume using coated conductors in the configuration of ‘eye-shaped’ closed loops [58–60]. In order to increase the typical size of high-temperature superconductors, recent studies showed the possibility of producing a superconducting solder between bulk materials [75, 76] but still fail to recover similar superconducting properties than the initial samples. It is worth mentioning than unlike the quasi-DC regime which requires a perfect superconducting closed path, in the AC regime, a sufficiently weak electrical resistance is allowed [56, 77]. Therefore, a solder between coated conductor tapes is possible to increase the typical size of the shields and several methods to develop a superconducting joint between coated conductor tapes have been investigated [78–80]. Tomków *et al.* report a magnetic shield combining a Bi-2223 bulk cylinder with YBCO tape rings [81]. This kind of shield operates well at frequencies $\gtrsim 20$ Hz but does not offer a closed superconducting path in the YBCO tape.

## Goal of the thesis

Bulk high-temperature superconductors demonstrated the ability to shield high values of magnetic flux density but they are difficult to manufacture as large size samples. Coated conductors can be manufactured over hundreds of meters but an efficient magnetic shield operating in quasi-DC regime would require a closed superconducting path. The goal of this thesis is to investigate methods to combine efficiently the properties of both kinds of materials in order to shield magnetic flux densities over a significant volume. To reach this goal, four objectives will be targeted.

The first objective of this work is to characterize precisely the electric and magnetic properties of both bulk superconductors and coated conductors that will be used. The second objective consists in the experimental investigation of sizeable magnetic shields combining coated conductors and bulk materials. These shields will be studied in configurations of increasing complexity both in terms of symmetry in the shield structure and in terms of uniformity of the applied field. This will give information on the shielding currents distribution as well as on the magnetic flux penetration mechanisms in the investigated structures under uniform and non-uniform applied field.

A third objective is to show how a hybrid (coated conductor + bulk material) structure can be used to screen the stray magnetic field in the vicinity of an electromagnet generating a large DC field.

A final objective of this thesis is to use numerical models dedicated to systems involving type II superconductors to predict the behavior of the investigated structures as well as to gain information on the flux density penetration and the current density distribution in such structures.

## Structure of the thesis

This thesis manuscript is divided in seven chapters.

In Chapter 1, the theoretical background related to superconductivity and magnetic shielding are introduced. In particular, the chapter focuses on the applications of type II superconductors and on the properties of high-temperature superconducting materials. The chapter also presents an overview of the general parameters influencing the magnetic shielding behavior. Finally, theoretical concepts regarding ferromagnetic materials are briefly introduced.

Chapter 2 presents the numerical techniques to model systems involving type II superconductors. In particular, this thesis deals with 2D axisymmetric configurations and 3D models. Therefore, these two cases will be introduced using two different formulations.

Chapter 3 describes the experimental setups developed to characterize the magnetic properties of the magnetic shields as well as the properties of the individual samples. The chapter also presents the sources of uniform and non-uniform magnetic field together with the magnetic sensors involved in the experimental setups.

The chapter 4 is devoted to the detailed characterization of the magnetic and electrical properties of the high-temperature superconducting samples used in this thesis. In particular, we investigate the flux trapping ability of bulk materials as well as their average critical current density. The magnetic properties of coated conductor tapes are also characterized. The knowledge of these properties is crucial to validate the numerical models used in the thesis.

In the first four chapters, the theoretical background, the numerical and experimental techniques to characterize HTS samples and magnetic shielding properties are settled. From this point, the electrical and magnetic properties of the individual samples are known and magnetic shields combining bulk superconductors and coated conductors can be investigated under configurations of increasing complexity.

In Chapter 5, a shield based on annuli of coated conductor tapes is studied in details in uniform external field, applied either parallel or perpendicular to the tapes. The coated conductors are based on a slightly ferromagnetic substrate whose influence on the shielding performance is also discussed. The experimental results are then compared to numerical models taking into account both superconducting and ferromagnetic properties. The chapter also presents the possibility to improve the shielding efficiency of the annuli by using bulk or ‘quasi-bulk’ materials made of stacked tapes.

In Chapter 6, we demonstrate experimentally and numerically the possibility offered by a screen combining bulk materials and coated conductors to screen the non-uniform magnetic field in the vicinity of a source winding. The screen consists of an array of bulk HTS samples, devoted to increase the shielded volume, combined with coated conductor tapes in the shape of closed loops. The latter aims at decreasing the influence of non-superconducting joints between the bulk samples.

Finally, Chapter 7 reports the shielding of the stray magnetic field in the vicinity of a superconducting magnet using an experimental magnetic screen prototype combining bulk samples and coated conductor tapes. This part of the thesis was carried out at the Department of Applied Science and Technology at Politecnico di Torino (Italy).

The last chapter draws the main conclusions and presents perspectives to further improve the shielding efficiency of significant stray magnetic fields by combining bulk materials and superconducting tapes.

# Chapter 1

# Theoretical concepts related to superconductivity and magnetic shielding

In this chapter, we present the theoretical background related to superconductors as well as their application to the magnetic shielding problem. First, the general properties of type I and type II superconductors are introduced with a focus on high-temperature superconductors and their practical applications. The general parameters used to characterize the magnetic shielding efficiency are also presented. Finally, this chapter briefly introduce the basic properties of ferromagnetic materials and especially ferromagnetic hysteresis.

## 1.1 Properties of superconductors

Some of the most striking properties of superconductors are [84]:

- The fact that a superconductor can behave as if it had no measurable DC electrical resistance below a given critical temperature $T_\mathrm{c}$.
- The fact that a superconductor can behave as a perfect diamagnet. A superconducting sample in thermal equilibrium in an applied magnetic field, provided the field is not too strong, carries electrical currents flowing along the surface of the sample. These currents give rise to an additional magnetic field that precisely cancels the applied magnetic field in the interior of the superconductor.

Above the critical temperature $T_\mathrm{c}$, the material is in the normal state but below $T_\mathrm{c}$, the material exhibits superconducting properties like the absence of measurable DC electrical resistance. As a result, below $T_\mathrm{c}$, DC currents can flow within a superconductor without energy dissipation. There are however some limitations:

- Superconductivity can be canceled by applying a sufficiently large magnetic field

- If the current exceeds a 'critical value' $I_\mathrm{c}$ or, in other words, if the current density exceeds the critical current density $J_\mathrm{c}$, the superconductivity is also canceled. This critical current density depends on the nature and the microscopic structure of the specimen, the temperature and the applied magnetic field.
- In the AC regime (i.e. under an AC current or an AC magnetic field), the superconducting material exhibits a finite electrical resistance and thus finite losses. These losses are usually much smaller than those occurring in a conventional material like copper, provided the frequency is not too high [85–88].

All superconducting materials are classified as either *type I* or *type II* superconductors and differ by their behavior in a magnetic field.

### 1.1.1 Type I superconductivity

Earliest theories on superconductivity concern type I superconductors. In addition to the zero electrical resistance under their critical temperature, these materials are characterized by a total field repulsion called the *Meissner effect* [89]. In the superconducting state (also called the Meissner state), any change in the magnetic flux is counterbalanced by macroscopic supercurrents flowing in the material without any resistance. The main characteristic of the Meissner effect is that any magnetic flux already present within the material during the phase transition from normal to superconducting state is expelled. The behavior of type I superconductors (i.e. zero electrical resistance as well as Meissner effect) is described by the two London equations [90].

$$\frac{\partial}{\partial t}\left(\mu_0 \lambda^2 \boldsymbol{J}\right) = \boldsymbol{E}, \tag{1.1}$$

$$\mathrm{curl}\ \left(\mu_0 \lambda^2 \boldsymbol{J}\right) = -\boldsymbol{B}, \tag{1.2}$$

where $\lambda$ is called the *London penetration depth.* At $T = 0$ K, the order of magnitude of $\lambda$ lies within the range 0.1 - 1 $\mu$m [91, 92]. The magnetic permeability of vacuum is constant and is assumed to be equal to $\mu_0 = 4\pi\ 10^{-7}$ [H/m]. It is worth mentioning that the two London equations are phenomenological. In other words, they do not explain how superconductivity occurs. In 1934, Gorter and Casimir proposed the so-called *two-fluid model* postulating the presence of two types of charge carriers contributing to the current density. Besides 'normal' ohmic electrons, the model assumes the existence of lossless super-electrons arising when the material is cooled down to its critical temperature $T_\mathrm{c}$ [93]. The density of super-electrons $n_\mathrm{s}$ in the material is temperature-dependent and is given by

$$n_\mathrm{s}(T) = n_0 \left(1 - \left(\frac{T}{T_\mathrm{c}}\right)^4\right) \qquad \text{for } T \leq T_\mathrm{c}. \tag{1.3}$$

In 1957, Bardeen, Cooper and Schrieffer proposed their microscopic model, the so-called BCS theory [94] considering the super-electrons as pairs of 'normal' electrons with opposite spin referred to as *Cooper pairs*.

Combining the two London equations with the Maxwell equations gives

$$\left(\frac{1}{\lambda^2} - \nabla^2\right) \boldsymbol{B} = 0. \tag{1.4}$$

Eq. (1.4) leads to an exponential decay of the magnetic field from the outer surface toward the core of the superconductor over a characteristic length equal to the London penetration depth $\lambda$.

As already mentioned, the temperature is not the only parameter relevant to initiate the phase transition between the normal and the superconducting phase. The material is in the superconducting state as long as the magnetic field and the current density are not too high. In practice, the superconducting state can be reached if the magnetic field $H$ is lower than a critical field $H_{\mathrm{c}}$ and if the current density is lower than a critical current density $J_{\mathrm{c}}$. Both $H_{\mathrm{c}}$ and $J_{\mathrm{c}}$ are dependent on temperature. In summary, superconductivity arises below a critical surface in the $(T, H, J)$-space as illustrated in Fig. 1.1.

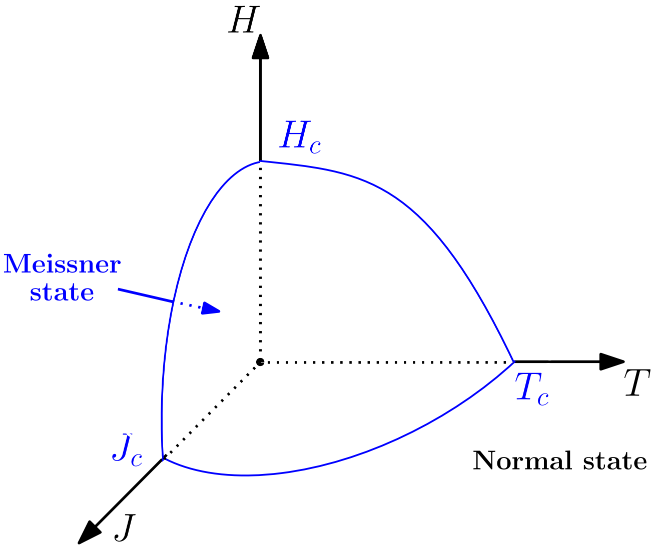

**Figure 1.1:** Illustration of the phase boundary between the normal and the Meissner (superconducting) state for isotropic type I superconducting materials. $H$, $J$ and $T$ are respectively the norm of the magnetic field, the norm of the current density and the temperature.

### 1.1.2 Type II superconductivity

As the critical field in conventional type I superconductors is quite small ($\mu_0 H_c < 0.1$ T), their practical use is rather restricted. Another class of superconducting materials called type II superconductors exhibits an intermediate state between the Meissner state and the normal state called the *mixed (or 'vortex') state*. We can distinguish two kinds of type II superconductors based on their critical temperatures. Low-temperature superconductors (LTS) are materials with a typical $T_c$ less than 20 K. They generally consist of metallic alloys like NbTi or $Nb_3Sn$. Due to their lower critical temperature, these superconductors usually require the use of liquid helium. Superconductors with a typical $T_c$ greater than 20 K are called high-temperature superconductors (HTS) and include different kinds of materials. In addition to $MgB_2$ ($T_c \approx 39$ K), some of the most popular HTS are basically ceramics and only require the use of liquid nitrogen (much cheaper than liquid helium) to reach their operating temperature.

#### Phase diagram

Type II superconductors are characterized by two critical magnetic fields $H_{c1}$ and $H_{c2}$ respectively called the lower and the upper critical field as shown in Fig. 1.2. For $H < H_{c1}(T)$, the material is in the Meissner state and is characterized by magnetic flux expulsion similarly to type I superconductors. For $H > H_{c2}(T)$, the material is no longer superconducting. The case in which $H_{c1}(T) < H < H_{c2}(T)$ corresponds to the mixed state: the magnetic flux penetrates but the material is still superconducting (with no measurable resistance).

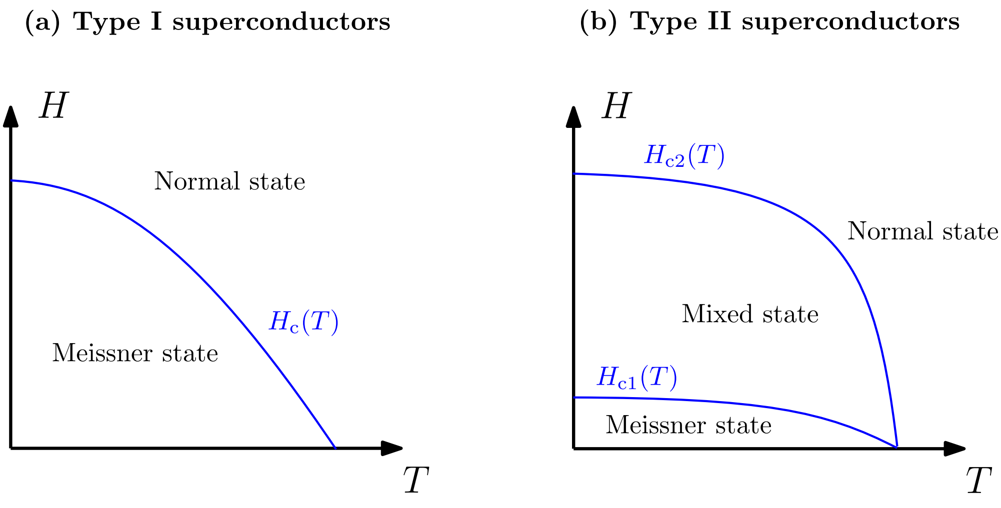
(a) Type I superconductors

(b) Type II superconductors

**Figure 1.2:** Phase diagrams of type I and type II superconductors in the $J = 0$ plane.

In the mixed state, the magnetic flux penetrates partially the superconductor in the form of thin filaments called vortices. A vortex consists in a core in which the flux density is strong and the material is in its normal state. The core of the vortex has a radius $\xi$ called the *coherence length* and is surrounded by flowing super-currents over a characteristic length $\lambda$. Each vortex carries a magnetic flux $\phi_0 = h/2e \approx 2.07\ 10^{-15}$ Wb called the flux quantum, where $h = 6.62\ 10^{-34}$ Js denotes the Planck constant and $e = 1.6\ 10^{-19}$ C is the electron charge. In an homogeneous superconductor, vortices arrange themselves in an hexagonal array called the Abrikosov lattice as shown in Fig. 1.3.

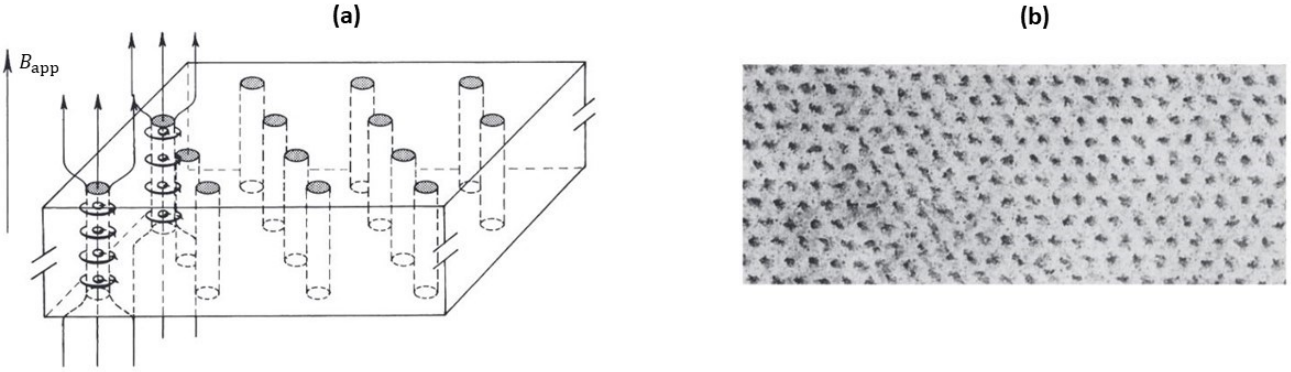

**Figure 1.3:** (a) Schematics of the vortex lattice in a type II superconductor and (b) image of the Abrikosov lattice obtained by electron microscopy thanks to magnetic flux decoration with iron colloids (from [108]).

### Flux flow and irreversible superconductors

The theoretical concepts described so far about type II superconductivity only refer to superconductors in which vortices are free to move. Those are called *reversible* (or *soft)* superconductors. If an electrical current flows in the material, vortices are subjected to a 'Lorentz-like' force $F_{\text{L}}$ given by

$$\boldsymbol{F}_{\text{L}} = \boldsymbol{J} \times \boldsymbol{B}, \tag{1.5}$$

where $\boldsymbol{J}$ is the electrical current density and $\boldsymbol{B}$ is the magnetic flux density which has penetrated the material. This force gives rise to a movement among the vortices (called *flux flow*) and thus a non-zero variation of the magnetic flux density $\frac{dB}{dt}$. Therefore, the induced electromotive force leads to losses in the material and the appearance of a non-zero electrical resistivity. As a result, reversible superconductors have little interest for engineering applications.

In order to prevent the flux flow in the material and the resulting energy dissipation, the vortices need to be pinned in the material. In practice, this pinning is achieved by defects and inhomogeneities in material which act as *pinning centers.* These pinning centers generate a pinning force $F_{\text{p}}$ on the vortex lattice and prevent any motion of the flux lines as long as $F_\mathrm{L} < F_\mathrm{p}$. Superconductors experiencing flux pinning are called *irreversible* (or *hard*) superconductors. When a transport current flows in the superconductor, the critical current density $J_\mathrm{c}$ can be seen as the current density at which the Lorentz force exceeds the pinning force and causes flux motion. Similarly, some type II superconductors exhibit a threshold field at which the vortices stop being pinned in the material. Beyond this field called the irreversibility field $H_\mathrm{irr}$, the vortices are free to move.

### The Bean model

When considering a reversible superconductor (in which vortices are free to move) submitted to an applied external field, the magnetic flux penetrates partially the material (vortex state) and the vortices are found to be uniformly distributed following the Abrikosov lattice illustrated in Fig. 1.3. However this uniform distribution does no longer hold if we consider an irreversible superconductor. Indeed the anchoring of vortices in the pinning centers gives rise to a non-uniform magnetic flux in the material.

The Bean model [95], or *critical state* model gives a rather simple description of how the flux penetrates a superconductor with strong pinning. The flux density is modeled as satisfying the general equation:

$$|\nabla \times \langle \boldsymbol{B}(\boldsymbol{r}) \rangle| = \mu_0 J_\mathrm{c}, \tag{1.6}$$

where $\langle \boldsymbol{B}(\boldsymbol{r}) \rangle$ is the average of the magnetic flux density over a large number of vortices. In other words, the Bean model states that any region in which we have a magnetic flux density variation will be the place of an induced current density equal to its maximal value, the critical current density. As a result, the curl of the average flux density can only take three values: $+\mu_0 J_\mathrm{c}$, $-\mu_0 J_\mathrm{c}$ or 0. The current density is 0 for regions that have never felt any magnetic flux density variation. The + or - sign depends on the direction of the magnetic flux density variation. Besides the strong pinning approximation, the Bean model also makes the following hypotheses: the applied magnetic field $H_\mathrm{app}$ is uniform, the lower as well as the upper critical fields are neglected: $H_\mathrm{c,1} = 0$ A/m and $H_\mathrm{c,2} \mapsto \infty$; the critical current density is assumed to be field-independent.

Figure 1.4 describes the distribution of the flux density considering the Bean model in a slab infinitely long in the direction of the applied field $H_\mathrm{app}$. As the applied field exceeds the lower critical field $H_\mathrm{c,1}$ (assumed to be zero in the scope of the Bean model), vortices are thermodynamically favored to penetrate the material from the boundaries toward the center. Under these assumptions, the flux density evolves linearly from the outside boundary to the center of the slab. In the situation 1 depicted in Fig. 1.4(a), the flux has not reached the center yet and the critical current only flows in the region which experiences a certain magnetic flux. At an applied field of $H_\mathrm{app,2}$, the sample is completely

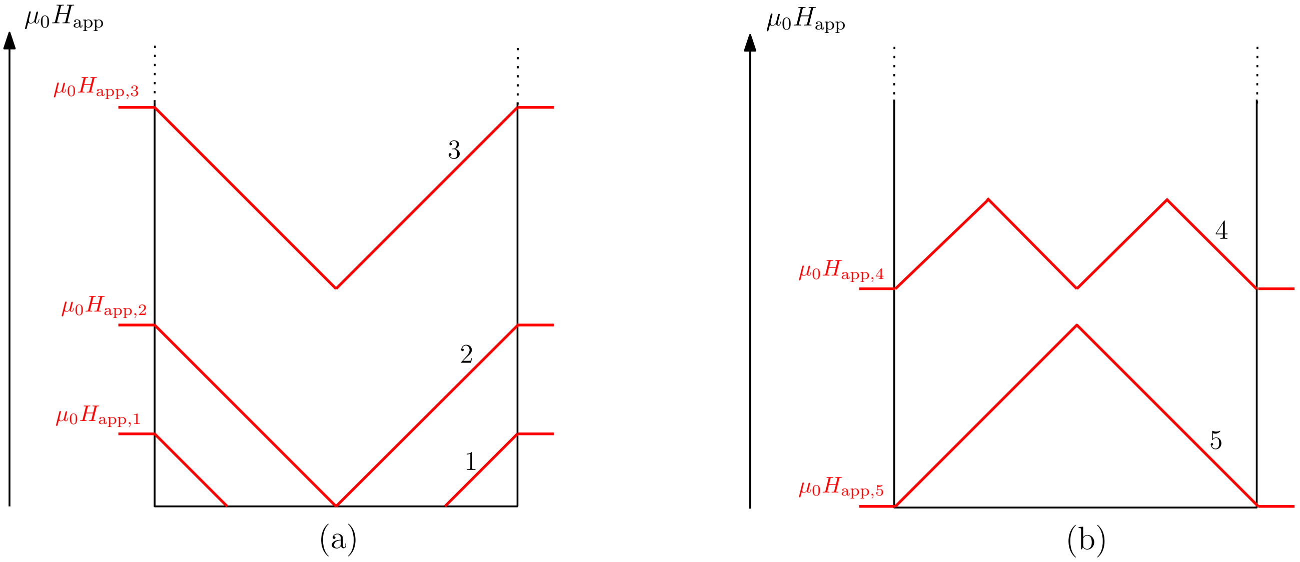

(a) (b)

**Figure 1.4:** Distribution of the magnetic flux density in an infinite superconducting slab in the framework of the Bean model. The applied field is first increased up to $\mu_0 H_{\rm app,3}$ (a) and then decreased down to $\mu_0 H_{\rm app,5} = 0$ T (b).

penetrated and the applied field $H_{\rm app,2}$ is often referred to as the full penetration field $H_{\rm p}$. Ampere's law directly gives $H_{\rm p} = dJ_{\rm c}/2$ where $d$ is the width of the slab. The decrease of the applied field leads to the linear distribution illustrated in Fig. 1.4(b). When the applied field is equal to $H_{\rm app,5} = 0$ A/m, a persistent critical current density continues to flow permanently in the material and the superconductor remains magnetized. Figure 1.5(a) and (b) show the average magnetic flux density and the magnetization, respectively.

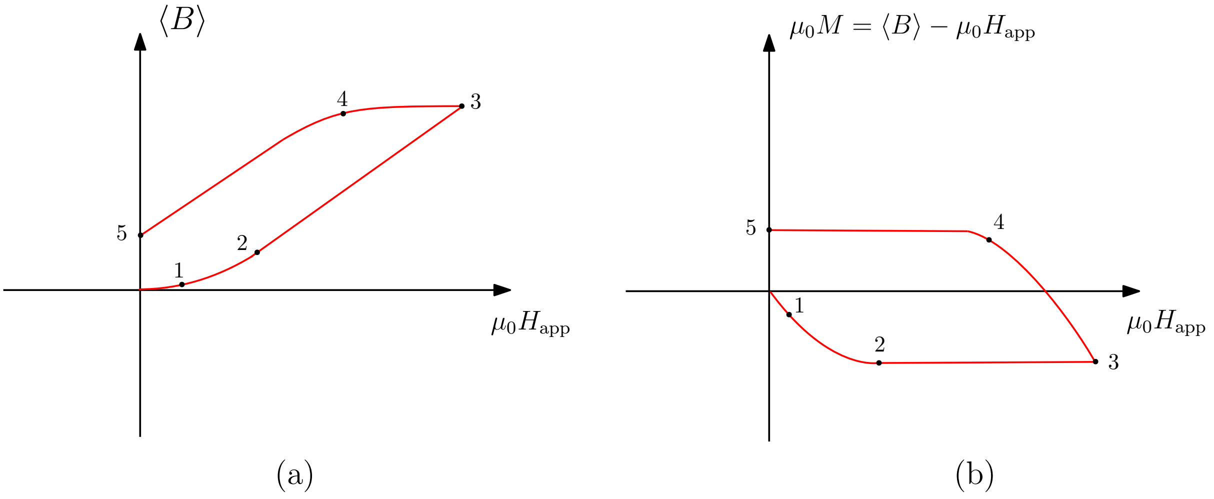

(a) (b)

**Figure 1.5:** (a) Volume average of the magnetic flux density as well as the (b) magnetization as a function of the applied field $H_{\rm app}$.

### Flux creep and power law model

The Bean model assumes that the magnetic state of a type II superconductor does not vary with time. In other words, when the magnetic flux has penetrated the material, the vortices will remain trapped in their pinning centers permanently and a current density equal to $J_c$ flows without any change. In practice, at finite temperature, due to thermal excitation and Lorentz force, some vortices are allowed to leave their pinning centers generating losses in the material even for $J < J_c$. This phenomenon is called the flux creep. Macroscopically the flux creep causes the flux density profile to smoothen over the time as the flux tends to leave the material through the outside boundaries.

Several models have been developed to describe as completely as possible the phenomena related to flux creep. These flux creep models are based on different $U(J)$ relationships, where $U$ is the activation energy of a vortex and $J$ is the current density [96]. For example, we can cite the Anderson-Kim model [97, 98] or the collective flux creep model [99]. In this thesis, we consider the flux creep model describing the behavior of HTS materials proposed by Zeldov [100]. This model assumes the activation energy to be a logarithmic function of the current density. The relaxation of the magnetic moment over time is sometimes approximated by the following power law [96, 101]:

$$m(t) = m_0 \left(1 + \frac{t}{t_0}\right)^{\frac{1}{1-n}}. \tag{1.7}$$

In Eq. (1.7), $m_0$ is the initial magnetic moment and $t_0$ is a characteristic time usually chosen as $t_0 = 1$ s or less. The *critical exponent* $n$ is defined as the ratio between the pinning energy barrier (activation energy) and the thermal energy [100].

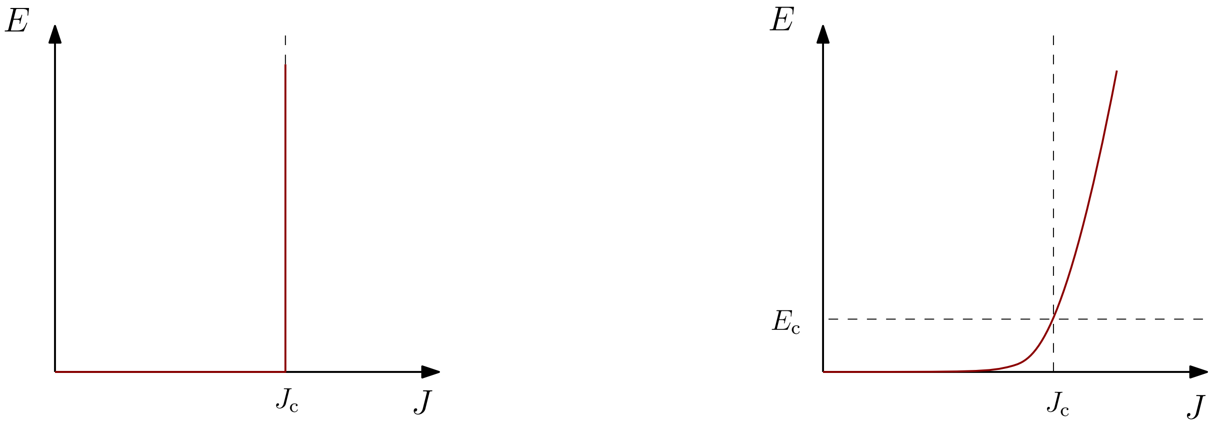

(a) Bean model (b) Flux creep

**Figure 1.6:** (a) $E(J)$ relationship predicted by the Bean model. (b) $E(J)$ relationship taking the flux creep into account.

One consequence of the flux creep, is the existence of an electric field even for current densities lower than $J_\mathrm{c}$ as illustrated in Fig. 1.6. Therefore, we need a criterion to define the critical current density. To do so, we introduce a threshold electrical field $E_\mathrm{c}$ at which we consider that $J = J_\mathrm{c}$. By convention, we often choose this threshold as $E_\mathrm{c} = 10^{-4}$ V/m.

At the macroscopic scale, the relationship between the electrical field and the current density is observed to be highly non linear. In practice, it can be modeled by the following power law [102–104]:

$$\boldsymbol{E}(\boldsymbol{J}) = \frac{E_\mathrm{c}}{J_\mathrm{c}} \left( \frac{\|\boldsymbol{J}\|}{J_\mathrm{c}} \right)^{n-1} \boldsymbol{J}. \tag{1.8}$$

The critical exponent $n$ describes the sharpness of the transition between the pinned state and the flux flow. When $n = 1$, the power law (1.8) is linear and corresponds to the Ohm's law. When $n \mapsto \infty$, the power law degenerates to the behavior predicted by the Bean model. In practice, the value of critical exponent lies between $n \sim 40 - 60$ for LTS like NbTi or Nb$_3$Sn and $n \sim 25 - 50$ for HTS like (RE)BCO or bismuth-based materials [104, 105]. Figure 1.7 shows the $E$-$J$ behavior for different values of $n$ between the two degenerated cases $n = 1$ and $n \mapsto \infty$.

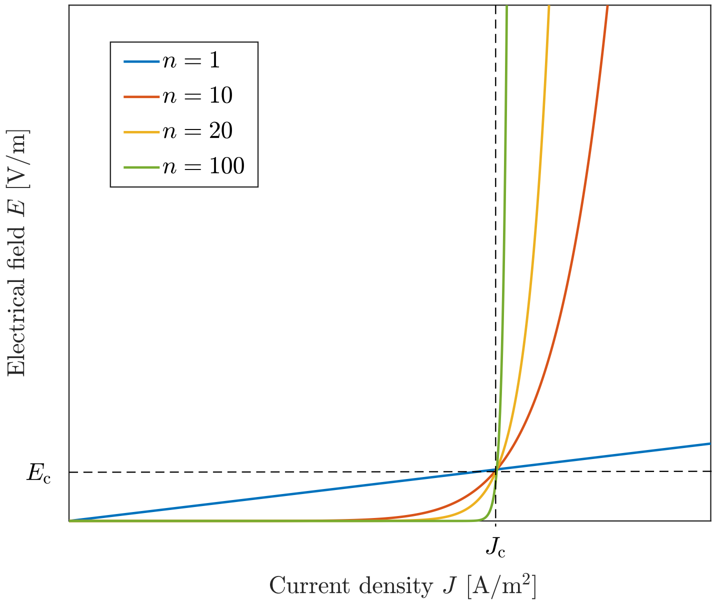

**Figure 1.7:** $E$-$J$ behavior for type II superconductors following the power law given by Eq.(1.8). Comparison for different values of $n$.

### The Kim law

As already mentioned, the previous considerations including the Bean model assumed a completely field-independent critical current density $J_\mathrm{c}$. However, it was observed that the critical current density decreases as the magnetic flux density increases. Kim *et al.* [106]

proposed a simple model assuming an hyperbolic decrease of the critical current density as a function of the magnetic flux density $B$:

$$J_\mathrm{c}(B) = J_{\mathrm{c},0}\left(1+\frac{B}{B_0}\right)^{-1}, \tag{1.9}$$

where $B$ is the norm of the magnetic flux density. $J_{\mathrm{c},0}$ and $B_0$ are two fitting parameters that can be estimated from experimental measurements of $J_\mathrm{c}(B)$.

## 1.2 Superconducting materials and applications

In this section, the most popular type II superconducting materials are introduced. They are classified in two categories depending on their critical temperature: low-temperature superconductors and high-temperature superconductors.

### 1.2.1 Low-Temperature Superconductors (LTS)

LTS are superconductors with a critical temperature below 30 K. These materials typically require liquid helium cooling ($T \approx 4.2$ K) to operate. The relative simplicity of manufacturing wires over many kilometers length as well as their good stability in carrying high current make them vary attractive candidates for high-field magnet applications: magnetic resonance imaging (MRI), Large Hadron Collider (LHC), thermonuclear reactor, etc. [107, 108].

The major industrially produced LTS are Nb-based compounds. NbTi alloy is the most predominant material for applications involving superconducting wires. The great technological interest of NbTi lies in its highly optimized microstructure which favors flux pinning and thus in-field current capability [107]. Its critical temperature is around 9.2 K [109] and its upper critical field is around $\mu_0 H_{\mathrm{c},2} \approx 11.4$ T at 4.2 K but decreases rapidly with temperature [110]. Its relatively low $H_{\mathrm{c},2}$ limits the interest of NbTi under high magnetic field. The $\mathrm{Nb_3Sn}$, discovered by Matthias *et al.* in 1954 [111] is characterized by $T_\mathrm{c} = 18.3$ K and $\mu_0 H_{\mathrm{c},2} = 32$ T at zero temperature [112, 113]. This compound is thus more suitable for high-field applications than NbTi. However, due to its brittleness and low strain tolerance, $\mathrm{Nb_3Sn}$ compound is difficult to process and the NbTi remains the preferred LTS for relatively low-field applications.

### 1.2.2 High-Temperature Superconductors (HTS)

#### Overview of HTS materials

High-Temperature superconductors refer to superconductors with a critical temperature $T_\mathrm{c} > 20$ K. HTS materials emerged in 1986 with the discovery of superconductivity (at liquid nitrogen temperature) in cuprates (superconductors consisting of planar copper-oxide layers). So far, huge advances have been made to produce cuprate superconductors with $T_\mathrm{c} > 77$ K (liquid nitrogen temperature).

Some of the most promising HTS materials for application at 77 K are (RE)$\mathrm{Ba_2Cu_3O_{7-x}}$ (often abbreviated REBCO) where (RE) refers to as a rare earth element which can be yttrium (Y), gadolinium (Gd), lanthanum (La),... These materials are characterized by a critical temperature of approximately 93 K [113]. Another kind of cuprates, namely bismuth-based materials, are also extensively studied HTS. Bi-based cuprates include $\mathrm{Bi_2Sr_2Ca_2Cu_3O_{10}}$ often abbreviated Bi-2223 which exhibit a critical temperature $T_\mathrm{c} \approx 110$ K [49, 113] and $\mathrm{Bi_2Sr_2CaCu_2O_8}$ (Bi-2212) with a critical temperature of $T_\mathrm{c} \approx 82 - 95$ K [49,115,116]. Moreover, cuprate superconductors are characterized by an upper critical field greater than 50 T at $T = 0$ K [117,118]. Besides cuprates, let us cite the magnesium diboride $\mathrm{MgB_2}$ as a material of interest for applications involving HTS. It is characterized by $T_\mathrm{c} = 39$ K [119, 120] and $\mu_0 H_{\mathrm{c},2} \approx 25 - 30$ T at $T = 4.2$ K [121]. By contrast with cuprates, $\mathrm{MgB_2}$ cannot be used in liquid nitrogen and requires either liquid helium or a cryocooler to operate. As a result $\mathrm{MgB_2}$ is sometimes referred to as a low-temperature superconductor.

### Irreversibility line

As introduced in Section 1.1.2, a superconductor is only efficient in the irreversible state in which the flux lines are pinned in impurities inserted in the material. This state can only be observed as long as the magnetic field is sufficiently low so that the pinning forces exceed the Lorentz force acting on the vortices. As a result, in addition to $H_{\mathrm{c},1}(T)$ and $H_{\mathrm{c},2}(T)$, we introduce the *irreversibility line* $H_\mathrm{irr}(T)$ as shown in Fig. 1.8. Between $H_{\mathrm{c},1}(T)$ and $H_\mathrm{irr}(T)$, the superconductor is in the irreversible state. On the contrary, between $H_\mathrm{irr}(T)$ and $H_{\mathrm{c},2}(T)$ the superconductor acts like a reversible type II superconductor. Among the REBCO cuprates, $\mathrm{YBa_2Cu_3O_7}$ is appropriate for high-field applications as its irreversibility field at 77 K is $\mu_0 H_\mathrm{irr} \approx 5$ T whereas bismuth-based superconductors become reversible at a considerably lower field ($\mu_0 H_\mathrm{irr} < 0.3$ T at 77 K) [122] and thus require an operating temperature $T < 77$ K in order to increase $\mu_0 H_\mathrm{irr}$ up to a few teslas.

### Granularity and anisotropy

In typical cuprate high-temperature superconductors, several intrinsic parameters may strongly influence the critical current density and thus affect macroscopic properties like magnetic shielding efficiency or flux trapping. Most of the time HTS materials consist of ceramics and have a strongly polycrystalline structure. They are composed of several superconducting grains juxtaposed one to each other but with potentially different crystallographic axes. At the grain boundaries, the superconductivity drops drastically. These

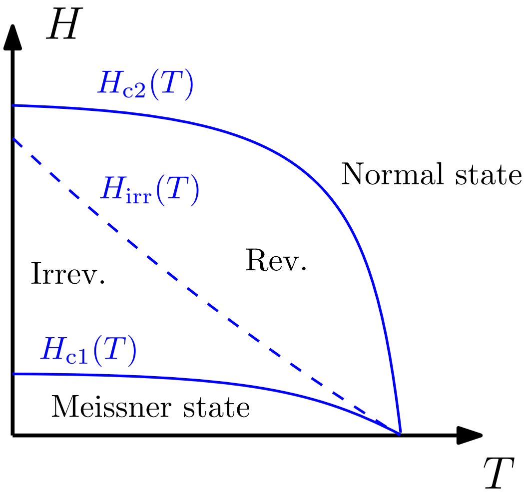

**Figure 1.8:** Phase diagram in the $(H, T)$ plane $(J = 0)$ of a type II superconductor with the irreversibility line.

boundaries are defects in the material and can act as pinning centers for the flux lines. As a result, we can distinguish two kinds of current density: the intragrain current density induced within each superconducting grain and the intergrains current density flowing in the whole sample as illustrated in Fig. 1.9.

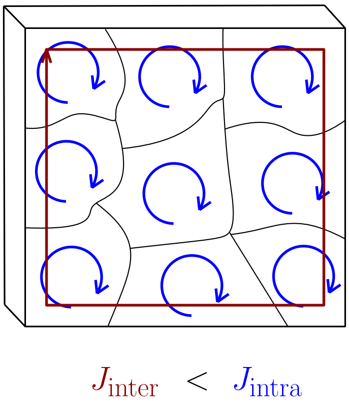

**Figure 1.9:** Illustration of the intragranular and the intergranular currents in the polycrystalline structure of a bulk HTS.

As the intergranular current flows across a large number of grain boundaries (acting as *weak links*), the magnitude of the intergranular critical current density may be several orders of magnitude lower than the intragranular critical current density. Accordingly, practical HTS cuprates need to be textured to reduce the misorientation angle between adjacent grains and optimize the critical current density. The so-called coated conductors basically consist of a very thin textured HTS layer and are usually characterized by a better critical current density than bulk HTS. On the other hand, advanced processing methods allow to synthesize single grain HTS materials with a significantly increased critical current density.

Another element affecting the properties of cuprate HTS is the anisotropy of the material. The crystallographic lattice is an orthorhombic structure which consists of multiple $CuO_2$ coplanar layers. In the superconducting state, the current flows within the $CuO_2$ planes leading to highly anisotropic properties. The plane parallel to the $CuO_2$ planes is often called the $(a, b)$-plane. The normal axis to these planes is called the $c$-axis. The best material efficiency for applications would be obtained in configurations in which the current density flows within the $(a, b)$-plane [123]. The magnetic properties are also affected by the crystal anisotropy. For example, for YBCO, $\mu_0 H_{\mathrm{irr}}$ parallel to the $(a, b)$-plane is more than twice $\mu_0 H_{\mathrm{irr}}$ parallel to the $c$-axis [124].

### 1.2.3 Applications of High-Temperature Superconductors

#### Bulk HTS

High-temperature superconductors manufactured in the shape of bulk monoliths have a great potential for electric and magnetic applications, in particular involving high magnetic fields. Bulk HTS can be used in magnetic bearings, levitated trains, rotating machines or as permanent magnets. Due to their strong flux pinning energy and high critical temperature (90-95 K), REBCO compounds are definitely promising for bulk applications at an operating temperature of 77 K. However, their highly polycrystalline structure strongly limits the critical current density due to the presence of numerous grain boundaries acting as weak links in the material. Therefore, bulk REBCO superconductors need to be textured in order to obtain single grain materials and minimize the number of weak links. To do so, several processing techniques can be used. The most established and widely used technique is the so-called Top Seeded Melt Growth process (TSMG) [125]. However, even if the TSMG technique enables to obtain high-$J_{\mathrm{c}}$ superconductors, it may lead to a number of macro-defects like voids, pores and cracks in the material [126–129]. The defects are less numerous by using optimized Top Seeded Infiltration Growth (TSIG) techniques [129, 130]. Regarding the critical current density at 77 K, bulk REBCO HTS can exhibit typical $J_{\mathrm{c}}$ from $10^7$ A/m$^2$ [131–133] up to $J_{\mathrm{c}} > 10^9$ A/m$^2$ for the best ones [134]. Bulk REBCO materials are well adapted to high-field engineering applications like low-loss magnetic bearings [135, 136], flywheel energy storage systems [136–138] or high-field magnets [139]. The field trapping ability of bulk REBCO has been highlighted by Tomita & Murakami, who achieved a trapped flux density of 17.24 T at 29 K in YBaCuO [140] and by Durrell *et al.* who obtained a trapped flux density of 17.6 T at 26 K in bulk GdBaCuO samples [141]. Under such high magnetic fields, bulk superconductors are limited by their mechanical tensile strength due to the large Lorentz force taking place in the material. As a result, the samples need to be reinforced by using, for instance, epoxy resin impregnation [140] or stainless steel rings [141]. Finally, due to their significant flux trapping properties, REBCO bulk superconductors have a strong potential for the design of efficient synchronous electric motors [142].

Bismuth-based materials (Bi-Sr-Ca-Cu-O or BSCCO) have a quite high critical temperature: up to 90 K for Bi-2212 and 110 K for Bi-2223. When they are used as bulk superconductors, bismuth compounds are generally manufactured as bulk tubes by isostatic pressing for Bi-2223 [143] or melt cast process for Bi-2212 [144]. Due to their low irreversibility field and the strong field dependence of their critical current density, bulk BSCCO are generally unsuitable for high field applications [108, 122]. However, BSCCO tubes can be used to trap magnetic field with very few flux relaxation [143] or for magnetic shielding applications [49, 60, 145].

Finally, let us mention the magnesium diboride $MgB_2$ which is also widely used as a bulk material. Although its critical temperature (39 K) is much smaller than that of BSCCO and REBCO compounds, its metallic structure and the absence of weak link behavior result in quite simple and cost-effective techniques to fabricate large bulk samples [146]. $MgB_2$ can be processed by hot-pressing of ball-milled Mg and $B_2$ powders [147,148], reactive liquid Mg infiltration [149] or field-assisted sintering technique [39,150,151]. $MgB_2$ exhibits a typical critical current density of $J_c > 10^8$ A/m$^2$ at 20 K [152]. Applications of bulk $MgB_2$ include magnetic field trapping (up to 5.4 T at 12 K [147]), magnetic levitation [153] and magnetic shielding [39–41, 66, 67, 154].

### Wires and tapes

The very first superconducting cables consisted of LTS materials like $Nb_3Sn$ thanks to the so-called *Powder-in-Tube* (PIT) technology [155]. This technology allowed to achieve high critical current density ($> 1000$ A/mm$^2$) and good mechanical properties [156]. Since the discovery of high-temperature superconductivity, scientists have shown great interest in developing superconducting flexible wires working at liquid nitrogen temperature. First HTS wires were made of bismuth-based materials (Bi-2212 or Bi-2223) [158–160]. Wires based on BSCCO superconductors were called first generation (1G) wires. Due to the relatively high cost of 1G wires, second-generation (2G) wires have been developed using REBCO superconductors [157]. These 2G HTS wires (often called HTS tapes) are based on a multilayer thin film architecture. A thin layer (1-2 microns) of REBCO is deposited on a metallic substrate using specific deposition techniques. The superconducting layer is separated from the metallic substrate by several buffer layers. In order to obtain a critical current density as high as possible, it is crucial to texture the REBCO layer. The two principal techniques used to obtain robust, long-length 2G wires are the Ion Beam Assisted Deposition (IBAD) [162,163] and the Rolling Assisted Biaxially Textured Substrate (RABiTS) technique [161]. The HTS layer is then deposited on the textured substrate, reducing significantly the presence of weak links. The resulting wires are often called 2G coated conductors.

Coated conductors have been used in several kinds of applications. Typically Bi-2212 has been widely used in accelerator magnets applications [164]. REBCO coated-conductors have been involved in the design of Roebel cables [165], Cables on Round Core (CORC®) [166,167] and cables with twisted stack of tapes [168,169]. Finally, recent studies have demonstrated the ability of HTS coated-conductor tapes to be stacked in order to obtain 'quasi-bulk' superconducting samples for applications including superconducting magnets and magnetic levitation [170–172]. The consequent advantage of using such quasi-bulk HTS instead of conventional bulk superconductors is that they present much improved mechanical and thermal stability and are promising to design much larger samples.

### Thin films

Several specific applications require high quality thin superconducting films. Accordingly, the disposition techniques remain an active research area. In particular, due to their rather uniform superconducting properties and their very low surface resistance, HTS thin films are well adapted for electronic and microwave applications. In particular, at microwave frequency range, the surface resistance of HTS materials is about 1000 times less than conventional conducting metals (Cu, Ag, etc.). As a result, HTS films can be used to design microwave filters with very good properties: narrow bandwidth, high out-of-band rejection, very low insertion loss, ... [173,174]. Applications involving Josephson junctions also require high quality thin superconducting films. For example Josephson junctions can be used for THz range antennas [175] or for extremely sensitive magnetometers like Superconducting Quantum Interference Devices (SQUID) [19]. The challenge of current and future applications is that they set extremely high requirements for the deposition of HTS thin films: perfect stoichiometry, perfect epitaxial growth, avoidance of defects and contaminants decreasing superconducting properties and avoidance of grain boundaries [176].

## 1.3 Properties of superconducting magnetic shields

### 1.3.1 Principles of passive magnetic shielding

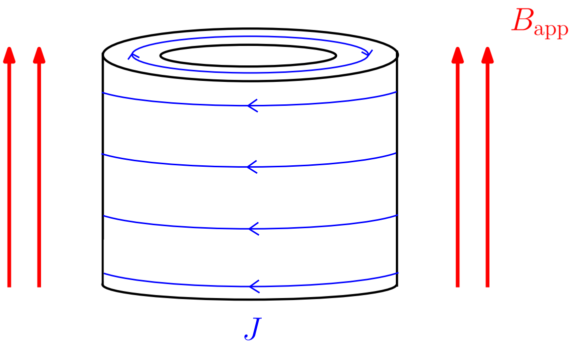

**Figure 1.10:** Illustration of the macroscopic shielding current induced in a superconducting cylinder under an axial applied field.

As illustrated schematically in Fig. 1.10 the magnetic shielding is due to macroscopic currents induced in the superconducting material under an applied field $B_{\text{app}}$. Due to the zero DC electrical resistance of the shield, the shielding currents are persistent and even a ‘quasi-DC’ magnetic field can be shielded. This would be impossible with conventional conducting materials. Moreover, unlike ferromagnetic materials, superconductors do not suffer from the magnetic saturation phenomenon and can shield much higher flux densities. The shielding efficiency depends on several parameters: the geometry of the shield, the material properties ($J_c(B)$, $E(J)$ law, ...) and the application rate of the applied field ($dB_{\text{app}}/dt$). In general, the shielding efficiency is characterized by two parameters: the shielding factor and the threshold flux density.

#### Shielding factor and threshold flux density

The shielding factor is a direct measurement of the efficiency of a magnetic shield. Several definitions of the shielding factor can be found in the literature. In this thesis, we define the shielding factor at a given location as the ratio between two magnetic fields measured at this location: the applied magnetic field (i.e. the field measured without any shield) $B_{\text{app}}$ and the field measured in the shield $B$:

$$SF = \frac{B_{\text{app}}}{B}. \tag{1.10}$$

Instead of one specific location point, the shielding factor can also be defined for a given volume (called the *shielded volume*). Experimental methods devoted to increase the shielded volume have been investigated by Wéra *et al.* [58–60].

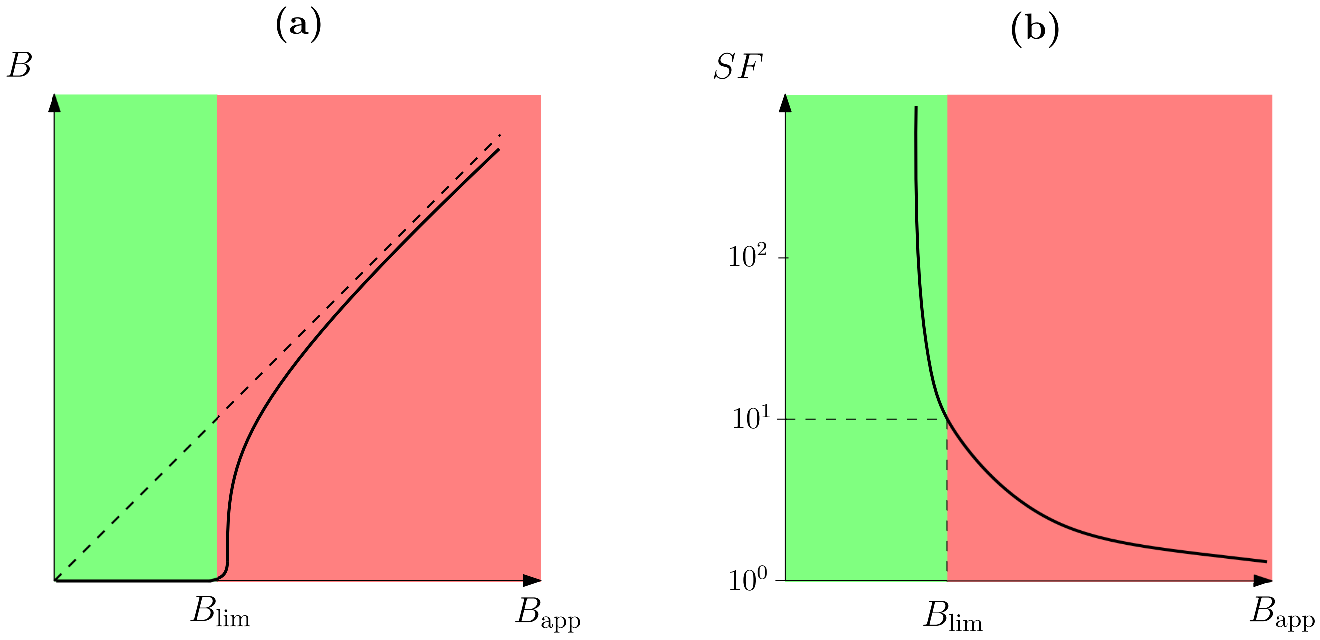

**Figure 1.11:** (a) Typical shielding curve and (b) evolution of the shielding factor as a function of the applied field. The threshold flux density $B_{\text{lim}}$ is defined here for $SF = 10$.

The threshold flux density $B_{\text{lim}}$ is defined as the applied flux density beyond which the $SF$ is lower than an arbitrarily chosen value. In other words, we consider that for an applied field greater than $B_{\text{lim}}$, the shield becomes inefficient. The $SF$ value for which $B_{\text{lim}}$ is defined is chosen depending on the specific application that is investigated. Figure 1.11 illustrates the definition of the shielding factor $SF$ and the threshold flux density $B_{\text{lim}}$ (here defined for $SF = 10$). This figure shows the typical evolution of the shielded field $B$ as a function of the applied field $B_{\text{app}}$ as well as the corresponding evolution of the shielding factor. The green region for $B_{\text{app}} < B_{\text{lim}}$ is the region where the shield is considered to be effective. In this region the shielded field is small compared to the applied field which leads to high values of shielding factor. On the contrary, the red region for which $B_{\text{app}} > B_{\text{lim}}$ corresponds to the applied field range in which the shield is no longer effective. The shielding factor is small and decreases asymptotically to $SF = 1$ with $B_{\text{app}}$.

### 1.3.2 Magnetic shielding in the critical state hypothesis

A simple and intuitive representation of the penetration of the magnetic field in a superconducting shield as well as the current density distribution in the material can be obtained in the framework of the critical state model (or the Bean model). Let us consider a long hollow cylindrical shield in a homogeneous applied field parallel to the axis of the shield. The hypotheses under which the Bean model is valid have already been introduced in Section 1.1. The field increases monotonously from 0 to its maximal value.

The distribution of the magnetic flux density in the shield for different levels of applied

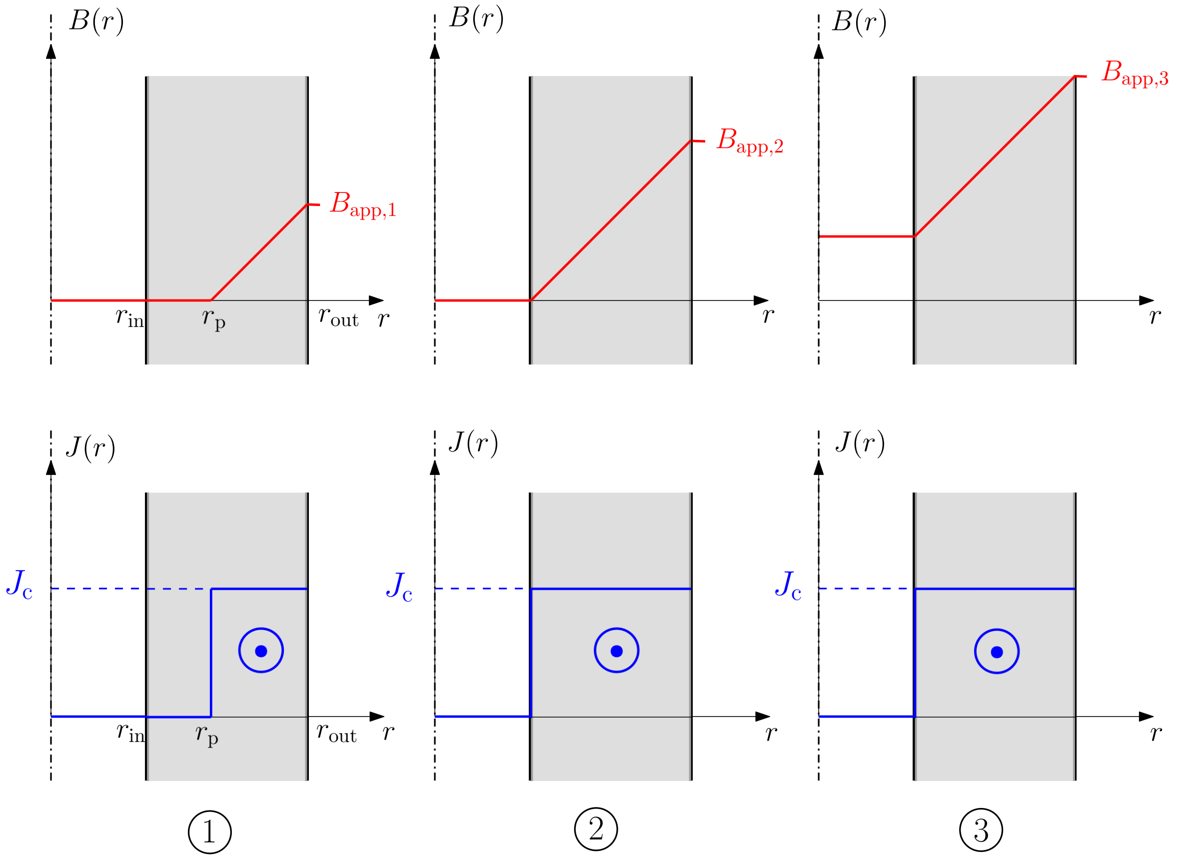

**Figure 1.12:** Radial distribution of the flux density and current density in a hollow cylindrical shield for an increasing external applied field. The field is homogeneous and is applied in the axial direction. The analysis is performed under the critical state hypothesis.

field as well as the corresponding current density are illustrated in Fig. 1.12. The cylinder internal and external radii are respectively $r_{\text{in}}$ and $r_{\text{out}}$. When the applied field increases, the flux penetrates the cylinder from the external surface. The region $r_{\text{in}} < r < r_{\text{p}}$ corresponds to the part of the shield which has not been penetrated yet. In this region, no current flows in the material. For $r_{\text{p}} < r < r_{\text{out}}$, the penetrated flux density evolves linearly with the radial position. When the applied flux density is equal to $B_{\text{app},2}$, the shield is fully penetrated and shielding currents flow in the whole material. A further increase of the applied field results in an increase of the field at the center of the shield $B_{\text{in}}$.

From this analysis, we easily understand that the threshold flux density is given by the full penetration field i.e. $B_{\text{app},2} = B_{\text{lim}}$. As shown in Fig. 1.13, in the critical state assumption, the threshold magnetic field is the applied field which leads to a non-zero $B_{\text{in}}$. In other words, the shielding factor defined by $SF = \frac{B_{\text{app}}}{B_{\text{in}}}$ is infinite for $B_{\text{app}} \leq B_{\text{lim}}$ and takes finite values for $B_{\text{app}} > B_{\text{lim}}$. Under these assumptions, the threshold flux density can be easily calculated and is equal to

$$B_{\text{lim}} = \mu_0 J_{\text{c}} (r_{\text{out}} - r_{\text{in}}). \tag{1.11}$$

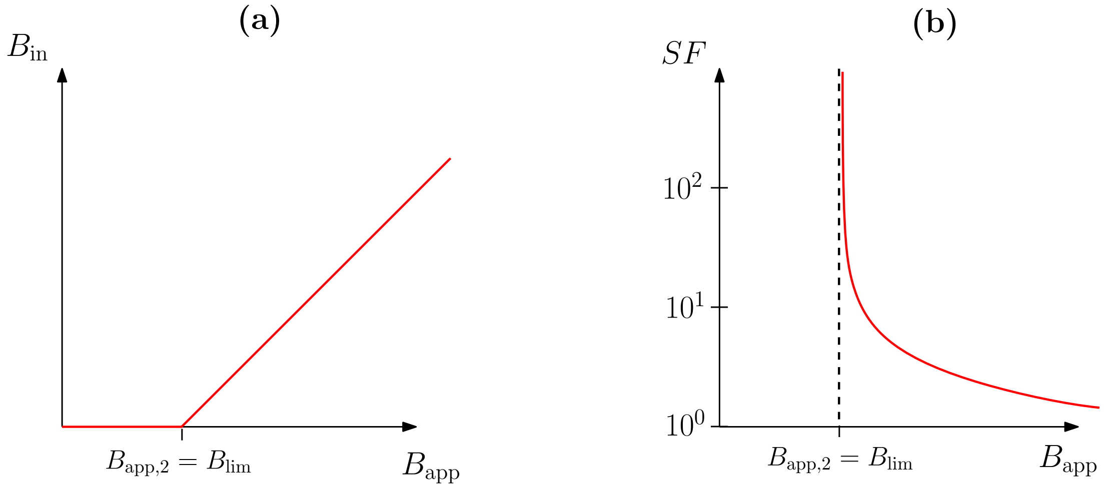

**Figure 1.13:** Evolution of (a) the magnetic flux density and (b) the shielding factor measured at the center of the shield ($r = 0$) with the external applied flux density under the critical state hypothesis.

Even if the Bean model provides a good intuitive representation of the shielding behavior of superconductors, the hypotheses of the critical state are quite restrictive and the practical shielding curves are different from the graph presented in Fig. 1.13. Indeed, a complete analysis should take into account the field dependence of the critical current density $J_c$. This can be done, for example, using the Kim law given by Eq. (1.9) introduced in Section 1.1.2. The shielding parameters depend also on the sweep rate (the frequency of the applied field). This effect can be modeled using the $E(J)$ relationship given by Eq. (1.8) also described in Section 1.1.2.

Finally, the geometry of the shield also has a major effect on the shielding properties. In the assumption of the Bean model, we consider a cylinder of infinite length and the magnetic flux only penetrates through the wall of the cylinder. In this case, the threshold flux density is given by Eq. (1.11). However, for a cylinder of finite length, in addition to the penetration through the wall, the field also penetrates through the open extremities. Consequently, both the shielding factor and the threshold flux density evaluated at the center of the cylinder decrease as the cylinder length decreases. Moreover, the shielding factor and the threshold flux density decrease following the cylinder axis from the center to the extremities. For a short cylinder, as the applied field increases, the flux starts to penetrate through the open extremities. Therefore, the field measured at the center of the shield is never zero even if the wall is not fully penetrated. The consequence is that, for a cylinder of finite length, the behavior is quite different from that illustrated in Fig. 1.13(b) [96]. The shielding factor exhibits finite values even for a low applied field ($B_{\mathrm{app}} < B_{\mathrm{lim}}$). The field dependence of the shielding factor becomes increasingly similar to Fig. 1.13(b) as the cylinder length increases.

### 1.3.3 Shielding of non-uniform magnetic field

If the shield is placed in a uniform magnetic field environment, the applied field amplitude and direction are known a priori everywhere. The shielding efficiency is therefore fully characterized by the measurement of the flux density in the shielded region. When dealing with non-uniform magnetic field, the situation is more complex. A non-uniform magnetic field is characterized by a gradient in both magnitude and orientation (i.e. field lines curvature). These two characteristics are intrinsically related [49, 177]. The flux density is described by a three dimensional vector $\boldsymbol{B}(\boldsymbol{r})$, where $\boldsymbol{r}$ is the position vector. If $\|\boldsymbol{B}\|$ is the strength of the magnetic flux density and $\boldsymbol{b}$ is the unit vector directed along the flux density, the Maxwell equation div $\boldsymbol{B} = 0$ leads to

$$(\text{grad } \|\boldsymbol{B}\|) \cdot \boldsymbol{b} + \|\boldsymbol{B}\|(\text{div } \boldsymbol{b}) = 0. \tag{1.12}$$

This relation means that if the gradient of the flux density strength along a field line is non-zero, the divergence of the unit vector is also non-zero. In other words, any gradient in the flux density magnitude leads to finite curvature of the field lines.

Consequently, when the shield is subjected to a non-uniform magnetic field of a nearby magnetic source, the generated magnetic field distribution needs to be characterized in the shielded region (i.e. the region where the superconducting shield will be placed).

#### Emission vs. immunity

When investigating magnetic shielding of non-uniform magnetic field sources, we generally distinguish two problems depending on what the magnetic shield is used for. We can either protect the environment from a given magnetic field source or protect a given region from an external stray field. The first situation is called an emission problem whereas the second one is called an immunity problem. The two situations are compared in Fig. 1.14. In an emission problem, the source of magnetic field is placed inside the shield creating a low field environment outside of the shield. In the immunity problem, the source of magnetic field is placed outside of the shield which aims at creating a given low field region. In this thesis, only the immunity problem is investigated. The magnetic shields considered are only devoted to reduce the flux density over a given volume in the vicinity of a magnetic source and investigate how to increase this shielded volume.

#### Shielding vs. screening

In this thesis, two kinds of configuration are studied. In the first configuration, the low field environment is created by a closed or semi-closed geometry like a hollow cylinder. In this case, the shielded flux density is measured inside of the shield. In the second configuration, the low field environment is created by a wall or a screen placed between

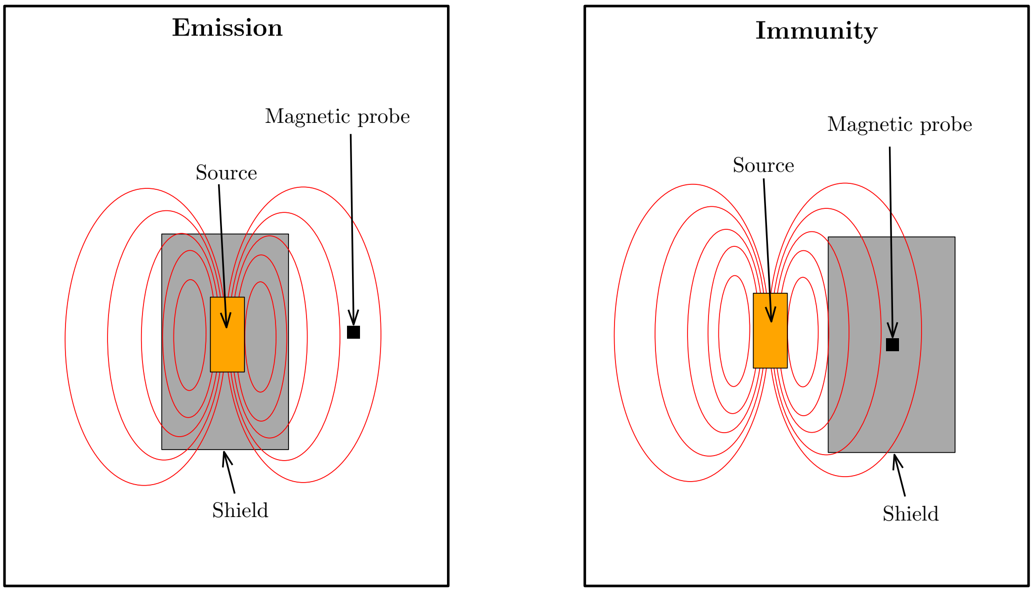

**Figure 1.14:** Comparison between an emission problem (left) and an immunity problem (right).

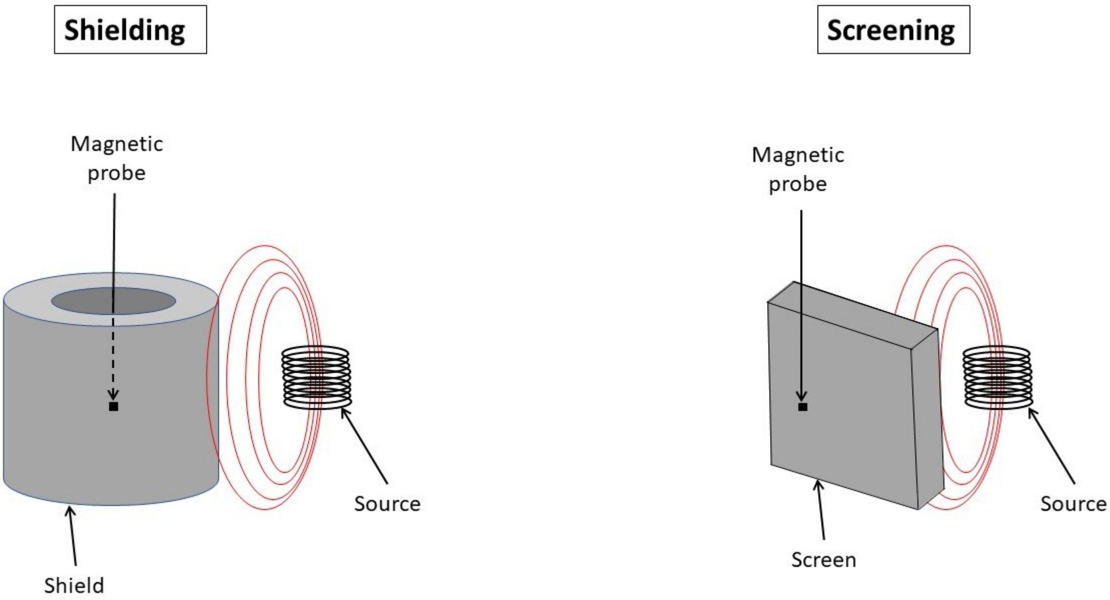

**Figure 1.15:** Comparison between the shielding (left) and the screening (right) configurations.

the magnetic field source and the region where the field is supposed to be attenuated. The first case corresponds to the *shielding* configuration and the second case, corresponds to the *screening* configuration. Magnetic shielding and screening are related to the same phenomenon, namely, the generation of shielding currents in the superconductor to reduce the magnetic field.

## 1.4 Ferromagnetic materials

Because some of the samples considered in this work combine superconducting and slightly ferromagnetic materials, it is worth introducing the basic properties of typical ferromagnets. The characteristics presented in this section hold for isotropic materials.

### 1.4.1 Hysteresis loops

Ferromagnetic materials are characterized by a strong magnetic response under an external applied field. The properties of a ferromagnetic material are described by the $B(H)$ relationship. As illustrated in Fig. 1.16, this relationship is highly non-linear and displays a hysteretic behavior.

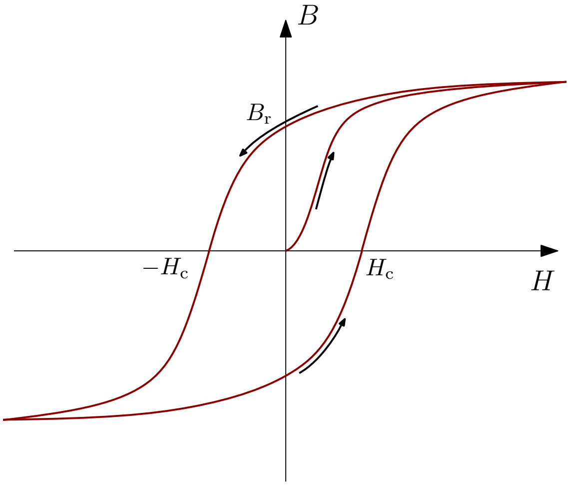

**Figure 1.16:** Typical $B(H)$ hysteresis loop as well as the associated parameters. The black arrows indicate the evolution of the material behavior starting from the demagnetized state $(H, B) = (0, 0)$.

Even if the flux density $B$ is the most physically intuitive quantity, the magnetic behavior of a material is often described by the magnetization $M$, i.e. the average magnetic moment per unit volume [178, 179] given by

$$B = \mu_0(H + M) \quad \text{or} \quad M = \frac{B}{\mu_0} - H. \tag{1.13}$$

When the magnetic field $H$ is equal to zero, a remanent flux density $B_\mathrm{r}$ (or a corresponding remanent magnetization $M_\mathrm{r}$) persists in the material. The coercive field $H_\mathrm{c}$ is the magnetic field necessary to cancel out the remanent flux density. Let us note that, due to Eq. (1.13), the coercive field can take a different value whether we consider the $B(H)$ loop or the $M(H)$ loop. However, for the relatively soft ferromagnetic materials considered in this thesis, the field dependences of the flux density and the magnetization are very similar. Therefore, we can assume that the difference in the coercive field values considering either the curve $B(H)$ or the curve $M(H)$ is negligible [180]. When $H$ is large enough such that magnetic saturation is reached ($M \approx M_\mathrm{s}$), the curve $B(H)$ increases linearly with a slope equal to $\mu_0$. At this stage, the flux density evolves in a reversible way with the field $H$. The corresponding magnetization $M_\mathrm{s}$ is called the saturation magnetization. When the field $H$ increases, the $M(H)$ curve asymptotically approaches the saturation magnetization value $M_\mathrm{s}$.

### Hysteresis losses

The hysteretic behavior of the ferromagnetic materials results in an energy irreversibly transferred into heat. This energy dissipation is called hysteresis loss and is due to the domain wall jumps (also called the *Barkhausen jumps*) resulting from the increase of external magnetic field. The area enclosed by the hysteresis cycle has an important physical meaning as it represents the hysteresis loss during one magnetization cycle per unit volume (J/m$^3$) [180]. The energy loss associated to an infinitesimal increase of the flux density $dB$ is given by:

$$dQ = H\ dB. \tag{1.14}$$

The total energy loss per unit volume associated to the hysteretic cycle is given by

$$Q = \oint_\mathrm{cycle} H\ dB. \tag{1.15}$$

If we express the energy loss per unit time instead of one cycle, we obtain the power loss $P$ per unit volume (W/m$^3$):

$$P = f \oint_\mathrm{cycle} H\ dB \tag{1.16}$$

where $f$ is the frequency (Hz).

### Minor loops

The hysteresis cycle going to the saturation state described in Fig. 1.16 is called the major loop. Minor hysteresis loops can be defined as any cycle different from the major loop and characterized by smaller amplitude of applied field $H$. Minor loops can be either symmetrical with respect to the origin or asymmetrical by superimposing a DC bias applied field.

### 1.4.2 Models for ferromagnetic hysteresis

**The Jiles-Atherton model**

The Jiles-Atherton (J-A) phenomenological approach is one of the most popular model to describe ferromagnetic hysteresis due to its relative simplicity to implement and the physical interpretation of the associated parameters [181–183]. In particular, this model has been successfully applied to major hysteresis cycles. Minor cycles could also be described using a modified approach combining the original idea from the J-A model with the Preisach model [184]. In this section, we briefly introduce the model and the equations describing the hysteresis cycle [185].

Based on the domain wall motion in the ferromagnetic materials during the magnetization process, the J-A model considers the total magnetization $M$ as the sum of an irreversible component $M_{\mathrm{irr}}$ and a reversible component $M_{\mathrm{rev}}$. The irreversible component of the magnetization is given by the following differential equation:

$$dM_{\mathrm{irr}} = \frac{M_{\mathrm{an}} - M_{\mathrm{irr}}}{k\delta - \alpha(M_{\mathrm{an}} - M_{\mathrm{irr}})} dH, \tag{1.17}$$

where $k$ and $\alpha$ are two of the J-A model parameters. In Eq. (1.17), $\delta = 1$ if $dH/dt > 0$ and $\delta = -1$ if $dH/dt < 0$. The anhysteretic magnetization $M_{\mathrm{an}}$ is given by the following Langevin's function:

$$M_{\mathrm{an}} = M_{\mathrm{s}} \left( \coth \frac{H_{\mathrm{e}}}{a} - \frac{a}{H_{\mathrm{e}}} \right), \tag{1.18}$$

where $M_{\mathrm{s}}$ is the saturation magnetization and $a$ is another parameter within the model. The effective field $H_{\mathrm{e}}$ plays an important role in the J-A model. The idea is similar to the Weiss Mean-Field theory [186] stating that the polycrystalline ferromagnetic material is a collection of several interacting magnetic domains, each of them carrying a single magnetic moment $\boldsymbol{m}$. The effective field $H_{\mathrm{e}}$ takes this interaction into account and is given by

$$H_{\mathrm{e}} = H + \alpha M. \tag{1.19}$$

Finally, the reversible magnetization is defined as a fraction $c$ of the difference between the anhysteretic and the irreversible magnetization: $M_{\mathrm{rev}} = c(M_{\mathrm{an}} - M_{\mathrm{irr}})$, the total magnetization is thus given by

$$M = cM_{\mathrm{an}} + (1 - c)M_{\mathrm{irr}}. \tag{1.20}$$

As a result, in addition to the saturation magnetization, the model includes four other parameters $c$, $k$, $a$ and $\alpha$. In the J-A model, these parameters actually have a physical interpretation. The dimensionless parameter $c$ gives the part of anhysteretic magnetization with respect to the reversible component. The value of $c$ is between 0 and 1 so that if $c = 1$, the behavior of the material is purely anhysteretic. The pinning parameter $k$, expressed in A/m, gives the coercivity and is directly related to the hysteresis energy losses. The parameter $a$ (A/m) is defined as

$$a = \frac{k_\mathrm{B} T}{\mu_0 \; m}, \tag{1.21}$$

where $k_\mathrm{B}$ is the Boltzmann constant and $m$ is the magnetic moment of a typical magnetic domain. Together with the saturation magnetization, $a$ gives the density of magnetic domains $n_\mathrm{mag}$. If we assume that the saturation magnetization is given by $M_\mathrm{s} = n_\mathrm{mag} m$, the density of magnetic domains is proportional to

$$n_\mathrm{mag} \propto \frac{a M_\mathrm{s}}{T}. \tag{1.22}$$

Finally, the dimensionless parameter $\alpha$ defines the coupling between magnetic domains.

### The Rayleigh model

The Rayleigh model is usually employed to describe low-field magnetization curves. The model assumes that, for low amplitudes of magnetization, the ascending and descending branches of the hysteresis loop as well as the first magnetization curve can be modeled using a quadratic function and are respectively described by the following equations [187, 188]:

$$M(H) = (\chi_i + b H_\mathrm{m}) H \pm \frac{b}{2} \left( H_\mathrm{m}^2 - H^2 \right), \tag{1.23}$$

$$M(H) = \chi_i H + b H^2, \tag{1.24}$$

where $\chi_i$ is the initial susceptibility obtained at the origin of the magnetization curve (demagnetized state) and $b$ is called the Rayleigh parameter. These two parameters $\chi_i$ and $b$ respectively stand for the reversible part and the irreversible part of the magnetic behavior. An example of magnetization loops obtained with the Rayleigh model for several field amplitudes is shown in Fig. 1.17. The peak magnetization and the hysteresis losses per unit volume for one cycle are respectively given by

$$M_\mathrm{m} = M(H_\mathrm{m}) = \chi_i H_\mathrm{m} + b H_\mathrm{m}^2. \tag{1.25}$$

and

$$Q = \frac{4}{3} \mu_0 b H_\mathrm{m}^3. \tag{1.26}$$

From Eq. (1.25) and (1.26), the hysteresis losses are given by

$$Q = \frac{\mu_0}{6 b^2} \left( -\chi_i + \sqrt{\chi_i^2 + 4 b M_\mathrm{m}} \right)^3. \tag{1.27}$$

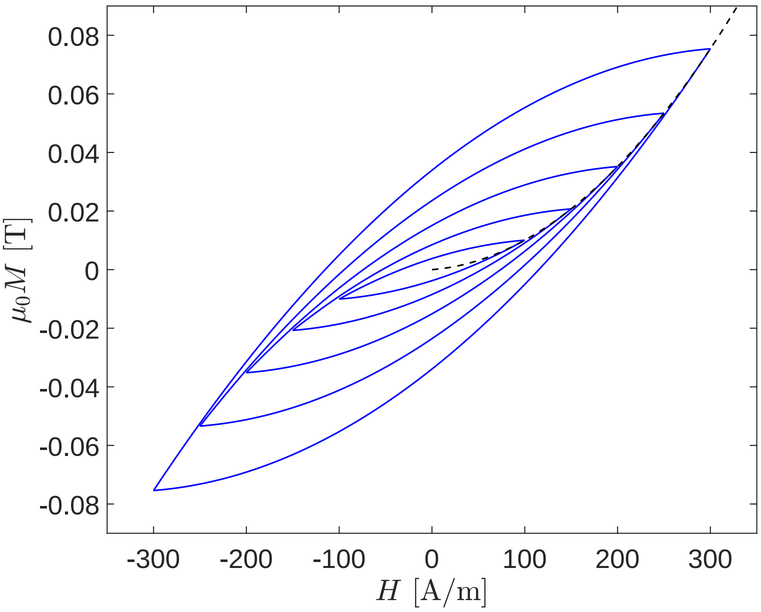

**Figure 1.17:** Magnetization cycles computed with the Rayleigh model up to a magnetic field amplitude $H_\mathrm{m} = 300$ A/m with $\chi_i = 20$ and $b = 0.6$. The black dashed line is the first magnetization curve.

If the magnetic behavior is mainly reversible ($b << 1$), Eq. (1.27) reduces to

$$Q = \frac{4}{3}\mu_0 b \left(\frac{M_\mathrm{m}}{\chi_i}\right)^3 \tag{1.28}$$

whereas if the irreversible part dominates the magnetic behavior ($b >> 1$), the losses are given by

$$Q = \frac{4}{3}\mu_0 b \left(\frac{M_\mathrm{m}}{b}\right)^{3/2} . \tag{1.29}$$

As a result, the Rayleigh model predicts a dependence $Q \propto M_\mathrm{m}^n$ with $n$ taking a value between 1.5 and 3 depending on the relative importance of the reversible and the irreversible components of the magnetic behavior. In general, the value of $n$ depends on the type of ferromagnetic material, temperature and mechanical stress [187].

## 1.5 Chapter summary

In this chapter, we introduced the theoretical background related to the physics of superconductors as well as their most relevant properties to understand magnetic shields. We first introduced the distinction between type I and type II superconductivity. In particular, for the latter, we discussed the flux pinning mechanism, flux low and irreversibility behavior as well as the flux creep. The very comprehensive Bean model was also introduced. Then, among type II superconductors, we distinguished low-temperature superconductors (LTS) and high-temperature superconductors (HTS) depending on the value of their critical temperature. We presented the most relevant properties of HTS materials for engineering applications including the different kinds and shapes of HTS that can be found.

This chapter also summarized the properties of superconducting magnetic shields. The notions and models presented for type II superconductors were applied to the case of passive magnetic shielding. The relevant parameters characterizing the efficiency of a magnetic shield were described. This chapter also introduced the context of superconducting shielding under non-uniform applied magnetic fields.

Finally, as this thesis involves structures combining HTS and ferromagnetic materials, this chapter presented a short introduction of the main properties of ferromagnetic materials as well as relevant models to analyze their magnetic hysteresis behavior.

# Chapter 2

# Numerical modeling techniques

This chapter presents the numerical techniques used to model structures involving high-temperature superconductors. Efficient modeling tools are crucial to help better understand the behavior of type II superconducting materials and more specifically the shielding mechanisms in different configurations not always easy to achieve in laboratories. Indeed, apprehending efficiently the mechanisms of flux penetration as well as the shielding current distribution is the key to design complex structures adapted to large scale engineering applications with strict specifications. In this chapter, a very synthetic overview of the finite element method mathematical framework applied to electromagnetism theory is presented. The concepts covered in this chapter are developed in details in the following reference [104].

The chapter is organized as follows. First we introduce the magnetodynamic (or quasi-static) approximation of Maxwell's equations. The problem is then completed by material constitutive laws as well as appropriate boundary conditions. Then we show how the system of partial differential equations can be formulated in a variational form (or weak form), better adapted for numerical implementation. In particular, the study is restricted to the $H$-$\phi$ formulation and the $A$-formulation depending on whether we express the problem is terms of the magnetic field $\boldsymbol{H}$ or the magnetic vector potential $\boldsymbol{A}$. After that, we describe briefly the idea behind the finite element method and the methods employed to discretize the problem. All the models presented in this thesis are solved using *Gmsh* and *GetDP*. The first is a three-dimensional finite element mesh generator and the latter is a finite element solver. Both of them are open-source softwares developed at the University of Liège [189, 190]. The models are based on the templates from the open source Life-HTS toolkit [191].

## 2.1 Magnetodynamic equations

In order to define the magnetodynamic problem, we start by defining a bounded domain $\Omega$ together with its 'piecewise smooth' boundary $\partial\Omega = \Gamma$. Any electrodynamic system is described by Maxwell's equations in the whole domain $\Omega$ [192, 193]:

$$\text{curl}\ \boldsymbol{E} = -\partial_t \boldsymbol{B}, \tag{2.1}$$

$$\text{curl}\ \boldsymbol{H} = \boldsymbol{J} + \partial_t \boldsymbol{D}, \tag{2.2}$$

$$\text{div}\ \boldsymbol{D} = \rho_{\text{f}}, \tag{2.3}$$

$$\text{div}\ \boldsymbol{B} = 0, \tag{2.4}$$

with $\boldsymbol{B}$ the magnetic flux density [T], $\boldsymbol{H}$ the magnetic field [A/m], $\boldsymbol{E}$ the electric field [V/m], $\boldsymbol{J}$ the electric current density [A/m$^2$], $\boldsymbol{D}$ the electric displacement field [C/m$^2$] and $\rho_{\text{f}}$ the free electric charges density [C/m$^3$]. The first two equations are referred to as Faraday's law (2.1) and Ampere-Maxwell's law (2.2). The last two equations are Gauss's law for the electric field (2.3) and Gauss's law for the magnetic field (2.4). To this set of equations, we need to add the following constitutive relations:

$$\boldsymbol{B} = \mu \boldsymbol{H}, \tag{2.5}$$

$$\boldsymbol{J} = \sigma \boldsymbol{E}, \tag{2.6}$$

$$\boldsymbol{D} = \varepsilon \boldsymbol{E}, \tag{2.7}$$

with $\mu$ the magnetic permeability [H/m], $\sigma$ the electrical conductivity [$\Omega^{-1} m^{-1}$] and $\varepsilon$ the electrical permittivity [F/m]. These parameters are generally complicated functions of magnetic field, electric field, temperature, mechanical stress and strain, ... Therefore, the constitutive equations (2.5)-(2.7) can be highly nonlinear.

In this work, we investigate phenomena at sufficiently low frequency to assume that the displacement current $\partial_t \boldsymbol{D}$ can be neglected with respect to the conduction current $\boldsymbol{J}$. This assumption is called the *magnetodynamic* (or *quasi-static*) approximation. In this case, the magnetodynamic system of equations can be written as follows:

$$\text{div}\ \boldsymbol{B} = 0, \tag{2.8}$$

$$\text{curl}\ \boldsymbol{E} = -\partial_t \boldsymbol{B}, \tag{2.9}$$

$$\text{curl}\ \boldsymbol{H} = \boldsymbol{J}, \tag{2.10}$$

with the constitutive relations:

$$\boldsymbol{B} = \mu(\boldsymbol{H})\boldsymbol{H}, \tag{2.11}$$

$$\boldsymbol{J} = \sigma(\boldsymbol{E}, \boldsymbol{B})\boldsymbol{E}. \tag{2.12}$$

Generally, we divide the numerical domain $\Omega$ into a conducting domain $\Omega_{\mathrm{c}}$ and a non-conducting domain $\Omega_{\mathrm{nc}}$. In the scope of this work, we also introduce the part of the domain where the possible excitation current can be applied $\Omega_{\mathrm{s}}$ which is thus different from $\Omega_{\mathrm{c}}$ and $\Omega_{\mathrm{nc}}$. The magnetic constitutive law (2.11) applies in the whole domain $\Omega$. The electric constitutive law (2.12) only applies in $\Omega_{\mathrm{c}}$. In the non-conducting domain $\Omega_{\mathrm{nc}}$, the current density $\boldsymbol{J}$ is strictly identical to zero. Consequently, from Ampere's equation (2.10), the magnetic field is curl-free in $\Omega_{\mathrm{nc}}$ and can be written as the gradient of a scalar magnetic potential $\phi$, i.e $\boldsymbol{H} = \text{grad } \phi$. The constitutive relations are sometimes written in terms of the magnetic reluctivity $\nu = \mu^{-1}$ and electrical resistivity $\rho = \sigma^{-1}$. We have $\boldsymbol{H} = \nu(\boldsymbol{B})\boldsymbol{B}$ and $\boldsymbol{E} = \rho(\boldsymbol{J}, \boldsymbol{B})\boldsymbol{J}$. Finally, let us mention that the system of equations (2.1)-(2.7) defines a full-wave problem, whereas the system of equations (2.8)-(2.12) in the quasi-static approximation defines a diffusion problem.

The constitutive relations (2.11) and (2.12) can now be detailed for the high-temperature superconductors considered in this work. As mentioned in Section 1.1.2, the behavior of HTS materials at macroscopic scale can be modeled using the power-law described by Eq. (1.8). As a result, the constitutive law of HTS materials can be detailed in terms of non-linear conductivity or resistivity. If we take the field dependence of the critical current density $J_{\mathrm{c}}(\boldsymbol{B})$, modeled using Kim's law (1.9), the non-linear conductivity for high-temperature superconductors can be written as follows

$$\sigma(\boldsymbol{E}, \boldsymbol{B}) = \frac{J_{\mathrm{c},0}}{E_{\mathrm{c}}} \frac{1}{1 + \frac{\|\boldsymbol{B}\|}{B_0}} \left( \frac{\|\boldsymbol{E}\|}{E_{\mathrm{c}}} \right)^{\frac{1-n}{n}} \tag{2.13}$$

and the non-linear resistivity can be written

$$\rho(\boldsymbol{J}, \boldsymbol{B}) = \frac{E_{\mathrm{c}}}{J_{\mathrm{c},0}} \left( 1 + \frac{\|\boldsymbol{B}\|}{B_0} \right)^{n} \left( \frac{\|\boldsymbol{J}\|}{J_{\mathrm{c},0}} \right)^{n-1}. \tag{2.14}$$

In purely superconducting materials, the magnetic permeability is assumed to be the vacuum permeability $\mu(\boldsymbol{H}) = \mu_0 = 4\pi\ 10^{-7}$ H/m.

In order to be fully addressed, the magnetodynamic problem defined by Eqs. (2.8)-(2.12) should be completed by the appropriate boundary conditions on the boundary $\Gamma$ as well as initial condition. In this work, we consider the particular case of homogeneous boundary conditions on the tangential components of $\boldsymbol{H}$ and $\boldsymbol{E}$:

$$\boldsymbol{H} \times \boldsymbol{n}|_{\Gamma_H} = \mathbf{0}, \tag{2.15}$$

$$\boldsymbol{E} \times \boldsymbol{n}|_{\Gamma_E} = \mathbf{0}, \tag{2.16}$$

where $\boldsymbol{n}$ is the external unit normal vector defined on $\Gamma$. The boundary $\Gamma$ has been divided into two subdomains $\Gamma_H$ and $\Gamma_E$ respectively defined as the part of $\Gamma$ on which the magnetic field boundary condition is imposed and the part of $\Gamma$ on which the electric field boundary condition is imposed.

## 2.2 Weak formulations

The set of partial differential equations (2.8)-(2.10) together with the constitutive relations (2.11) and (2.12) entirely define a magnetodynamic problem once they are completed with boundary conditions and initial condition. This set of equations is referred to as the *strong form* of the problem. Written like this, the problem is poorly adapted to a numerical implementation of the finite element method. In order to discretize the partial differential problem, it should first be expressed in a *weak form*.

First, let us recall the two Green's identity. The first Green's identity, also called the *grad-div* identity in a compact domain $\Omega$ writes:

$$(\boldsymbol{u} \ , \text{grad } v)_\Omega + (\text{div } \boldsymbol{u} \ , v)_\Omega = \langle \boldsymbol{u} \cdot \boldsymbol{n} \ , v \rangle_\Gamma, \tag{2.17}$$

where $\Gamma = \partial\Omega$ is the boundary of the domain $\Omega$ and $\boldsymbol{n}$ is the unit normal vector to the boundary of $\Omega$ directed outward. The second Green's identity, also called the *curl-curl* identity writes:

$$(\boldsymbol{u} \ , \text{curl } \boldsymbol{v})_\Omega - (\text{curl } \boldsymbol{u} \ , \boldsymbol{v})_\Omega = \langle \boldsymbol{u} \times \boldsymbol{n} \ , \boldsymbol{v} \rangle_\Gamma. \tag{2.18}$$

In Eqs. (2.17) and (2.18), we introduced the following simplified notation that will be used throughout this chapter:

$$(X \ , Y)_\Omega = \int_\Omega X * Y d\Omega \qquad \text{and} \qquad \langle X \ , Y \rangle_\Gamma = \int_\Gamma X * Y d\Gamma \tag{2.19}$$

where $*$ stands for either the dot product if $X$ and $Y$ are vector fields or the scalar multiplication if they are two scalar fields.

In the following, we introduce how the strong form of the magnetodynamic problem can be transformed into a weak form and in particular, how the problem can be reformulated in terms of either a magnetic vector potential (*A-formulation*) or the magnetic field (*H-$\phi$-formulation*).

### 2.2.1 $A$-formulation

As the magnetic flux density $\boldsymbol{B}$ is divergence-free (Gauss's law for the magnetic field), we can define a vector potential $\boldsymbol{A}$ (called the magnetic vector potential) in the whole domain $\Omega$ such that

$$\boldsymbol{B} = \text{curl}\ \boldsymbol{A}. \tag{2.20}$$

From Eq. (2.9), the electric field is given by

$$\boldsymbol{E} = -\partial_t \boldsymbol{A} - \text{grad}\ V, \tag{2.21}$$

where $V$ is a scalar potential called the electric scalar potential defined in $\Omega_\text{c}$. Injecting Eqs. (2.20) into Ampere's law (2.10) leads to

$$\text{curl}\,(\nu\ \text{curl}\ \boldsymbol{A}) - \boldsymbol{J} = 0, \tag{2.22}$$

where $\nu = \mu^{-1}$ is the reluctivity. The current density $\boldsymbol{J}$ can be separated into two contributions: a reaction term equal to $\sigma \boldsymbol{E}$ defined in $\Omega_\text{c}$ and a source term $\boldsymbol{J}_\text{s}$ defined in $\Omega_\text{s}$. Therefore, the current density is given by

$$\boldsymbol{J} = \sigma \boldsymbol{E} + \boldsymbol{J}_\text{s} = -\sigma\,(\partial_t \boldsymbol{A} + \text{grad}\ V) + \boldsymbol{J}_\text{s}. \tag{2.23}$$

We finally end up with the following formulation

$$\text{curl}\,(\nu\ \text{curl}\ \boldsymbol{A}) + \sigma\,(\partial_t \boldsymbol{A} + \text{grad}\ V) - \boldsymbol{J}_\text{s} = 0. \tag{2.24}$$

The equation (2.24) corresponds to the $A$-$V$-formulation of the magnetodynamic problem as it formulates the system of partial differential equations in terms of the magnetic vector potential $\boldsymbol{A}$ and the electric scalar potential $V$. It is worth mentioning that, as is, the solution of Eq. (2.24) for the magnetic vector potential is not unique. Indeed, any scalar function whose gradient is added to $\boldsymbol{A}$ leaves the magnetic flux density $\boldsymbol{B}$ unchanged. In order to guarantee the uniqueness of $\boldsymbol{A}$, a gauge condition should be used. For instance, a gauge that is commonly used is the Coulomb gauge which imposes the magnetic vector potential to be divergence-free. In this work, we consider the particular case in which the electric scalar potential is zero ($V = 0$). As a result, Eq. (2.24) writes

$$\text{curl}\,(\nu\ \text{curl}\ \boldsymbol{A}) + \sigma \partial_t \boldsymbol{A} - \boldsymbol{J}_\text{s} = 0, \tag{2.25}$$

which corresponds to the $A$-formulation (where $\boldsymbol{A}$ is sometimes called the *modified* vector potential) of the magnetodynamic problem as it is only expressed in terms of the magnetic vector potential.

In order to obtain a weak form of the $A$-formulation, we multiply Eq. (2.25) by an arbitrary function $\boldsymbol{A'}$ called a *test function* and we integrate over the whole volume $\Omega$ leading to

$$(\text{curl}\,(\nu\ \text{curl}\ \boldsymbol{A})\ ,\boldsymbol{A'})_{\Omega} + (\sigma\partial_t\boldsymbol{A}\ ,\boldsymbol{A'})_{\Omega_\text{c}} - (\boldsymbol{J}_\text{s},\ \boldsymbol{A'})_{\Omega_\text{s}} = 0. \tag{2.26}$$

Without entering into details, the test function $\boldsymbol{A'}$ belongs to the same space as $\boldsymbol{A}$, i.e. the space $H(\text{curl};\Omega) = \{\boldsymbol{A} \in \boldsymbol{L}^2(\Omega) : \text{curl}\ \boldsymbol{A} \in \boldsymbol{L}^2(\Omega)\}$ where $\boldsymbol{L}^2(\Omega)$ is the set of square-integrable vector fields. Using the curl-curl Green's identity, we end up with

$$\boxed{\begin{aligned}&(\nu\ \text{curl}\ \boldsymbol{A}\ ,\text{curl}\ \boldsymbol{A'})_{\Omega} - \langle\nu\ \text{curl}\ \boldsymbol{A}\times\boldsymbol{n}\ ,\boldsymbol{A'}\rangle_{\Gamma_H}\\ &\qquad\qquad + (\sigma\partial_t\boldsymbol{A}\ ,\boldsymbol{A'})_{\Omega_\text{c}} - (\boldsymbol{J}_\text{s},\ \boldsymbol{A'})_{\Omega_\text{s}} = 0.\end{aligned}} \tag{2.27}$$

Because we considered the homogeneous boundary condition (2.15), the second term is equal to zero. The formulation given by Eq. (2.27) is a weak form of the $A$-formulation for the magnetodynamic problem and should be forced to hold for all test functions $\boldsymbol{A'}$.

### 2.2.2 $H$-$\phi$-formulation

The magnetic field formulation can be obtained from Faraday's equation (2.9) that writes

$$\text{curl}\ \boldsymbol{E} + \partial_t(\mu\boldsymbol{H}) = 0. \tag{2.28}$$

Multiplying Eq. (2.28) by an arbitrary test function $\boldsymbol{H'}$ that belongs to the same function space as $\boldsymbol{H}$ and integrating over the whole domain $\Omega$ leads to

$$\begin{aligned}&(\partial_t(\mu\boldsymbol{H})\ ,\boldsymbol{H'})_{\Omega} + (\text{curl}\ \boldsymbol{E}\ ,\boldsymbol{H'})_{\Omega} = 0\\ \Leftrightarrow\ &(\partial_t(\mu\boldsymbol{H})\ ,\boldsymbol{H'})_{\Omega} + (\boldsymbol{E}\ ,\text{curl}\ \boldsymbol{H'})_{\Omega} - \langle\boldsymbol{E}\times\boldsymbol{n}\ ,\boldsymbol{H'}\rangle_{\Gamma_E} = 0\\ \Leftrightarrow\ &(\partial_t(\mu\boldsymbol{H})\ ,\boldsymbol{H'})_{\Omega} + (\boldsymbol{E}\ ,\text{curl}\ \boldsymbol{H'})_{\Omega_\text{c}} - \langle\boldsymbol{E}\times\boldsymbol{n}\ ,\boldsymbol{H'}\rangle_{\Gamma_E} = 0,\end{aligned} \tag{2.29}$$

where the curl-curl Green's identity has been used as well as the fact that curl $\boldsymbol{H'} = 0$ in the non-conducting domain. The test function $\boldsymbol{H'}$ belongs to the subset of $H(\text{curl};\Omega)$ in which all vector fields are curl-free in the non-conducting domain. Using Ampere's law, the electric field is given by

$$\boldsymbol{E} = \rho\boldsymbol{J} = \rho\ \text{curl}\ \boldsymbol{H} + \rho\boldsymbol{J}_\text{s}, \tag{2.30}$$

where the current density has been separated into a reaction and a source term. Injecting Eq. (2.30) into Eq. (2.29), we end up with

$$\boxed{\begin{aligned}&(\partial_t(\mu\boldsymbol{H})\ ,\boldsymbol{H'})_{\Omega} + (\rho\ \text{curl}\ \boldsymbol{H}\ ,\text{curl}\ \boldsymbol{H'})_{\Omega_\text{c}}\\ &\qquad\qquad + (\rho\boldsymbol{J}_\text{s}\ ,\text{curl}\ \boldsymbol{H'})_{\Omega_\text{s}} - \langle\boldsymbol{E}\times\boldsymbol{n}\ ,\boldsymbol{H'}\rangle_{\Gamma_E} = 0.\end{aligned}} \tag{2.31}$$

Because we considered the homogeneous boundary condition (2.16), the last term is equal to zero. The formulation given by Eq. (2.31) is a weak form of the $H$-$\phi$-formulation for the magnetodynamic problem and should be forced to hold for all test functions $\boldsymbol{H'}$. Even if $\phi$ does not appear explicitly in Eq. (2.31), the formulation is still called $H$-$\phi$ as the curl-free property of $\boldsymbol{H}$ is crucial in the development of the weak form.

### 2.2.3 Sources

In the formulations (2.27) and (2.31) introduced in this section, we systematically considered two contributions to the current density: a reaction term in the conducting domain $\Omega_\mathrm{c}$ and a source term $\boldsymbol{J}_\mathrm{s}$ in the source domain $\Omega_\mathrm{s}$. The conducting domain $\Omega_\mathrm{c}$ where the reaction currents are induced is therefore different than the source domain $\Omega_\mathrm{s}$ where the source current is imposed.

Another method would be to apply a uniform source magnetic field in the whole domain $\Omega$. In this case the classical method is to decompose the total field $\boldsymbol{H}$ into a source term $\boldsymbol{H}_\mathrm{s}$ and a reaction term $\boldsymbol{H}_\mathrm{r}$ such that $\boldsymbol{H} = \boldsymbol{H}_\mathrm{s} + \boldsymbol{H}_\mathrm{r}$. Then, we can inject this decomposition into the weak form (2.31) and $\boldsymbol{H}_\mathrm{r}$ becomes the new unknown of the problem. This approach is called the *reaction H-formulation*. Another approach, sometimes more efficient, is to solve directly for the total field $\boldsymbol{H}$ [194]. In this case, the uniform applied field is imposed by means of boundary conditions on $\partial\Omega$. In particular, the magnetic scalar potential $\phi$ is fixed to a linear function in order to induce a constant source field. This approach is called the *total H-formulation*. Consequently, in the total field approach, the unknown $\boldsymbol{H}$ is fixed to the value of the applied field on the boundary of the domain. In the reaction field approach, the unknown $\boldsymbol{H}_\mathrm{r}$ is fixed at zero on the boundary. These two approaches were illustrated here in the case of the $H$-formulation. The same reasoning can be applied to the $A$-formulation by introducing the total and reaction magnetic vector potentials.

## 2.3 Finite Element Method

The well-established formulations (2.27) and (2.31) are not suited yet for numerical implementation as no approximation has been introduced in their development. Indeed, the unknown quantities belong to infinite dimension spaces and need to be discretized. The problem is then solved in the resulting discrete function spaces to end up with an approximate solution.

In summary, the finite element method (FEM) consists in a twofold discretization followed by a time discretization. First the method involves a spatial discretization of the numerical domain $\Omega$ into simple geometrical shapes. These shapes are basically line segments in 1D space, triangles or quadrangles in 2D space and volume elements like tetrahedra, hexahedra or triangular prisms in 3D space. The whole partition of these geometrical shapes is called a *mesh* and should be carefully constructed when seeking an accurate approximation of the unknown fields.

The second discretization concerns the function spaces in which the approximate solution is sought. Typically, in the finite element method, the unknown function is approximated by a linear combination of well-chosen *basis functions*. To illustrate the idea in a 1D case, let us consider the unknown function $u(x)$ that is approximated by the following linear combination of basis functions $\psi_i(x)$:

$$u(x) \approx \sum_i u_i \psi_i(x). \tag{2.32}$$

In this case, a convenient way of defining the basis functions is such that $\psi_i = 1$ at the node $i$ and 0 at the other nodes. The discretization of the function $u$ is illustrated in Fig. 2.1. In this case, the 1D spatial domain is discretized by 7 line elements (between 8 nodes). A higher number of elements would provide a more accurate approximation of $u$ but would require a higher computational cost. The equation (2.32) represents the discretization of the function space. The combination of a geometrical element together with the associated basis functions defines what is called a *finite element*.

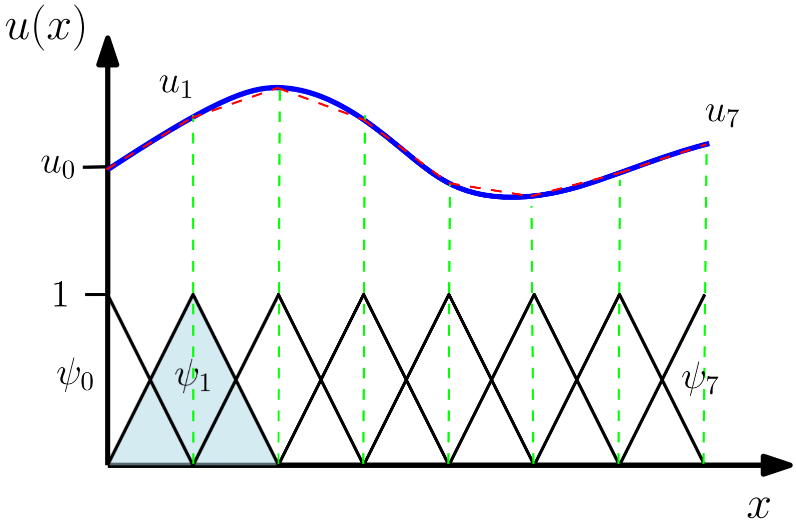

**Figure 2.1:** Illustration of the finite element discretization in 1D using line elements. The unknown function $u(x)$ in blue is approximated by a linear combination of basis functions $\psi_i$. The approximation is shown is red dashed line.

### 2.3.1 Discretization of the magnetic field $\boldsymbol{H}$

In the $H$-$\phi$-formulation, the function space to which the unknown field $\boldsymbol{H}$ belongs should be discretized and the resulting field inserted into the weak formulation (2.31). The magnetic field being a vector field, it is approximated as a linear combination of *edge functions* $\boldsymbol{\psi_e}$ (associated to every edge of the mesh):

$$\boldsymbol{H} \approx \sum_{e=1}^{N_e} H_e \boldsymbol{\psi_e}, \tag{2.33}$$

where $N_e$ is the number of edges in the mesh. Basically, an edge function is non-zero in the elements containing this edge. The coefficient $H_e$ can be interpreted as the circulation of $\boldsymbol{H}$ along the corresponding edge $e$. In the non-conducting domain, the magnetic field is curl-free and requires a supplementary constraint. In the non-conducting domain $\Omega_{\mathrm{nc}}$, we have $\boldsymbol{H} = \text{grad } \phi$. Because $\phi$ is a scalar function, it is discretized as a linear combination of *node functions*:

$$\phi \approx \sum_{n=1}^{N_n} \phi_n \psi_n, \tag{2.34}$$

where $\psi_n$ are the node functions and $N_n$ is the set of nodes in the considered region. As the curl-free property is only valid in $\Omega_{\mathrm{nc}}$, the final magnetic field discretization writes:

$$\boldsymbol{H} \approx \sum_{e \in N_{\mathrm{c}}} H_e \boldsymbol{\psi_e} + \sum_{n \in N_{\mathrm{nc}}} \phi_n \text{ grad } \psi_n, \tag{2.35}$$

where $N_{\mathrm{c}}$ is the set of edges in the conducting domain $\Omega_{\mathrm{c}}$ excluding those on its boundary and $N_{\mathrm{nc}}$ is the set of nodes in $\Omega_{\mathrm{nc}}$ including those on its boundary.

#### Multiply connected domains

The magnetic field approximation (2.35) is true only for *simply connected* non-conducting domain. Without entering into details, a domain is said to be simply connected if any closed loop in this domain can be shrunk continuously into a point without leaving this domain. A region which is not simply connected is said to be *multiply connected.* For example, a practical case of multiply connected non-conducting domain arises when holes are present in the conducting domain (e.g. inductor, ring-shaped conductor, ...). In this case, Eq. (2.35) is no longer valid. Details about treatment of multiply connected regions can be found in [195]. In practice, the domain can be made simply connected thanks to the introduction of *cuts* (surfaces defined in the multiply connected domain such that any closed loop going through the hole has to cross it). This brings an additional constraint and the field is now discretized as follows

$$\boldsymbol{H} \approx \sum_{e \in N_{\mathrm{c}}} H_e \boldsymbol{\psi_e} + \sum_{n \in N_{\mathrm{nc}}} \phi_n \text{ grad } \psi_n + \sum_{i \in C} I_i \boldsymbol{c_i}, \tag{2.36}$$

where $C$ is the set of cuts, $I_i$ is a set of functions bringing the discontinuity in the scalar potential in the non-conducting domain and $\boldsymbol{c_i}$ is the set of edge functions associated to the cuts.

### 2.3.2 Discretization of the magnetic vector potential $\boldsymbol{A}$

In the scope of this work, the vector potential formulation is only involved in the case of an axisymmetric configuration. Let us assume the problem geometry in the $(r, z)$ plane with $z$, the symmetry axis. In this case, the magnetic flux density has no azimuthal component and is entirely defined in the $(r, z)$ plane. Therefore, the vector potential has only one non-zero component in the azimuthal direction, namely $A_\theta$. The vector potential is expressed as a linear combination of *perpendicular edge functions* associated to every nodes in the mesh:

$$\boldsymbol{A} \approx \sum_{i \in N} A_{\theta,i} \; \boldsymbol{\psi_i}, \tag{2.37}$$

where $N$ is the number of nodes in the whole mesh and $\boldsymbol{\psi_i}$ are the perpendicular edge basis functions.

The coefficients associated to the unknown quantities $\boldsymbol{H}$ or $\boldsymbol{A}$ can be found by injecting the discretizations (2.36) and (2.37) into the corresponding weak formulations. Doing so, instead of integrating the weak forms over the whole domain $\Omega$, the integrals only need to be evaluated on each geometrical element. In the discretizations (2.36) and (2.37) the number of coefficients are called the *degrees of freedom* (DOF). If $K$ is the total number of DOF, we need to solve $K$ equations with $K$ unknowns. As a result, we need $K$ linearly independent test functions. A common method is to choose the same test functions as the basis functions used in the discretization process (the so-called *Galerkin* method [196]). Finally, the system of partial differential equations is reduced to a system of algebraic equations which can be expressed as the following generic matrix equation

$$\mathbf{A}\;\mathbf{x} = \mathbf{b}, \tag{2.38}$$

where $\mathbf{x}$ is the $K \times 1$ vector of unknown quantities, $\mathbf{A}$ is a $K \times K$ matrix sometimes known as the *stiffness matrix* and $\mathbf{b}$ is a $K \times 1$ vector. The system (2.38) is then solved using a variational method. Let us mention that due to the specific choice of basis functions described in this section, the $K \times K$ matrix is sparse making the problem (2.38) much easier to be solved numerically. Finally, the time resolution of the magnetodynamic problem is solved using a backward Euler method (with an adaptive time stepping procedure). The non-linearities of the constitutive laws are addressed using the Newton-Raphson method [104].

## 2.4 Chapter summary

In this chapter we introduced in a very synthetic way the general mathematical framework of the finite element method to solve Maxwell's system of equations in the magnetodynamic approximation. The resulting system of partial differential equations needed to be reformulated in a weak form, more adapted to numerical implementation of the FEM. Doing so, we introduced the concept of test functions and we obtained the magnetic field and vector potential formulations of the magnetodynamic problem. Finally, we presented the idea behind the finite element method and how it greatly simplifies the numerical implementation of the weak forms by introducing a double discretization: a spatial discretization into simple geometrical elements and a discretization of the function spaces associated to the unknown quantities; followed by a time discretization.

# Chapter 3

# Experimental techniques

This chapter introduces the different experimental techniques employed to characterize the properties of the individual samples used in this thesis as well as the magnetic shielding and screening performances of experimental prototypes under a uniform or non-uniform magnetic field.

The chapter starts with an introduction of the different sources of uniform and non-uniform magnetic field (Section 3.1). Their dimensions as well as their main characteristics are described. Magnetic flux density measurements are carried out to characterize superconducting samples in terms of shielding efficiency on one hand, and flux trapping ability on the other hand. Therefore, well chosen magnetic sensors should be used and measurements should be performed following well defined procedures. Both these sensors and procedures are introduced in this chapter (Section 3.2). As mentioned in Chapter 1, the distinction is made between magnetic shielding and screening. Although the procedures followed to characterize shielding and screening properties are similar, the experimental set-up slightly differs from each other. These set-ups are presented in Section 3.3. Finally, several experimental systems are used to characterize the properties of the different individual superconducting samples. In particular, this chapter presents a flux-extraction magnetometer (Section 3.4), the Physical Property Measurement System (Section 3.5) and a homemade set-up dedicated to the measurement of magnetic hysteresis cycles for characterization of ferromagnetic materials at several temperatures (Section 3.6).

## 3.1 Sources of magnetic field

In this thesis, different sources of magnetic field are used. Basically, we can distinguish two categories of sources depending on their applications: sources that are used to create a uniform magnetic field region and sources that are used to generate a significant non-uniform stray magnetic field. In this section, we present the different sources of magnetic field used throughout this thesis, their dimensions as well as their main characteristics.

### 3.1.1 Sources of uniform magnetic field

The sources of uniform magnetic field are required in order to perform shielding measurements under a uniform external field on one hand, and flux trapping experiments to characterize individual superconducting samples on the other hand. Figure 3.1 shows pictures of the uniform field sources: a copper solenoid coil (a) as well as two electromagnets (b) and (c).

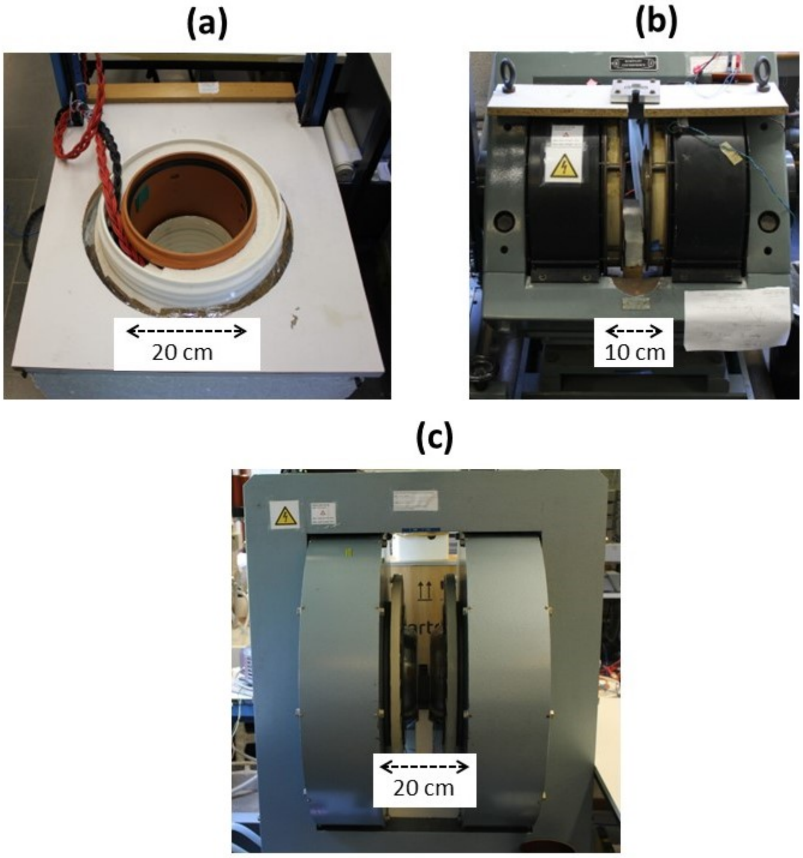

**Figure 3.1:** Overview of the sources of uniform magnetic field used in this thesis.

The copper solenoid coil (a) is characterized by a field to current ratio of 3.064 mT/A and can generate a uniform field up to 60 mT at its center. This coil was calibrated using a GM07 gaussmeter (uncertainty of less than 0.2 % on the flux density measurement). The uniformity of the magnetic field inside the coil, at its center, is found to be better than 0.1 % over 8 cm along the vertical axis [49]. This coil is powered using a Delta Elektronika SM 70-22 power supply. The electromagnet displayed in Fig. 3.1(b) can be used to apply a uniform field up to $\sim$ 670 mT. The air gap is 5 cm and the field uniformity was found to be better than 0.5 % over a surface of 6 cm × 6 cm. The field to current ratio does not exhibit a linear behavior over a large field range. Accordingly, the electromagnet was calibrated using the GM07 gaussmeter and the measurement data were interpolated with the following quadratic law:

$$B = -1.95 I^2 + 82.56 I - 4.47, \tag{3.1}$$

where $B$ and $I$ are the magnetic flux density [mT] and the injected current [A], respectively. The measurement data as well as the quadratic interpolation are shown in Fig. 3.2. Considering the calibration uncertainty of the gaussmeter, the error on the measured flux density is less than 0.2 %. This electromagnet is typically supplied with a 1 kW HP 6030A power supply. The electromagnet displayed in Fig. 3.1 (c) is powered using the 3 kW BK Precision 9117 DC Power Supply and can generate a field up to approximately 1.5 T. The field to current ratio is 32.5 mT/A and is found to be constant over the whole field range (up to 1.5 T). As the air gap of the electromagnet is 2.8 cm, it is not adapted to study the efficiency of sizeable superconducting shields. As a result, this electromagnet will be used to magnetize bulk superconducting samples in order to perform flux trapping experiments.

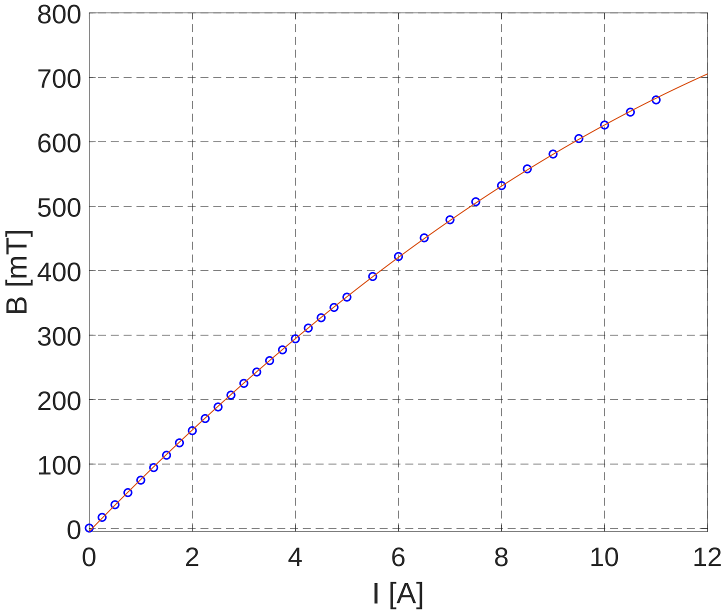

**Figure 3.2:** Calibration curve of the electromagnet displayed in Fig. 3.1(b). The blue circles are the measurement data and the red line is the quadratic law interpolation by Eq. (3.1). The relative error on the measurement is less than 0.2 %.

### 3.1.2 Sources of non-uniform magnetic field

In order to investigate the performance of superconducting magnetic screens, magnetic sources with a sufficiently high stray field are required. Figure 3.3 shows the two sources of non-uniform field that are used in the scope of this thesis: (a) a homemade copper coil with a Mn-Zn ferrite core and (b) a superconducting NbTi large bore magnet. As the exciting field generated by these sources is non-uniform, the characterization is more complex than for the sources described in the previous section. Consequently, in this section, we only present the general characteristics of these sources to give an estimation of the field amplitude it is possible to reach. An accurate characterization of the applied field will be performed in the related chapters (Chapter 6 for coil (a) and Chapter 7 for magnet (b)).

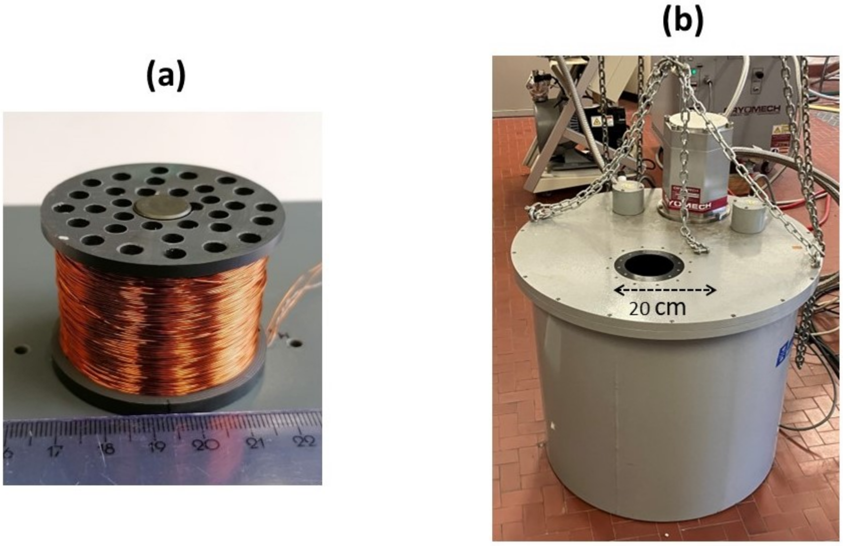

**Figure 3.3:** Overview of the sources of non-uniform magnetic field used in this thesis: (a) a copper coil with a Mn-Zn ferrite core and (b) a superconducting NbTi magnet with large bore from the Department of Applied Science and Technology (DISAT) of Politecnico di Torino, Italy.

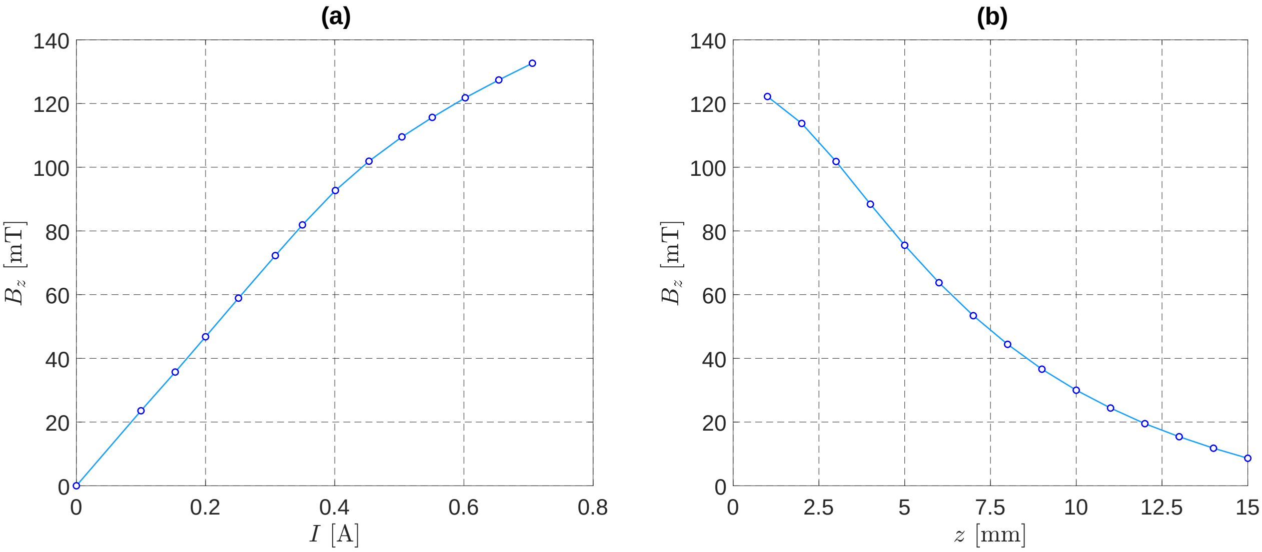

**Figure 3.4:** Axial component of the magnetic flux density (a) as a function of the injected current measured 2 mm above the core surface, at the central position and (b) as a function of the distance from the core surface on the vertical axis for an injected current of 0.7 A.

The coil displayed in Fig. 3.3(a) is made of 4300 turns of copper wire (0.3 mm diameter) wound along a height of 33 mm. The outer coil diameter is approximately 45 mm. The coil has an electrical resistance of $\sim$ 100 $\Omega$ at room temperature and $\sim$ 12.3 $\Omega$ at 77 K. In order to increase locally the applied stray magnetic field, a ferrimagnetic core is inserted in the coil bore. The core is a Mn-Zn ferrite rod having a height of 41.3 mm and a diameter of 12.3 mm [197]. In order to monitor the temperature at the center of the coil during the current injection, a type T (copper-constantan) thermocouple was placed inside the coil before starting the winding process. The type T thermocouple is well adapted for applications in cryogenic environment [198]. Figure 3.4(a) shows the magnetic flux density measured at 2 mm above the core top surface (on the coil central axis), as a function of the injected current. Figure 3.4(b) shows the evolution of the flux density as a function of the axial distance from the top surface of the core for an injected current of 0.7 A. These results show that it is possible to obtain a stray flux density greater than 20 mT at approximately 10 mm from the coil top surface, on the central axis.

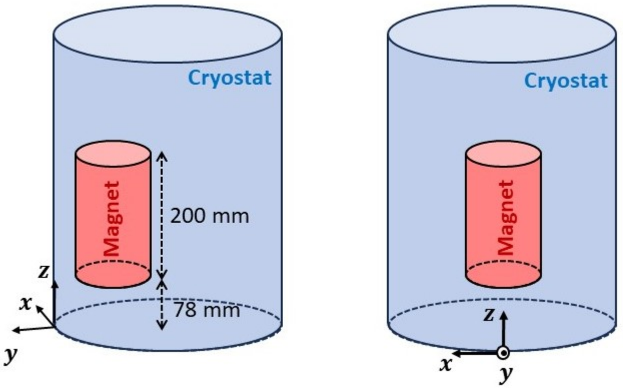

**Figure 3.5:** Schematic illustration of the relative position of the NbTi magnet with respect to the cryostat. The center of the magnet is located in the $yz$-plane.

To obtain a larger stray field over broader volume, we used the large bore superconducting magnet displayed in Fig. 3.3(b) localized in the Department of Applied Science and Technology (DISAT) at Politecnico di Torino (Italy), in the scope of a collaboration with Prof. L. Gozzelino. The magnet consists of 14 735 turns of NbTi wire wound in a total of 36 layers. The magnet has an internal diameter of 14.6 cm and an external diameter of 17.8 cm. The height is approximately 200 mm. The magnet is placed in a cryostat whose diameter is 61 cm and its height is 117 cm. The bore has a diameter of 10.2 cm. The magnet can generate up to 4 T at the central position inside the bore. An illustration of the relative position of the magnet with respect to the cryostat is shown in Fig. 3.5. The center of the magnet is positioned in the $yz$-plane at $z$ = 178 mm. Figure 3.6 shows the three components of the modeled stray flux density in the $yz$-plane (zero azimuthal field component) as a function of the vertical position. The results are

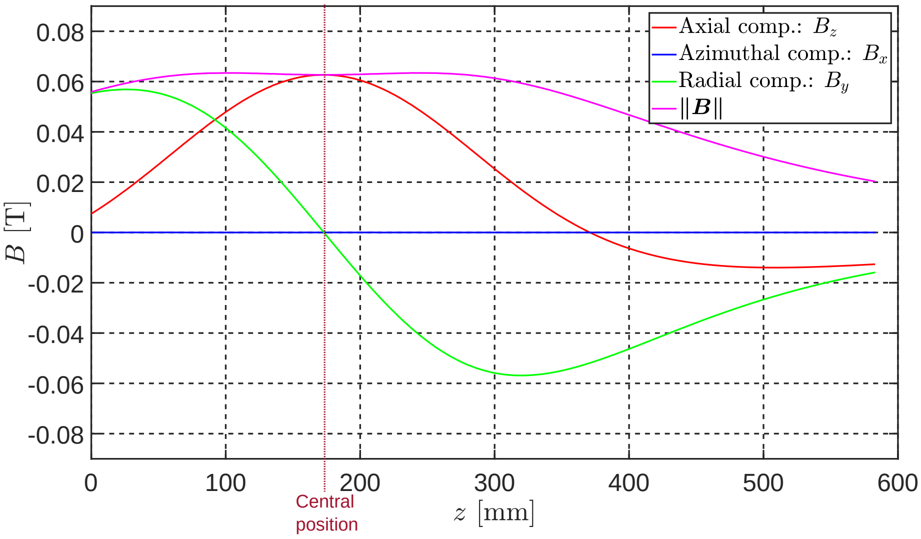

**Figure 3.6:** Numerical modeling of the three components of magnetic flux density as a function of the vertical position. The results are obtained in the $yz$-plane, 70 mm away from the cryostat external surface ($y = 70$ mm). The central position of the magnet is located at $z = 178$ mm. The $(x, y, z)$ coordinates system is shown in Fig. 3.5.

obtained numerically at 70 mm away from the cryostat wall ($y = 70$ mm). These results show that it would be possible to investigate the efficiency of an experimental magnetic screen in a stray flux density higher than 60 mT.

## 3.2 Magnetic sensors and measurement procedures

In this section, we introduce the sensors used to measure the magnetic flux density as well as their main characteristics. An experimental displacement system dedicated to obtain mappings of the magnetic flux density is also presented. Finally, the procedures followed to carry out the multiple experiments in this thesis are also described.

### 3.2.1 Magnetic flux density sensors

In the scope of this thesis, magnetic flux density measurements should be carried out with sensors that meet the following requirements: able to measure DC or AC flux densities, high sensitivity (to characterize the shielding efficiency), good linearity, small active area and able to perform measurements in a cryogenic environment. These requirements are met by the cryogenic Hall probes commercialized by *Arepoc*®. These probes are able to work in a wide temperature range (1.5 K to 350 K) and can measure flux densities up to 5 T. Moreover, they exhibit a good sensitivity, linearity and high signal-to-noise ratio. Table 3.1 gives a summarized description of the Hall sensors used in this thesis as well as their characteristics. Figure 3.7 shows an overview of these probes.

| Hall probes | Description | Nominal current | Average sensitivity at nominal current | |
|---|---|---|---|---|
| | | | 300 K | 77 K |
| (a) *Arepoc*® Axis-3S | Fixed on a polycarbonate holder (12 mm in diam.). | 10 mA | 16.04 T/V | 15.79 T/V |
| (b) *Arepoc*® Axis-3S | Fixed on a *Permaglas* holder (10 mm in diam.) for flux density mapping. | 10 mA | 11.53 T/V | 10.8 T/V |
| (c) Homemade 3-axis Hall probe set-up | 3-axis Hall probe placed in a cylindrical G10 insert. | CAN bus interfacing | | |

**Table 3.1:** Characteristics of the magnetic sensors used in this thesis.

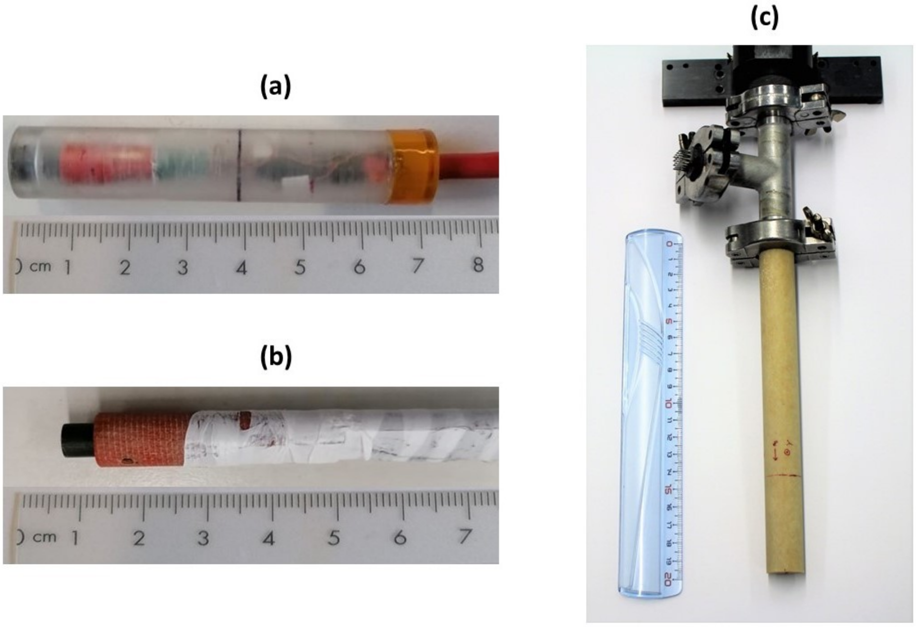

**Figure 3.7:** Hall probes used for magnetic flux density measurement in this thesis.

The *Arepoc*® Axis-3S (a) and (b) are both 3-axis Hall sensors. Each of them is mounted on a different holder in order to accommodate the situations that will be described in the related chapters. The average sensitivity provided in Table 3.1 is the average of the sensitivities of each individual axis. The active surface of each elementary sensor is 0.0025 mm$^2$. These probes are characterized by a typical sensitivity higher than 70 mV/T at a nominal current of 10 mA. The calibration of these probes was performed at room temperature and 77 K in the uniform magnetic field generated by the copper solenoid coil (a) described in Section 3.1.1. The relative uncertainty was estimated to be of the order of 2 % of the measured flux density with a noise level of approximately 50 $\mu$T. It is worth mentioning that another source of uncertainty comes from the misalignment of the probe with respect to the sample or the magnetic field source. This misalignment depends on the specific experimental system in which the probe is placed. As a result, this will be detailed in the related specific chapters.

As the Hall probes (a) and (b) are 3-axis Hall sensors, they could be used in every kind of situation involving either uniform or non-uniform magnetic field. However, over the time and likely due to repeated applications of temperature cycles, one of the transverse axis has been damaged and is now inoperable for both of them. Today, 3-axis cryogenic Hall sensors are no longer commercialized. Consequently, a homemade 3-axis Hall probe set-up able to operate at cryogenic temperature has been designed and built in our laboratory by Rotheudt *et al.* [199] (magnetic sensor (c) described in Table 3.1) in order to characterize the three components of non-uniform flux densities. The system consists in a non-cryogenic 3-axis Hall sensor thermally anchored to a copper rod in a G10 fiberglass insert to isolate it from the cryogenic environment. A 50 $\Omega$ heater made of constantan wire is wound anti-inductively on the copper rod to keep the sensor at approximately 25 °C. The Hall probe signal acquisition as well as the temperature control are performed by interfacing electronics integrated to the system. The diameter of the G10 insert is 2 cm and the probe active surface is located at approximately 2.4 mm from the bottom outer side of the insert. The measurement system is characterized by an uncertainty on the flux density measurement of $\pm 100$ $\mu$T for the axial field component (along the axis of the cylindrical insert) and $\pm 200$ $\mu$T for the transverse field components.

### 3.2.2 Mapping system

As we deal with non-uniform magnetic fields, the spatial field distribution is an important information to characterize superconducting samples and shields. To do so, an experimental system allowing to map the flux density in the vicinity of a sample can be used. This system consists in displacing a Hall probe in a 2D plane and record the magnetic flux density over this plane. The Hall probe mapping is a very common technique to characterize trapped field abilities of bulk HTS pellets [129, 132, 200–205] or stack of superconducting tapes [206–208].

The mapping system used in this thesis, is driven by three linear motorized stages orthogonal to each other from *Thorlabs*®. A Hall probe is fixed to the system by means of an adapted holder. In this thesis, both probes (b) and (c) from Table 3.1 and Fig. 3.7 will be used with the mapping system to characterize superconducting samples. Figure 3.8 shows a picture of the 3-axis mapping system with the homemade 3-axis cryogenic Hall probe (c). The motors have a displacement range of 5 cm thus allowing the probe to be positioned within a 5 cm-side cubic volume. Their absolute on-axis accuracy is 290 $\mu$m.

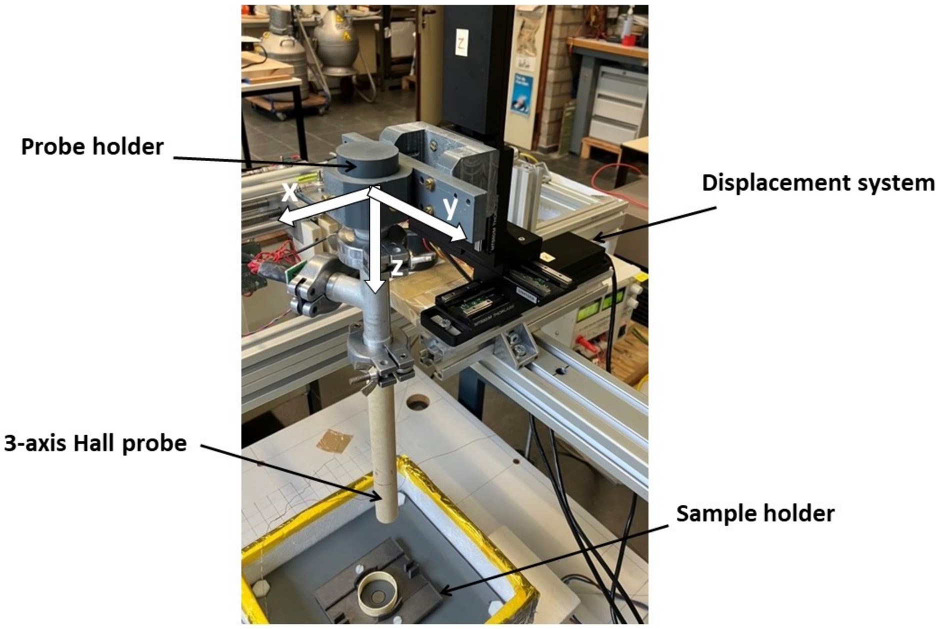

**Figure 3.8:** Picture of the flux density mapping system.

Accordingly, this experimental set-up can be used to perform 1D mappings (measurement along one axis), 2D mappings or 3D mappings. In particular, recently, the system has been used to map the magnetic flux density around more complex structures like superconducting cylinders [47, 49, 60], short-circuited 'eye-shaped' tapes [199] or superconducting linear Halbach array [209].

### 3.2.3 Measurement procedures

This thesis involves several kinds of magnetic measurements to characterize the superconducting samples. Experiments generally fall in two categories: trapped field measurements and magnetic shielding measurements.

#### Trapped field measurement

Measurements of the trapped magnetic field are performed following a field cooling (FC) procedure as shown in Fig. 3.9. The figure shows the time evolution of the magnetic flux density $B(t)$ simultaneously with the time evolution of the temperature $T(t)$.

In practice, the measurement procedure involves the four following steps:

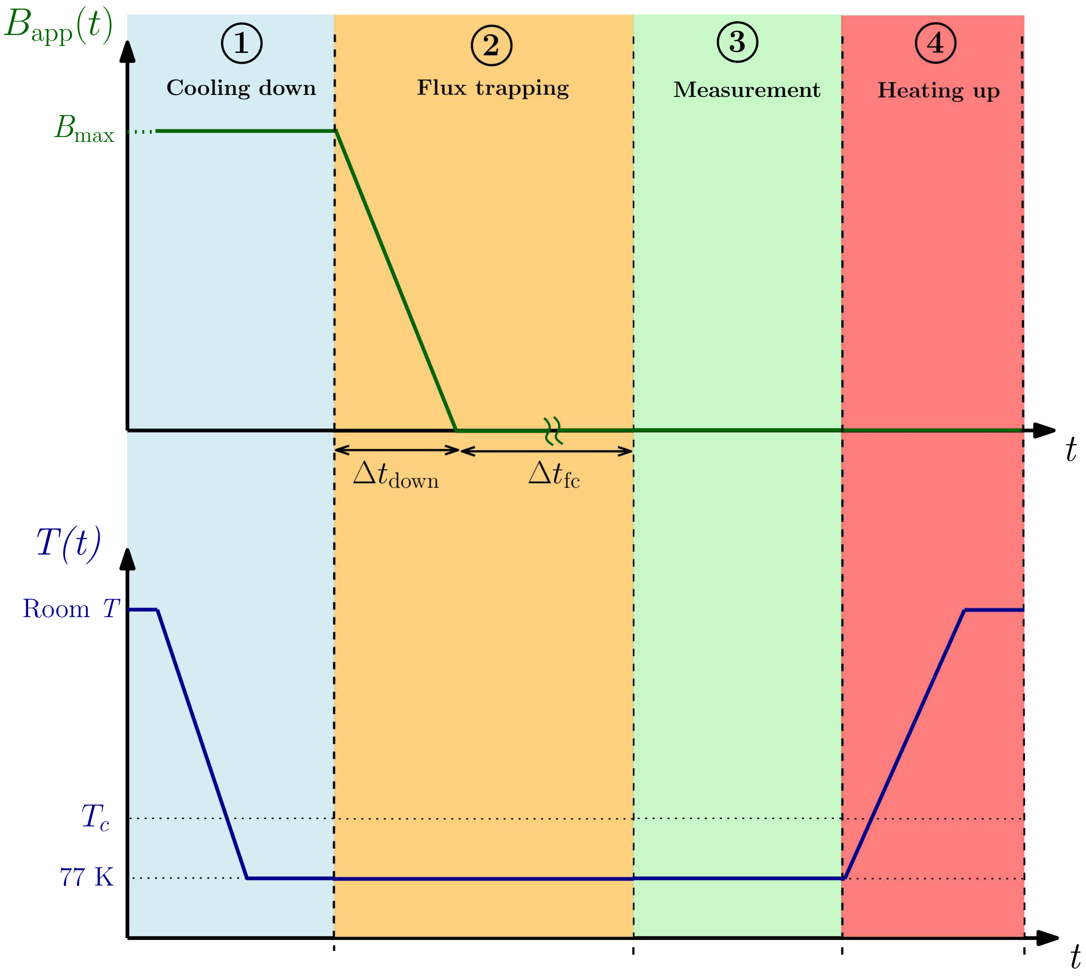

**Figure 3.9:** Experimental procedure for measurement of trapped magnetic flux density in a superconductor. Evolution of both the magnetic flux density $B(t)$ and the temperature $T(t)$ over the time. $B_{\rm max}$ is the maximum applied field and $T_c$ is the critical temperature. The measurement is performed after the time required to switch off the applied field $\Delta t_{\rm down}$ and a possible waiting time $\Delta t_{\rm fc}$.

- **1. Cooling down.** First, the superconducting sample should be magnetized following a FC procedure. To do so, the magnetic flux density is first applied up to its maximum value $B_{\rm max}$. The rate of application of the magnetizing field in this step is not of any importance as the sample is not superconducting yet. Then, the temperature is decreased below the critical temperature $T_c$. In the work reported in this thesis, the coolant is always liquid nitrogen. Therefore, the operating temperature is 77 K.

- **2. Flux trapping.** The magnetic flux density is decreased down to 0 at a rate of $-B_{\rm max}/\Delta t_{\rm down}$ resulting in a magnetized superconducting sample. After that, the trapped field decreases over time due to flux creep. We thus need to wait for a sufficiently long period $\Delta t_{\rm fc}$ so that the flux density is stable enough during the measurement time. In general, it is recommended to wait for at least $\Delta t_{\rm fc} =$ 1000 s [201].

- **3. Measurement.** The third step is the trapped flux density measurement using an appropriate magnetic sensor. Note that the time during which the measurement is carried out is important as the sample continues to undergo flux creep. Typically, if $\Delta t_{\mathrm{fc}} > 1000$ s, the measurement time should be smaller than 10 000 s. This detail has to be taken into account when performing time consuming measurement like a 2D mapping of the flux density, for instance.

- **4. Heating up.** Finally, once the measurement step is completed, the sample is heated up to room temperature in order to remove the trapped flux from the material.

### Shielding measurement

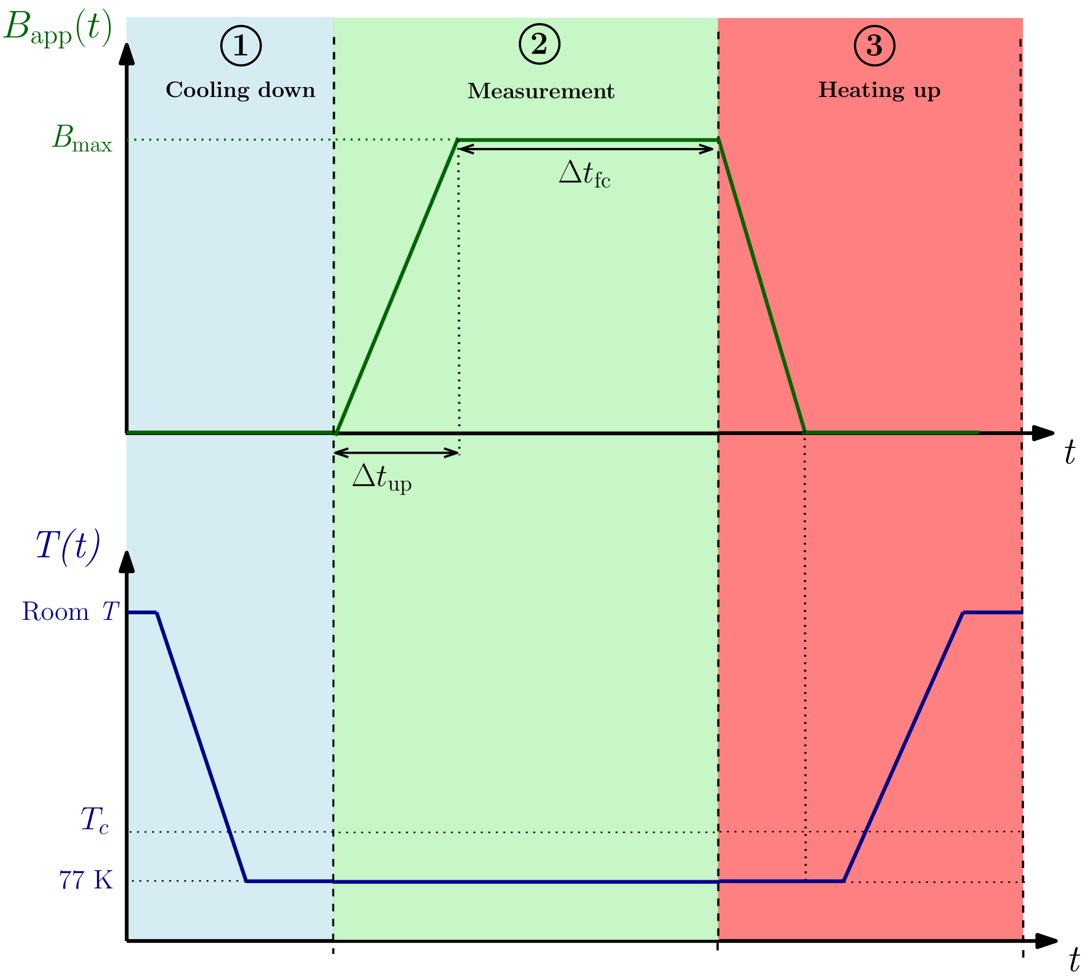

**Figure 3.10:** Experimental procedure for measurement of magnetic shielding with superconductors. Evolution of both the magnetic flux density $B(t)$ and the temperature $T(t)$ over the time. $B_{\max}$ is the maximum applied field and $T_c$ is the critical temperature. The measurement is performed during a rising time $\Delta t_{\mathrm{up}}$ or after a possible waiting time $\Delta t_{\mathrm{fc}}$.

For magnetic shielding experiments, the measurements are performed in zero field cooling (ZFC) conditions. The shielding measurement procedure is shown in Fig. 3.10 and is described below:

- **1. Cooling down.** First, the superconducting shield is cooled down to 77 K (liquid nitrogen temperature) in absence of any applied magnetic field in order to be in ZFC conditions.
- **2. Measurement.** Once the superconducting shield is at its operating temperature, the magnetic field is applied at a constant rate of $B_{\mathrm{max}}/\Delta t_{\mathrm{up}}$. The shielded field is measured during this applied field ramp to obtain the 'dynamic' dependence $B(B_{\mathrm{app}})$ at several points of interest. When the applied field has reached its maximum value, it is still possible to perform shielding measurement under a constant field. In this case the sample can be subjected to flux creep and it may be necessary to wait for an appropriate time $\Delta t_{\mathrm{fc}}$.
- **3. Heating up.** Finally, the shield is reset to its original state. The applied field is first decreased down to 0. Then, the shield is heated up to room temperature and prepared for a possible second round of measurements.

## 3.3 Shielding measurement systems

As mentioned in Chapter 1, shielding and screening experiments differ as follows: 'Shielding' refers to a superconducting enclosure submitted to an external magnetic field while in 'screening', the superconductor consists in a wall or a screen placed next to a magnetic field source. Even if the characterization of a superconducting screen follows the same measurement procedure than that described for the characterization of a superconducting shield (Section 3.2.3), the experimental set-up slightly differs.

### 3.3.1 Experimental set-up for shielding measurement

A schematic representation of the experimental system used for shielding measurements is shown in Fig. 3.11. The superconducting shield is submitted to an external magnetic field, which is always uniform in this work. A cryogenic Hall probe is located inside the superconducting shield which is immersed into a liquid nitrogen bath (77 K). The bath itself is placed in the uniform field region of a source coil. The probe is supplied by a Keithley 2400 current source. The current in the source coil is injected by means of a specific power supply and is measured through a 1 m$\Omega$ shunt. The power supply is chosen depending on the power requirements of the magnetic source coil. In practice, we use either the Delta Elektronika SM 70-22 power supply or the HP 6030A power supply. The

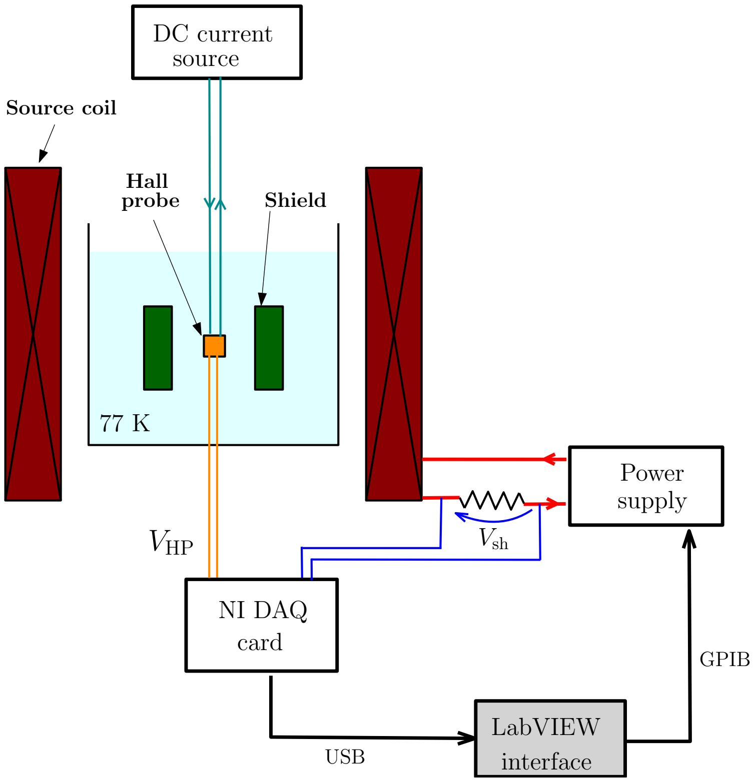

**Figure 3.11:** Schematic representation of the experimental set-up for shielding measurements. $V_{\mathrm{HP}}$ and $V_{\mathrm{sh}}$ denote the voltage drop across the Hall probe and the shunt respectively.

Hall probe voltage $V_{\mathrm{HP}}$ and the voltage across the shunt $V_{\mathrm{sh}}$ are recorded using a NI USB-6281 acquisition card. Both the DAQ card and the power supply are computer controlled through the *LabVIEW* interface.

### 3.3.2 Experimental set-up for screening measurement

In the screening experimental set-up, the superconductor is placed between the Hall probe and the magnetic field source as illustrated in Fig. 3.12. Here, the source coil itself is also immersed in the liquid nitrogen bath so that it can be fed with sufficiently high current without excessive heating. In this case, the excitation field is non-uniform. The screening efficiency is thus characterized by a 3-axis cryogenic Hall probe attached to the mapping system described in Section 3.2.2. The current in the source coil is supplied by a Delta Elekronika SM 70-22 power supply and is controlled using an ammeter. The Hall probe voltages are recorded using a NI USB-6281 acquisition card. The aquisition card, the power supply and the micropositioning drive system are all controlled with a LabVIEW program. It is worth mentioning that, in the shielding experimental set-up described in the previous subsection, the uniform applied field was given by the precise knowledge of the current in the source coil. In this case, however, the applied field is non-uniform and can no longer be known a priori knowing the injected current. The measurement procedure always requires to measure accurately the applied field in the absence of superconductor

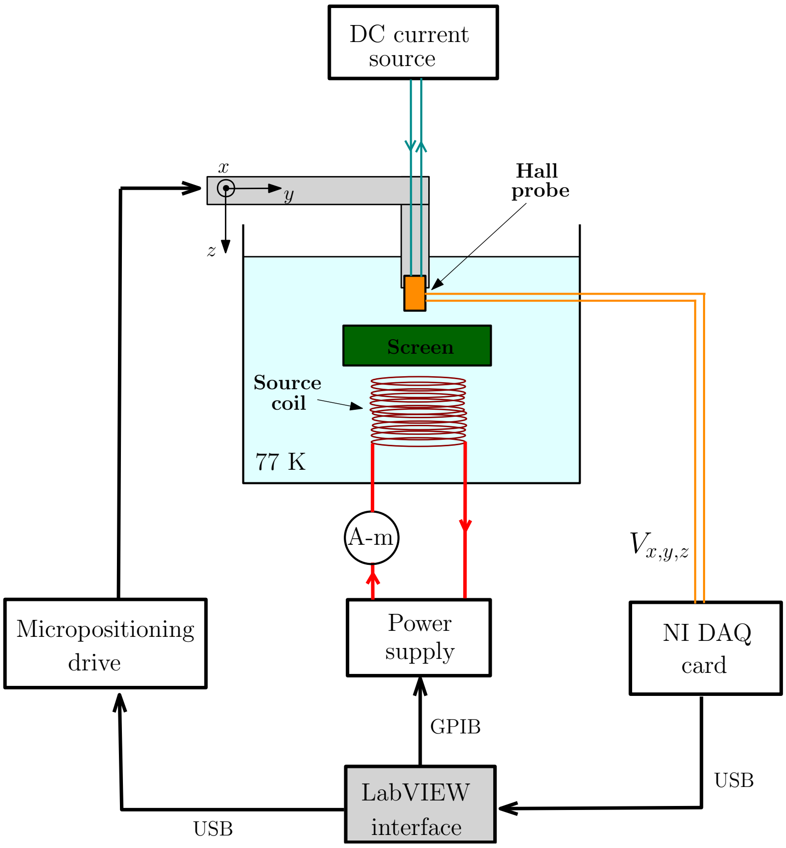

**Figure 3.12:** Schematic representation of the experimental set-up for screening measurements. $V_{x,y,z}$ denote the three voltage drops across the 3-axis Hall probe.

before characterizing the screening efficiency. Consequently, the precise knowledge of the injected current is no longer required. Finally, let us mention that when the mapping system is used with the homemade 3-axis Hall probe set-up described in Table 3.1, the supply of the Hall probe as well as the data acquisition are performed using a CAN bus interfacing powered by a Velleman DC voltage source. The CAN bus is also controlled with the LabVIEW program.

## 3.4 Flux extraction magnetometer

One common technique to estimate the critical current density and the $n$ value in bulk HTS consists in performing magnetization relaxation measurements. After the HTS sample has been magnetized, its magnetic moment exhibits a power law behavior as a function of time. Measurements of the magnetic moment over time can provide us with the law parameters by fitting the measurement data with the theoretical law given by Eq. (1.7). Limiting oneself to the approximation of a constant $J_\mathrm{c}$, the critical current density of a cylindrical high-temperature superconductor is given by [210, 211]

$$J_c \approx \frac{3m_0}{2\pi a^3 b}, \tag{3.2}$$

where $2a$ and $2b$ denote the diameter and the height of the cylinder respectively.

Magnetic moment measurement of previously magnetized bulk superconductors is performed using a flux extraction magnetometer suitable to sizeable samples (typically up to 15 mm diameter) developed in our laboratory by Egan *et al.* [212]. A flux extraction magnetometer provides a measurement of the volume magnetic moment of a magnetic sample (e.g. permanent magnet or magnetized superconductor) by creating a relative linear movement between the sample and a set of 2 pick-up coils connected in series opposition. The magnetic moment can be obtained by direct time integration of the electromotive force (e.m.f) signal. The system is based on a multipole expansion also proposed for other magnetometry techniques [213].

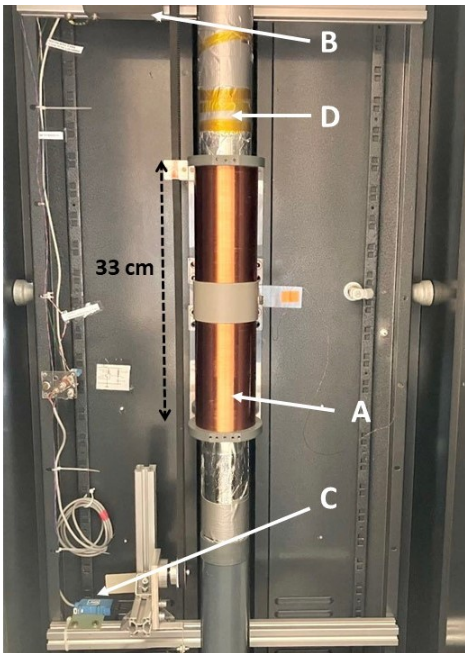

**Figure 3.13:** Picture of the flux extraction magnetometer designed by Egan *et al.* [212] together with the new cryostat (namely D in the picture).

A picture of the flux extraction magnetometer is shown in Fig. 3.13. The pick-up coils connected in series opposition (A) follow a linear motion actuated by an electric motor surrounded by a ferromagnetic shield (B). An optical position sensor (C) is used to control the position of the pick-up coils. In the scope of this thesis, the sample holder and the liquid nitrogen cryostat (D) have been adapted to accommodate bigger samples compared to the original system.

## 3.5 Physical Property Measurement System (PPMS)

The *Physical Property Measurement System* is a versatile instrument commercialized by *Quantum Design* [214]. It allows to carry out physical measurements in high magnetic field environment like AC susceptometry, DC magnetometry, torque magnetometry, electrical transport properties or heat capacity. The PPMS available in the lab (showed in Fig. 3.14) can perform measurements under an applied field up to 9 T with a maximum sweep rate of 170 Oe/s (17 mT/s). Moreover, the system allows to carry out measurements in a wide temperature range (1.9 K to 400 K). Therefore, it can also be used to characterize magnetic shields under high magnetic field and low temperature conditions [38, 42]. However, the PPMS is limited by the small size of the experimental chamber (inner diameter of 25 mm) and by the fact that the field can only be applied along one axis. As a result, this system cannot be used to study the shielding efficiency of the samples investigated in this work. As shown in Fig. 3.14 and Fig. 3.15, the PPMS consists of different parts: a liquid helium cryostat surrounded by a liquid nitrogen cryostat, a probe and a processing unit including the current source of the superconducting magnet. The probe (Fig. 3.15) is composed of a sealed vacuum experimental chamber, a superconducting (NbTi) magnet and an instrumented 'puck' accommodating the sample which is connected to the bottom of the experimental chamber.

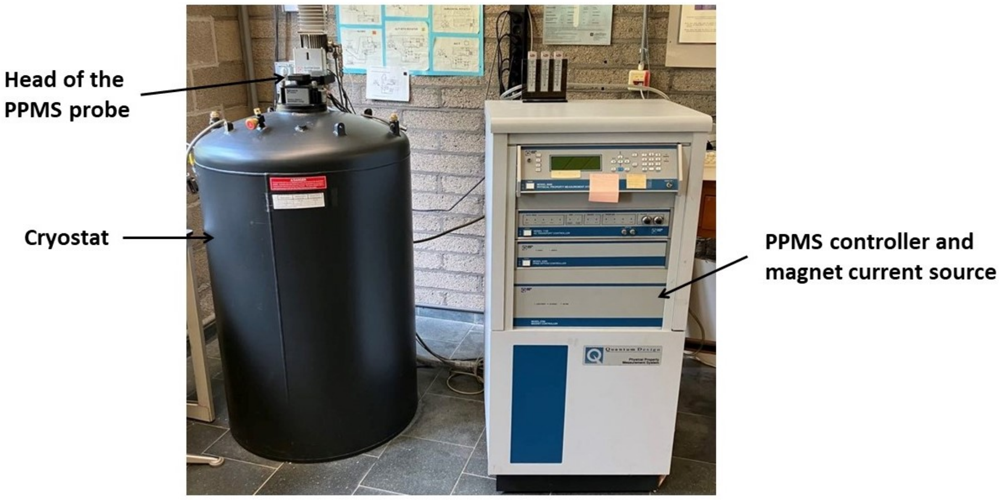

**Figure 3.14:** Picture of the Physical Property Measurement System (PPMS) including the cryostat and the control unit.

In the scope of this thesis, the PPMS is used to perform DC magnetization measurements to characterize a bulk, large grain superconducting sample. As a result, we only describe here the ACMS option for DC magnetic characterization of small samples [216]. In the DC magnetometry process, the system measures the magnetic moment in a certain applied magnetic field at a given temperature. The measurement is based on the

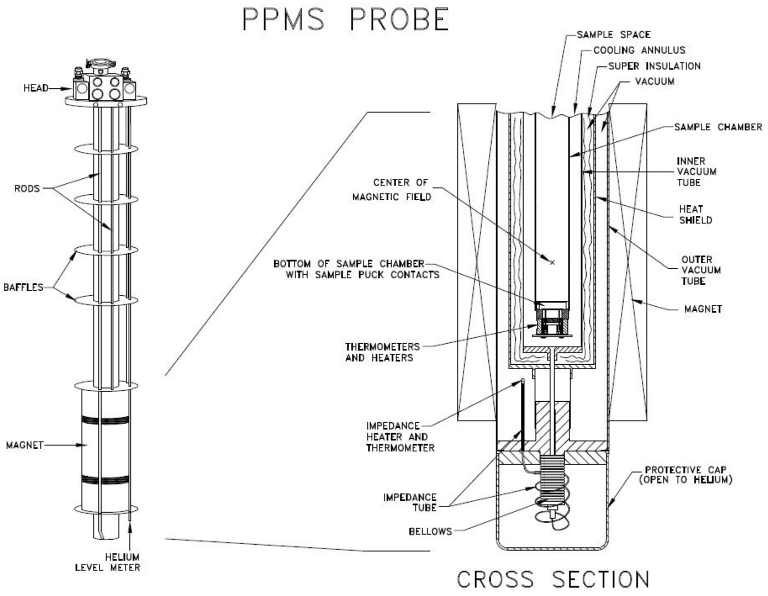

**Figure 3.15:** Schematic representation of the PPMS probe assembly which is inserted into the cryostat (from [215]).

extraction method and is similar to the method described in Section 3.4. The PPMS superconducting magnet provides a constant magnetic field in the sample space and a DC servo motor moves the sample through a set of counter-wound pick-up coils connected in series. The induced voltage across the pick-up coils is then analyzed to determine the sample's magnetic moment.

## 3.6 Measurement system for hysteresis cycles

As the work of this thesis involves superconducting tapes based on a slightly ferromagnetic substrate, it is important to characterize the magnetic properties of this substrate. In this thesis, an experimental system was developed to measure magnetic hysteresis cycles on an almost toroidal ferromagnetic sample with a nearly square cross section.

The sample on which the measurement system is mounted is a stack of coated conductor (CC) annuli based on a Ni-5at.%W alloy substrate [217, 218] which is weakly ferromagnetic. Figure 3.16(a) shows a picture of this sample which was extracted from a bigger stack of tapes and that will be described in more details in Chapters 4 and 5. This sample is in the shape of a closed magnetic circuit bringing the following advantages: (i) the convenience to magnetize the sample uniformly up to rather high magnetic flux density values by simply winding a magnetizing coil around it and (ii) the absence of demagnetizing field in the direction of magnetization. The resulting magnetic circuit has a toroidal shape with a nearly square cross section [219, 220].

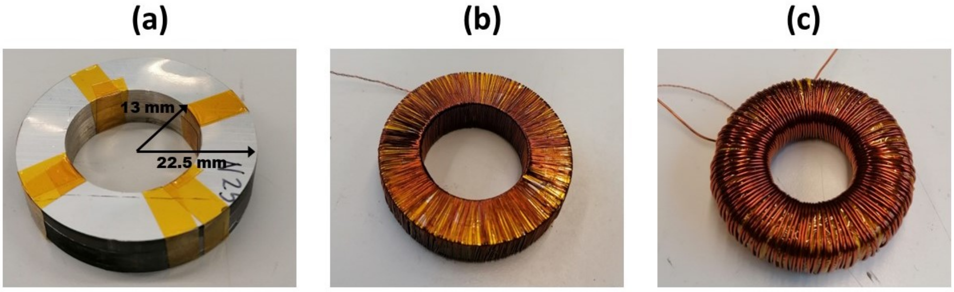

**Figure 3.16:** Pictures of (a) the ferromagnetic sample, (b) the secondary winding made of 0.15 mm diameter wire dedicated to the e.m.f measurement and (c) the primary winding made of 0.6 mm diameter wire used to inject the current.

The measurement method involves two windings: the primary winding made of 0.6-mm diameter wire in order to inject a current up to 0.6 A is used to generate the applied magnetic field $H$. The magnetic field strength $H$ can be found from the injected current $I$ and the number of turns in the magnetizing coil $n_{\mathrm{p}}$ through

$$H = \frac{n_{\mathrm{p}} I}{l}, \tag{3.3}$$

where $l$ is the mean magnetic path, which can be determined in a good approximation by

$$l = 2\pi \frac{R_{\mathrm{out}} - R_{\mathrm{in}}}{\ln(R_{\mathrm{out}}/R_{\mathrm{in}})} \tag{3.4}$$

with $1.1 < R_{\mathrm{out}}/R_{\mathrm{in}} < 1.6$ to ensure a sufficient magnetic field uniformity within the sample [219]. The secondary winding is devoted to the electromotive force (e.m.f) measurement. It is made of one layer of 0.15-mm diameter wire to maximize the number of turns (433 in this case) directly wound on the sample to minimize the influence of the stray field. The magnetic flux density $B$ is then obtained by time integration.

Both the secondary and primary windings are shown in Figures 3.16(b) and (c) respectively. As reported in Tumanski's comprehensive handbook [219], a parasitic effect may arise from how the primary is wound due to the fact that, in practice, the windings are slightly slanted with respect to the torus cross section and may generate a spurious magnetic field along the torus axis of revolution. Therefore, if no precaution is taken, a coil uniformly wound is equivalent to a hypothetical single turn located at the mean circumference. This turn may be coupled to a hypothetical single turn formed by the secondary winding. In order to reduce this effect, the primary winding is made of an even number of layers wound along the ring circumference following alternatively the clockwise and anticlockwise way. With such pairs of layers, the turns are slightly slanted in such a way that the contributions of two neighboring layers to the field component along the axis of revolution are expected to cancel out each other.

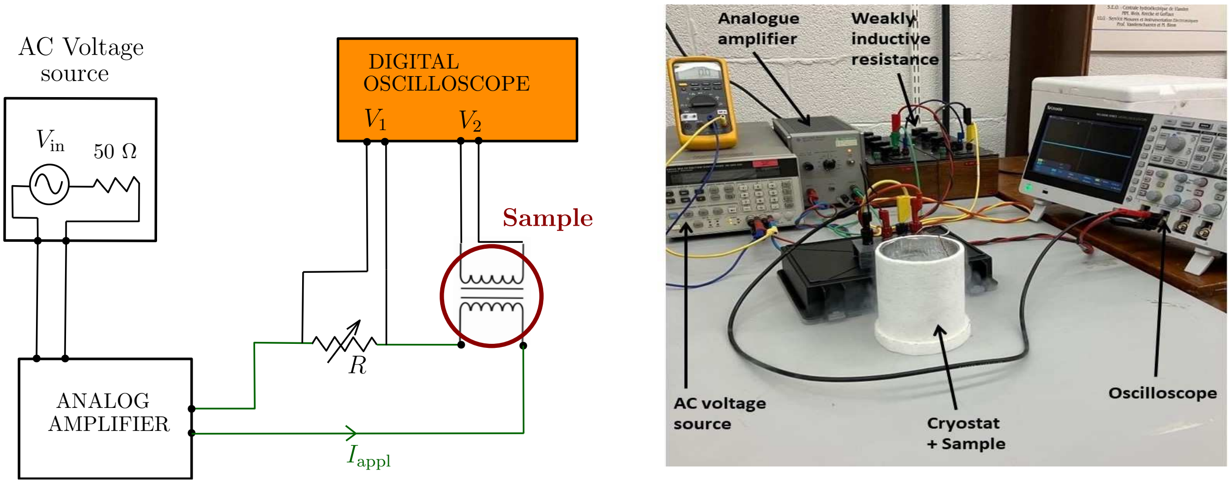

**Figure 3.17:** Schematic representation of the electrical connections (left) together with a picture (right) of the experimental set-up for magnetic hysteresis cycles measurement.

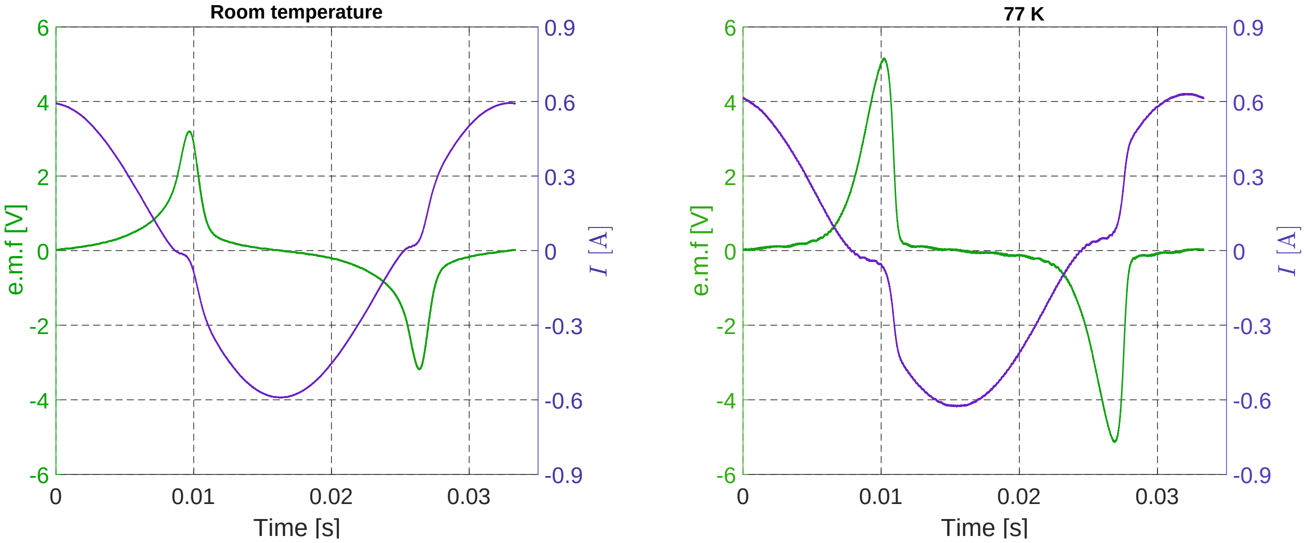

**Figure 3.18:** Comparison of the current signal $I$ applied to the primary winding of the sample and the e.m.f signal measured across the secondary winding. The signals are obtained at room temperature (left side) and 77 K (right side) on a stack of 2G CC annuli with Ni-5at.%W alloy substrate. Only one period of the signal is shown in the figure.

The measurement system is shown schematically in Fig. 3.17. The magnetizing coil (primary winding of the sample) is fed with an AC current at a frequency of 30 Hz using a HP 8904A voltage source. A HP 467A analog amplifier is connected between the voltage source and the sample to ensure impedance matching. The magnetizing current is measured by connecting a weakly inductive resistor $R = 16\ \Omega$ in series with the primary winding of the sample. The voltage signal $V_1$ across the resistor $R$ is measured through the first channel of a TBS 2204B digital oscilloscope. This signal is a direct measurement of the magnetizing current signal. The e.m.f across the secondary winding of the sample ($V_2$) is directly measured through the second channel of the oscilloscope. For measurements carried out at liquid nitrogen temperature (77 K), the sample is placed in the polystyrene cryostat showed on the right picture in Fig. 3.17. As an example, Fig. 3.18 shows the current signal applied to the primary winding as well as the electromotive force (e.m.f) signal measured across the secondary winding on a stack of 2G coated conductor tapes shown in Fig. 3.16(a). Figure 3.18 shows one period of the signals at both room temperature and 77 K. The time dependence of the magnetizing field $H(t)$ is directly obtained from the $I(t)$ signal using Eq. (3.3). The magnetic flux density $B(t)$ is obtained from the electromotive force:

$$B(t) = \frac{1}{SN_s} \int_0^T \text{e.m.f } (t) \text{ dt} \tag{3.5}$$

where $S$ is the cross section area of the ferromagnetic sample and $N_s$ is the number of turns of the secondary winding.

## 3.7 Chapter summary

In this chapter, we introduced the details of the experimental methods used throughout this thesis, including measurement techniques, instrumentation and experimental set-ups. First, the chapter introduced the different magnetic field sources used to characterize the superconducting shields making the distinction between sources of uniform and non-uniform applied field. Then, we described the different magnetic sensors and measurement procedures to characterize superconducting shields. In particular, we detailed the experimental systems designed for magnetic shielding and screening measurements. The technical specifications and estimation of measurement uncertainties regarding the instrumentation devices are also provided. Finally, the chapter summarized several measurement systems and instruments devoted to the characterization of individual samples: the flux extraction magnetometer, the Physical Property Measurement System (PPMS) and a bespoke measurement system for ferromagnetic hysteresis cycles developed in the framework of this thesis.

# Chapter 4

# High-Temperature Superconducting samples: electrical and magnetic properties

In order to characterize the efficiency of magnetic shields and screens, it is necessary to obtain information on the electrical and magnetic properties of the HTS samples used to design such shields or screens. Superconducting samples were basically obtained either from academic collaboration or from industry. In both cases, the relevant data necessary to investigate the shielding efficiency are needed. The chapter focuses on the samples that have been subjected to a detailed in-house characterization. Accordingly, all the samples investigated in the scope of this thesis are not introduced in this chapter. HTS samples for which we assumed that the data provided by the manufacturer were sufficient will be presented in next chapters. In particular, the coated conductors provided by *Shangai Superconductors*® and *Superpower*® of which the magnetic and electrical properties do not require further characterization, will be introduced in Chapters 6 and 7 respectively.

First, the chapter presents the characterization performed on bulk HTS samples. These data are important to compare the quality of these different samples and to be integrated into numerical models. Then, some of the HTS coated conductors used in this thesis are based on Ni-alloy substrates. These substrates are shown to be slightly ferromagnetic and can thus have a significant influence on the magnetic shielding (or screening) efficiency. As a result, the ferromagnetic properties of superconducting tapes based on a Ni-5at.%W Rolling Assisted Biaxially Textured Substrate (RABiTS) are investigated using a well adapted sample obtained by international collaboration.

## 4.1 HTS bulk samples

Five single grain melt-textured bulk HTS samples are investigated in this thesis. Four cylindrical $GdBa_2Cu_3O_7$ samples were fabricated in the shape of bulk cylinders by the Top-Seeded Infiltration and Growth (TSIG) technique [44, 45]. The fifth sample is an $YBa_2Cu_3O_7$ rectangular prism from Adelwitz Technologiezentrum GmbH (ATZ®). Pictures of the five bulk superconducting samples are displayed in Fig. 4.1. The dimensions of the four cylinders are described in Table 4.1.

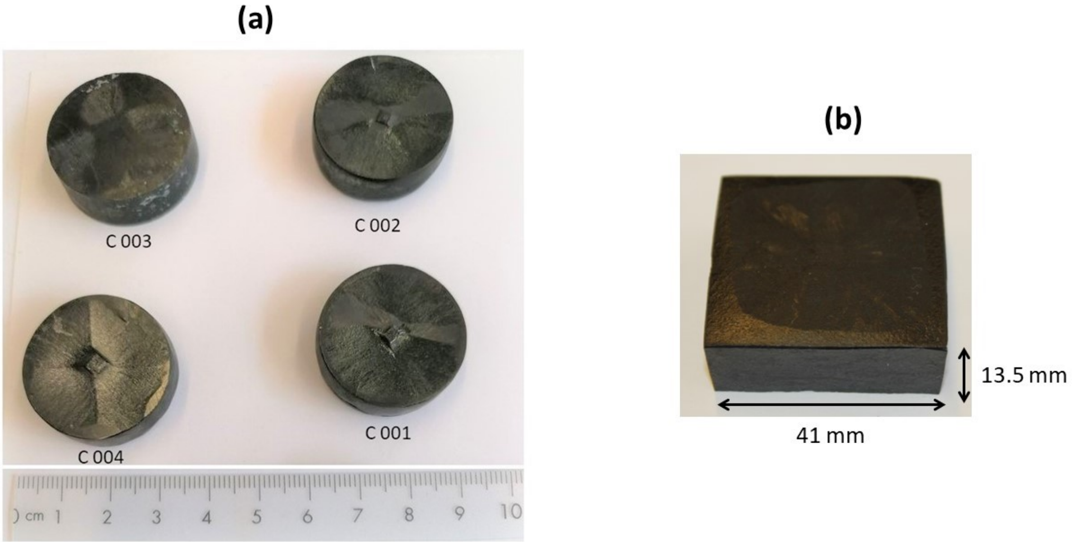

**Figure 4.1:** Picture of (a) four cylindrical bulk samples and (b) an YBCO rectangular prism.

| | **C 001** | **C 002** | **C 003** | **C 004** |
|---|---|---|---|---|
| Diameter [mm] | $31.8 \pm 0.2$ | $31.77 \pm 0.11$ | $33.36 \pm 0.09$ | $31.95 \pm 0.35$ |
| Height [mm] | $9.3 \pm 0.15$ | $9.15 \pm 0.25$ | $10.38 \pm 0.06$ | $9.6 \pm 0.3$ |

**Table 4.1:** Dimensions of the GdBCO cylindrical samples displayed in Fig. 4.1(a).

This section is devoted to the characterization of the properties of each individual sample. Moreover, the bulk cylinders displayed in Fig. 4.1(a) are expected to exhibit strong $J_c$ inhomogeneities as stressed out by Yang *et al.* [45]. Consequently trapped field measurements are also performed on these samples in order to possibly locate defects.

### 4.1.1 Estimation of $J_c$

The critical current density of the bulk HTS samples described above is estimated by inductive methods using either the flux extraction magnetometer described in Section 3.4 or the Physical Property Measurement System (PPMS) described in Section 3.5. The cryostat and the sample holder of the flux extraction magnetometer have been adapted to accommodate the GdBCO bulk cylinders. However, the size of the YBCO rectangular sample (Fig. 4.1(b)) is still too large to be placed in the magnetometer cryostat. Consequently a small rectangular rod extracted from the same sample is placed in the PPMS experimental chamber to perform the measurement of magnetization cycles.

#### Characterization with the flux extraction magnetometer

The four GdBCO cylindrical samples are characterized in the flux extraction magnetometer by performing flux relaxation measurement. To do so, the sample is first magnetized up to 1.5 T following a field cooled (FC) procedure. Then the sample is placed in the magnetometer and its magnetic moment is measured over time. The time evolution of the magnetic moment is given by the law Eq. (1.7). As a result, the time dependence of the magnetic moment can provide us with the initial magnetic moment $m_0$ as well as the critical exponent $n$. The critical current density for a HTS cylinder can be estimated by Eq. (3.2). The time dependence measured by the magnetometer for the different samples is plotted in Fig. 4.2. The circles are the measurement data and the dashed lines show the fitting of the measurement data with the law given by Eq. (1.7). The estimated parameters, namely the initial magnetization, the critical exponent and the critical current density are provided in Table 4.2.

| SAMPLES | **C 001** | **C 002** | **C 003** | **C 004** |
|---|---|---|---|---|
| $m_0$ [Am$^2$] | 7.8 | 5.5 | 1.8 | 6 |
| $n$ [-] | 35.9 | 33.6 | 36.9 | 29.9 |
| $J_c$ [A/m$^2$] | $1.99 \times 10^8$ | $1.3 \times 10^8$ | $4.2 \times 10^7$ | $1.4 \times 10^8$ |

**Table 4.2:** Parameters obtained by flux relaxation measurement on the GdBCO HTS cylinders with the flux extraction magnetometer.

The results shown in Fig. 4.2 and Table 4.2 clearly indicate that the GdBCO sample with the higher critical current density is the C 001 cylinder for which $J_c \approx 2 \times 10^8$ A/m$^2$. The sample with the lowest critical current density is the cylinder C 003 with $J_c \approx 4 \times 10^7$ A/m$^2$. The samples C 002 and C 004 display very similar superconducting properties in terms of magnetic moment relaxation and critical current density. From these results,

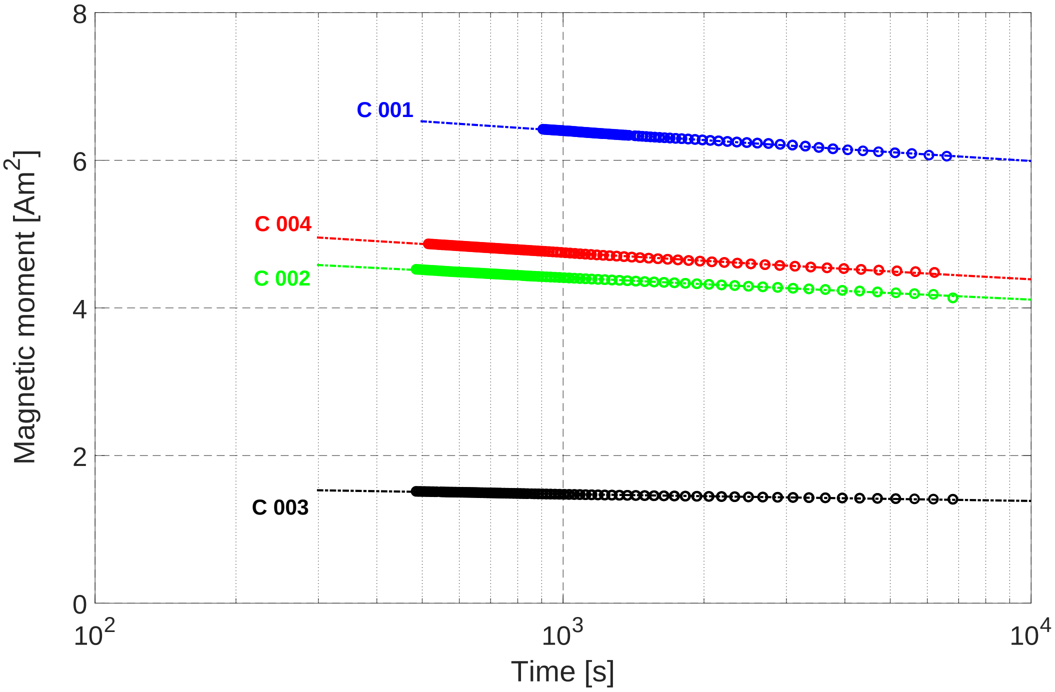

**Figure 4.2:** Measured time dependence of the magnetic moment of the four bulk GdBCO cylinders described in Fig. 4.1 and Table 4.1. The samples have been permanently magnetized under 1.5 T in field cooled conditions. The circles are the measurement data and the dashed lines are interpolations with Eq. (1.7).

we choose to discard the sample C 003 as it seems that the superconducting properties have suffered from much more degradation than for the three other samples. The critical exponent $n$ is shown to be very similar for the different samples.

### Characterization with the PPMS

As the cryostat of the magnetometer does not accommodate the rectangular YBCO sample from ATZ®, a small rod of nearly squared cross section is extracted from the initial bulk sample and placed in the PPMS experimental chamber to perform DC magnetization measurements. The sample as well as its dimensions are shown on the left side of Fig. 4.3. Let us stress here that, as this characterization is destructive for the bulk sample, it is actually performed after obtaining the experimental results presented in Chapter 5. The magnetization measurement is performed in a field applied parallel to the longest side of the sample. The hysteresis magnetization cycle is recorded for a maximal external field of 2 T and can be seen on the right side of Fig. 4.3.

The critical current density of the YBCO sample can be deduced from the magnetization cycle displayed in Fig. 4.3. In the limit of the Bean model, the critical current

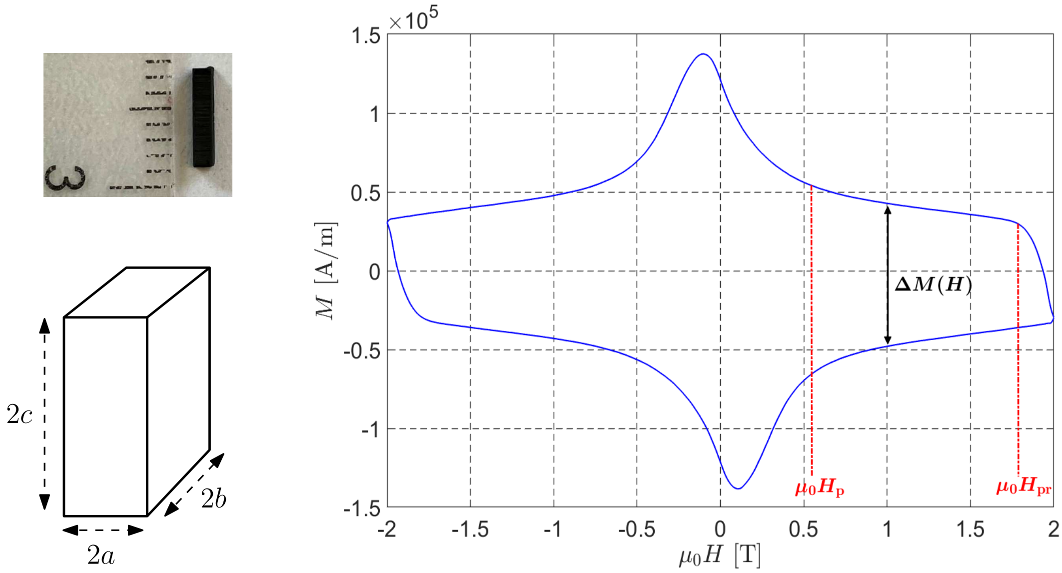

**Figure 4.3:** (Left) Picture and schematic of the sample extracted from the YBCO bulk sample that is placed in the PPMS experimental chamber. The dimensions are $2c = 6.5$ mm, $2b = 1.46$ mm and $2a = 1.41$ mm. (Right) Magnetization as a function of the external applied field at 77 K.

density of a rod with a rectangular cross section ($2a \times 2b$) is given by [221]

$$J_\mathrm{c} = \Delta M(H)\left[a\left(1 - \frac{a}{3b}\right)\right]^{-1}, \tag{4.1}$$

where $\Delta M(H)$ is the magnetization difference between the ascending branch and the descending branch of the magnetization cycle at a given field $H$. Eq. (4.1) together with the measured magnetization cycle can give an estimation of the field dependence of $J_\mathrm{c}$. In theory, considering a field-dependent $J_\mathrm{c}$ is contrary to the assumptions used to derive the Bean model equations. In a very good approximation, however, it is possible to estimate the field dependence of $J_\mathrm{c}$ in the framework of the critical state when the superconductor is in the fully penetrated state [221–223]. In practice, the formula given by Eq. (4.1) is valid in the field range

$$1.5\mu_0 H_\mathrm{p} < \mu_0 H < \mu_0 H_\mathrm{pr}, \tag{4.2}$$

where $H_\mathrm{p}$ is full penetration field and $H_\mathrm{pr}$ is called the full reverse penetration field, defined below. An estimation of the full penetration field under the Bean model assumptions for this specific geometry is given by

$$\mu_0 H_\mathrm{p} \approx \mu_0 J_\mathrm{c} a. \tag{4.3}$$

The manufacturer provides measurement data on melt-textured YBCO cylinders and specifies a critical current density in the range $1.5 - 6 \times 10^8$ A/m$^2$ at self-field and 77 K. Typically, for $J_\mathrm{c} = 6 \times 10^8$ A/m$^2$, the full penetration field is equal to $\mu_0 H_\mathrm{p} \approx 0.53$ T. The full reverse penetration field corresponds to the bending of the descending magnetization curve and is approximately equal to 1.8 T. Both field values are indicated in the graph of Fig. 4.3. The field dependence of the critical current density determined from the magnetization curve is plotted in Fig. 4.4. The measurement data are obtained by Eq. (4.1) and are fitted using the following Kim law,

$$J_\mathrm{c}(B) = J_\mathrm{c,0}\left(1 + \frac{B}{B_0}\right)^{-1}, \tag{4.4}$$

with $J_\mathrm{c,0} = 3.5 \times 10^8$ A/m$^2$ and $B_0 = 1.2$ T. The measurement data in the range $\mu_0 H < 1.5\mu_0 H_\mathrm{p}$ cannot be used to obtain the field dependence using Eq. (4.4). Indeed, in this range, the superconductor is no longer in its fully penetrated state. Using this Kim law allows a proper fit of the experimental data in the range $1.5\mu_0 H_\mathrm{p} < \mu_0 H < \mu_0 H_\mathrm{pr}$. Moreover the value $J_\mathrm{c,0} = 3.5 \times 10^8$ A/m$^2$ is consistent with the range of critical current density specified by the manufacturer at self-field and 77 K.

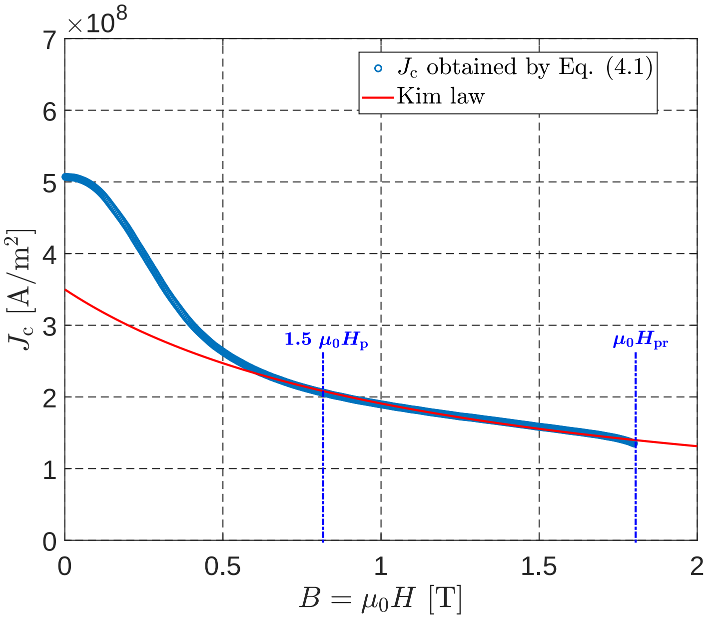

**Figure 4.4:** Field dependence of the critical current density deduced from DC magnetization measurement on the sample described in Fig. 4.3. The blue circles are the measured data obtained from Eq. (4.1). The red line is a fitting by Eq. (4.4).

Finally, let us note that the field-dependent critical current in Fig. 4.4 is plotted as a function of the external applied field and not as a function of the local field in the superconductor. The local field is actually given by

$$H_\mathrm{i} = H - N_\mathrm{m} \cdot M, \tag{4.5}$$

where $N_\mathrm{m}$ is the magnetometric demagnetizing factor. An estimation of the demagnetizing factor for the sample geometry described in Fig. 4.3 can be obtained from Chen *et al.* [224]

in the particular case $a/b = 1$. In the range $1.5\mu_0 H_\mathrm{p} < \mu_0 H < \mu_0 H_\mathrm{pr}$, the demagnetizing factor is approximately equal to $N_\mathrm{m} \approx 0.10$. Consequently, in this range, the local field is very close to the external field.

### 4.1.2 Trapped flux density measurement

As mentioned by Yang *et al.* [45], the melt-textured GdBCO cylinders described in this section are expected to exhibit inhomogeneous superconducting properties. The characterization performed in the flux extraction magnetometer gives an estimation of a somehow averaged $J_\mathrm{c}$ over the volume of the sample. However, this characterization technique does not reflect the potential defects in the near-surface morphology that can arise during the TSIG process, affecting the $J_\mathrm{c}$ homogeneity. To do so, a mapping of the trapped magnetic flux density is performed on the sample C 001. We chose to analyze in details this sample as it is characterized by the highest $J_\mathrm{c}$. The trapped field distribution is measured over the top surface (with the visible seed) and the bottom surface. The sample is magnetized (FC process) under a field of 1.5 T. The field is then decreased with a sweep rate of 16 mT/s. Then, the mapping is started after a waiting time of approximately 1500 s to minimize the effect of flux creep. The resulting flux density distribution is shown in Fig. 4.5.

The flux density measured over the top surface shows the typical cone-like distribution which is characteristic of the current flow distribution in single grain high-temperature superconductors. The maximum trapped field measured at 1 mm above the surface is 701 mT for the top surface and 535.5 mT for the bottom surface. However the distribution is not axisymmetric, which is an evidence of microstructural features affecting the current flow. The facet lines separating the four growth sectors are also clearly visible on the mapping. We note the typical shape of the trapped flux distribution over the top surface that approaches a square geometry for which the diagonals coincide, in a good approximation, with the facet lines. This ‘square-like’ shape distribution has already been observed on single grain GdBCO samples [225]. It can be explained by the inhomogeneous distribution of pinning sites between the growth sector regions and the growth sector boundaries (i.e. the facet lines). In particular, the growth sector boundaries are characterized by a stronger pinning (and a higher $J_\mathrm{c}$) resulting in an increased trapped magnetic flux. The growth sector regions, however, are characterized by a weaker pinning (lower $J_\mathrm{c}$) and thus a reduced trapped flux. These ‘square-like’ distributions have been confirmed by numerical modeling using an inhomogeneous current density spatial distribution in the *ab*-plane as a function of the angular position $\theta$ with respect to one of the facet lines [226, 227]. In practice, these models consider a critical current density $J_\mathrm{c}(\theta)$ varying as a cosine function whose maxima are located on the growth sector boundaries. Regarding the bottom surface, the flux distribution exhibits a maximum trapped flux density smaller than for the top surface. This also indicates inhomogeneous $J_\mathrm{c}$ decreasing

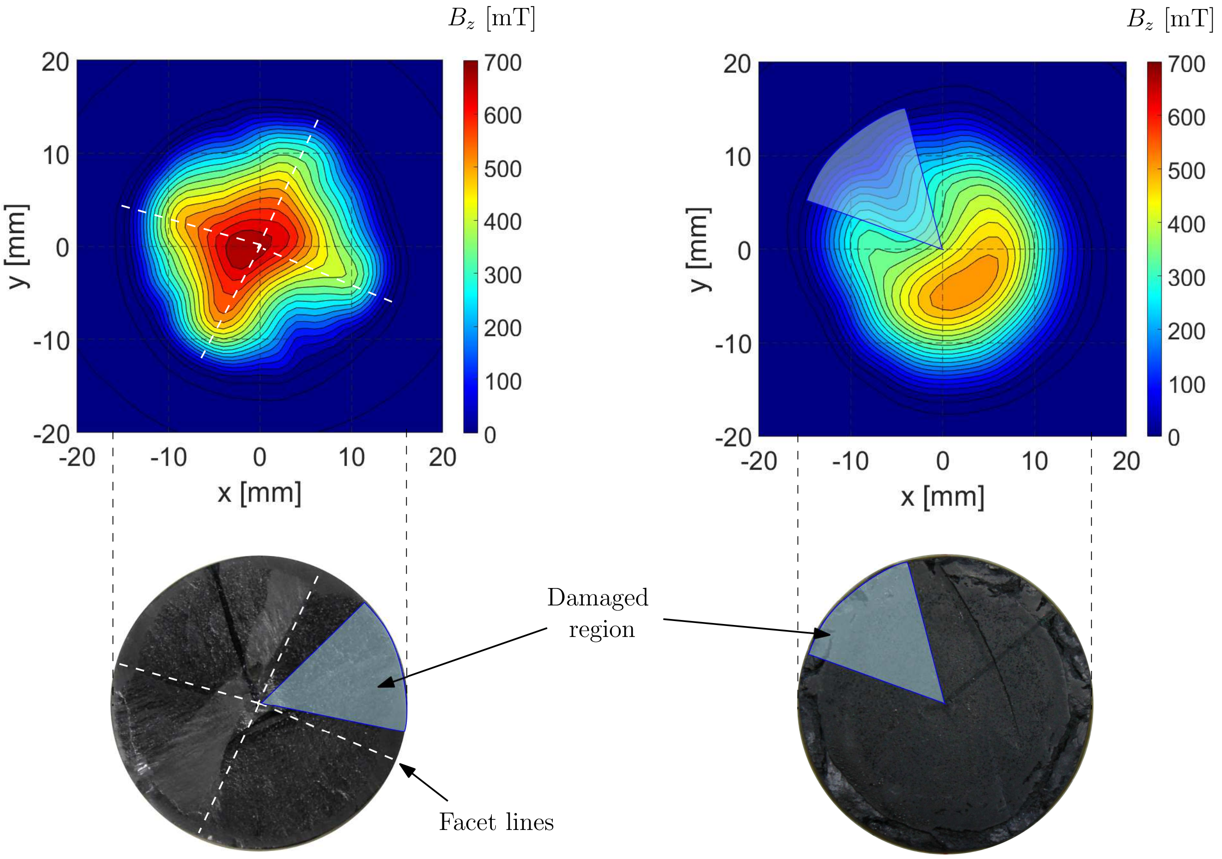

**Figure 4.5:** Distribution of the trapped magnetic flux density (component parallel to the revolution axis) over the top surface (left) and the bottom surface (right) of the sample C 001. The sample was magnetized under a field of 1.5 T (FC). The mapping is performed at $\sim 1$ mm above the surface.

from the top surface to the bottom of the sample. Another characteristic of this large-size sample is the presence of what could be a crack or any other macroscopic defect close to the bottom surface. The defect impedes the proper flow of current, which results in a 're-entrant' part of the trapped flux distribution for $x < 0$ and $y > 0$. The zone where this defect is presumably located is indicated on the pictures of the sample in Fig. 4.5 by the light blue region on both the top and bottom surfaces.

Trapped flux density measurements were also performed on the samples C 002 and C 004 in order to compare them with the sample C 001. Let us recall that the sample C 003 has been discarded due to its too low critical current density. The flux density distributions over the top and bottom surfaces of both samples are shown in Fig. 4.6. The magnetization process as well as the mapping measurement were performed following the same procedure as for the sample C 001. The first observation from results displayed in Fig. 4.6 is that the maximum trapped flux density is significantly lower for these two samples than for C 001. More precisely, the sample C 002 is characterized by a maximum trapped flux density of 489 mT above the top surface and 504 mT above the bottom surface. The maximum trapped flux is 517 mT above the top surface of C 004

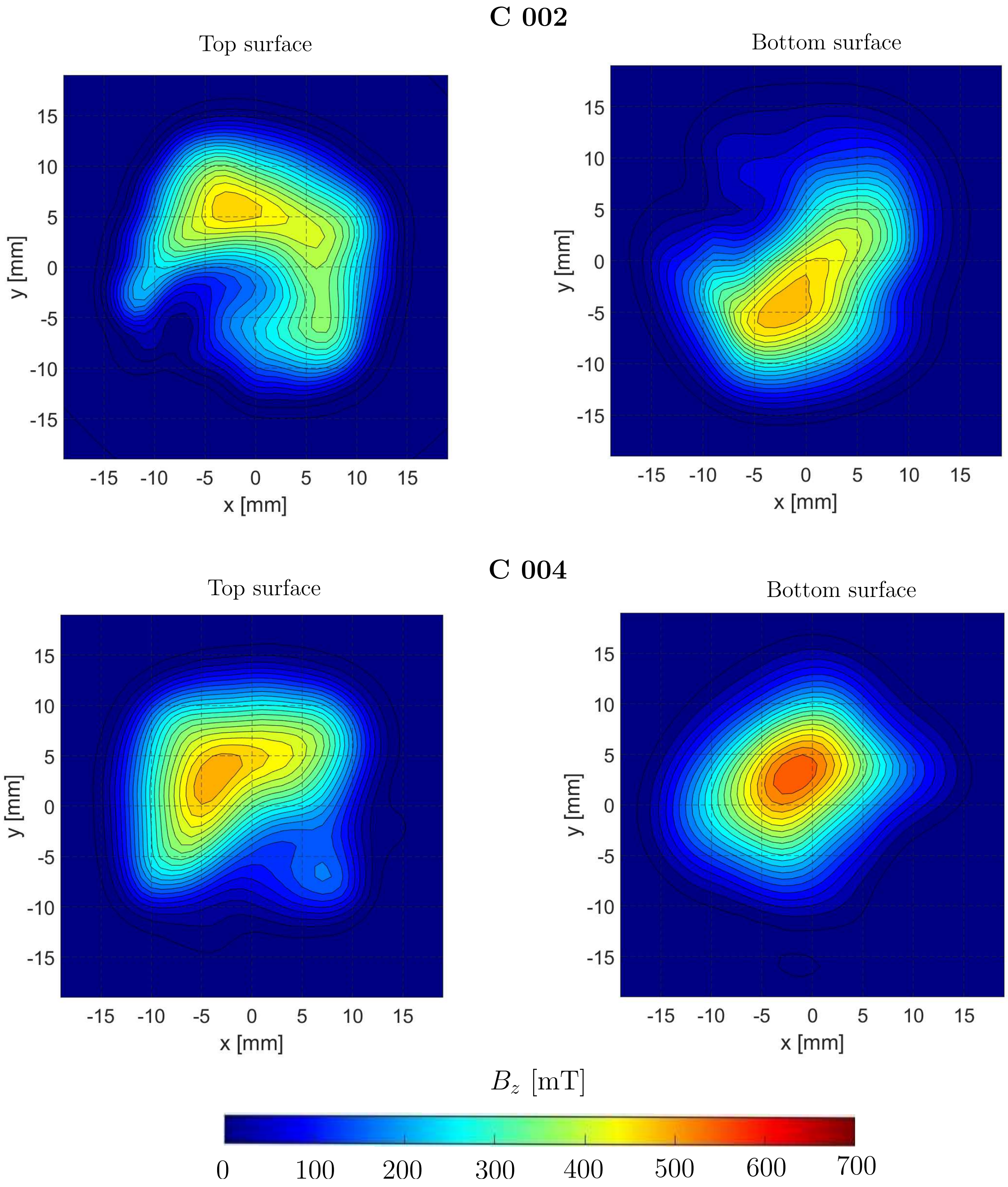

**Figure 4.6:** Distribution of the trapped magnetic flux density (component parallel to the revolution axis) over the top surface (left) and the bottom surface (right) of the samples C 002 and C004. The samples were magnetized under a field of 1.5 T (FC). The mapping is performed at $\sim 1$ mm above the surface. The coordinates $(x, y) = (0, 0)$ correspond to the geometrical center of the cylindrical samples.

and 577 mT above its bottom surface. These results are consistent with the average critical current densities obtained with the flux extraction magnetometer and that are found $\sim$ 30% smaller than for Sample C 001 (see Table 4.2). Another observation from the results in Fig. 4.6 is that the two samples exhibit a strong inhomogeneous behavior: the two samples are characterized by inhomogeneous $J_\mathrm{c}$ probably due to the presence of macro defects in the sample. The fact that the maximum trapped flux density is higher above the bottom surface than the top surface can also be associated with this noticeable inhomogeneity. As the GdBCO bulk cylinders will be used to design sizable magnetic screens, it will be of interest to analyze the effect of the inhomogeneous critical current density on the screening efficiency of these samples. A more detailed investigation on this will be carried out in Chapter 6.

## 4.2 HTS coated conductors: ferromagnetic properties of Ni-W substrate

Some of the HTS coated conductors investigated in this thesis are based on a Ni-alloy substrate. In particular, Ni-W alloys are widely used using the RABiTS technique to obtain highly textured HTS layers. These particular Ni-based substrates are shown to be slightly ferromagnetic [228, 229]. The magnetic properties of these substrates can have a significant effect of the shielding efficiency. As a result, this section is devoted to the detailed characterization of ferromagnetic properties of Ni-5at.%W alloy.

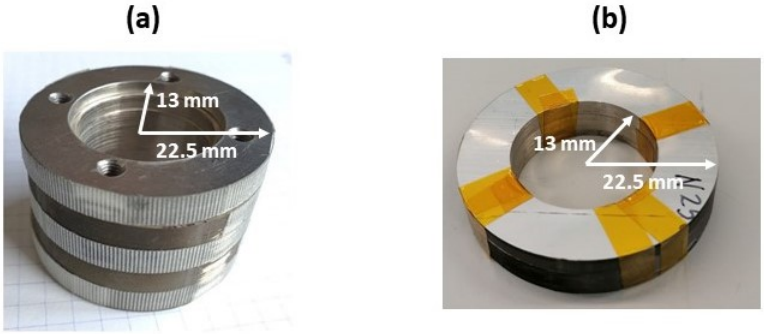

**Figure 4.7:** Pictures of (a) the initial stack of tapes based on Ni-5at.%W substrates (height = 24 mm) and (b) the toroidal sample extracted from the initial stack (height = 9.8 mm).

To do so, a sample obtained by international collaboration appears to be well suited to measure the magnetic properties. This sample is a stack of coated conductor annuli with a large internal diameter. Such a specimen exhibits excellent magnetic shielding abilities as will be demonstrated in Chapter 5. The coated conductors from which the annuli are cut, are 46-mm-width $YBa_2Cu_3O_{7-d}$ coated conductors from American Superconductors® [217]. The HTS tapes are based on a Ni-5at.%W RABiTS with a thickness of 75 $\mu$m followed by buffer layers deposited by reactive sputtering [218]. The superconducting layer is then deposited using a metal-organic deposition process of trifluoroacetate (TFA)-based precursors. Its thickness is approximately 1 $\mu$m. It is characterized by a nominal critical current by unit width ranging between 200 and 350 A·cm$^{-1}$ at self-field and 77 K (specified by the manufacturer). Finally, the stabilizer consists of a 3-$\mu$m-thick silver layer. First, a central 26 mm hole was laser-cut in each tape [217]. Then, the surface of the loose square annuli was cut by spark erosion machining resulting in circular annuli of 45 mm outer diameter [218]. A total of 294 annuli are stacked over a height of 24 mm. A picture of the stack is shown in Fig. 4.7(a).

A toroidal shape sample with a nearly square cross section was extracted from the initial sample in order to perform the magnetic characterization of the tapes as can be seen in Fig. 4.7(b). The main advantage of this kind of sample is that it is in the form of a closed magnetic circuit. Therefore, there is no demagnetizing field so that we can access the true $B(H)$ dependence. Moreover, this shape offers a convenient way to magnetize the sample uniformly up to rather high flux density values by simply winding a magnetizing coil around it. The full experimental set-up used to measure the magnetic properties has already been described in details in Chapter 3 (Section 3.6). It is based on a primary winding which consists of 0.6-mm diameter wire devoted to apply the magnetizing field $H$ and a secondary winding directly wound on the sample surface made of 0.15-mm diameter wire devoted to the measurement of the electromotive force and thus the flux density $B$. In this configuration, possible differences in the magnetic response may arise depending on whether the direction of the local magnetizing field is parallel to the long side of the tape or parallel to its width. Using the sample shown in Fig. 4.7(b), the field is applied along the circumference of annuli cut from the tape. Hence, these differences are fully averaged and the magnetic properties of the ferromagnetic substrate are then assumed to be isotropic. In order to carry out measurements at different temperatures, the magnetic circuit and coils are either placed at room temperature (293 K) or cooled, either by a commercial freezer (238 K), dry ice (solid $CO_2$) pellets (195 K), or liquid nitrogen (77 K). The temperatures are measured with a type K thermocouple connected to a FLUKE 87 V multimeter. The applied magnetic field is always parallel to the tapes, so it is assumed that the 1-2 $\mu$m thick superconducting layers do not contribute to the measured magnetic properties, even under $T_c$ (77 K).

### 4.2.1 Hysteresis curves at several temperatures

We first describe major $B(H)$ hysteresis curves, from which the magnetic permeability or the hysteresis losses can be deduced. The $B(H)$ hysteresis loops at 4 different temperatures (293 K, 238 K, 195 K and 77 K) are compared in Fig. 4.8. The frequency of the AC magnetic field is 30 Hz. When varying the frequency of the applied magnetic field between 20 Hz and 200 Hz, no perceptible difference between the hysteresis curves is found. From the results plotted in Fig. 4.8, it can be seen readily that the average width of the hysteresis cycle and the saturation magnetization both increase with decreasing temperature. Moreover the reversible region of the curve (i.e. the overlap between ascending and descending branches) is reached at higher magnetic flux densities for lower temper-

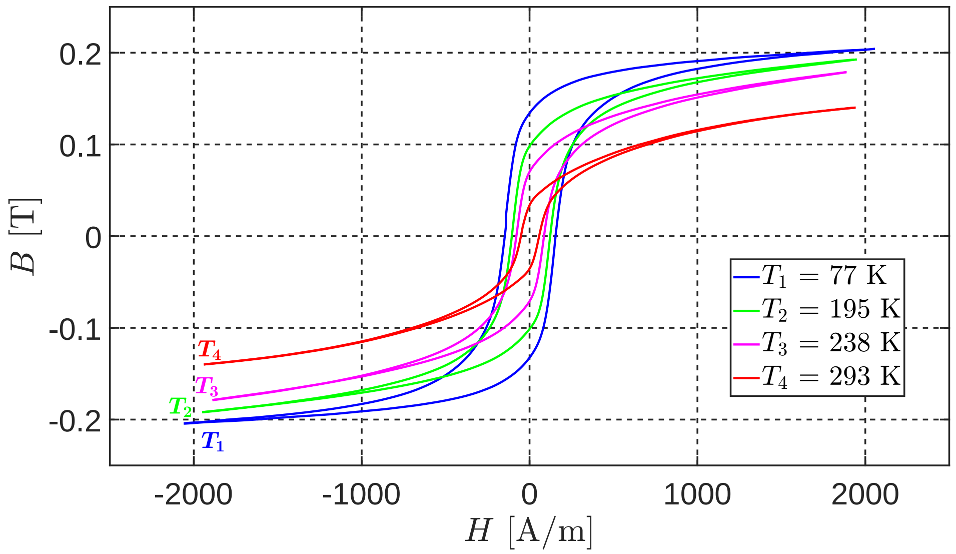

**Figure 4.8:** Hysteresis magnetic cycles recorded at four temperatures on the Ni-5at.%W substrate. The data are obtained at a frequency of 30 Hz.

atures. These phenomena are due to the variation of the magnetocrystalline anisotropy with temperature. When the temperature is close to the Curie temperature (339 K and 330 K, as reported in the literature for Ni-5at.%W alloy [230, 231]), the magnetic properties are dominated by the thermal agitation and the behavior is mainly anhysteretic. As the temperature decreases, the behavior is mainly dominated by the anisotropy, the coercive field and, the increase in remnant magnetization.

### 4.2.2 Magnetic permeability

Next, we investigate the effect of the field amplitude on the hysteresis curves. Several magnetizing fields $H = H_\mathrm{m}\sin(\omega t)$ of increasing amplitude $H_\mathrm{m}$ are applied and the amplitude of the magnetic flux density $B_\mathrm{m}$ is recorded for each amplitude $H_\mathrm{m}$. Figure 4.9 shows this $B_\mathrm{m}(H_\mathrm{m})$ dependence at different temperatures as well as the successive applied cycles at 77 K in the inset. From a classic analysis of ferromagnetic materials [180], the $B_\mathrm{m}(H_\mathrm{m})$ curves give equivalent results to the first magnetization curves. The relative magnetic permeability can be defined as follows:

$$\mu_\mathrm{r} = \frac{B_\mathrm{m}}{\mu_0 H_\mathrm{m}} \tag{4.6}$$

with $\mu_0$ the magnetic permeability of vacuum.

The effect of temperature on the relative permeability is shown in Fig. 4.10. Several observations can be made. The first one is that all $\mu_\mathrm{r}(B_\mathrm{m})$ curves display a non-monotonic behavior, with a maximum shifted continuously toward higher magnetic flux densities $B_\mathrm{m}$ as the temperature decreases from 293 K to 77 K. Second, the temperature does not have a major effect on the peak intensity of the relative permeability, which is found to lie in the

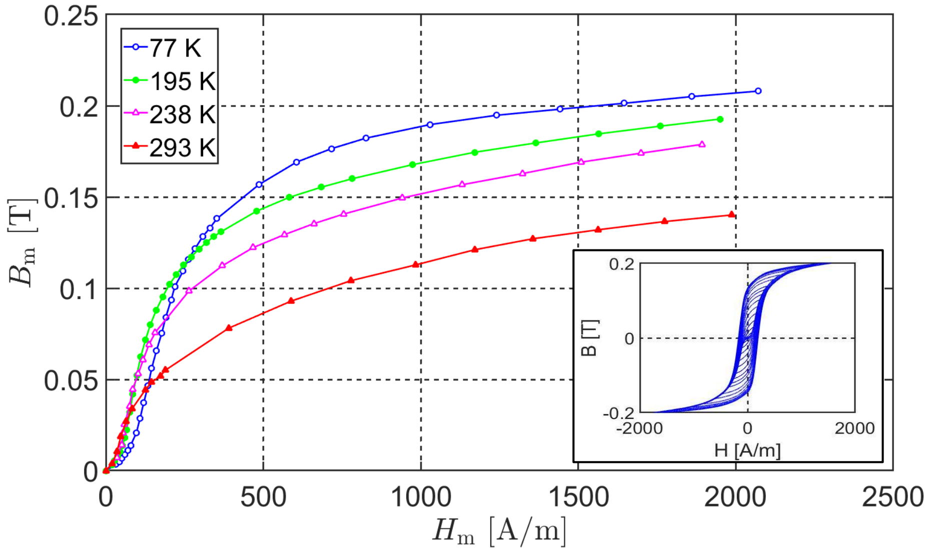

**Figure 4.9:** Peak magnetic flux density $B_m$ as a function of the maximal applied magnetic field $H_m$ at different temperatures. Several cycles with increasing $H_m$ are applied to the sample as shown in the inset for $T$ = 77 K.

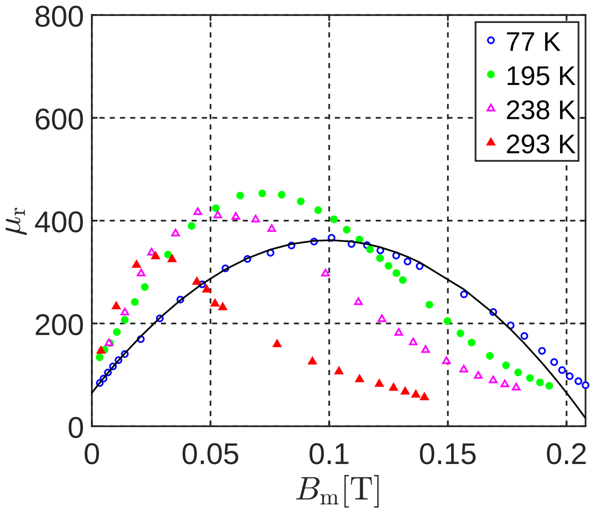

**Figure 4.10:** Relative magnetic permeability as a function of the maximal magnetic flux density at 4 different temperatures. The solid line is the quadratic fitting given by Eq. (4.7).

range 330 - 440. The measured maximum permeability at 293 K is $\mu_{r,max} = 330$ at $B_{max} = 30$ mT and 362 at $B_{max} = 100$ mT at 77 K. These results are different from those obtained by Miyagi *et al.* [232] on a weakly magnetic substrate: although the $B_{max}$ are the same as in the present study, the values of the peak relative permeability are different ($\mu_{r,max} \approx 700$ at room temperature, and $\mu_{r,max} \approx 212$ at 77 K). At liquid nitrogen temperature, our results nicely agree with those found by Claassen *et al.* [233, 234] who found $\mu_{r,max} = 380$ on the same material. As can be seen in Fig. 4.10, the initial permeability $\mu_{r,i}$ (obtained by linear extrapolation down to $B_m = 0$ T) lies around $\mu_{r,i} \approx 120$ for the three highest temperatures (293 K, 238 K, 195 K) and is equal to $\mu_{\rm r,i} \approx 70$ at 77 K. The latter value is about 1.5 times the one ($\mu_{\rm r} \approx 46$) obtained by Miyagi *et al.* [232] and similar to that found by Claassen *et al.* ($\mu_{\rm r} \approx 65$) [233, 234]. Moreover, the permeability curves measured at 195 K and above exhibit a typical asymmetric shape which has already been highlighted on different ferromagnetic materials when approaching the Curie temperature [235]. The $\mu_{\rm r}(B_{\rm m})$ data at 77 K are almost symmetric on both sides of the maximum. Remarkably, it is found that in the investigated field range, the experimental points obtained at 77 K can be fitted with a simple parabolic law, i.e.

$$\mu_{\rm r}(B_{\rm m}) = \mu_{\rm r,i} + (\mu_{\rm r,i} - \mu_{\rm r,max}) \left[ \left( \frac{B_{\rm m}}{B_{\rm max}} \right)^2 - 2\frac{B_{\rm m}}{B_{\rm max}} \right], \tag{4.7}$$

as shown by the solid line in Fig. 4.10, using the fitting parameters: $\mu_{\rm r,i} = 70$, $\mu_{\rm r,max} = 362$ and $B_{\rm max} = 100$ mT. Such a $\mu_{\rm r}(B_{\rm m})$ dependence as well as the first magnetization curve suggest that the dominating hysteresis mechanism at 77 K is the pinning of domain walls [180]. The results shown in Fig. 4.9 and Fig. 4.10, as well as the parabolic law described by Eq. 4.7, provide useful experimental data which can be incorporated in numerical modeling of structures and applications involving 2G HTS tapes based on Ni-5at.%W RABiTS. Indeed, below the critical temperature, the superconducting properties are dependent on the field distribution inside the HTS layers and thus, their analysis requires an accurate modeling of the ferromagnetic layers themselves. Regarding the data measured at $T > T_{\rm c}$, the results described above can be used to predict the magnetic reluctance of a structure made of such superconducting tapes that can be used e.g. for magnetic shielding. If the structure is subjected to relatively low magnetic fields (e.g. with $B_{\rm m} < 0.1$ T), the relatively high values of the magnetic permeability give evidence that a non-zero magnetic shielding effect will persist even if the temperature accidentally rises above the critical temperature of the superconductor.

### 4.2.3 Coercive field

We now turn to the evolution of the coercive field $H_{\rm c}$, which is also a quantity of definite interest when studying the magnetic properties of a specific material. The temperature has a significant effect on the coercive field as can be seen in Fig. 4.11.

The panels (a) and (b) show, for each temperature, the coercive field $H_{\rm c}$ expressed either as a function of the amplitude $H_{\rm m}$ of the applied magnetic field or the corresponding amplitude magnetization $M_{\rm m}$ given by

$$M_{\rm m} = \frac{B_{\rm m}}{\mu_0} - H_{\rm m}. \tag{4.8}$$

Fig. 4.11(c) shows the temperature dependence of the coercive field $H_{\rm c}$ determined at three field amplitudes $H_{\rm m} = 50$, 100 and 1500 A/m. At large amplitudes, the coercive field

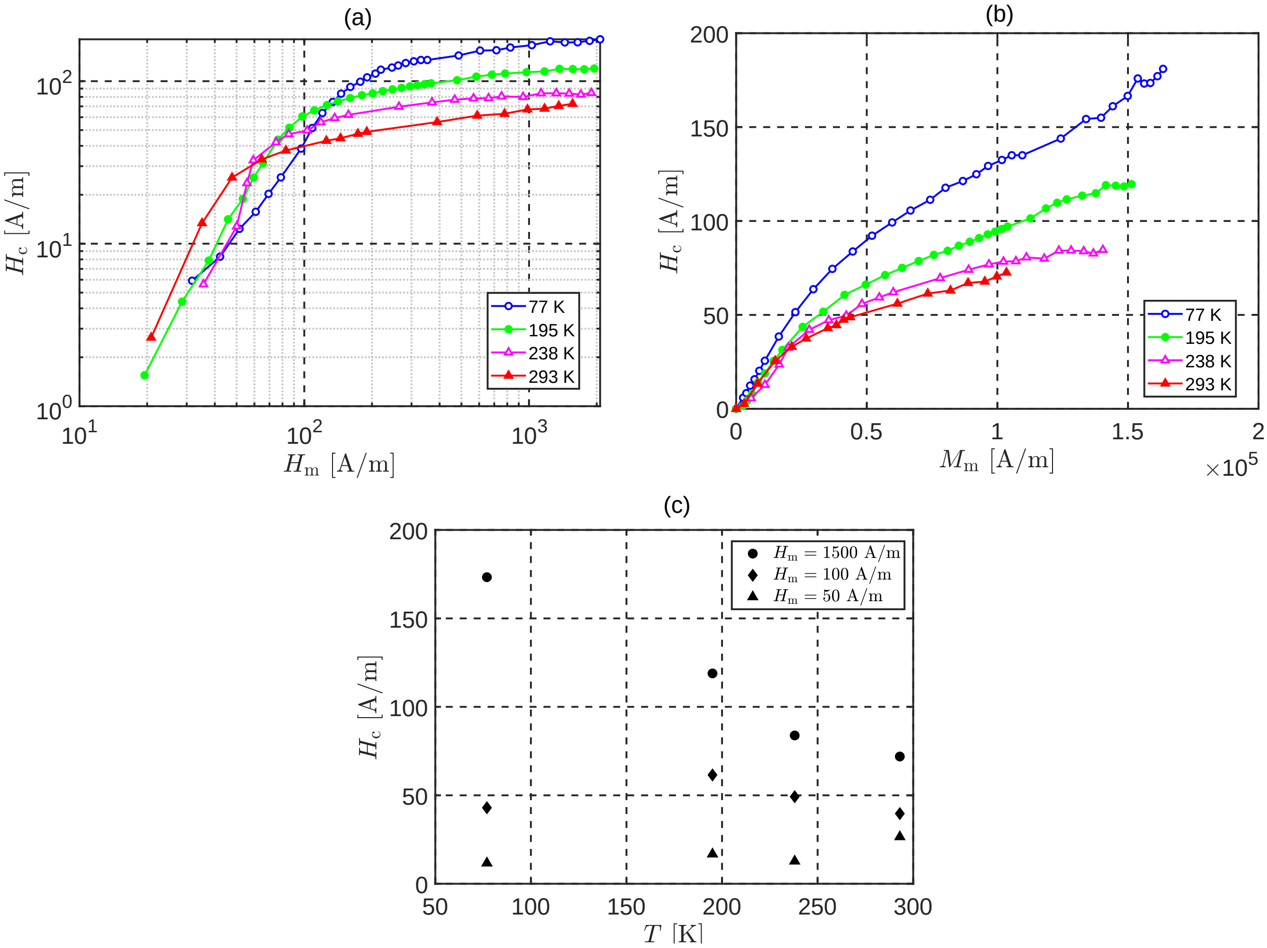

**Figure 4.11:** Evolution of the coercive field $H_c$ as a function of (a) the peak magnetizing field $H_m$, (b) the peak magnetization $M_m$, and (c) as a function of temperature.

clearly decreases as the temperature increases. The influence of temperature is much less pronounced for low values of magnetizing field. The $H_c(T)$ measured at 1500 A/m displays a quasi-linear behavior. In the crude assumption that $H_c$ vs. $T$ remains linear at higher temperatures, an extrapolation shows that $H_c$ goes to 0 at $T \approx 420$ K. This value is higher than Curie temperatures for Ni-5at.%W lying between 330 K and 340 K as specified in Section 4.2.1. This suggests that a linear approximation does not hold when approaching the Curie temperature. When plotted as a function of the applied field $H_m$ (Fig. 4.11(a) in log-log scale), the $H_c$ data follow roughly a power law behavior, $H_c \sim (H_m)^n$ at low fields, with $n$ close to 2, followed by a clear kink above which a much weaker field dependence is found ($n \sim 0.3$). A cross-over of the $H_c$ curves is found between these two regimes, i.e. at low field the highest $H_c$ is found at room temperature (293 K), whereas at high field, the highest $H_c$ occurs at 77 K. It is to be noted that, although a well-defined trend does not clearly emerge, the cross-over found in Fig. 4.11(a) almost disappears when the coercive field is plotted as a function of the magnetization $M_m$ as shown in Fig. 4.11(b), leading to the conclusion that for any given value of the magnetization $M_m$, the highest coercive field is observed at the liquid nitrogen temperature. Finally, let us mention that the amplitude of the coercive field and its temperature dependence can be used, using interpolation of the data plotted in Fig. 4.11, to predict the hysteretic behavior of the magnetic substrate at temperatures different from those investigated in the present work and, in particular temperatures ranging between 77 K and the critical temperature of the superconductor.

### 4.2.4 Hysteresis losses of major loops

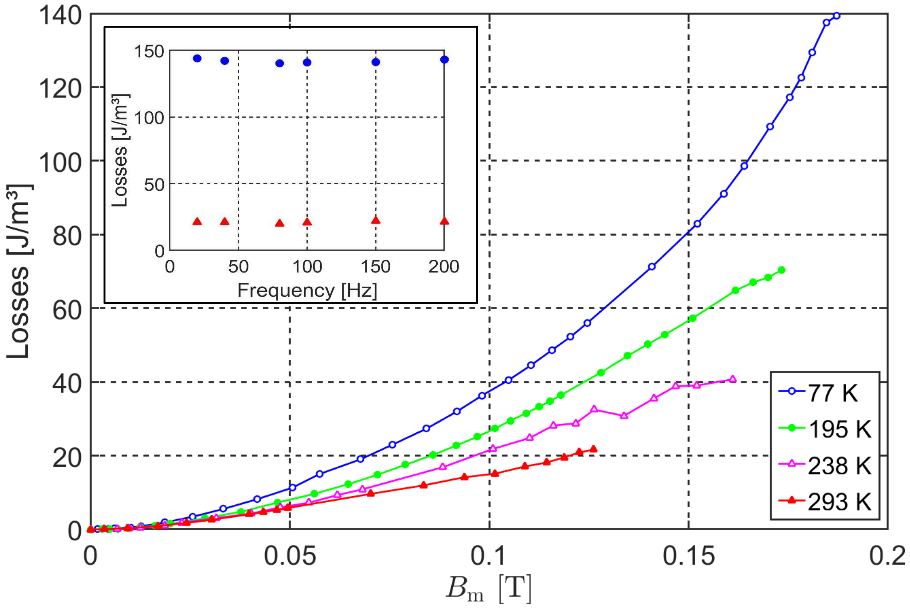

**Figure 4.12:** Hysteresis losses ($Q$ [J/m$^3$] for one cycle) as a function of the peak magnetic flux density recorded at different temperatures (at a frequency of 30 Hz). In the inset, the losses are plotted as a function of the frequency at 77 K (●) and 293 K (▲) for a fixed $H_m$ of 2000 A/m.

The hysteresis losses in the magnetic substrate are an additional source of losses in HTS coated conductors. In the present configuration, the magnetizing field is applied parallel to the tapes, the superconducting layer is negligible and the only contribution to the losses are those of the magnetic substrate. Depending on the current and the frequency, the hysteresis losses may represent a sizeable fraction of the total AC loss [236]. It is therefore crucial to characterize accurately the hysteresis losses inside the ferromagnetic layers. The evolution of the magnetic losses as a function of the cycle amplitude $B_m$ can be seen in Fig. 4.12. The losses clearly increase with decreasing temperature. In the present case the frequency has no influence on the measured losses as can be deduced from the inset of Fig. 4.12 showing the losses (for one cycle) in the frequency range 20 Hz - 200 Hz. Accordingly, the main loss contribution comes from hysteresis losses and not from eddy current losses due to the small thickness of the ferromagnetic substrate ($\approx 75\ \mu$m). Moreover, we can estimate the eddy current contribution to the losses which is given by

$$Q_{\text{eddy}} = \frac{(\pi t B)^2 f}{6\rho}, \tag{4.9}$$

where $t$, $B$ and $f$ are respectively the thickness of the substrate, the magnetic flux density and the frequency. The electrical resistivity $\rho$ has been obtained at 77 K and 293 K by a 4-wire sensing method. As can be seen in Table 4.3, the eddy current losses contribution is negligible compared to the hysteresis losses. This result is in agreement with those previously obtained by Miyagi *et al.* [232] on their weak magnetic substrate. For the 4 temperatures investigated, it can be readily seen that the hysteresis losses follow roughly a power law as a function of the amplitude of $B$ (i.e. $Q \sim Q_0 \left(\frac{B_\text{m}}{B_0}\right)^n$), as found experimentally by Miyagi *et. al.* [232], where $Q_0$ are the losses at the particular flux density $B_\text{m} = B_0$. The values of $Q_0$ and $n$ at the four investigated temperatures can be found in Table 4.4; $B_0$ is chosen arbitrarily to $B_0 = 0.15$ T to allow for a direct comparison with results from the literature at the liquid nitrogen temperature. Using an empiric fit of the 77 K experimental data, values of $n = 2$ and $n = 1.884$ are found in Gömöry *et al.* [233] and Nguyen *et al.* [237] respectively. The power law behavior is analyzed further in the section below by comparing the losses with or without DC offset.

| | **B** [T] | $\rho$ [Ωm] | **Q**$_{\text{eddy}}$ [J/m$^3$] |
|---|---|---|---|
| **77 K** | 0.2 | 2.71 $\times 10^{-7}$ | 0.041 |
| **293 K** | 0.14 | 3.6 $\times 10^{-7}$ | 0.015 |

**Table 4.3:** Values of the eddy current losses computed with Eq. (4.9) both at 77 K and 293 K at a frequency of $f = 30$ Hz.

| **T** [K] | **Q$_0$** [J/m$^3$] | **n** [-] |
|---|---|---|
| 77 | 85.02 | 2.114 |
| 195 | 55.74 | 1.779 |
| 238 | 38.77 | 1.533 |
| 293 | 27.38 | 1.434 |

**Table 4.4:** Power law's parameters fitting the hysteresis losses plotted in Fig. 4.12 at the different temperatures.

Note that the present geometry, where the magnetizing field is applied parallel to the tapes, corresponds e.g. to the situation arising when the tapes are used to shield a magnetic field parallel to them. The magnetic field configuration here is different from what would be obtained e.g. when the tapes carry an electrical current. If other similar configurations are considered, the obtained intrinsic $B(H)$ data and hysteresis loss data can then be inserted in numerical modeling of the whole structure. In the case where the field is applied perpendicular to the tapes plane, the main contribution to the losses would certainly come from eddy currents which can be computed. Although the field range in our measurements (2000 A/m) is smaller than the field possibly produced by the tapes nominal critical current, the results show that the Ni-W alloy is almost saturated and that magnetizing the sample up to higher field would not drastically change the conclusions. The main change would be to add the (computable) contribution of the eddy current losses.

### 4.2.5 Power law behavior of hysteresis losses

Finally, the application of minor hysteresis loops, i.e. hysteresis loops with a peak magnetization $M_\mathrm{m}$ well below the saturation and superimposed to a DC bias field is also investigated in terms of losses. Minor loops can be found in several power engineering applications including rotating machines or when the superconductor is subjected to ripple voltage from power converters [238]. Moreover, minor hysteresis loops can also be used for the non-destructive detection of structural defects in ferromagnetic materials [239]. Here, we investigate centered hysteresis loops (without any bias DC field) and minor loops with a 500 A/m bias DC field. The evolution of the losses with respect to the peak magnetization $M_\mathrm{m}$ is shown in Fig. 4.13. From this figure, we can directly deduce that the hysteresis losses are proportional to $\left(\frac{M_\mathrm{m}}{M_\mathrm{s}}\right)^n$ with $M_\mathrm{s}$, the saturation magnetization. The method to estimate the saturation magnetization is described in Section 4.2.6. The evolution of the $n$ exponent for several magnetization ranges is also represented in Fig. 4.13. The general trend is a decreased value of $n$ as the ratio $\frac{M_\mathrm{m}}{M_\mathrm{s}}$ increases. The losses are always significantly higher at 77 K than at room temperature.

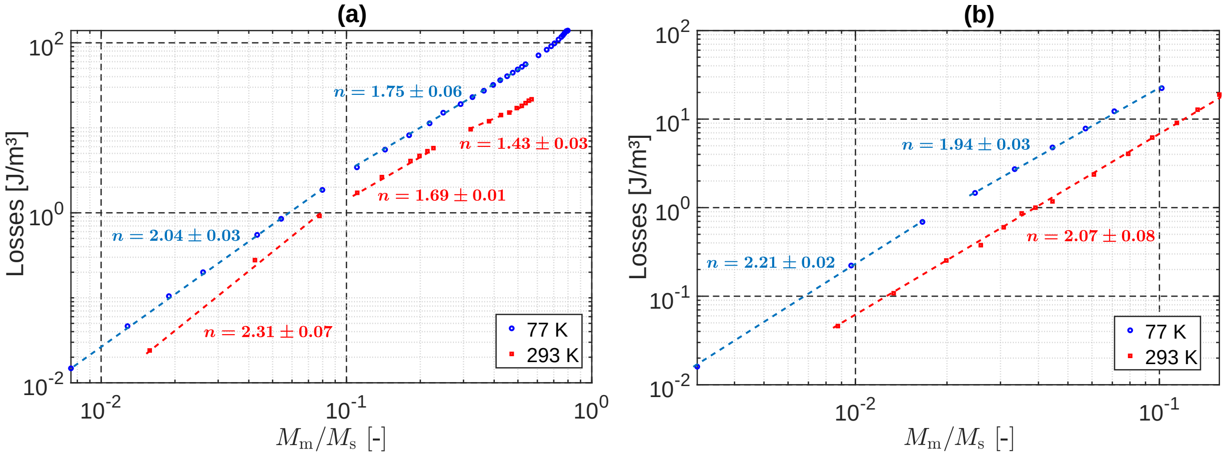

**Figure 4.13:** Evolution of the losses ($Q$ [J/m$^3$] for one cycle) with the magnetization $M_\mathrm{m}$ under the application of minor hysteresis loops. The hysteresis loops are either (a) centered with a bias applied field of 0 A/m or (b) not centered with a bias applied field of 500 A/m. The results are recorded at 293 K and 77 K. The frequency of operation is 30 Hz.

At low fields, the dependence of the losses as a function of the peak magnetization

$M_\mathrm{m}$ can be partly explained with the Rayleigh model. The model, already introduced in Section 1.4.2 assumes that, for low amplitudes of magnetization, the ascending and descending branches of the hysteresis loop can both be modeled using a quadratic function. Equations (1.28) and (1.29) show that the Rayleigh model predicts a dependence $Q \propto M_\mathrm{m}^n$ with $n$ taking a value between 1.5 and 3 depending on the relative importance of the reversible and the irreversible components of the magnetic behavior. For the set of experimental data obtained in the present work, the exponents found are well within the theoretically expected range.

### 4.2.6 Temperature dependence of hysteresis parameters

The dependence on temperature of the magnetic properties of Ni-5at.%W magnetic substrate is rather complex to explain and the experimental results remain difficult to interpret physically. The literature remains indeed very descriptive when relating the effect of temperature on the hysteresis macroscopic magnetic properties. Nevertheless, we choose to discuss the experimental results by fitting them with the phenomenological Jiles-Atherton (J-A) model [181]. The model equations have already been introduced in Section 1.4.2. In addition to the saturation magnetization, the J-A model equations highlighted four other fitting parameters $c$, $k$, $a$ and $\alpha$ from which modeled hysteresis curves can be deduced. In order to find the set of parameters leading to the best fit of the experimental curves, the procedure is inspired from that described by Pop and Caltun [185].

The comparison between the experimental hysteresis cycles and the fitting curves as well as the corresponding model parameters are shown in Fig. 4.14 for the different considered temperatures. The experimental hysteresis cycles shown in Fig. 4.14 are the same than those shown in Fig. 4.8 but for the magnetization $M(H)$ instead of the flux density $B(H)$.

As can be seen in Fig. 4.15, the five parameters show a monotonic evolution with temperature. As already mentioned in Section 1.4.2, the parameters have a physical interpretation and their evolution with temperature can give insights on the effect of temperature on the material's magnetic behavior. The dimensionless parameter $c$ gives the part of anhysteretic magnetization with respect to the irreversible component. According to the J-A model, the value of $c$ is between 0 and 1 so that if $c = 1$, the material's behavior is purely anhysteretic. Experimentally, we observe a value of $c$ exhibiting a monotonic increase from 0.3 to 0.83 between 77 K and 293 K (Fig. 4.15(a)). The pinning parameter $k$ expressed in A/m gives the coercivity and is directly related to the hysteresis energy losses. In the limit case of very soft ferromagnets, one can assume $k \approx H_\mathrm{c}$, where $H_\mathrm{c}$ is the coercive field. In the present case, the value of $k$ (Fig. 4.15(b)) is found to be 1.5-3 times larger than $H_\mathrm{c}$ but its value decreases with temperature, a behavior

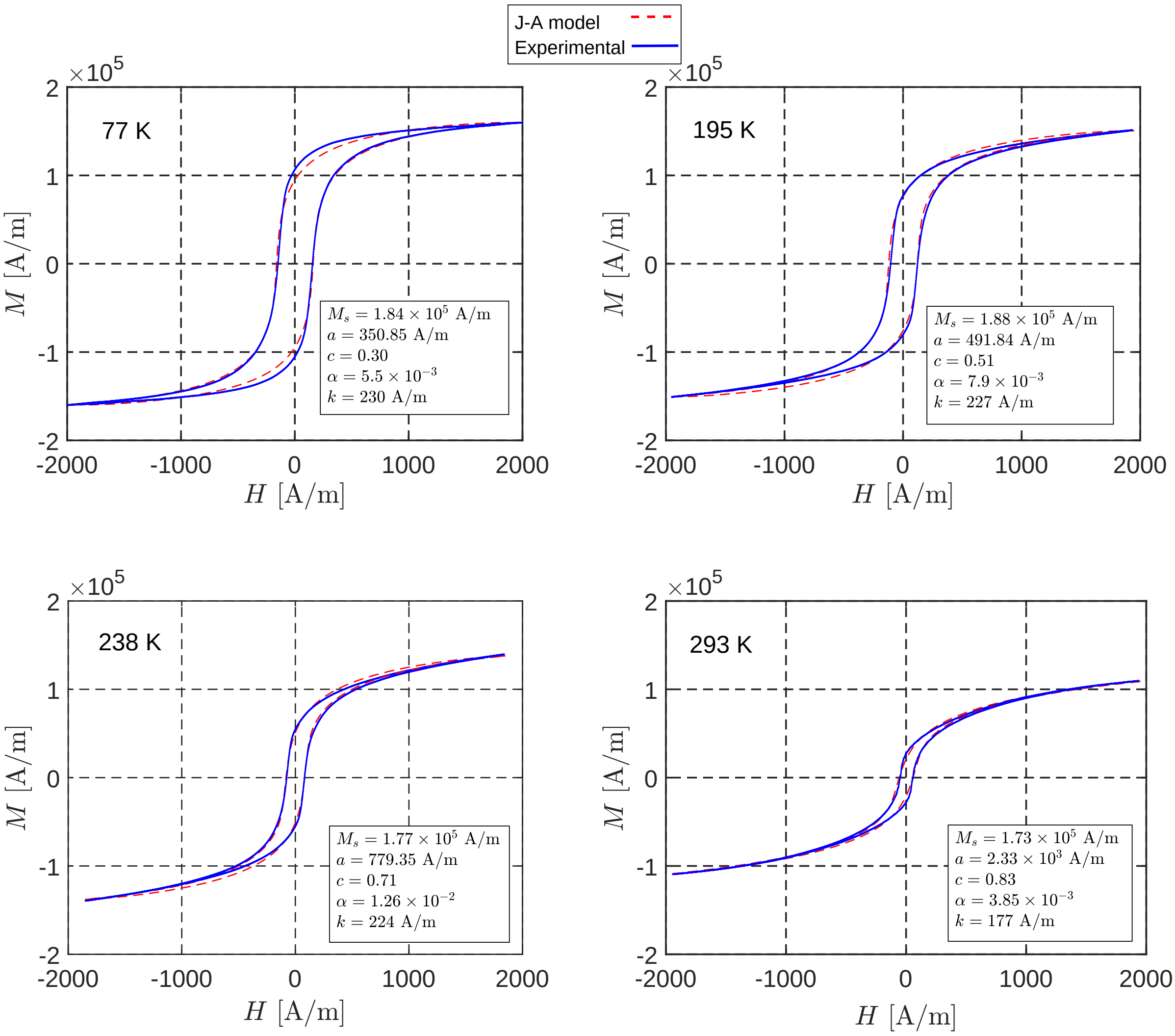

**Figure 4.14:** Fitting of the experimental hysteresis cycles (in blue) with the J-A model (in dashed red) at the different investigated temperatures as well as the corresponding fitting parameters.

which is consistent with the evolution of $H_\mathrm{c}$ observed in Fig. 4.11. The parameter $a$, defined by Eq. (1.21) and whose evolution is shown in Fig. 4.15(c), exhibits a monotonic increase with temperature. The non-linear temperature dependence of $a$ with an upward concavity indicates that the average magnetic moment of magnetic domains decreases with temperature. The dimensionless parameter $\alpha$ (Fig. 4.15(d)), defining the coupling between magnetic domains, is found to increase with temperature while being much smaller than 1 for all investigated temperatures. Finally, the saturation magnetization $M_\mathrm{s}$ is plotted in Fig. 4.15(e). A first estimation of the saturation magnetization is obtained assuming that the magnetization $M_\mathrm{m}$ at high field follows a law of type

$$M_\mathrm{m}(H_\mathrm{m}) = M_\mathrm{s} - \frac{b}{H_\mathrm{m}}. \tag{4.10}$$

Thus, $M_\mathrm{s}$ is considered as a fifth parameter in the J-A model and the first estima-

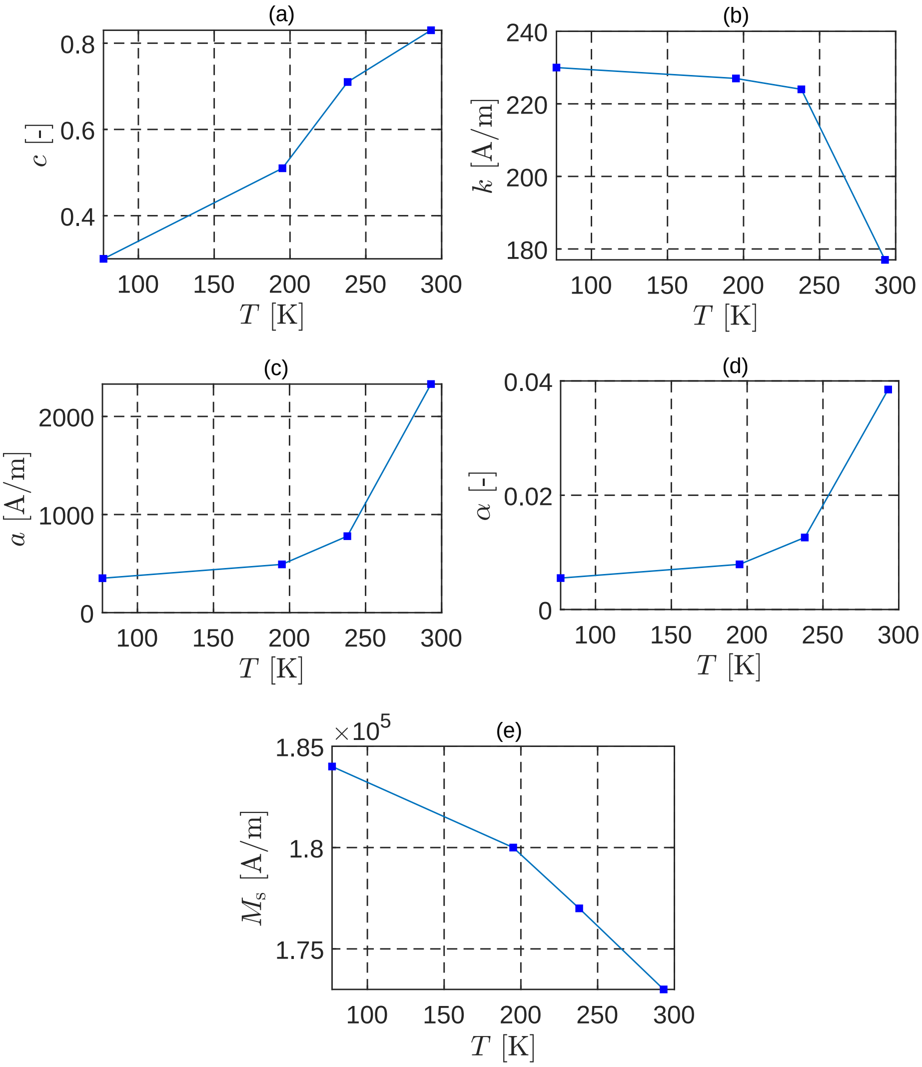

**Figure 4.15:** Evolution of the J-A model parameters as a function of temperature.

tion is adjusted with the other J-A parameters to obtain a good agreement between the model and the experimental results. The saturation magnetization is found to be weakly temperature-dependent. The $M_\mathrm{s}$ values can be compared to those obtained on Ni-5at.%W using commercial magnetometers. At $T = 300$ K, Gao *et al.* measured $M_\mathrm{s}$ in the range 11.98-13.04 emu/g (corresponding to $1.25 - 1.45 \times 10^5$ A/m, assuming a density of 9.64 g/cm$^3$). Song *et al.* determined $M_\mathrm{s}$ values of $\sim$ 14 G cm$^3$/g ($1.35 \times 10^5$ A/m) at 298 K and $\sim$ 25 G cm$^3$/g ($2.4 \times 10^5$ A/m) at 77 K. At $T = 5$ K, Ijaduola *et al.* determined $M_\mathrm{s}$ in the range 27.4-28 G cm$^3$/g, corresponding to $2.64 - 2.69 \times 10^5$ A/m. As a result, the $M_\mathrm{s}$ value seems to be underestimated at low temperature (77 K) and, on the contrary, overestimated at room temperature compared to previous works. It is likely that this difference originates from the fact that the hysteresis cycles are obtained at a maximum magnetizing field $H_\mathrm{m}$ which is too low to bring the material close to saturation. In spite of this discrepancy, $M_\mathrm{s}$ is found to decrease with temperature and the values allow the experimental hysteresis cycles to be reproduced using the J-A model. It can be also noticed that the exact knowledge of the parameter $M_\mathrm{s}$ does not affect the power law behavior discussed in Section 4.2.5.

## 4.3 Chapter summary

In this chapter we characterized the magnetic and electrical properties of the individual high-temperature superconducting samples used throughout the thesis. First, the chapter introduced the characterization of bulk HTS samples. Two kinds of bulk samples were studied: four GdBCO bulk cylinders and one YBCO rectangular prism. The characterization was performed following two steps. First, the critical current density $J_\mathrm{c}$ was estimated. The four GdBCO cylinders were characterized using the flux extraction magnetometer and the results clearly showed that one of the samples exhibited a much lower $J_\mathrm{c}$ and was thus chosen to be discarded. The YBCO prism was characterized thanks to magnetization cycle measurement using the PPMS. Doing so, the field dependence of $J_\mathrm{c}$ could be estimated. The second characterization step consisted in measuring the trapped flux ability of the three remaining GdBCO cylindrical samples. The trapped flux distributions evidenced a strong inhomogeneous behavior likely to be due to macroscopic defects impeding the proper current flow. The typical rectangular trapped flux profile that was observed is also characteristic of an inhomogeneous pinning centers distribution between the facet lines and the growth sector regions.

In the second part of this chapter, we investigated the magnetic properties of Ni-5at.%W substrate of coated conductor tapes at several temperatures. The measurements were carried out on a toroidal stack of coated conductors, which constitutes naturally a closed magnetic circuit and is the ideal configuration due to the absence of demagnetizing effect. The field was applied parallel to the tapes so that the contribution of the HTS layers to the losses was negligible. Hysteresis magnetic loops were obtained in the AC regime (30 Hz) at 293 K (room temperature), 238 K, 195 K and 77 K. No significant effect was observed in the 20-200 Hz range showing that the losses are mainly hysteretic in this regime. The relative permeability was shown to display a non-monotonic behavior with a smooth evolution between 293 and 77 K. The coercive field measured for high-amplitude hysteresis cycles was found to exhibit a linear decrease with temperature. The hysteresis losses were found to follow a power law behavior at low field. The power law exponents were shown to be consistent with the Rayleigh model. Finally, the results were shown to be successfully reproduced using the phenomenological Jiles-Atherton model. The five parameters of the model have been identified at different temperatures and exhibit a monotonic evolution. Consequently, these results can be used to obtain, by interpolation, the magnetic properties at every temperatures between 77 and 293 K for every magnetic field below 2000 A/m to take into account the magnetic behavior of Ni-5at.%W alloy. Systems using coated conductors based on Ni-5at.%W substrate can be found in several applications including magnetic shielding applications where the ferromagnetic properties can be usefully exploited.

# Chapter 5

# Magnetic shielding using a stack of HTS coated conductor annuli

In this chapter, we investigate experimentally the magnetic shielding ability of a stack of coated conductor annuli with large internal diameter (26 mm). The field is applied either along the axis of the stack (axial field) or perpendicular to it (transverse field, i.e. parallel to the plane of the tapes). Since the coated conductors are deposited on a Ni-5at.%W RABiTS, this chapter also aims at determining the possible benefits brought by their ferromagnetic substrate. Interestingly, the presence of a substrate with a substantial permeability allows a conventional shielding mechanism to occur even above the critical temperature of the superconductor. Therefore, the shielding properties of such a stack will be examined at both room temperature and liquid nitrogen temperature (77 K).

We investigate three stacks of annuli of different heights. The set of experimental data will be compared to finite element modeling carried out either in 2D (axial configuration) and 3D (transverse configuration). Then, these models will be used to investigate and discuss the influence of the properties of both the superconducting layer and the ferromagnetic substrate. In particular, this chapter will show the interest of using a field-dependent critical current as well as a field-dependent magnetic permeability in order to model properly the shielding performance of the stack of annuli. In addition, the models will be used to predict the shielding capabilities of higher stacks.

Finally, this chapter considers different ways to improve the shielding performance of the investigated stack of annuli. First, the shielding ability of an axial external magnetic field is enhanced using a semi-closed configuration: one of the extremities of the stack is closed using a superconducting cap. This geometry is shown to significantly increase the shielding factor as well as the threshold flux density. Then we demonstrate the possibility to improve the shielding efficiency under a transverse applied field by wrapping the stack of annuli in a large width (40 mm) HTS coated conductor of large dimensions.

## 5.1 Introduction

In this chapter, we study superconducting shields made of stacked annuli. In this section, we start by introducing the materials and the dimensions of the shields. We also present the experimental set up devoted to the measurement of the shielding factor. Finally, we introduce the techniques used to model this hybrid structure.

### 5.1.1 Experimental set-up

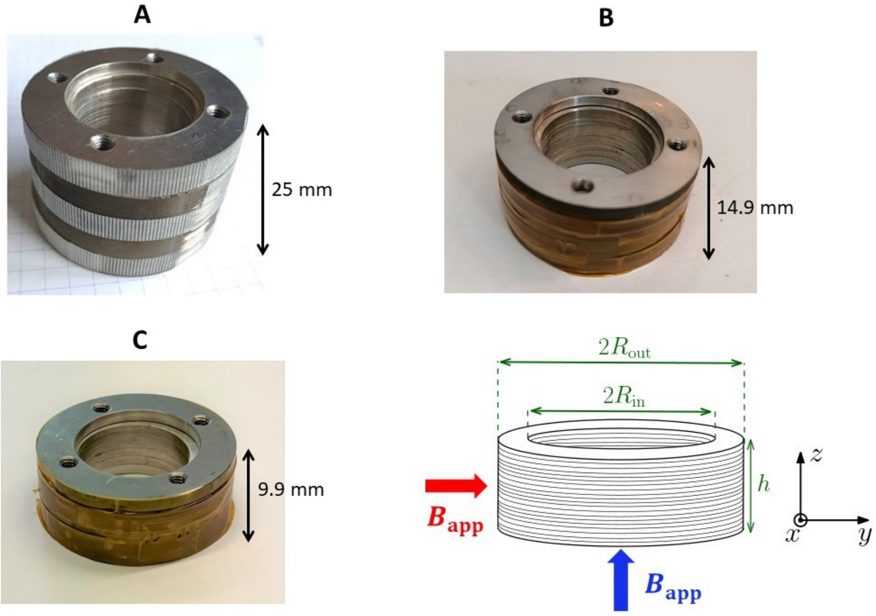

**Figure 5.1:** Pictures of the three shields A, B and C with their respective height and schematic illustration of the direction of the axial and transverse magnetic fields. Their full geometrical characteristics are provided in Table 5.1.

The magnetic shield consists of a stack of YBCO tape annuli cut from a 46 mm wide coated conductor. The annuli were extracted from a superconducting tape deposited on a rolling assisted biaxially textured Ni-5at.%W substrate (RABiTS). The substrate is approximately 75 $\mu$m thick and its magnetic properties have been characterized in the previous chapter (Section 4.2). The filling factor $f$, i.e. the volume fraction of ferromagnetic material in the stack, is $f \approx 0.92$. The HTS layer, made of $\mathrm{YBa_2Cu_3O_{7-d}}$ has an approximate thickness of 1 $\mu$m and a nominal critical current between 200-350 A per cm width at self-field and 77 K. Three magnetic shields of different height are studied. The pictures of the three stacks of annuli as well as their dimensions are shown in Fig. 5.1 and Table 5.1 respectively.

| | **Sample A** | **Sample B** | **Sample C** |
|---|---|---|---|
| $\boldsymbol{R}_{\mathbf{in}}$ **[mm]** | 13 | 13 | 13 |
| $\boldsymbol{R}_{\mathbf{out}}$ **[mm]** | 22.5 | 22.5 | 22.5 |
| $\boldsymbol{h}$ **[mm]** | 25 | 14.9 | 9.9 |
| **Number of tapes [-]** | 294 | 182 | 121 |
| $\boldsymbol{f}$ **[-]** | 0.92 | 0.92 | 0.92 |

**Table 5.1:** Characteristics and geometrical dimensions of the three stacks investigated. $R_{\text{in}}$, $R_{\text{out}}$ and $f$ respectively stand for the internal radius, the external radius and the ferromagnetic material filling factor.

The magnetic shielding properties of the stacks are investigated under a uniform magnetic field $B_{\text{app}} = \mu_0 H_{\text{app}}$ applied either parallel (axial configuration) or perpendicular (transverse configuration) to their axis at both 77 K and 293 K (room temperature). The magnetic field is measured inside the shield, at the central position with a 3-axis Arepoc® Axis-3S Hall probe. The system is shown in Fig. 5.2 for Sample A.

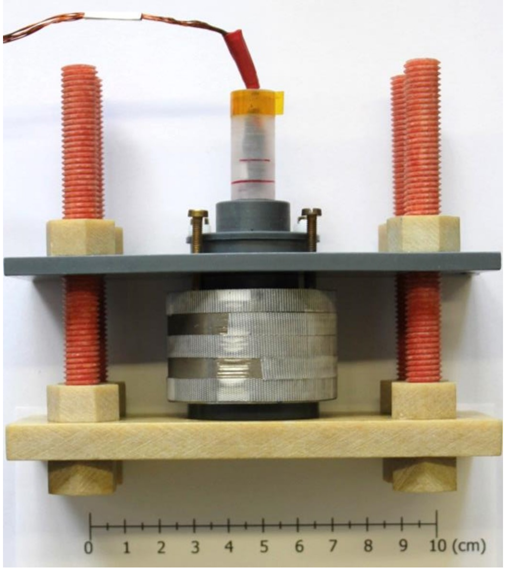

**Figure 5.2:** Experimental system for the measurement of the magnetic flux density inside the sample. The Hall probe is fixed so that the field is measured at the central position.

### 5.1.2 Homogeneous model

Modeling systems combining high-temperature superconducting (HTS) and ferromagnetic (FM) materials is always challenging due to the strong non-linearities of the constitutive laws [194]. In this work, we use a 2D-axisymmetric model in the axial configuration and a 3D model in the transverse configuration. In both cases, the stack of coated conductors is modeled by replacing the detailed layered structure by a homogeneous hybrid (fictitious) material displaying both ferromagnetic and superconducting properties [104, 240–243]. The models were developed by J. Dular from the Department of Electrical Engineering and Computer Science, University of Liège [104] including the ferromagnetic properties measured in Chapter 4. In this chapter, we actively use the models to study the influence of the geometry and material properties. We refer to the reference [244] for a detailed study regarding numerical performance of these models. The problem geometry is illustrated in Fig. 5.3. As 3D models can be time consuming, only one eighth of the geometry is modeled to take advantage of the problem symmetry, imposing appropriate boundary conditions.

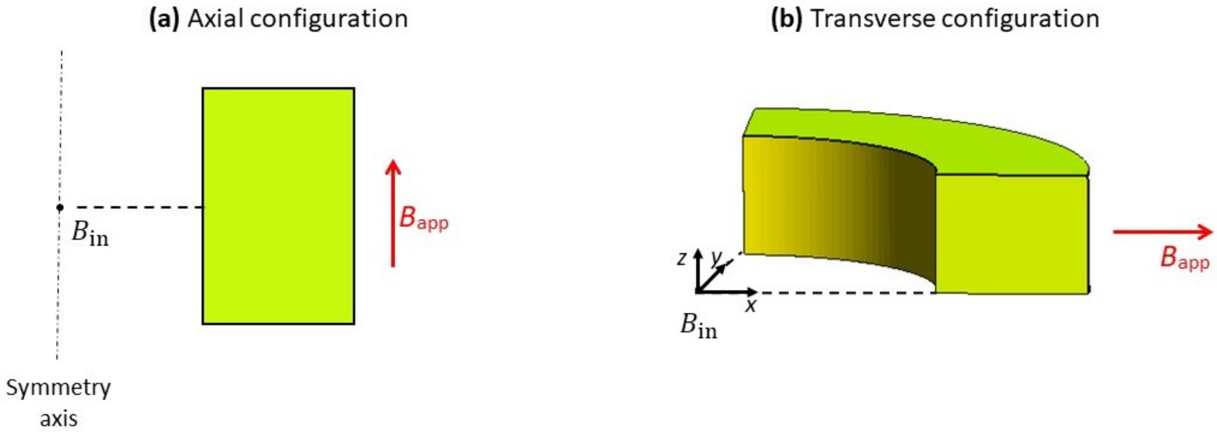

**Figure 5.3:** Homogeneous model in axial and transverse configurations. $B_{app}$ is the external applied flux density and $B_{in}$ is the flux density measured at the central position inside the cylinder.

The problem is solved in terms of local average fields $\boldsymbol{H}$, $\boldsymbol{B}$, $\boldsymbol{J}$ and $\boldsymbol{E}$ where it is assumed that each finite element covers a sufficiently high number of tapes in the $z$-direction. The homogeneous material illustrated in Fig. 5.3 consists of a volume fraction $f$ of ferromagnetic material. The remaining volume consists of HTS and buffer layers. The homogeneous model assumes that the HTS layer occupies a volume fraction $1 - f$ of the stack. Due to the layered structure, the material is modeled using anisotropic magnetic permeability and electrical resistivity. These two quantities are introduced in the following.

### Anisotropic permeability

The anisotropic relative permeability tensor can be written as follows [242]:

$$\boldsymbol{\mu}_{\mathbf{an}}(H) = \begin{pmatrix} \mu_{x,y}(H) & 0 & 0 \\ 0 & \mu_{x,y}(H) & 0 \\ 0 & 0 & \mu_z(H) \end{pmatrix}, \tag{5.1}$$

with $\mu_{x,y}(H) = f\mu_{\mathrm{r}}(H) + (1-f)$ for the $(x,y)$-components and $\mu_z(H) = \frac{1}{\frac{f}{\mu_{\mathrm{r}}(H)}+(1-f)}$ for the $z$-component. The $(x,y,z)$-coordinates system is shown in Figs. 5.1 and 5.3. The field dependence of the relative permeability $\mu_{\mathrm{r}}(H)$ of the ferromagnetic substrate at 77 K and room temperature have been presented and discussed in the previous chapter (Section 4.2). Interpolations of the measured first magnetization curves and permeability curves at room temperature (293 K) and at 77 K are shown in Fig. 5.4.

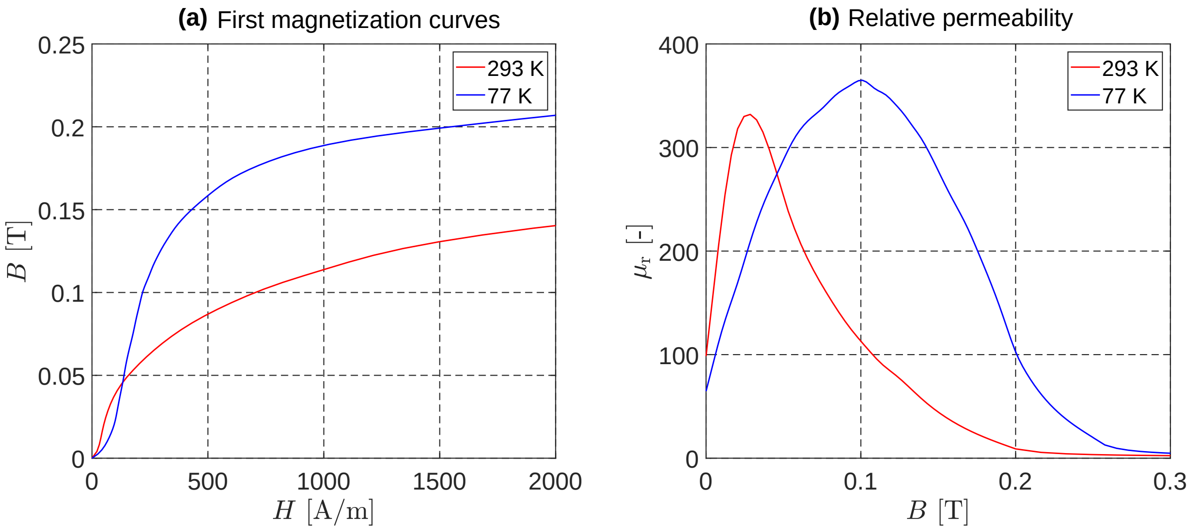

**Figure 5.4:** (a) First magnetization curves and (b) relative magnetic permeability as a function of the applied field at both room temperature and 77 K. The curves are obtained by interpolation of measurement results presented in Chapter 4.

### Anisotropic resistivity

As the current can only flow in the $(x,y)$-plane, the model introduces a high resistivity value $\rho_\infty$ in the $z$-direction [104, 243]. The anisotropic resistivity tensor is given by

$$\boldsymbol{\rho}_{\mathbf{an}}(\boldsymbol{J}) = \begin{pmatrix} \rho(\boldsymbol{J}) & 0 & 0 \\ 0 & \rho(\boldsymbol{J}) & 0 \\ 0 & 0 & \rho_\infty \end{pmatrix}, \tag{5.2}$$

where $\rho_\infty$ is chosen as high as possible while avoiding numerical instabilities ($\rho_\infty = 0.01$ Ωm in practice). The resistivity $\rho(\boldsymbol{J})$ is defined as a function of the average current density $\boldsymbol{J}$ through the power law given by Eq. (2.14) introduced in Chapter 2, where the critical electric field and the dimensionless exponent are respectively fixed at $E_\mathrm{c} = 10^{-4}$ V/m and $n = 20$. The model is implemented using a field-dependent critical current density $J_\mathrm{c}(\boldsymbol{B})$ following Kim's law,

$$J_\mathrm{c}(\boldsymbol{B}) = J_{c,0}\left(1 + \frac{\|\boldsymbol{B}\|}{B_0}\right)^{-1}, \tag{5.3}$$

where $J_{c,0} = 3.44 \times 10^8$ A/m$^2$ and $B_0 = 0.2$ T. The procedure followed to estimate these two parameters will be detailed in Section 5.3.1.

The homogeneous model assumes that the tapes composing the samples are much thinner than the typical mesh size (due to the high number of tapes). The critical current density described by Eq. (5.3) is thus an averaged quantity over a high number of tapes in which the superconducting material is assumed to occupy a small fraction of the whole volume. Accordingly, the critical current density used in this model is largely underestimated compared to the actual critical current density of the superconducting layers.

## 5.2 Results

### 5.2.1 Magnetic shielding at room temperature

In this section, the magnetic shielding is investigated at room temperature for the samples A, B and C in both axial and transverse configurations. Figure 5.5 shows the field dependence of the shielding factor $SF = B_\mathrm{app}/B_\mathrm{in}$ measured at the central position of the stack. The experimental results are compared to numerical simulations carried out using the method and the material parameters described in Section 5.1.2.

We start by examining the experimental data for Sample A, appearing as plain lines in Fig. 5.5(a). The first characteristic is that the stack exhibits a finite magnetic shielding (i.e. $SF > 1$) for both orientations. At low fields, the $SF$ is found to be the highest in the transverse direction but decreases monotonically with the applied field. Oppositely, when the field is axial, the $SF$ is rather small and almost field-independent.

In the transverse configuration, the monotonic decrease of the $SF$ with $B_\mathrm{app}$ suggests that the shielding factor would be maximum when the applied field $B_\mathrm{app}$ goes to 0. However, at room temperature, Fig. 5.4 shows that $\mu_\mathrm{r}$ exhibits a maximal value in the very low field region ($H \sim 68$ A/m, corresponding to $B \sim 28$ mT) which also suggests that

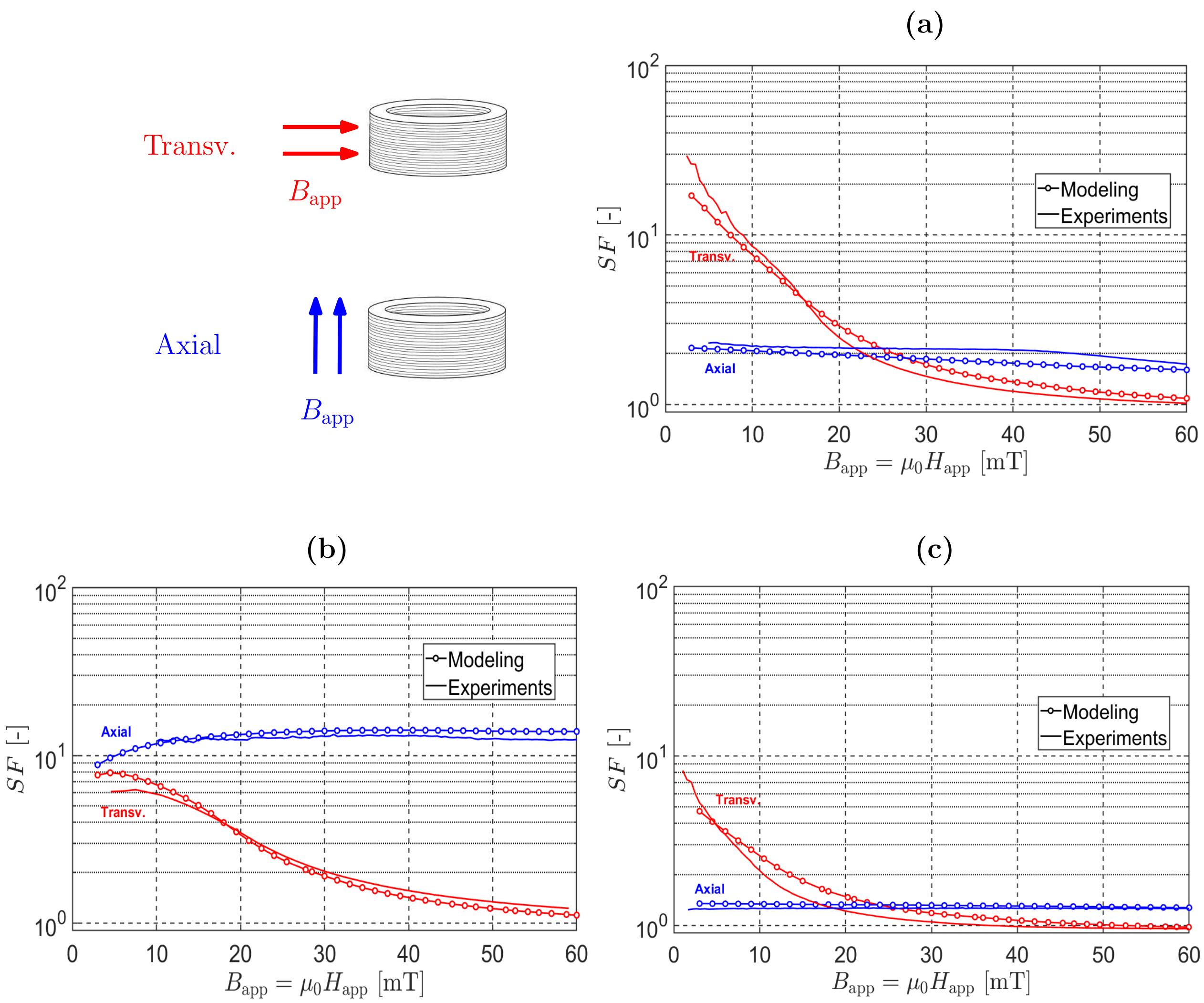

**Figure 5.5:** Shielding factor as a function of the applied magnetic flux density for (a) Sample A, (b) Sample B and (c) Sample C at room temperature. The experimental results are compared to numerical modeling in axial and transverse configurations. The field is applied at a rate of 0.75 mT/s.

the $SF$ curve should reach a maximum located around $B_{\mathrm{app}} \sim 3$ mT. This applied field yields a magnetic flux density inside the shield ($B_{\mathrm{in}}$) below the noise level and the possible maximum of the $SF$ curve cannot be verified experimentally. However, we can reasonably assume that the maximum $SF$ occurs between the $SF$ extrapolated at zero applied field ($SF_0$) and the first measurement data ($SF_1$). In a first approximation, the mean value between $SF_0$ and $SF_1$ should provide us with an adequate estimation of the maximal shielding factor. Doing so for both transverse and axial configurations, Fig. 5.5(a) shows that Sample A is characterized by $SF \approx 35.67$ in the transverse configuration and $SF \approx 2.35$ in the axial configuration. As can be seen in Figs. 5.5(b) and 5.5(c), the corresponding values for Samples B and C respectively are $SF \approx 10.2$ and $SF \approx 8.85$ in the transverse configuration, and $SF \approx 1.53$ and $SF \approx 1.25$ in the axial configuration. Since the superconductor does not contribute to the magnetic shielding at room temperature, the shielding factor is due to the ferromagnetic substrate only. The substrate of the tapes appears to contribute mainly to shield the magnetic field component parallel to the tapes. The shielding efficiency depends directly on the aspect ratio of the sample. The results plotted in Fig. 5.5 can be compared to estimations from analytical formulae derived by Mager and applicable to purely ferromagnetic cylindrical shields with a field-independent permeability [245, 246]. If we assume a homogenized anisotropic permeability of which axial and tangential components are respectively defined by [242]

$$\mu_{x,y} = f\mu_{\mathrm{r}}, \tag{5.4}$$

$$\mu_z = \frac{1}{f/\mu_{\mathrm{r}} + (1-f)}, \tag{5.5}$$

the shielding factor can be separated in two contributions: $SF_{\mathrm{wall}}$ standing for the field penetration across the cylinder wall, and $SF_{\mathrm{open}}$ standing for the field penetration through the open ends. In the transverse configuration, the two contributions are given by the following analytical formulae:

$$SF_{\mathrm{wall}} = 1 + \frac{1}{4}\mu_{x,y}\left[1 - \left(\frac{R_{\mathrm{in}}}{R_{\mathrm{out}}}\right)^2\right], \tag{5.6}$$

$$SF_{\mathrm{open}} = \frac{3}{2}e^{\left[3.83\left(\frac{h}{2R_{\mathrm{in}}}\right)\right]}, \tag{5.7}$$

with $R_{\mathrm{in}}$ and $R_{\mathrm{out}}$ the internal and external radii respectively and $h$ the height of the cylinder. In the axial configuration, the two contributions to the shielding factor are given by

$$SF_{\mathrm{wall}} = 1 + 4N_z\left\{1 + \frac{1}{4}\mu_z\left[1 - \left(\frac{R_{\mathrm{in}}}{R_{\mathrm{out}}}\right)^2\right]\right\}, \tag{5.8}$$

$$SF_{\mathrm{open}} = e^{\left[2.405\left(\frac{h}{2R_{\mathrm{in}}}\right)\right]}\left[2.6\sqrt{\frac{h}{2R_{\mathrm{out}}}}\right]^{-1}, \tag{5.9}$$

where $N_z$ is the demagnetizing factor along the axis of the cylinder. The demagnetizing factors for cylinders can be found in the paper from Chen *et al.* [247]. We use here the magnetometric demagnetizing factor, leading to $N_z = 0.4116$ for Sample A, $N_z = 0.5260$ for Sample B and $N_z = 0.614$ for Sample C. The overall shielding factor, taking into account the flux penetration through the walls and through the open ends, is given by

$$\frac{1}{SF} = \frac{1}{SF_{\mathrm{wall}}} + \frac{1}{SF_{\mathrm{open}}}. \tag{5.10}$$

The results obtained by the Mager analytical formulae for Samples A, B and C are gathered in Table 5.2 for a magnetic relative permeability of $\mu_{\mathrm{r}} = 332$ which is the maximal permeability measured at room temperature. From the results shown in the table, we can conclude that the shielding factors obtained from the experimental measurements at low field are in a fair agreement with analytical formulae applicable to a purely ferro-

| SAMPLE A | | | | |
|---|---|---|---|---|
| | $\boldsymbol{SF_{\text{wall}}}$ | $\boldsymbol{SF_{\text{open}}}$ | $\boldsymbol{SF}$ | **Experimental** $\boldsymbol{SF}$ |
| **Axial** | 5.96 | 4.85 | 2.67 | 2.35 |
| **Transverse** | 51.87 | 51.46 | 25.83 | 35.67 |

| SAMPLE B | | | | |
|---|---|---|---|---|
| | $\boldsymbol{SF_{\text{wall}}}$ | $\boldsymbol{SF_{\text{open}}}$ | $\boldsymbol{SF}$ | **Experimental** $\boldsymbol{SF}$ |
| **Axial** | 7.34 | 2.65 | 1.95 | 1.53 |
| **Transverse** | 51.87 | 13.47 | 10.7 | 10.2 |

| SAMPLE C | | | | |
|---|---|---|---|---|
| | $\boldsymbol{SF_{\text{wall}}}$ | $\boldsymbol{SF_{\text{open}}}$ | $\boldsymbol{SF}$ | **Experimental** $\boldsymbol{SF}$ |
| **Axial** | 8.4 | 2.05 | 1.65 | 1.25 |
| **Transverse** | 51.87 | 6.45 | 5.74 | 8.85 |

**Table 5.2:** Shielding factor estimation from the Mager analytical formulae [245, 246] for Sample A, Sample B and Sample C. The results are obtained for a maximum relative magnetic permeability of $\mu_{\text{r}} = 332$, assumed to be field-independent.

magnetic cylindrical shield. Such formulae, therefore, can be used to estimate, in a first approximation, the shielding factor of the stack of annuli at room temperature and low applied field. The comparison between $SF_{\text{wall}}$ and $SF_{\text{open}}$ shows that, for the dimensions equal to that of Sample A, the penetration of the magnetic flux in the cylinder is shared almost equally between the walls and the open ends, i.e. $SF_{\text{wall}} \sim SF_{\text{open}}$ for both orientations. When the height is decreased, as it is the case for Samples B and C, the flux penetration is mainly dictated by the open ends ($SF_{\text{open}} < SF_{\text{wall}}$). In order to model the decrease of the $SF$ when the applied magnetic field is ramped from 0 to 60 mT, the field dependence of the magnetic permeability should be included. The numerical modeling, carried out following the procedure described in Section 5.1.2 including a field-dependent permeability, leads to the results shown in Fig. 5.5. As can be seen, the numerical modeling is able to reproduce the field dependence of the experimental shielding factor with a nice agreement for both orientations.

### 5.2.2 Magnetic shielding at 77 K

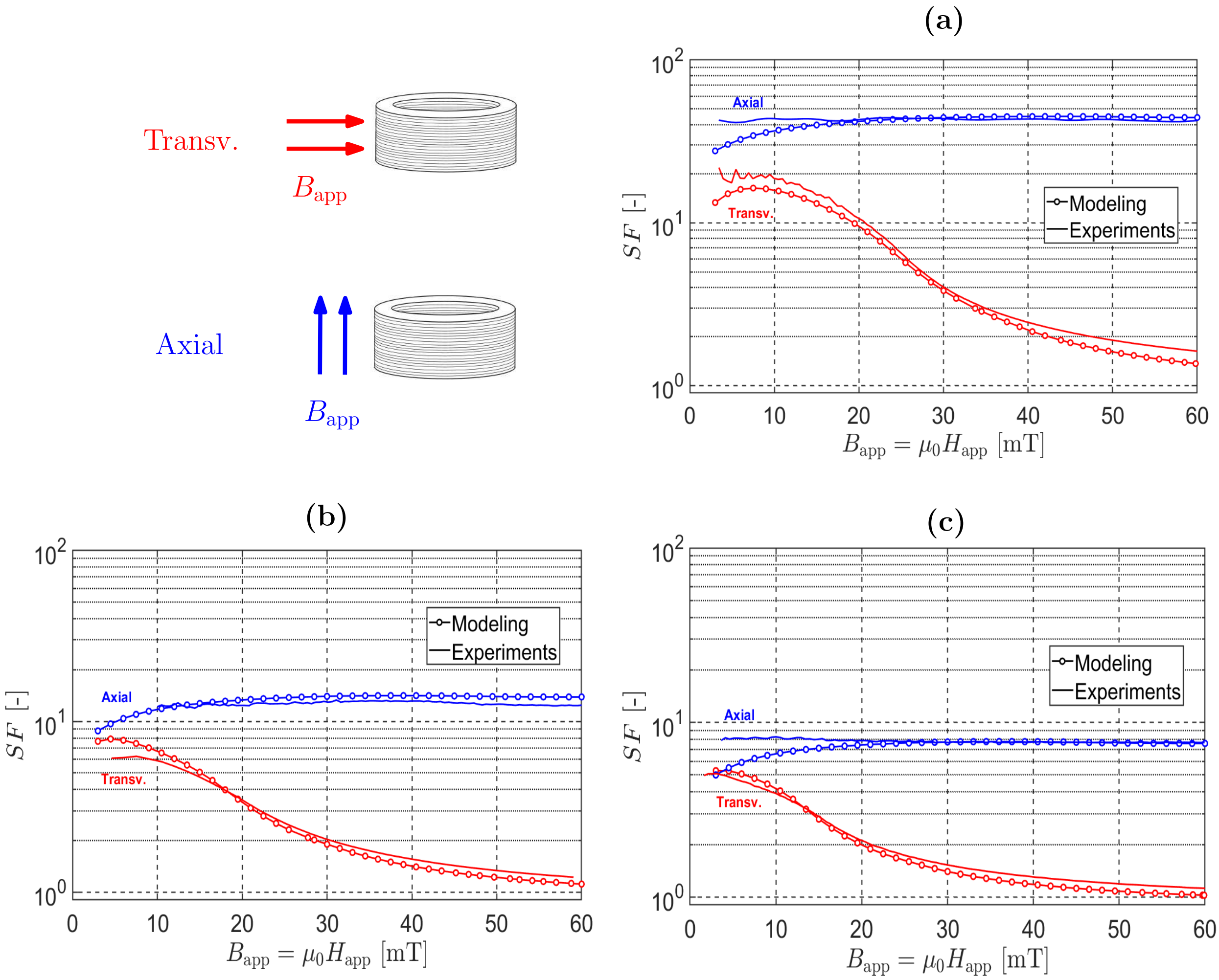

**Figure 5.6:** Shielding factor as a function of the applied magnetic flux density for (a) Sample A, (b) Sample B and (c) Sample C at 77 K. The experimental results are compared to numerical modeling in axial and transverse configurations. The field is applied at a rate of 0.75 mT/s.

We now investigate the shielding at 77 K in order to assess the effect of the HTS layers on the shielding efficiency. Figure 5.6 shows the field dependence of the shielding factor under either an axial or a transverse field as well as a comparison with numerical modeling (using $J_{c,0} = 3.44 \times 10^8$ A/m$^2$ and $B_0 = 0.2$ T for the $J_c(\boldsymbol{B})$ law as described in Section 5.1.2) for the samples A, B and C. As can be seen in Fig. 5.6(a), in the axial configuration and in the considered field range ($B_{\mathrm{app}} < 60$ mT), an almost field-independent shielding factor is obtained for Sample A ($SF \approx 45$). The value of $SF$ is much bigger than at room temperature due to the contribution of the shielding current loops flowing in the HTS layers. Under a transverse applied field, i.e. parallel to the HTS layers, we expect their contribution to be negligible at first order. The transverse magnetic shielding, therefore, is mainly due to the ferromagnetic substrates. The results of Fig. 5.6 show that the ferromagnetic layers give rise to a significant transverse shielding factor ($SF \approx 20$ for Sample A), despite the layered structure. The transverse shielding factor, however, is always lower than the axial one in the considered field range. The $SF$ first exhibits a plateau (or a very smooth bump) and then, decreases monotonically. Similar conclusions can be drawn for Samples B and C (Figs. 5.6(b) and 5.6(c)) except that the shielding factor values are lower than for Sample A due to their lower height. The results obtained by numerical modeling, shown in Fig. 5.6, are found to be in excellent agreement, both qualitatively and quantitatively, with the experimental results for the axial and transverse orientations.

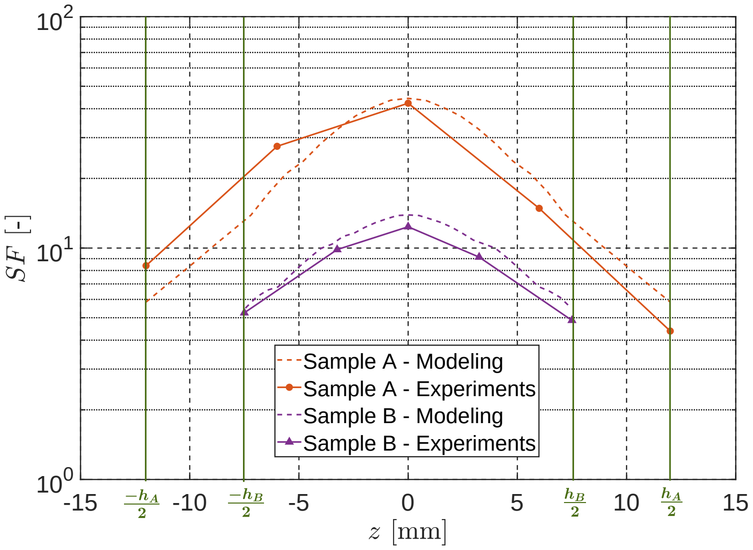

**Figure 5.7:** Shielding factor as a function of the position on the $z$-axis inside the sample for an axial applied field of 60 mT. Comparison between modeling and experimental results for Sample A and Sample B at 77 K. The central position corresponds to $z = 0$ mm. The vertical green lines show the position of the open ends for the two samples, $\pm h_A/2$ for Sample A and $\pm h_B/2$ for Sample B.

In addition to the data above, all measured at the center of the shield, it is interesting to look at the evolution of the shielding efficiency along the axis of the shield. Figure 5.7 shows the measured and modeled axial shielding factor along the $z$-axis inside the samples A and B at $T = 77$ K, for a 60 mT axial applied field. As expected, the highest shielding factors are obtained in the region around the central position ($z = 0$ mm). The experimental results obtained for Sample A happen to be slightly dissymmetric around the central position. This dissymmetry can be explained either by the uncertainty on the vertical position of the probe during the measurement process or by a non-uniform distribution of the critical currents of the coated conductors composing the sample. The causes of this dissymmetric behavior will not be discussed further. By construction, the numerical model is perfectly symmetric with respect to the $z = 0$ plane. The results plotted in Fig. 5.7 show that the numerical modeling is able to reproduce the distribution of the shielding factor inside the stack. Interestingly, it is found that in the vicinity of the open ends ($z = \pm h/2$), a shielding factor $SF \sim 6$ is observed for both geometries. Going from the open end towards the center of the sample, the shielding factor is found to increase almost exponentially with the distance $z'$ from the open end, as evidenced from the quasi-linear behavior observed in the semi-log scale of Fig. 5.7. Such an exponential increase is also expected for type-I superconductors [248].

In order to investigate the behavior of the shield at larger fields, the shielding factor was also measured under an axial applied field up to 670 mT on Sample B (Sample A was no longer available by the time of these measurements). To obtain these measurement data, the stack was place in the air gap of an electromagnet. A 1-axis HHPVU Hall probe from Arepoc® was placed at the center of the stack so that the experimental set up could accommodate the space between the poles of the electromagnet. The field dependence of the shielding factor is shown in Fig. 5.8 and is found to decrease monotonically with the applied field. From these measurements, it is possible to obtain a rough estimation of the critical current density as will be shown in the next section.

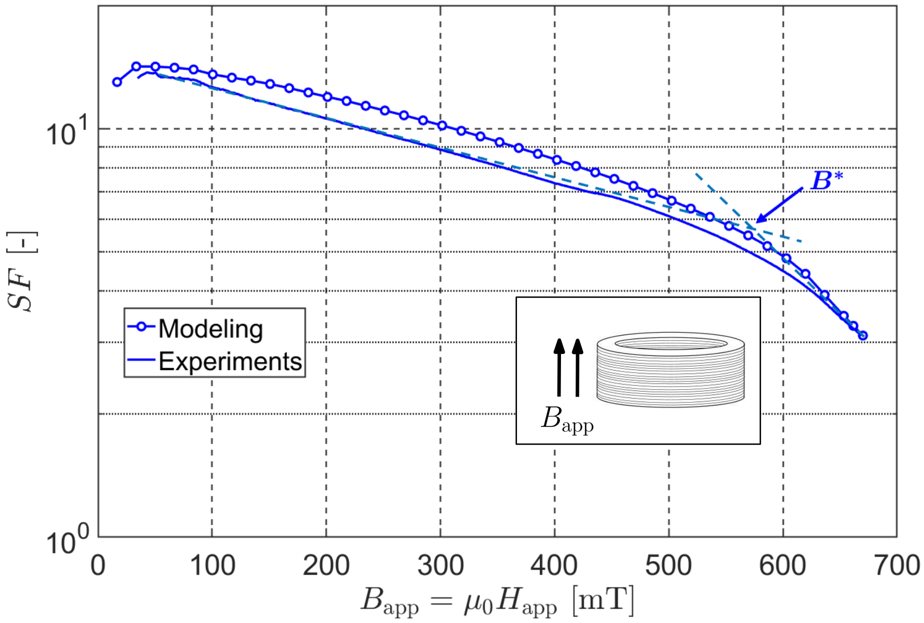

**Figure 5.8:** Shielding factor as a function of the axial applied magnetic flux density for Sample B. Comparison between experimental and modeling results. $T = 77$ K. The field is applied at a rate of 5 mT/s.

## 5.3 Discussion

In this section, we examine in more details how the results obtained in Section 5.2 can be used to determine the critical current density of the stack (5.3.1), to predict the behavior of higher stacks (5.3.2) and to understand how the shielding factor is influenced either by the $J_\mathrm{c}(B)$ of the superconductor or the $\mu_\mathrm{r}(B)$ of the ferromagnet (5.3.3).

### 5.3.1 Determination of $J_\mathrm{c}$

In order to determine the critical current density from the magnetic shielding measurements, we use the data plotted in Fig. 5.8, obtained for an axial applied field ($B_\mathrm{app} \parallel z$). Due to the layered structure, there is no superconducting current flowing along the axial direction. By symmetry, we can also assume that there is no shielding current flowing in the radial direction. Moreover, under an axial field at 77 K, it is expected that the magnetic shielding contribution of the magnetic substrates is very low compared to the contribution of the superconducting layers. Therefore, in a first approximation, one can assume that the magnetic shielding at 77 K is caused by azimuthal currents flowing in the individual superconducting layers only. From a macroscopic point of view, this is equivalent to having a plain superconductor (with no ferromagnetic substrate and no gap between the superconducting layers) in which a bulk, macroscopic, azimuthal 'engineering' current density $J_\mathrm{e}$ can flow. Figure 5.8 shows that the axial shielding factor first decreases smoothly with the applied field before going through a more abrupt decrease after 500 mT. We show below that this steeper decrease is related to the applied field under which the sample is fully penetrated. More precisely, the abrupt decrease gives rise to a slope break in the $SF(B)$ measurement, spotted by the flux density value $B^*$ in Fig. 5.8. For Sample B, this value is approximately equal to $B^* \approx 568$ mT. It is of interest to investigate whether this $B^*$ value is proportional to $B_\mathrm{pen}$, the full penetration field of the sample, i.e. whether one has $B^* = KB_\mathrm{pen}$, where $K$ is a constant. In the assumption of a field-independent current density, $B_\mathrm{pen}$ is given by the following formula [249]

$$B_\mathrm{pen} = \mu_0 J_\mathrm{e} d \left(\frac{h}{4\bar{R}}\right) \ln\left(\frac{4\bar{R}}{h} + \sqrt{1 + \left(\frac{4\bar{R}}{h}\right)^2}\right), \tag{5.11}$$

where $\bar{R}$, $h$ and $d$ are respectively the mean radius, the height, and the wall thickness of the cylinder.

In order to determine $K$, a simple 2D-axisymmetric model of a bulk purely superconducting cylinder with the geometrical dimensions of Sample B was used. The model was solved with an $H - \phi$ formulation. Figure 5.9 shows the field dependence of the shielding factor for three constant critical current densities $J_\mathrm{c}$ - within the plausible range that can be expected - for which the slope break can be graphically determined. We obtain

$B_1^* \approx 238$ mT , $B_2^* \approx 334$ mT and $B_3^* \approx 475$ mT respectively yielding to $K_1 \approx 0.839$, $K_2 \approx 0.841$ and $K_3 \approx 0.837$. From this analysis, we can conclude that the factor $K$ is independent of the critical current density in the range of $J_c$ considered. If we take the average of these values, we obtain $K_{avg} \approx 0.839$. Hence, using the formula (5.11), the average, engineering current density can be approximated from the measurement of $B^*$ and the knowledge of the factor $K$ as well as the sample geometry. The same procedure was applied on the sample C and the results for the two samples are compared in Table 5.3. Accordingly, even if this procedure is rather arbitrary, it leads to a rough estimation of the engineering current density which happens to be weakly dependent on the sample geometry.

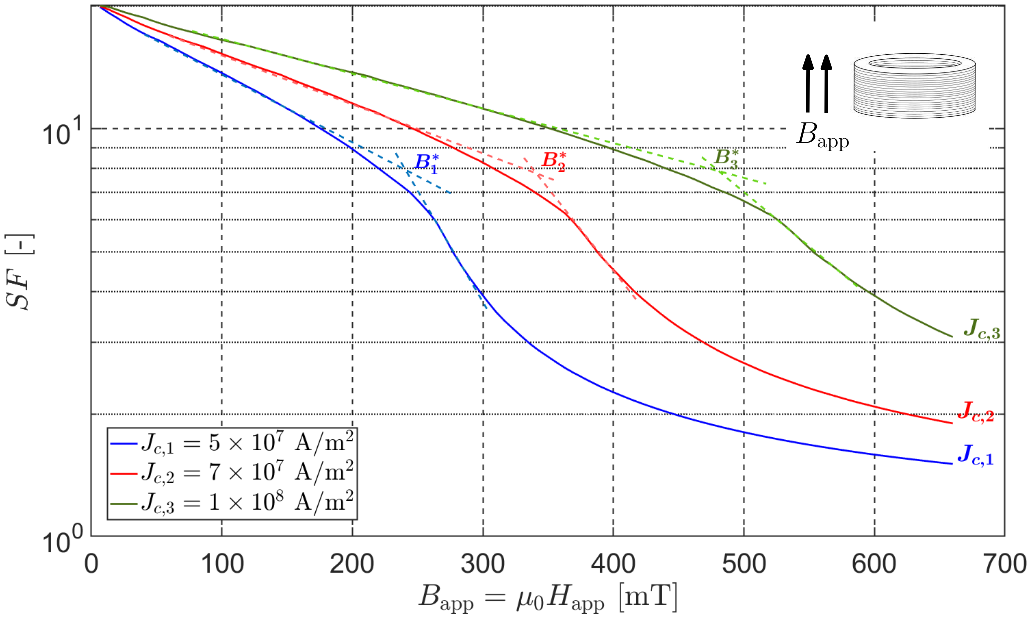

**Figure 5.9:** Field dependence of the SF obtained by a 2D-axisymmetric modeling of a bulk superconducting cylinder with the same geometrical dimensions than Sample B. The results are obtained for three different values of constant $J_c$. $T = 77$ K.

| | $B^*$ | $K_{avg}$ | $J_e$ |
|---|---|---|---|
| **Sample B** | 568 mT | 0.839 | $1.19 \times 10^8$ A/m$^2$ |
| **Sample C** | 479 mT | 0.842 | $1.28 \times 10^8$ A/m$^2$ |

**Table 5.3:** Comparison of the experimental slope break $B^*$, the averaged $K$ factor and the engineering current density $J_e$, assumed to be field-independent for two different aspect ratios.

The modeling results obtained with a field-dependent critical current density described by Eq. (5.3) of the axial shielding up to 670 mT are shown to be in a rather good agreement with the experimental results as we can see in Fig. 5.8. In order to justify the numerical

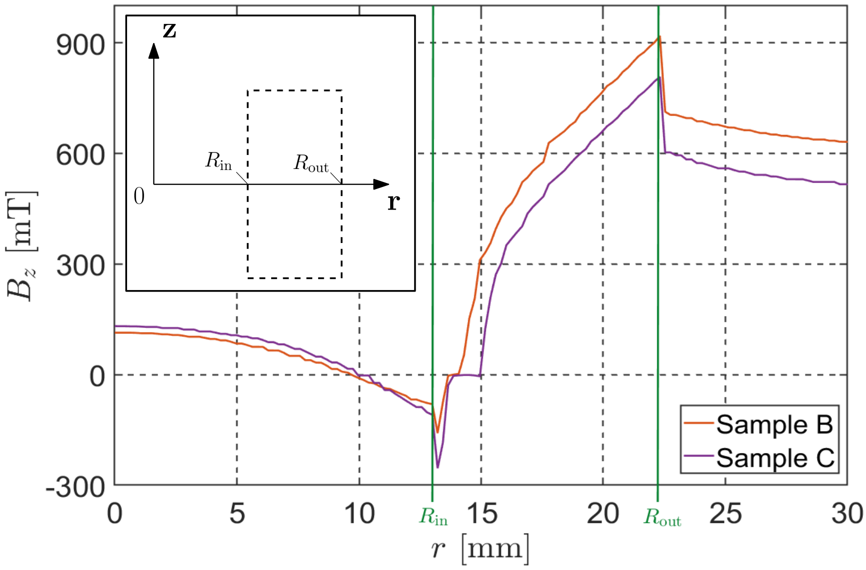

**Figure 5.10:** Numerical modeling of the $z$-component of the magnetic flux density as a function of the radial distance $r$ from the center of the cylinder. The flux density over $r$ is obtained for both Sample B and Sample C when the applied field is equal to $B^*$ (568 mT for Sample B and 479 mT for Sample C).

values used for the two parameters $J_{c,0}$ and $B_0$ appearing in Eq. (5.3), we can show that they lead to consistent values compared to those depicted in Table 5.3. The parameter $J_{c,0}$ is estimated by using the data provided by the manufacturer. As mentioned in Section 5.1.1, the critical current at self field is 200-350 A by cm width. Taking the average value of 275 A/cm and assuming that the current flows in the entire cross section, the engineering current density can be easily calculated. Taking a tape thickness of 80 $\mu$m, we obtain $J_{e,0} = 3.44 \times 10^8$ A/m$^2$. This value is then used for the first parameter of Kim's law, $J_{c,0}$. From this, the parameter $B_0$ can be estimated by finding the value leading to the best fit between the experimental and numerical data. This yields $B_0 = 0.2$ T. This set of parameters $(J_{c,0}, B_0)$ leads to the modeling results shown in Fig. 5.8. In order to check if the parameters of the $J_c(\boldsymbol{B})$ law make sense, the value of $J_c$ should be consistent with the average engineering current density values in Table 5.3 obtained at an applied flux density of $B_{\text{app}} = B^*$. Figure 5.10 shows the 2D modeling of the magnetic flux density component perpendicular to the tapes along the radial direction (the axis system is shown in the inset) when the external applied field is equal to $B^*$. The figure shows the flux density inside the sample B and the sample C. Since the value of $B^*$ differs for both samples ($B^* = 568$ mT for Sample B and $B^* = 479$ mT for Sample C), the two sets of data are obtained for two different values of applied flux densities. As can be seen in Fig. 5.10, the flux density strongly varies between the internal and the external walls of the cylinder and so does the critical current density. If we consider, in a first approximation, that the field is perpendicular to the tapes, the flux density $B$ in the superconducting layer is equal to that in the ferromagnetic layer and Kim's law (5.3) becomes:

$$J_c(\boldsymbol{B}) = J_c(B_z) = J_{c,0}\left(1 + \frac{|B_z|}{B_0}\right)^{-1}. \tag{5.12}$$

Knowing the values of $B_z$ from Fig. 5.10, we can compute the value of $J_c(B_z)$ along $r$ for Sample B and Sample C. The average values of the critical current density computed between $R_{\text{in}}$ and $R_{\text{out}}$ are $J_c \approx 1.17 \times 10^8$ A/m$^2$ for Sample B and $J_c \approx 1.4 \times 10^8$ A/m$^2$ for Sample C. These values are found to be fully consistent with the experimental engineering current densities depicted in Table 5.3 and give confidence in the determination of the parameters of the $J_c(\boldsymbol{B})$ law from the magnetic shielding measurements.

### 5.3.2 Prediction of the shielding behavior of higher stacks

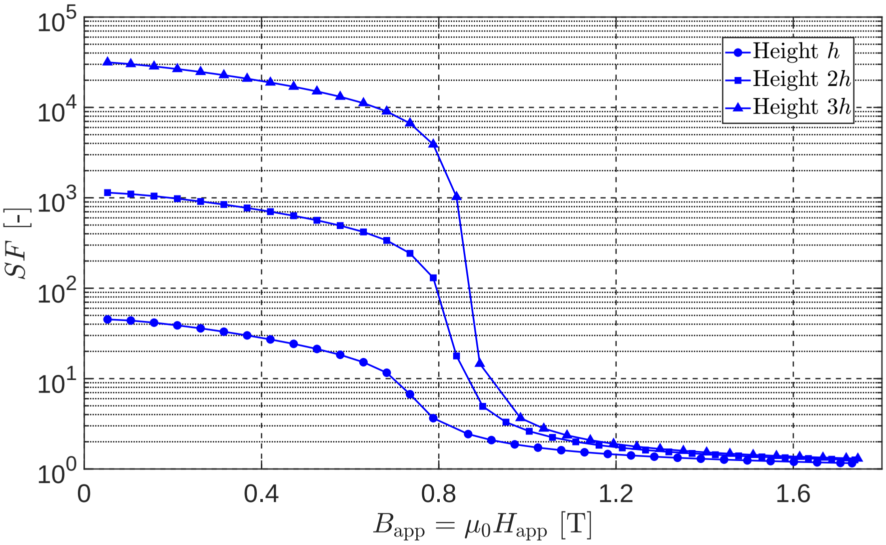

**Figure 5.11:** Shielding factor as a function of flux density applied in the axial direction for three different sample's height. Here $h = 24$ mm. The internal and external radii are the same than for Samples A, B and C. The results are obtained at 77 K. The field is applied at a rate of 5 mT/s.

In the following, we investigate the effect of the height of the sample on the magnetic shielding performances. As the results plotted in Fig. 5.8 show a good agreement between the 2D-axisymmetric homogeneous model using a field-dependent critical current density and the experimental measurements under an axial field value up to 670 mT, this model can then be used to assess the field dependence of the shielding performance for samples with higher dimensions. Figure 5.11 shows the modeled shielding factor as a function of the applied axial field for three samples of different heights. From this figure, the slope break characteristic of the sample full penetration appears not to depend strongly on the height of the sample. Indeed, for a sample of height $h = 25$ mm, the slope break is observed at an applied axial flux density of approximately 700 mT. For samples of height

$2h$ and $3h$, the slope breaks occur at approximately 748 mT and 812 mT respectively. Figure 5.11, however, clearly shows that the height has a significant impact on the value of the shielding factor itself. At lower fields ($B_{\mathrm{app}} < 200$ mT), a sample with a height equal to $h = 25$ mm can reach a $SF \sim 45$ (see Fig. 5.6(a)), whereas a sample three times higher can reach a shielding factor $SF > 30000$. Above $B_{\mathrm{app}} \approx 1$ T the shielding factor drops to values smaller than $SF = 3$ whatever the height of the stack. The practical consequence of a significant dependence of the shielding factor as a function of the aspect ratio - as is the case for bulk superconductors - is that the field at which the $SF$ reaches a given user-defined threshold, e.g. $SF = 10$, increases noticeably with increasing height. In the present case, these values are 0.7 T, 0.876 T and 0.931 T for stacks of height $h$, $2h$ and $3h$ respectively. This shows the potential of such stacks of tapes to shield fields up to $\sim 0.9$ T at 77 K.

### 5.3.3 Effect of $J_{\mathrm{c}}$ and $\mu_{\mathrm{r}}$ on the shielding efficiency

When the magnetic shield is operated at 77 K, the shielding results from a combined action of the superconducting layers and the ferromagnetic substrates, both of which being characterized by field-dependent parameters. In this section, we investigate in more details the effect of the superconducting layers and the ferromagnetic substrates on the magnetic shielding under either an axial or a transverse applied field.

First, the effect of the critical current density on the shielding efficiency is studied. Figure 5.12 compares the shielding factor modeled with a field-dependent critical current density $J_{\mathrm{c}}(B)$ given by Eq. (5.3), with the $SF$ modeled with a constant $J_{\mathrm{c}}$ ($5 \times 10^7$, $1.2 \times 10^8$ and $2 \times 10^8$ A/m$^2$), or with no superconductor ($J_{\mathrm{c}} = 0$ A/m$^2$). The modeling results are also compared with the experimental data. Here, we consider only Sample B. Figure 5.12(a) shows the shielding factor measured for a transverse field. As can be seen, within the range of investigated values, the modeled field dependence of the shielding factor is found to follow a qualitative behavior that is independent of the value of $J_{\mathrm{c}}$: a smooth bump followed by a monotonic decrease. Interestingly, the low-field ($B_{\mathrm{app}} < 15$ mT) $SF$ that would be measured without superconductor is slightly higher than when the superconductor is present, while the opposite behavior is observed above 15 mT. These results underline that the superconducting layers have a minor effect on the shielding process in the transverse configuration, but that this effect is not zero. More precisely, at low field, the bending of the magnetic flux lines caused by the ferromagnetic substrates leads to a non-zero axial component $B_z$ which, in turn, generates shielding currents in the superconducting layers. In particular, for $B_{\mathrm{app}} < 15$ mT, the shielding process is mainly due to the ferromagnetic material in which the flux lines are channelled following the path of least magnetic reluctance. With the presence of superconducting material ($J_{\mathrm{c}} \neq 0$ A/m$^2$), the shielding currents induced in the superconductor because of the non-zero $B_z$, oppose

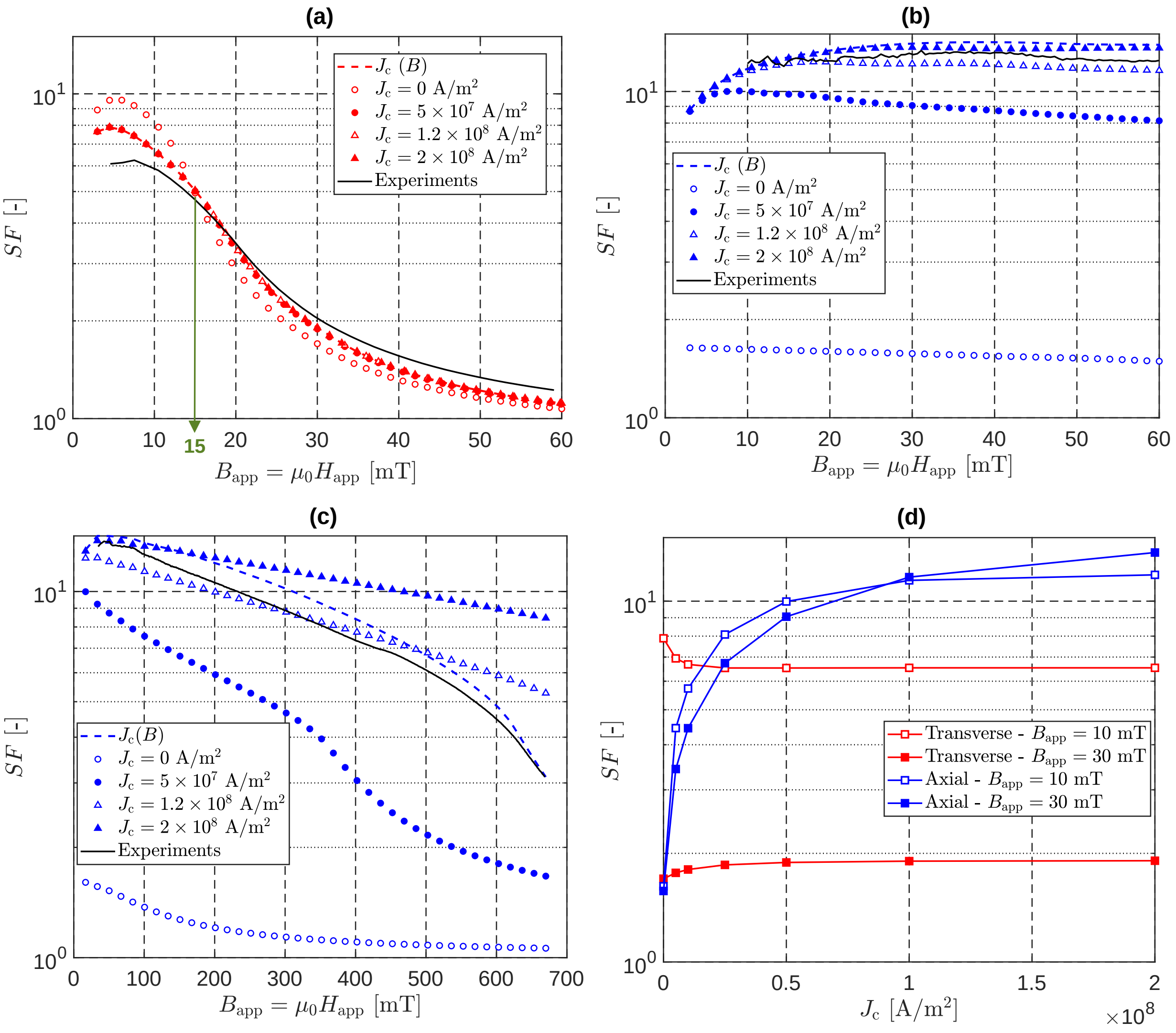

**Figure 5.12:** Comparison between experimental and numerical modeling results of the shielding factor with different values of $J_c$. The considered stack is Sample B. The shielding factor is plotted in (a) transverse configurations under a field range $< 60$ mT, (b) axial configurations under a field range $< 60$ mT and (c) in axial configuration under a field range up to 670 mT. The vertical arrow in graph (a) is used to indicate the crossover between the curves modeled with or without superconductor ($J_c = 0$). The graph (d) shows the modeled shielding factor as a function of $J_c$ at two applied fields (10 mT and 30 mT). The temperature is 77 K.

to the applied field. Hence, they increase the global magnetic reluctance and prevent the magnetic flux lines from being properly channelled by the ferromagnetic material. At the center of the cylinder, this phenomenon results in a transverse shielding factor smaller than that predicted in the absence of superconductor ($J_c = 0$ A/m$^2$). When no superconducting material is present, however, the ferromagnetic material saturates more rapidly (i.e. the permeability decreases with increasing magnetic flux density channelled within the sample). At an applied field $B_{\mathrm{app}} > 15$ mT, the shielding efficiency is thus slightly improved by the presence of shielding currents ($J_c \neq 0$). To illustrate the effect of the applied transverse field on the relative permeability, Fig. 5.13 shows the relative magnetic permeability within the sample (Sample B) considering either superconducting and ferromagnetic materials (HTS + FM) or only ferromagnetic material (FM). These results show that when the applied field is low, a larger volume of the material exhibits a high permeability value in the case FM compared to the case HTS + FM. However, when the applied field increases the permeability in the sample decreases. Nevertheless, Fig. 5.13(a) shows that a substantial part of the volume still exhibits high values of permeability at $B_{\text{app}} > 15$ mT whereas the material seems more saturated in the case FM. In spite of this effect, the results plotted in Fig. 5.12(a) give evidence that the shielding process is mainly due to the ferromagnetic substrate and emphasize the benefits of Ni-W alloys for a magnetic shielding application.

**(a) HTS + FM**

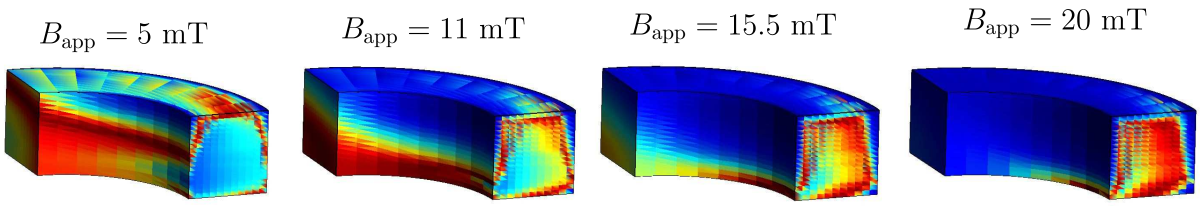

**(b) FM**

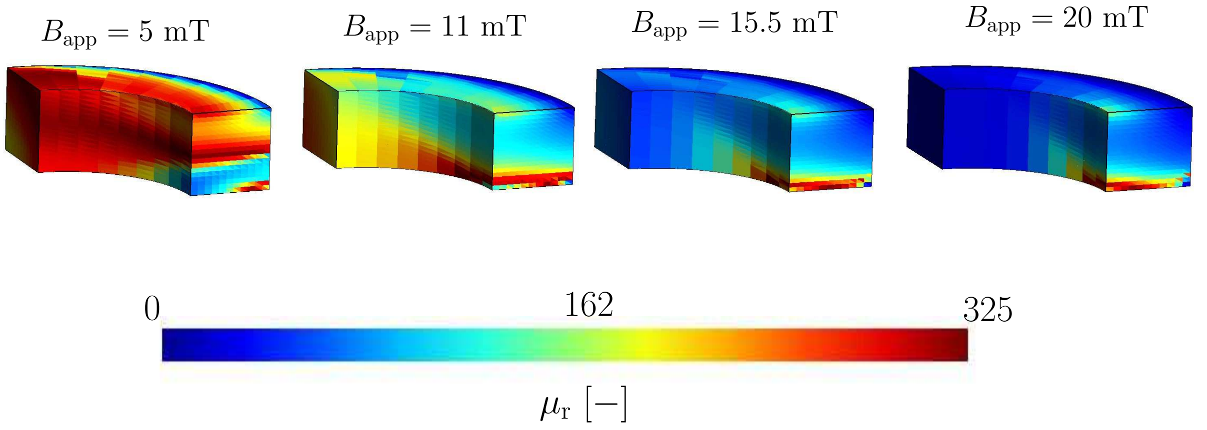

**Figure 5.13:** Magnitude of the relative magnetic permeability within the sample at different transverse applied field in the case where (a) superconducting and ferromagnetic materials are present (HTS + FM) and (b) only ferromagnetic material is present (FM). $T = 77$ K. The results are obtained on Sample B.

We now turn to the behavior of the shield subjected to an axial field. In the range $B_{\text{app}} < 60$ mT (Fig. 5.12(b)), considering a constant $J_{\text{c}}$ in the axisymmetric model does not change significantly the shape of the field dependence of the shielding factor. In this magnetic field range, the experimental data are within the modeled curves for a constant $J_{\text{c}} = 10^8$ A/m$^2$ and $J_{\text{c}} = 2 \times 10^8$ A/m$^2$. This is no longer true for higher fields (Fig. 5.12(c)) for which the impact of the value of the constant critical current density becomes more and more important as the axial field increases. A critical current density $J_c = 2 \times 10^8$ A/m$^2$ clearly overestimates the shielding factor at the highest fields. These results point out the interest of using a simple field-dependent $J_c(B)$ in the model as described in Section 5.1.2. It is worth mentioning that when we consider a zero $J_c$, the axial shielding factor keeps a value $> 1$ ($\sim 1.6$ at low field, then monotonically decreasing) due to the weak effect of the magnetic substrates on the magnetic shielding. The maximum $SF$ value at low field is comparable to that measured at room temperature ($\sim 1.5$) since the flux penetration mainly occurs through the open ends in this regime. Consistently with the previous results, Fig. 5.12(d) shows how the modeled shielding factor at two different applied fields (10 mT and 30 mT) changes as the critical current density increases from 0 to $2 \times 10^8$ A/m$^2$. This figure shows the increase of the shielding factor with the critical current density at a fixed applied axial field. This is due to the increase of the shielding current density in the superconducting layers. In the axial regime, we also observe that the $SF$ first increases sharply with the $J_c$ and then saturates. At 30 mT, the saturation is slower and occurs at a higher $SF$ than at $B_{\text{app}} = 10$ mT. Under a transverse applied field, Fig. 5.12(d) shows the small variation of the $SF$ with the critical current density in the very low $J_c$ regime (as already discussed above in this paragraph). For higher $J_c$, the curves exhibit no variation of the shielding factor with the critical current density at all.

Finally, we investigate the effect of the magnetic permeability of the substrate, and compare a constant $\mu_r$ to a field-dependent permeability $\mu_r(B)$. Modeling results of the shielding factor of Sample B considering a field-dependent permeability or a constant permeability under a transverse field are compared in Fig. 5.14(a) in the field range $B_{\text{app}} < 60$ mT. When the magnetic permeability is fixed to a constant value, the transverse shielding factor is shown to be field-independent in this field range. This remains consistent with the fact that the transverse shielding is mainly due to the ferromagnetic substrates. We also observe that the constant shielding factor increases with the constant magnetic permeability, as also shown in Fig. 5.14(d) which displays the $SF$ vs. $\mu_r$ dependence for two given applied fields $B_{\text{app}} = 10$ mT and $B_{\text{app}} = 30$ mT. Such a behavior is in agreement with the theoretical behavior that can be expected from Eqs. (5.6) and (5.7) that are valid for a purely ferromagnetic shield. When a field–dependent permeability $\mu_r(B)$ is considered, the SF is found to decrease with the applied field monotonically up to 60 mT. This result may look paradoxical since $\mu_r(B)$ at 77 K increases in this field range as reported in Chapter 4 and shown in Fig. 5.4(b). The explanation comes from the fact that the (non-uniform) magnetic flux density inside the FM when the stack is used to shield an applied transverse field $H_{\text{app}}$ might be higher than the uniform flux density $B_{\text{app}} = \mu_0 H_{\text{app}}$. When $B_{\text{app}} > 15$ mT the flux density in the material globally exceeds 100 mT. As a result, when the applied field is in the range 15 mT $< B_{\text{app}} <$ 60 mT, most of the material is located on the descending part of the $\mu_r(B)$ dependence. This justifies the decreasing $SF$ shown is Fig. 5.14(a). When the model does not take the

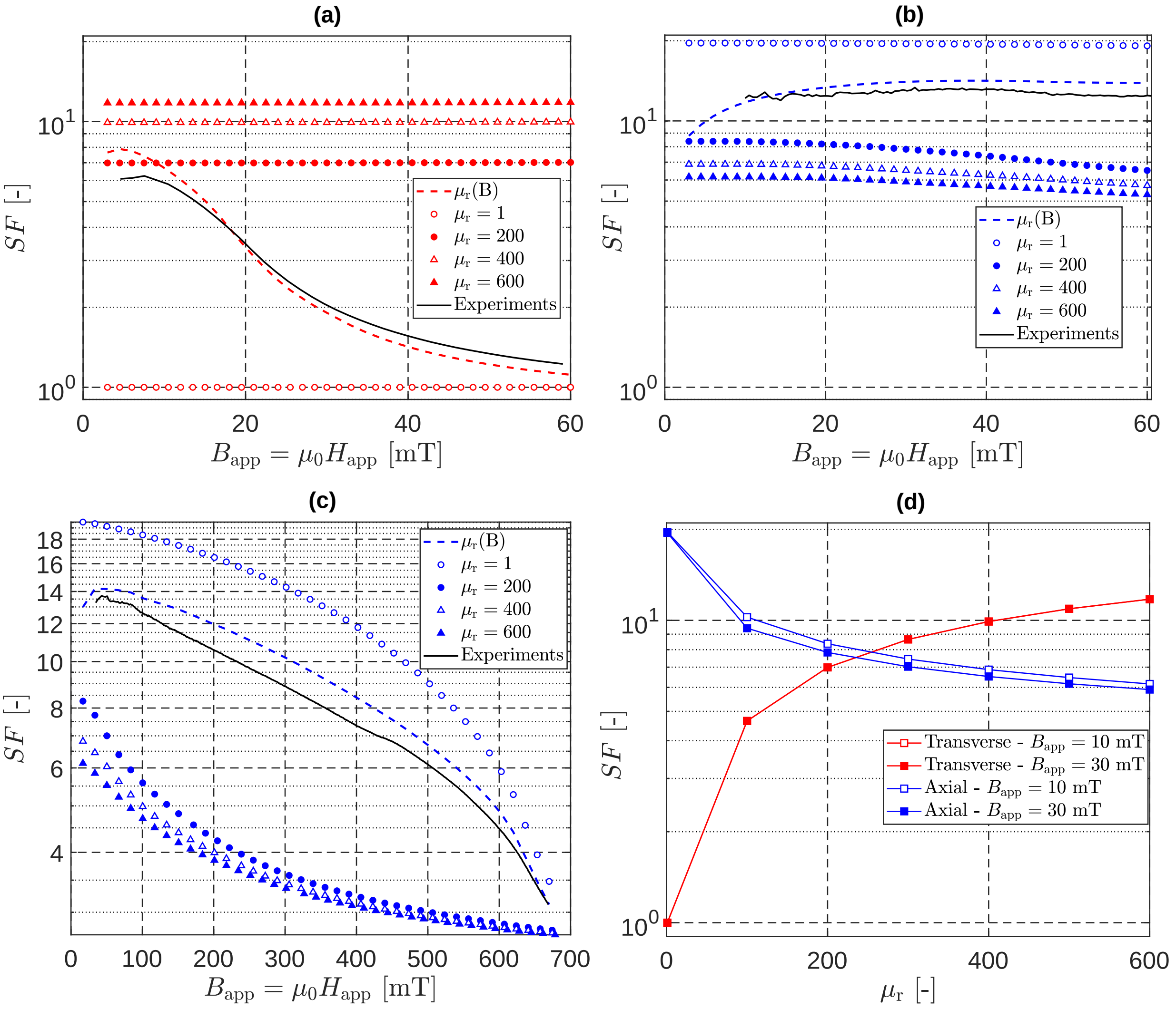

**Figure 5.14:** Comparison between experimental and numerical modeling results of the shielding factor with different values of $\mu_r$. The stack considered is Sample B. The shielding factor is plotted in (a) transverse configurations under a field range $< 60$ mT, (b) axial configurations under a field range $< 60$ mT and (c) in axial configuration under a field range up to 670 mT. The graph (d) shows the modeled shielding factor as a function of $\mu_r$ at two applied fields (10 mT and 30 mT). The temperature is 77 K.

ferromagnetic material into account ($\mu_r = 1$), we do not observe any shielding effect at all in the transverse case, as expected intuitively. Under an axial applied field (Fig. 5.14(b)), the results show that modeling the shielding factor by taking a field-dependent permeability as described in Section 5.1.2 for the ferromagnetic substrates is fully justified to fit properly the experimental results. When the field is applied in the axial direction, the shielding efficiency increases as the magnetic permeability decreases and we obtain a maximal magnetic shielding in the case where $\mu_r = 1$. This is also observed under an applied field up to 670 mT (Fig. 5.14(c)). This behavior can be explained by two elements. First, under the presence of a ferromagnetic material, the flux lines are attracted by it. The amplitude of the axial component of the flux density inside the sample, and thus

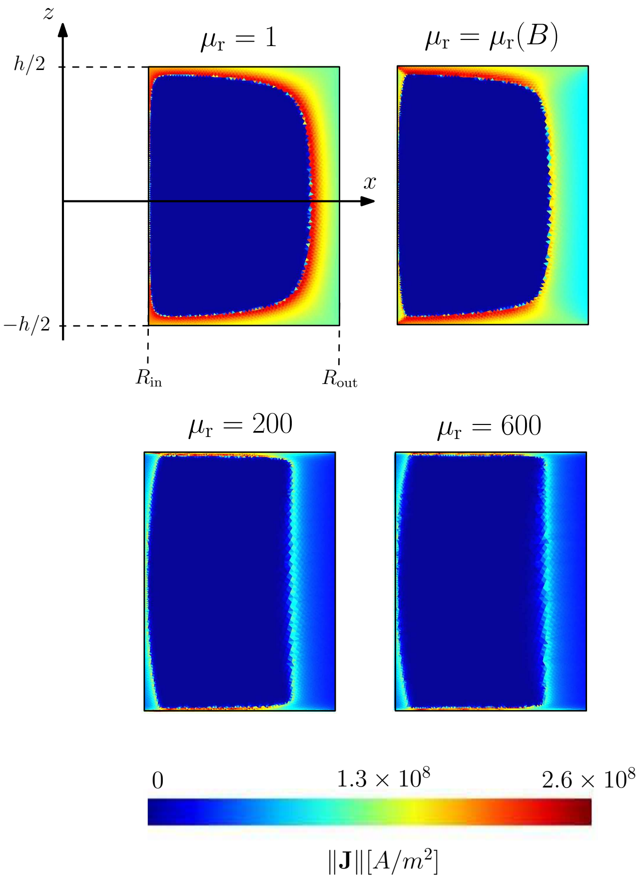

**Figure 5.15:** Shielding current density distribution on the section following the $(x, z)$ plane for different values of anisotropic relative permeabilities under an applied axial field of 200 mT. The results are obtained with a model using the $J_\mathrm{c}(B)$ dependence (5.3). The geometry used is that of Sample B.

inside the HTS layers, is increased. If the material is modeled using a field-dependent $J_\mathrm{c}$, this increase of the flux density will result in a reduced critical current density and then a reduced shielding efficiency. Fig. 5.15 shows the distribution of the shielding current density over the section of the sample under an applied external field $B_\mathrm{app} = 200$ mT for different values of magnetic permeabilities. The results shown in this figure are obtained using a 2D-axisymmetric model with a field-dependent critical current density following Eq. (5.3). The effect of the variation of the critical current density clearly appears in this figure which shows that the shielding currents are reduced when using a permeability $\mu_\mathrm{r} > 1$ compared to those obtained in the case where no ferromagnetic material is considered ($\mu_\mathrm{r} = 1$). Figure 5.15 also shows that the shielding currents are weakly affected by the permeability in the range $\mu_\mathrm{r} = 200$ to 600. This is consistent with the results plotted in Fig. 5.14(c) showing that the $SF$ exhibits quite similar values when $\mu_\mathrm{r} > 200$. The second element giving rise to an improved axial $SF$ as the permeability decreases is the flux density profile around the sample. Fig. 5.16 shows the distribution of the magnetic flux density as well as the magnetic flux lines when only superconducting material is considered (Fig. 5.16(a)), only ferromagnetic material is considered (Fig. 5.16(b)) and

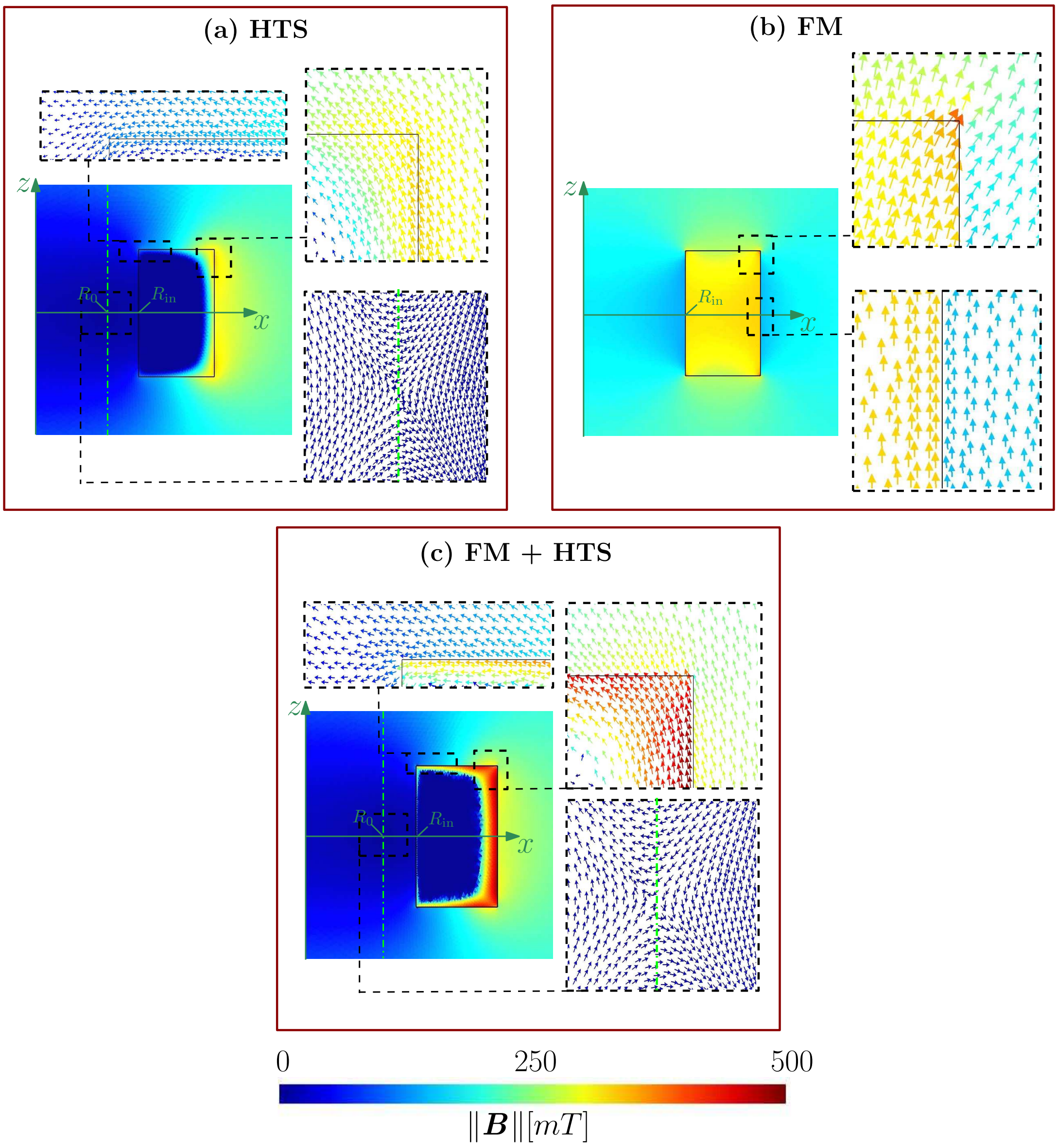

**Figure 5.16:** Distribution of the magnetic flux density $\|\boldsymbol{B}\|$ and magnetic flux lines in the $(x, z)$ plane for an axial applied field of 200 mT. The flux density distribution is shown for a shield consisting of (a) only superconducting material (HTS), (b) only ferromagnetic material (FM) and (c) a combination of ferromagnetic (92%) and superconducting (8%) material (FM+HTS). The dash-dotted green line in (a) and (c) spots the zero-$B_z$ region. The geometry used is that of Sample B.

when both materials are considered (Fig. 5.16(c)). When the only contribution comes from the superconducting material ($\mu_{\mathrm{r}} = 1$), the flux density concentrates mainly close to the external lateral wall. As the value of $\mu_{\mathrm{r}}$ increases and because of the anisotropy of the permeability, concentrations of the flux density also occur in the vicinity of the upper and lower surfaces which in turn, increases the penetration of the flux through the openings and thus decreases the shielding factor. As can be seen in Fig. 5.16(a) and (c), the flux density profile inside the shield reveals a region in which the axial component of the flux density $B_z$ cancels out. This region is spotted by the dash-dotted line at a radius $R_0$ and is characterised by a $SF > 1000$. According to the modeling results, far enough from the openings, this region forms a ring of radius $R_0 = 0.663R_{\text{in}}$ in the case HTS and $R_0 = 0.685R_{\text{in}}$ in the case FM+HTS. These values are quite close to the theoretical radius $R_0 = 0.628R_{\text{in}}$ expected for a type-I superconducting tube [34, 250].

## 5.4 Improvement of the shielding performance in the axial configuration

In this section, we investigate experimental methods to improve the shielding efficiency of the stack of HTS annuli under an axial applied magnetic field. To do so, the shielding performances of the stack are studied in a semi-closed configuration: one of the extremities of the stack is covered using a superconducting cap. This cap either consists of a bulk YBCO sample or a stack of HTS tapes. The shielding efficiency is still characterized by measuring the magnetic flux density at the center of the cylinder (stack of annuli). Pictures of the different caps as well as the whole structure combining the stack of annuli and the cap can be seen in Fig. 5.17. The investigated cylinder is the sample B introduced in Section 5.1.1. The shield combining Sample A and a cap would be too large to be inserted in the air gap of the 0.67 T electromagnet.

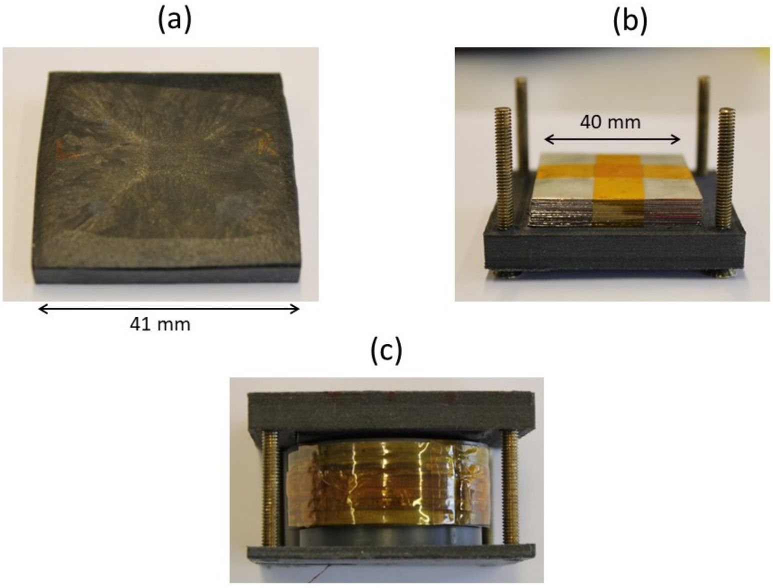

**Figure 5.17:** Pictures of (a) the cap based on a bulk YBCO HTS with a thickness of ∼ 6.5 mm, (b) the cap based on a stack of HTS tapes and (c) the whole semi-closed structure combining the stack of annuli (Sample B) with the cap (the picture shows the bulk YBCO cap).

The bulk superconducting cap shown in Fig. 5.17(a) is obtained from the YBCO rectangular prism from ATZ® introduced and characterized in Section 4.1.1. The shield resulting from the YBCO prism and Sample B would be too large to be inserted in the air gap of the electromagnet. As a result, the YBCO prism was cut along the $(a, b)$-plane using a diamond wire saw at approximately 6.5 mm from seed surface. The cap shown in Fig. 5.17(b) is a stack of $N$ HTS squared tapes of 40-mm-width. These tapes were previously cut from a 2G coated conductor of 40-mm-width provided by Deutsche Nanoschicht®. The tapes are 65 $\mu$m thick. They consist of a Ni-5at.%W substrate with a thickness of approximately 60 $\mu$m and a HTS YBCO layer with a thickness of $\sim 1 - 1.5$ $\mu$m. The HTS layer is separated from the substrate by buffer layers. The average critical current, specified by the manufacturer, is 1350 A which corresponds to $\sim 338$ A per cm-width at self-field and 77 K. This leads to an engineering current density $J_e \approx 5.2 \times 10^8$ A/m$^2$. In the whole structure containing the cylinder of stacked annuli and the cap (either the square tapes or the bulk YBCO prism) shown in Fig. 5.17(c), the HTS side of the tapes is systematically placed against the cylinder. When the cap is the bulk YBCO sample, the seed surface, expected to display the best superconducting properties, is placed against the cylinder.

### 5.4.1 Results and discussion

**Experimental study**

The shielding efficiency of the semi-closed structure 'cylinder + cap' is characterized in several configurations: a cap consisting of a bulk YBCO sample and a cap consisting of $N$ stacked HTS tapes. The configuration where the cylinder is used without any cap (already studied is the previous sections) is also compared to these semi-closed configurations. The experimental field dependences of the shielding factors at 77 K are summarized in Fig. 5.18.

The first observation is a significant increase in the shielding factor by closing one of the extremities of the cylinder with both a bulk cap and a stack of tapes. Compared to a fully open cylinder, the results show that using a bulk HTS cap allows to increase the $SF$ by a factor exceeding 2 for $B_{\text{app}} < 200$ mT and bigger than 3 for $B_{\text{app}} > 200$ mT. We also observe that in this case, the applied field is too low to observe the characteristic slope break in the $SF$ curve. When the cap is a stack of $N$ superconducting tapes, the shielding efficiency is also significantly improved compared to open configuration. Figure 5.18 shows the $SF$ measurements for several numbers of tapes composing the cap. In the investigated field range, the case $N = 100$ leads to a similar $SF$ than for the bulk YBCO cap. For $N = 50$, we observe a slope break at approximately $B_{\text{app}} \approx 595$ mT. The field at which the slope break occurs is found to decrease monotonously as the number of tapes $N$ decreases. Before the slope break, the $SF$ value weakly depends on the number of tapes. Figure 5.18 also shows that even when the cap is based on only one tape, the low-field shielding efficiency is improved: the $SF$ for $N = 1$ is at least twice the $SF$ for the open cylinder at $B_{\text{app}} < 150$ mT. Knowing this, it would be of interest to see if the orientation of a single tape has an observable effect on the shielding factor. Figure 5.19 shows the

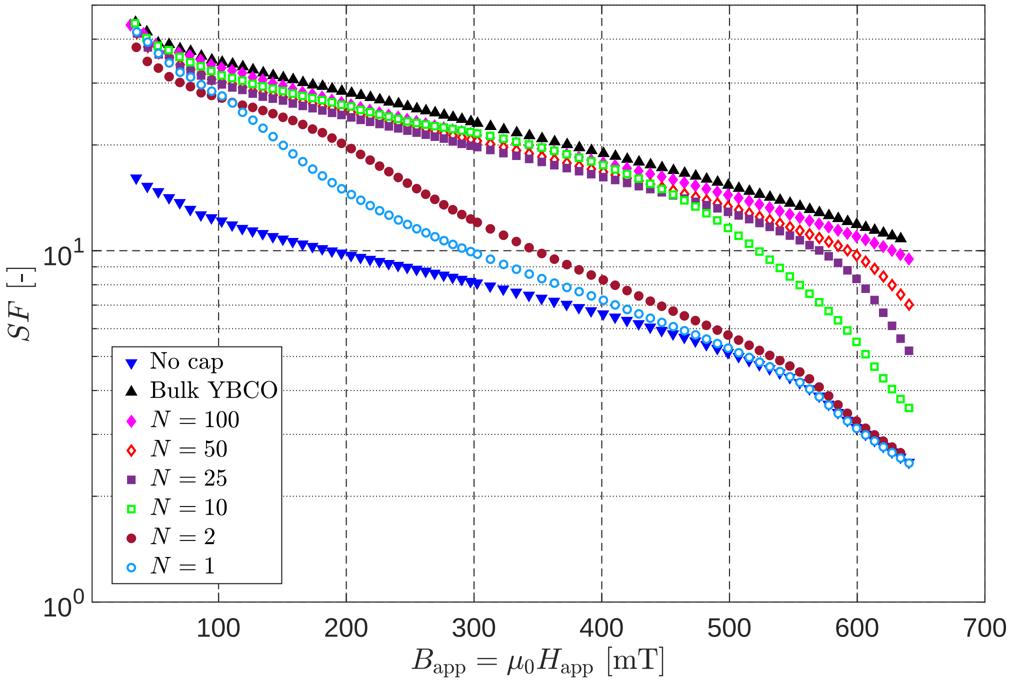

**Figure 5.18:** Shielding factor as a function of the external applied flux density (in the axial direction) for several semi-closed configurations. The case without any cap is compared to the different semi-closed cases (with either a bulk YBCO cap or a cap composed of $N$ HTS tapes). The operating temperature is 77 K.

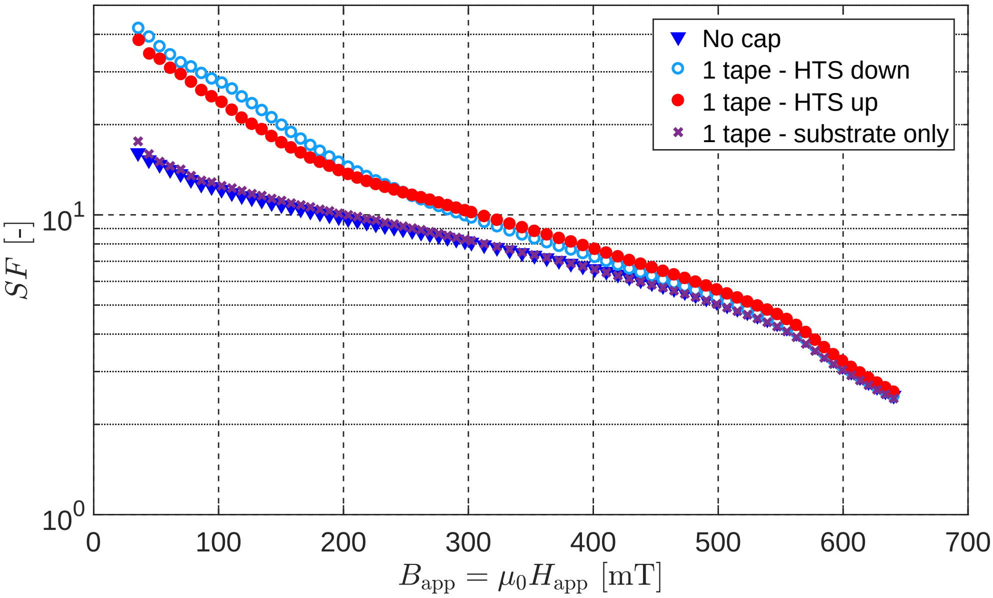

**Figure 5.19:** Shielding factor as a function of the external applied flux density (in the axial direction) when the cap is made of 1 tape either with the HTS layer against the cylinder (case 'HTS down') or with the substrate against the cylinder (case 'HTS up'). Comparison with a cap made of a purely ferromagnetic tape and with the open cylinder configuration. The temperature is 77 K.

shielding curve for a cap made of a single tape either oriented with the HTS layer against the cylinder ('HTS down') or with the ferromagnetic substrate against the cylinder ('HTS up'). The figure also shows the shielding curve for a cap made of a single tape for which the HTS layer was removed resulting in a purely ferromagnetic tape. These results are compared to the case in which the cylinder is fully open. The experimental results plotted in Fig. 5.19 show that the orientation of the tape with respect to the cylinder does not have a major influence on the shielding efficiency. The figure also shows that using a single purely ferromagnetic tape has almost no effect on the shielding efficiency compared to the fully open case.

### 2D-axisymmetric model

As the 2G coated conductors constituting the cap are based on a Ni-5at.%W substrate, numerical modeling can be based on the homogeneous model introduced in the previous sections. Strictly speaking, the problem can only be fully addressed using a 3D model. However, solving the problem using a 3D homogeneous model proves to be quite challenging. Under an axial applied field and due to the presence of ferromagnetic properties, the model, in the $H-\phi$ formulation, happens to hardly converge and the solutions obtained are not of good accuracy. A detailed layered model as presented in [104,240] would probably be more appropriate. However, in axial configuration, this detailed model is quite sensitive to the quality of the mesh refinement which, in 3D, would lead to time consuming computation in order to obtain an acceptable solution. As a result, we chose to approximate the 3D problem, illustrated in Fig. 5.20(a) by the 2D-axisymmetric model illustrated in Fig. 5.20(b). The true rectangular cap, is therefore replaced by a cylindrical cap with a radius equal to the external radius of the stack of annuli.

In order to validate the 2D-axisymmetric model, the numerical solution, is compared to the experimental results. First, it is worth mentioning that the measurement results plotted in Fig. 5.18 for the cylinder without any cap are slightly different than those presented in Section 5.2 for Sample B. This difference can be explained by the numerous manipulations and temperature cycles to which the samples have been subjected that may have slightly altered the quality of the tapes. Consequently, the model parameters described in Section 5.1.2 for the stack of annuli have been slightly adapted to fit the experimental curve in Fig. 5.18. The cylinder is now modeled using a Kim law with the following parameters: $J_{c,0} = 2.75 \times 10^8$ A/m$^2$ and $B_0 = 0.22$ T. Fig. 5.21 compares the results obtained by the 2D-axisymmetric model with the experimental results for a cap based on different numbers of stacked tapes. The cap is modeled using a Kim law with the following parameters: $J_{c,0} = 5.2 \times 10^8$ A/m$^2$ and $B_0 = 0.1$ T. The graphs shown in Fig. 5.21 show a rather good agreement between the measurement data and the numerical results up to 650 mT for the three cap sizes. The differences between experiments

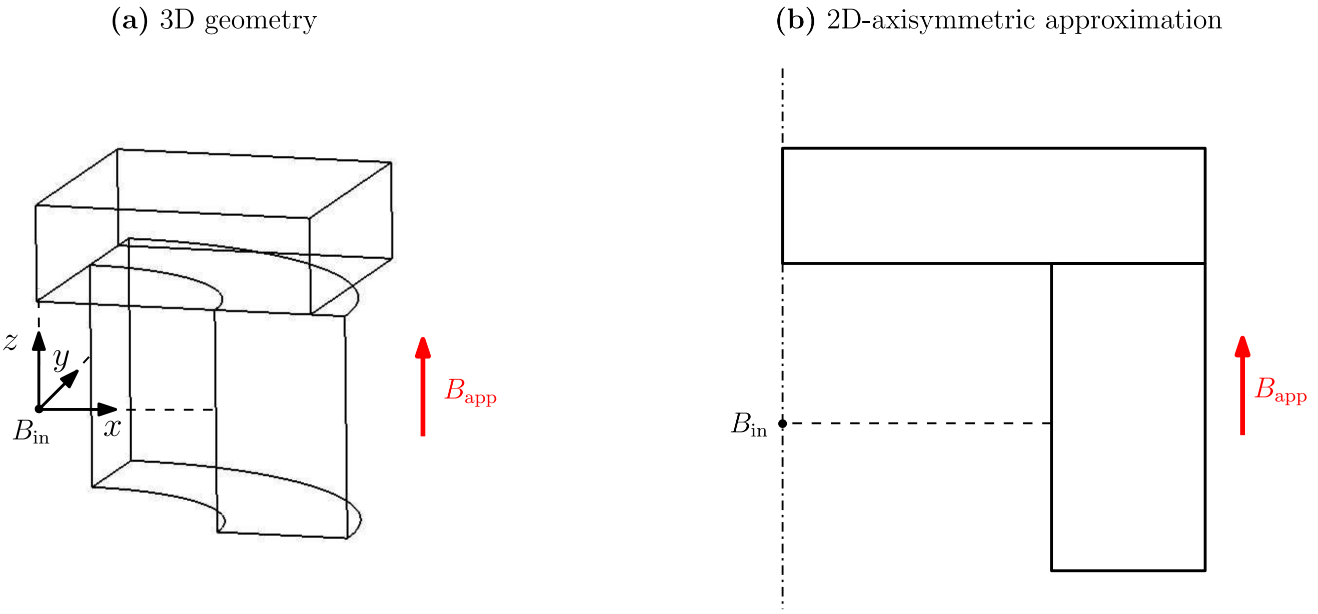

**Figure 5.20:** Illustration of the 3D structure (a) taking the problem symmetry into account and (b) the 2D-axisymmetric approximation.

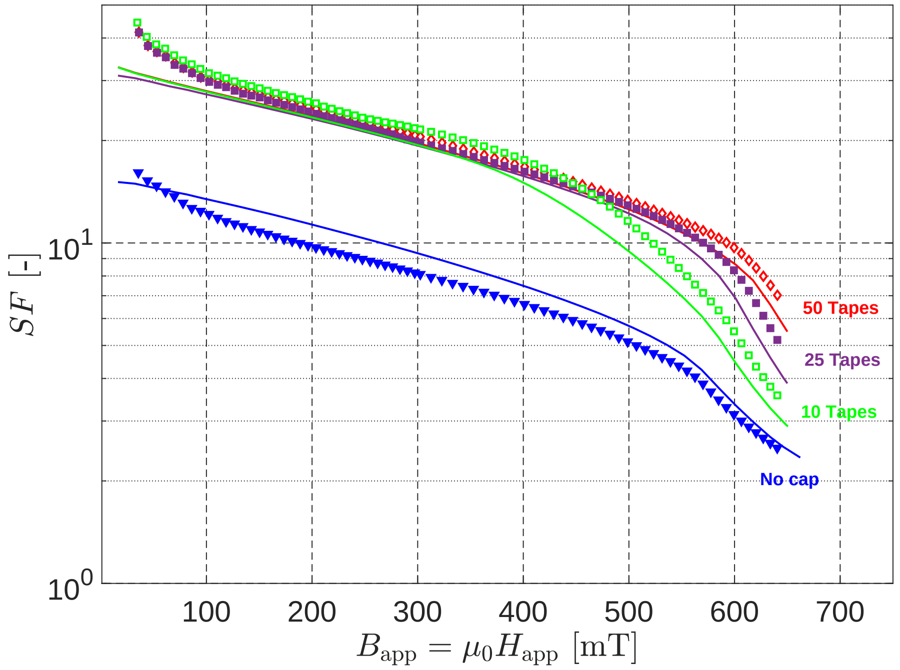

**Figure 5.21:** Comparison between the 2D-axisymmetric modeling results and experimental results for a cap made of different numbers of stacked tapes as well as for a fully open cylinder. The solid lines are the numerical results and the symbols are the experimental data.

and modeling observed at lower fields ($B_{\text{app}} < 100$ mT) is likely to be related the mesh size. Indeed, in the axial configuration, the solution at low applied field is found to be quite sensitive to the mesh size. An optimized mesh could possibly reduce the difference between experiments and modeling results.

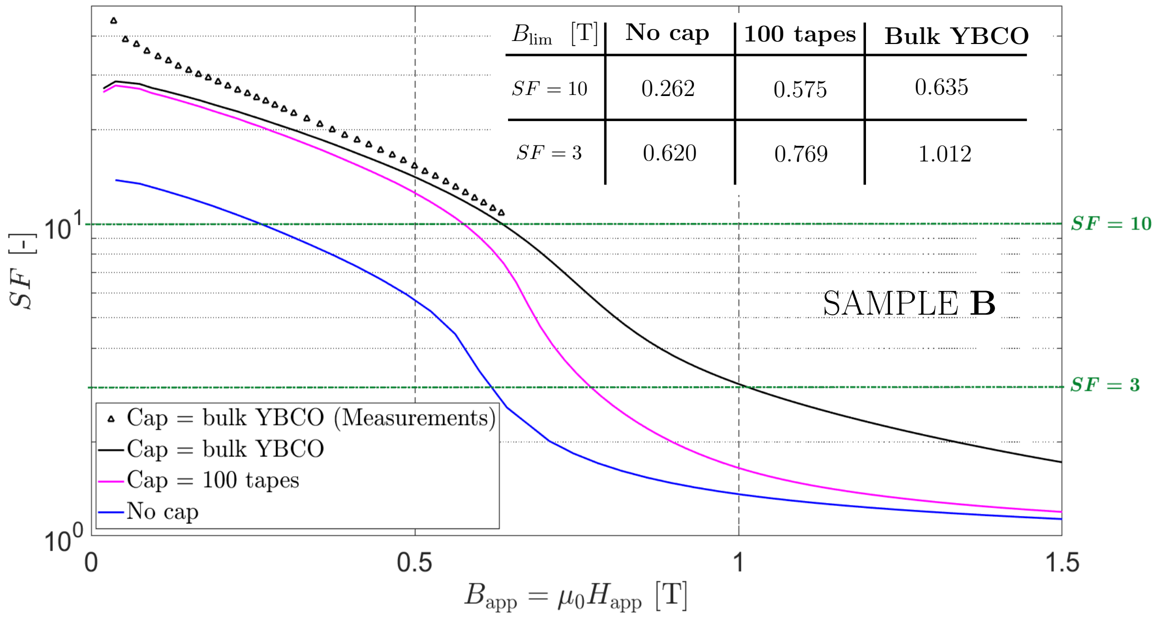

| $B_{\mathrm{lim}}$ [T] | **No cap** | **100 tapes** | **Bulk YBCO** |
|---|---|---|---|
| $SF = 10$ | 0.262 | 0.575 | 0.635 |
| $SF = 3$ | 0.620 | 0.769 | 1.012 |

**Figure 5.22:** Shielding factor as a function of the axial applied field obtained using the 2D-axisymmetric model up to 1.5 T. The results are obtained for Sample B combined to a cap made of either a bulk YBCO HTS or 100 stacked tapes. The numerical results for the bulk cap are compared to the measurement data at 77 K. The table in the insert compares the threshold flux densities obtained in the different configurations.

Due to the correct agreement between the experimental results and the results obtained by a 2D-axisymmetric model of a structure combining a cylinder with the dimensions of Sample B and a cap made of $N$ stacked tapes, the model can be used to predict the behavior of such a structure under a higher applied field. Figure 5.22 shows the results obtained by modeling the shield up to an applied field of 1.5 T. The figure shows the $SF$ as a function of the applied field in three different configurations: the case without any cap, a cylinder combined with a cap made of 100 stacked tapes and a cylinder combined to a bulk YBCO cap. In the latter configuration, the modeling results are compared to the measurement data already presented in Fig. 5.18. The bulk YBCO cap is modeled using a purely superconducting cap ($\mu_{\mathrm{r}} = 1$) with a field-dependent critical current density following a Kim law with the following parameters: $J_{\mathrm{c},0} = 3.5 \times 10^8$ A/m$^2$ and $B_0 = 1.2$ T, corresponding to the data obtained experimentally from $M$-$H$ curves on the bulk sample (Chapter 4, Section 4.1.1). The table inserted in Fig. 5.22 shows the threshold flux density values for $SF = 10$ or $SF = 3$ in the three investigated configurations. The results plotted in Fig. 5.22 give evidence that the structure combining the stack of annuli B with a bulk YBCO cap has the potential to shield uniform magnetic flux densities up to $\sim 1$ T with a shielding factor value exceeding 3 at 77 K. If we define the threshold flux density for a shielding factor of 10, the combination of Sample B and a bulk YBCO cap can efficiently shield flux densities higher than 635 mT at 77 K.

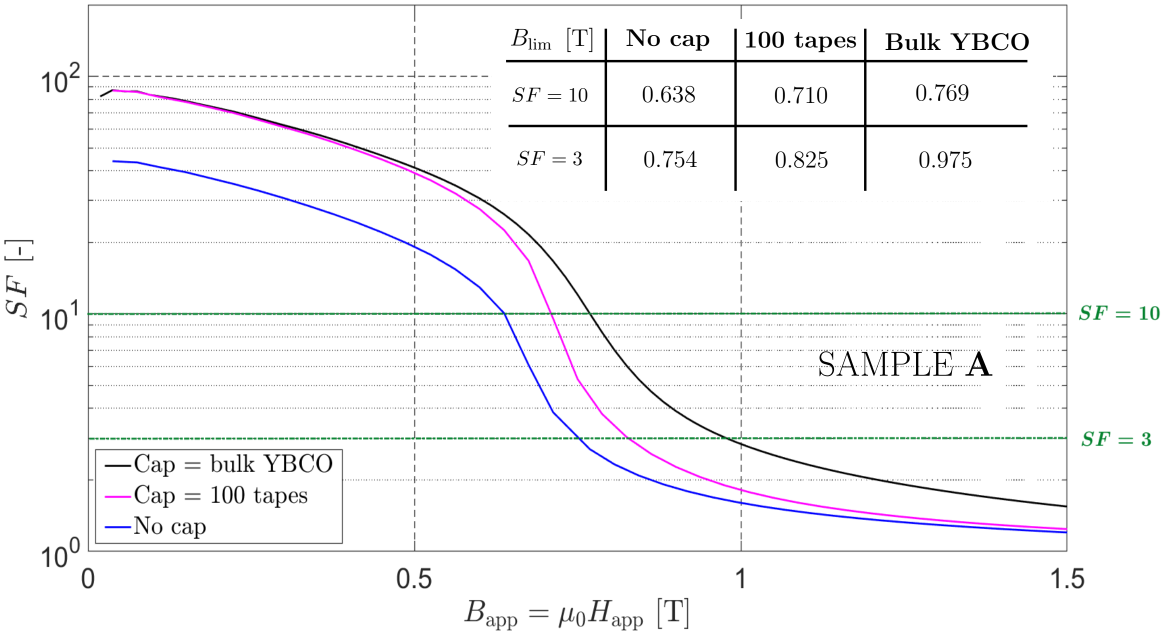

| $B_{\mathrm{lim}}$ [T] | **No cap** | **100 tapes** | **Bulk YBCO** |
|---|---|---|---|
| $SF = 10$ | 0.638 | 0.710 | 0.769 |
| $SF = 3$ | 0.754 | 0.825 | 0.975 |

**Figure 5.23:** Modeled shielding factor as a function of the axial applied field obtained using the 2D-axisymmetric model up to 1.5 T. The results are obtained for Sample A combined to a cap made of either a bulk YBCO HTS or 100 stacked tapes. The table in the insert compares the threshold flux densities obtained in the different configurations.

It is also of interest to investigate the modeled shielding efficiency in the same three configurations but using a taller cylinder with dimensions of Sample A instead of Sample B. Because such a structure cannot be inserted in the air gap of the electromagnet, there is no available measurement result up to $B_{\mathrm{app}} = 650$ mT. Figure 5.23 shows the modeled shielding curves. Again, the table in the insert indicates the threshold flux densities defined either for $SF = 10$ or $SF = 3$ for the three configurations. First, we note that the structure combining Sample A with a bulk YBCO cap has the potential to shield up to 770 mT with a shielding factor higher that 10 at 77 K. However, we observe that this structure exhibits a $B_{\mathrm{lim}}$ defined for $SF = 3$ ($\approx 0.975$ T) lower than for the structure based on Sample B ($\approx 1.012$ T). The fact that a taller sample exhibits a smaller $B_{\mathrm{lim}}$ looks paradoxical. To find an element of explanation, we can look at Fig. 5.24 which plots the field dependence of the shielding factor for Sample A and Sample B both combined to a bulk YBCO cap in four theoretical situations. In all cases, we consider a purely superconducting cylindrical stack ($\mu_{\mathrm{r}} = 1$). In the first situation, we consider a cap and a cylinder with the same $J_{\mathrm{c}}(B)$ dependences than those used for the results plotted in Figs. 5.22 and 5.23. The corresponding shielding factor is plotted in Fig. 5.24(a). In this case we observe a crossover between the two $SF$ curves, Sample B exhibits a $B_{\mathrm{lim}}$ (defined for $SF = 3$) which is slightly higher than for Sample A. The Figure 5.24(b) shows the shielding factor when both the cap and the cylinder are characterized by a constant $J_{\mathrm{c}}$.

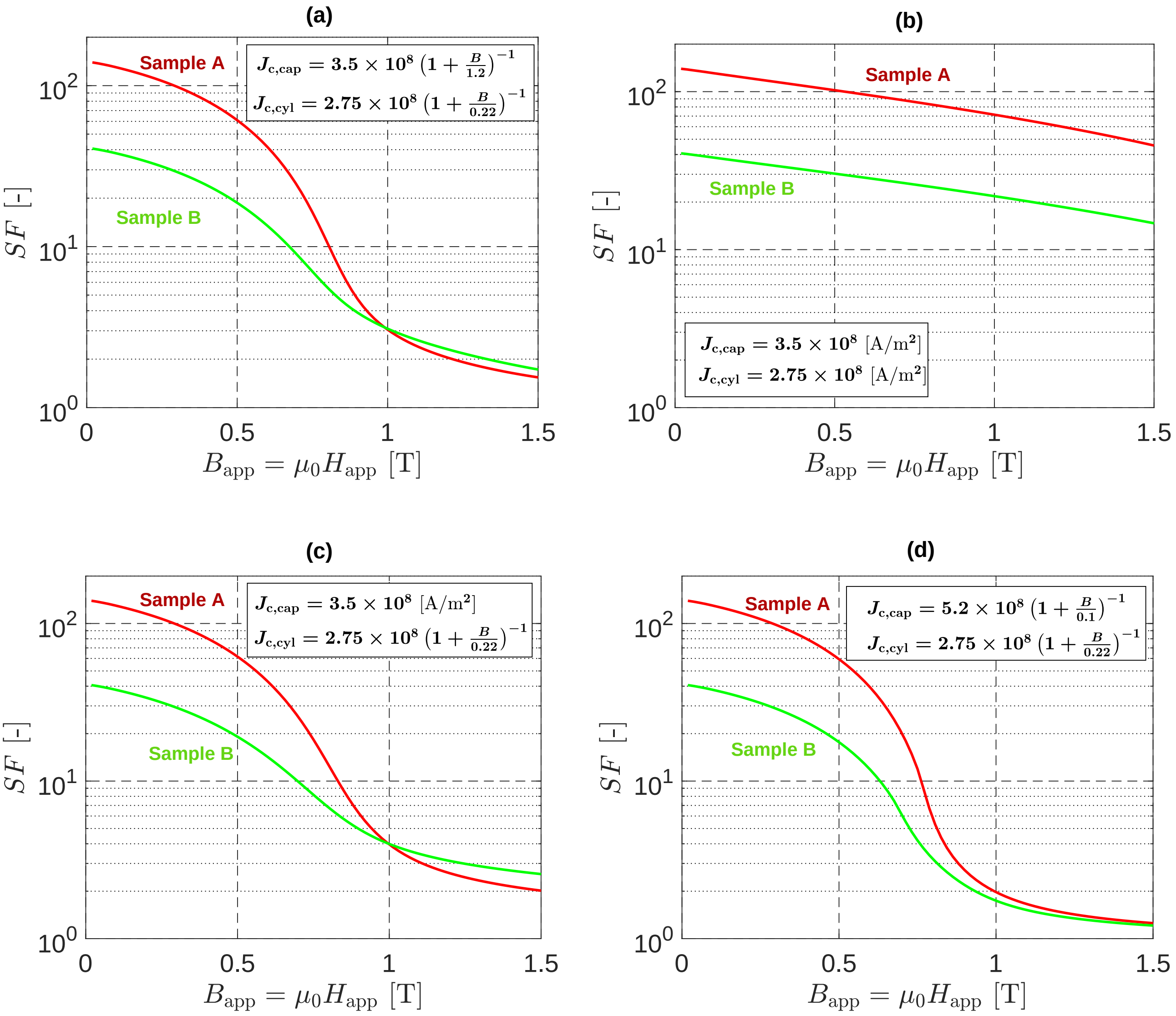

**Figure 5.24:** Shielding factor as a function of the axial applied field obtained using the 2D-axisymmetric model up to 1.5 T. The results compare Sample A (-) to Sample B (-) when both samples are combined to a bulk HTS cap. (a) Both the cap and the cylinder are characterized by a $J_c(B)$ behavior. (b) Both the cap and the cylinder are characterized by a constant $J_c$. (c) The cap is characterized by a constant $J_c$ while the cylinder is characterized by a $J_c(B)$ behavior. (d) Both the cap and the cylinder are characterized by a field-dependent $J_c$ but the cap is modeled with a different $J_c(B)$ law than in case (a). In all cases, the cylindrical stack is purely superconducting ($\mu_r = 1$). $B$ is always expressed in T and $J_c$ in A/m$^2$.

In this case, the $SF$ obtained for Sample A is always higher than $SF$ obtained for Sample B, as expected intuitively. In the third case (Fig. 5.24(c)), the cylinder is characterized using a field-dependent critical current density but the cap is modeled using a constant $J_c$. Again, in this case, a crossover is observed between the two curves. Finally, in the last case, the cap is characterized by a stronger $J_c(B)$ dependence ($J_{c,0} = 5.2 \times 10^8$ A/m$^2$ and $B_0 = 0.1$ T). The shielding factor is plotted in Fig. 5.24(d) and we recover an expected behavior. As a conclusion, the unexpected crossover between the $SF$ curves of Sample A and Sample B seems to result from the particular $J_c(B)$ dependence of the cap and not from the ferromagnetic characteristics of the cylinder. Indeed, the presence or absence of this crossover can be reproduced by numerical modeling for a non-ferromagnetic cylinder.

## 5.5 Improvement of the shielding performance in the transverse configuration

In the previous section, we investigated methods to improve the shielding efficiency of the stack of annuli in the axial configuration. However, the semi-closed geometries investigated are not expected to increase the shielding efficiency under a transverse applied field. Here, we investigate possible ways to increase the shielding factor in the transverse configuration. The method is based on the coated conductor (CC) of 40-mm-width introduced in the previous section. The idea is to wrap the initial stack of annuli with coated conductors in order to take advantage of the HTS layer under a transverse applied field.

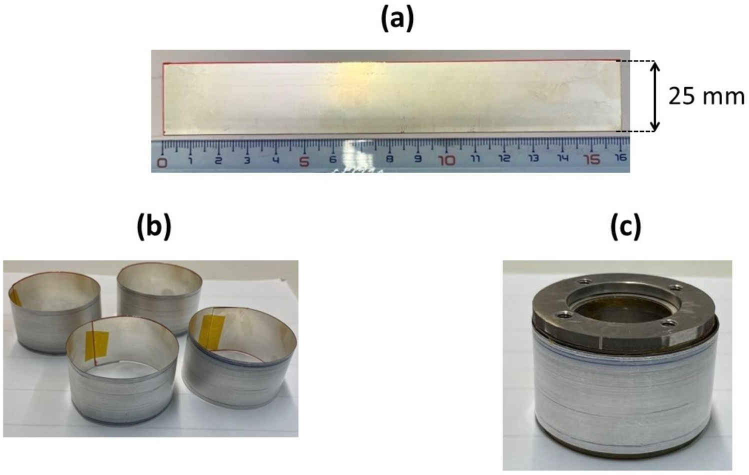

**Figure 5.25:** (a): Picture of a typical tape cut from the initial 40-mm-width CC. (b): Rings of HTS CC made of tapes similar to that showed in the picture (a). (c): Assembly of the stack of annuli (Sample A) and the four CC rings showed in the picture (b). The HTS layer in the rings is facing the stack of annuli.

The pictures in Fig. 5.25 illustrate the method to improve the transverse shielding efficiency. First, a tape of 160 mm in length and 25 mm in width is cut from the initial 40-mm-width coated conductor. A typical tape is showed in Fig. 5.25(a). From this tape a ring is made with the appropriate diameter. Finally, the resulting HTS ring is placed around the cylindrical stack of annuli with the HTS layer side against the stack. Figures 5.25(b) and (c) respectively show four HTS rings and the assembly of these rings with the stack corresponding to Sample A. The new shield resulting from the assembly of

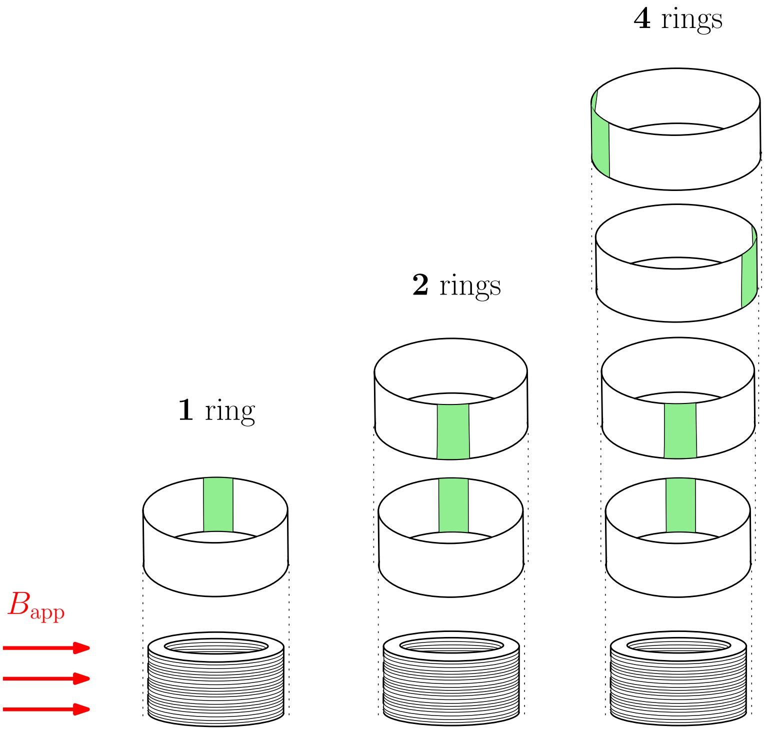

**Figure 5.26:** Illustration of the three investigated configurations with either 1, 2 or 4 HTS rings. The green region is the overlapping area between the two extremities of the tape.

the stack and the rings is studied when the stack is surrounded by either 1, 2 or 4 HTS rings. The shield is submitted to a uniform transverse external field. Special care should be placed on the way the overlap surface area between the two extremities of the tapes is oriented with respect to the direction of the applied flux density. The choice was made to place the rings as illustrated in Fig. 5.26. This figure shows the three studied configurations as well as the orientation of each ring with respect to the applied flux density $B_{\text{app}}$.

Figure 5.27 shows the shielding factor as a function of the applied transverse flux density up to 60 mT. The three assembly configurations (stack of annuli with 1, 2 and 4 rings) are compared to the stack without any ring. Figure 5.27(a) shows that the shielding factor is not influenced by the 4 surrounding rings at room temperature. Indeed, at room temperature only the ferromagnetic substrate can influence the shielding behavior. In the transverse configuration, the additional thickness of ferromagnetic material (FM) brought by the four rings (along the direction of the applied field) is negligible compared to the FM thickness of the initial stack of annuli. Figure 5.27(b) shows that, at 77 K, the HTS rings significantly improve the shielding performance of the stack. In transverse configuration, the external field is normal to the rings surface and macroscopic shielding currents can take place in the HTS layers of the surrounding tapes. We observe that at $B_{\text{app}} = 60$ mT, the shielding factor increases from $SF \approx 1.64$ to $SF \approx 3.66$ by combining the stack to 4 HTS rings. We also observe that the shielding factor decrease with the applied field is almost linear in this field range. The shielding factor values in the very low field range

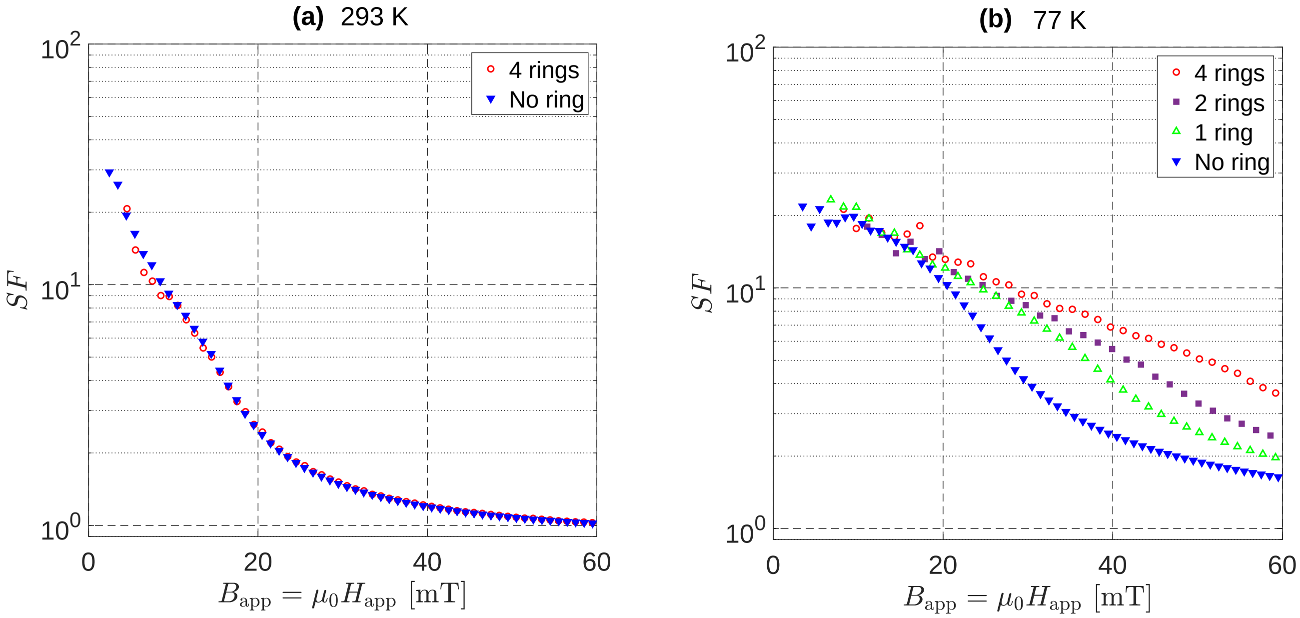

**Figure 5.27:** Shielding factor as a function of the transverse applied flux density for the cylindrical stack corresponding to Sample A surrounded by several numbers of HTS rings. These different configurations are compared to the stack of annuli without any surrounding ring. The results are obtained at (a) room temperature (293 K) and (b) 77 K.

($B < 15$ mT) are similar the those obtained with the stack alone. Finally, as the number of rings decreases, the shielding factor gets closer to the one measured without any ring. Nevertheless, we note that the shielding efficiency is still improved even by combining the stack with only 1 ring, e.g. at $B_{\text{app}} = 30$ mT, the shielding factor is $SF = 7.6$ against $SF = 4$ when no ring is used.

In summary, the concentric HTS rings can significantly improve the shielding factor of the stacks of annuli investigated throughout this chapter. The study could be pursued further by examining the influence of the ring orientation with respect to the applied field. The results displayed in Fig. 5.27 show that it could be possible to further improve the shielding efficiency of the stack by increasing the number of rings or using 'Swiss roll' geometries [251, 252] to reduce the effect of the overlap surface area.

## 5.6 Chapter summary

In this chapter, we first investigated experimentally the ability of a stack of coated conductor (CC) annuli of large bore (26 mm of inner diameter) to shield a magnetic field applied either along the axis of the stack (axial configuration) or perpendicular to it (transverse configuration). The study was carried out on three samples with different heights at both room temperature and 77 K. The CCs combine a Ni-5at.%W substrate and a (RE)BCO superconducting (SC) layer. At room temperature, the results were shown to be in a reasonable agreement with analytical formulae applicable to purely ferromagnetic (FM) cylindrical shields. In particular, the FM material allows for a shielding factor $> 1$ for both directions of applied field. At 77 K, the SC layers mostly contribute to the shielding of the axial component of the applied magnetic field whereas the FM substrates mainly shield the transverse component. Results obtained by numerical models considering a field-dependent magnetic permeability $\mu_r(B)$ were shown to be in very good agreement with experimental results. Magnetic shielding measurements in axial field showed the ability of such stacks to shield magnetic flux densities up to 0.67 T where the shielding factor, decreasing with the applied field, is always $> 3$.

Secondly, we showed how these experimental results could be used to estimate the engineering current density $J_e$ of the coated conductors. The results were almost independent of the aspect ratio of the stack. Numerical modeling of a stack with different aspect ratios showed that at low field, the $SF$ is strongly influenced by the height of the stack, i.e. $SF$ increases from 45 to $> 30000$ when the height is tripled. The practical consequence is that a stack of 72 mm height would be able to maintain a shielding factor exceeding 10 up to 0.93 T at 77 K.

Next, the effect of the critical current density and the magnetic permeability was investigated numerically. The $J_c$ appears to have a finite but very weak effect on the transverse magnetic shielding. On the contrary, it strongly affects the axial shielding factor especially at $B_{app} > 100$ mT. Using a field-dependent $J_c(B)$ allows for a better agreement with the experimental results than a constant $J_c$. An increasing magnetic permeability was shown to be detrimental to the axial magnetic shielding and to improve the transverse shielding. The comparison between the experimental and the numerical results underlines the necessity to take into account the field dependence $\mu_r(B)$.

Finally, ways of improving the shielding efficiency were introduced. First, we investigated the possibility to improve the axial shielding efficiency of the stack of annuli by covering one of the extremities using a superconducting cap. The cap either consisted of a bulk YBCO sample or a stack of HTS tapes. In both cases, the results showed a significant improvement in the shielding efficiency compared to a fully open cylinder. In particular, we showed that using a bulk YBCO cap could increase the axial $SF$ by a factor exceeding 2 for $B_{\mathrm{app}} < 200$ mT and bigger than 3 for $B_{\mathrm{app}} > 200$ mT. We also reproduced successfully the experimental results with a 2D-axisymmetric model considering a field-dependent $J_{\mathrm{c}}(B)$ for the superconducting cap. On the other hand, we demonstrated the possibility to wrap the stack of annuli with 40-mm-width CC tapes to increase the shielding efficiency under a transverse applied field. Doing so, we showed that the $SF$ could be more than doubled under an applied field of 60 mT.

As a conclusion, this chapter gave evidence of the shielding ability of a structure consisting of a stack of CC annuli based on a slightly ferromagnetic substrate, the latter allowing for a finite shielding effect either under a transverse applied field or at a temperature higher than $T_{\mathrm{c}}$, i.e. in experimental conditions where using a stack of SC layers only would not provide any magnetic shielding.

# Chapter 6

# Study of a magnetic screen combining bulk HTS and coated conductor tapes

In this chapter, we investigate the possibility to screen a non-uniform magnetic field by a hybrid structure based on bulk high-temperature superconductors (HTS) and coated conductor (CC) tapes. The possibility of increasing the screened volume using arrays of bulk HTS has already been investigated in previous works [72–74]. However, the non-superconducting gaps between the bulk samples remain an issue. The tapes are arranged as 'eye-shaped' loops around the array of bulk HTS to form the hybrid screen as illustrated in Fig. 6.1.

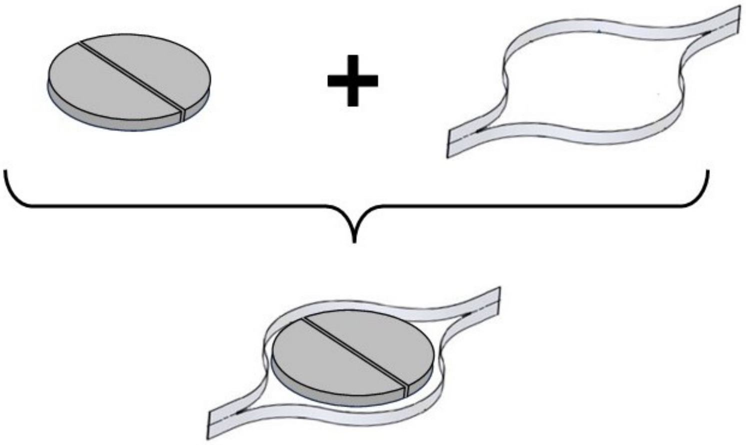

**Figure 6.1:** Schematic illustration of the hybrid magnetic screen combining two bulk HTS separated by a gap with a coated conductor closed loop.

In order to analyze the magnetic flux penetration mechanisms in such structures, this chapter focuses on the elementary structure consisting of two bulk half cylinders, separated by a gap, combined with a stack of closed loops of CC tapes. In order to assess the beneficial effect brought by the CC tapes, the hybrid screen is compared to the screen consisting of bulk samples only. The efficiency of the magnetic screen is characterized in terms of the *screening factor* $SF$. Due to the strong non-uniformity of the field, the screening factor is defined as:

$$SF = \frac{\|\boldsymbol{B}_{\mathbf{app}}\|}{\|\boldsymbol{B}\|} = \frac{\sqrt{B^2_{\text{app},x} + B^2_{\text{app},y} + B^2_{\text{app},z}}}{\sqrt{B^2_x + B^2_y + B^2_z}}. \tag{6.1}$$

Finally the experimental results are compared to finite-element models. A 2D axisymmetric model is used to obtain the parameters characterizing the magnetic field source. A 3D model is then used for the hybrid screen configuration. All finite-element models presented in this chapter are solved using GetDP [189]. The geometries and meshes were generated using Gmsh [190].

## 6.1 Experimental set-up

In this section, we start by giving a general overview of the system designed to carry out magnetic screening measurements. A picture of the measurement system can be seen in Fig. 6.2. It consists of a source of magnetic field fixed below the superconducting screen. The zone highlighted in green in Fig. 6.2 is the region where we aim at reducing the magnetic field. The measurements of the magnetic flux density (with and without screen) are thus performed in this region. The whole experimental system devoted to screening measurements is described in details in Section 3.3.2. During the measurement procedure, the set-up shown in Fig. 6.2 is immersed in liquid nitrogen (77 K). The individual parts of the set-up are described in the following.

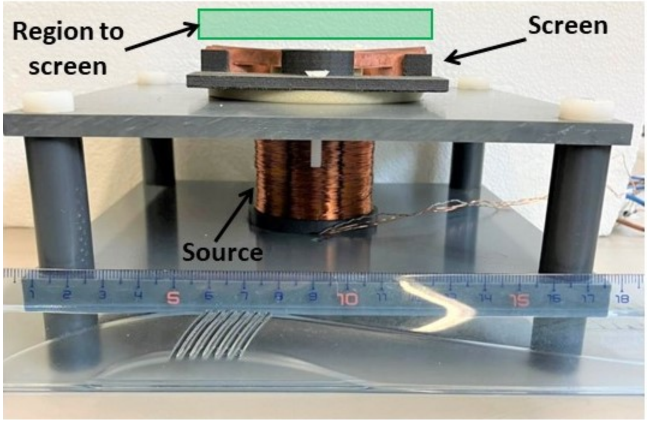

**Figure 6.2:** Experimental system for magnetic screening measurement.

### 6.1.1 Source of magnetic field

The source of magnetic field used in this thesis has already been introduced in Section 3.1.2. In this section, we describe the source in more details and how it is embedded in the experimental set-up investigated in this chapter. The source is a coil based on 4300 turns of 0.3-mm diameter copper wire. In order to increase the amplitude of the applied magnetic flux density, a ferrimagnetic Mn-Zn core is inserted in the coil bore. Pictures of the source coil and the ferrite core can be seen in Fig. 6.3. The core has a length of 41.3 mm and a diameter of 12.3 mm.

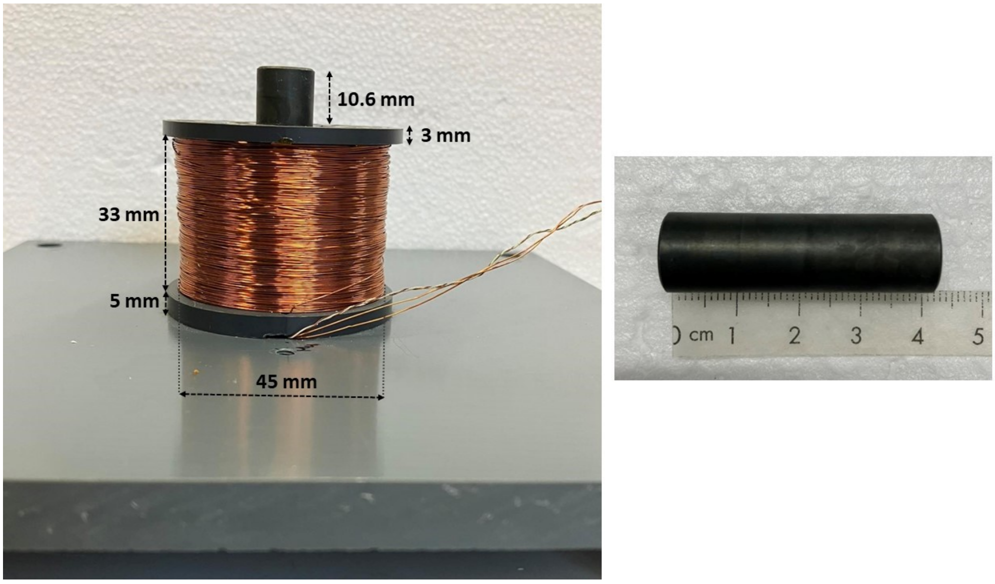

**Figure 6.3:** Picture and dimensions of the magnetic field source (left picture) and the Mn-Zn ferrite core (right picture).

As can be seen in Fig. 6.2, the screen is separated from the coil by a gap. In order to further increase the magnetic flux density, the ferrite core is raised by 10.6 mm from the top extremity of the coil support. Doing so the top end of the core is placed directly at short distance from the screen and the applied field in the screened region is increased. In order to maximize the injected current and avoid overheating of the wire, the coil is operated in liquid nitrogen. A type T (copper-constantan) thermocouple is placed inside the coil to monitor the temperature at the center of the coil during the current injection.

### 6.1.2 Superconducting screen

The magnetic screen investigated in this chapter is based on two bulk GdBCO half cylinders separated by a 1-mm gap. The two bulk samples are surrounded by a stack of 28 coated conductor tapes in closed loop configuration. A picture of the complete 'hybrid' screen can be seen in Fig. 6.4. The superconducting screen is assembled on a Permaglas

M730 sample holder combined with a support made of carbon fiber reinforced polyamide. The individual HTS samples composing the screen are described in more details in the following paragraphs.

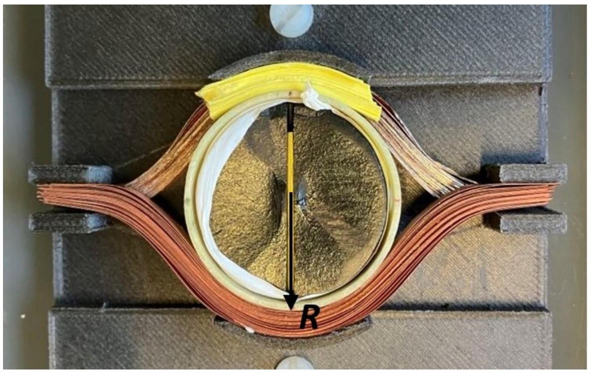

**Figure 6.4:** Picture of the hybrid screen. Two half bulk GdBCO cylinders are surrounded by a stack of 2G CC tapes in closed loop with an opening radius $R = 17.5$ mm.

The two bulk half-cylinders are obtained from the GdBCO sample C001 described and characterized in Section 4.1. This sample has been chosen over the three other cylinders as it exhibits the best superconducting properties ($J_\mathrm{c} \approx 1.99 \times 10^8$ A/m$^2$, $n \approx 36$). In order to obtain the two half-cylinders shown in Fig. 6.4, the GdBCO sample C001 should be cut using a diamond wire saw. This raises the question to determine whether the cut should bisect the facet lines or if it should be made along one of them. The results described in Section 4.1.2 displaying mappings of the trapped flux density over the top and bottom surfaces of cylindrical GdBCO bulk samples indicate the presence of a defect presumably located between two facet lines and impeding the current flow. Therefore, it seems reasonable to perform the cut between these two facet lines, along the possible location of the defect. Moreover, Tutt *et al.* [76] showed that cutting the sample either along the facet lines or bisecting them has a limited effect on the superconducting properties. A picture showing the cut direction of the sample C001 is shown in Fig. 6.5.

In order to obtain the coated conductor loops surrounding the bulk GdBCO samples, we used 28 tapes from Shangai Superconductor® in which a slit has been milled along the centerline. These tapes have a length of 92 mm and a width of 10 mm. They are based on a Hastelloy® substrate and have a total thickness of 90 $\mu$m. The approximate thickness of the HTS layer is 1 $\mu$m. The critical current of the coated conductor in 'eye-shaped' loop configuration has been estimated from measurements of the trapped flux density after field cooled magnetization [253]. On average, the critical current in a single loop can be estimated as $I_\mathrm{c} \approx 150$ A. Considering the dimensions of the coated conductors, we can

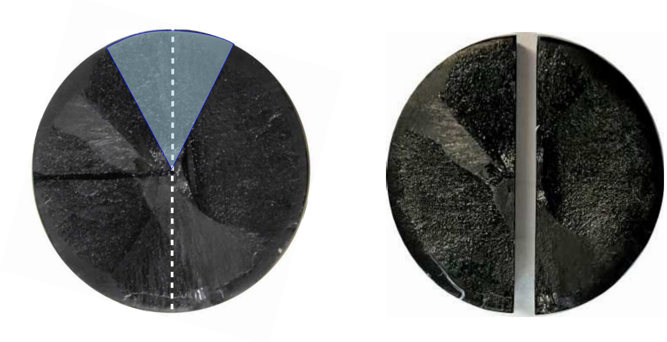

Figure 6.5: Pictures of the plain C001 GdBCO bulk cylinder (left) and the bulk cylinder after cut. The blue zone on the left picture shows the possible location of the macroscopic defect described in Section 4.1.2. The white dashed line shows the cut direction.

estimate the engineering current density,

$$J_\mathrm{e} \approx \frac{150}{5\ 10^{-3} \times 90\ 10^{-6}} \approx 3.33 \times 10^{8} \quad \mathrm{A/m^2} \tag{6.2}$$

Then, the 28 tapes were stacked together. A picture with the dimensions of a single tape is shown in Fig. 6.6. As detailed in [60], the length of the slit is given by

$$L_\mathrm{slit} = \frac{4\pi}{3} R \approx 72 \text{ mm}. \tag{6.3}$$

Where $R$ is the opening radius shown in Fig. 6.4. Here, we neglect the difference between the outer and inner radius of the stack. As a result, all the tapes are milled with a 72 mm central slit.

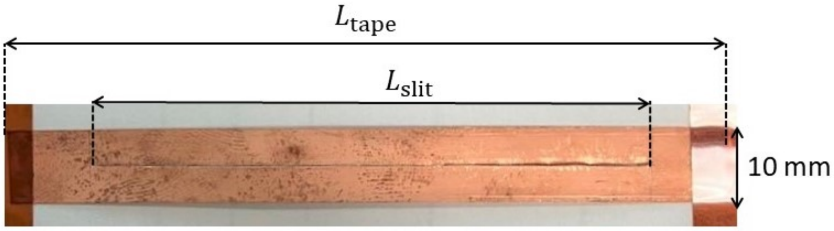

Figure 6.6: Picture and dimensions of a single slitted CC tape. The total length of each tape is $L_\mathrm{tape} \approx 92$ mm and the length of the central slit is $L_\mathrm{slit} \approx 72$ mm.

## 6.2 Numerical modeling

In this section, we introduce the numerical models used to address the problem of magnetic screening combining bulk high-temperature superconductors with coated conductor tapes. In particular, the model is made of several parts: the magnetic field source and the superconducting screen based on CC tapes and bulk samples. The whole problem geometry needs to be tackled using a 3D model. The magnetic source is characterized by the unknown permeability of the core which needs to be tuned to obtain a good fit with the measurement data. Because 3D models are usually time consuming, the set of parameters characterizing the source is estimated using a 2D-axisymmetric model. This model is also suitable to estimate the screening behavior of a plain bulk cylinder alone and assess the influence of the structural inhomogeneities observed in Section 4.1.2. Finally we introduce the 3D model of the whole structure. The value of the permeability is validated by verifying that it leads to similar results of applied flux density when moving from the 2D-axisymmetric case to a 3D model.

### 6.2.1 2D-axisymmetric model

In order to model the hybrid screen in 3D, we need to estimate the best value for the permeability of the core to model the source of magnetic field. As a reminder, the source is a copper coil with a ferrite core. A 2D-axisymmetric model is well suited to model this kind of geometry. Then, the axisymmetric model can be used to estimate the screening efficiency of the plain bulk sample C001 (before doing the cut). In the numerical models used in this work, the coil domain is characterized by its maximal current $I_{\max}$ and the number of turns $N$. In this case, $I_{\max}$ is fixed at 0.5 A and $N$ is set at 4300 (number of turns in the actual coil). The core domain is approximated as a ferromagnetic domain with a constant relative permeability $\mu_{\mathrm{r,core}}$. The modeling results for the applied magnetic flux density are compared to experimental measurements. In the model, the maximal current $I_{\max}$ as well as the number of turns $N$ are kept unchanged. In practice, besides the magnetic permeability, the diameters of the coil and the core are slightly tuned in order to obtain a good fit between the numerical results and the experimental data.

A schematic illustration of the 2D-axisymmetric model is shown in Fig. 6.7. The dimensions indicated in this figure are the final dimensions obtained by fitting the numerical results with the experimental data. In order to avoid the issue regarding the multiply connected region defined by the winding domain, the model is solved with an $A$-formulation. The graphs plotted in Fig. 6.8 show the flux density above the top surface of the source obtained with the 2D-axisymmetric model compared to the experimental data. The numerical results are obtained for $N = 4300$ turns and a constant core permeability of $\mu_{\mathrm{r,core}} = 43$. The experimental data were obtained using the $z$-axis of the Arepoc® Axis-

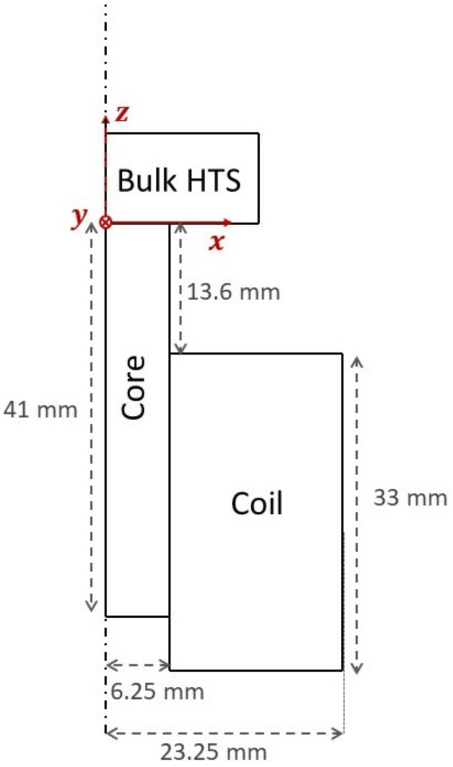

**Figure 6.7:** Illustration of the 2D-axisymmetric model which consists of the magnetic source (with the final dimensions) and the plain bulk HTS cylinder (sample C001).

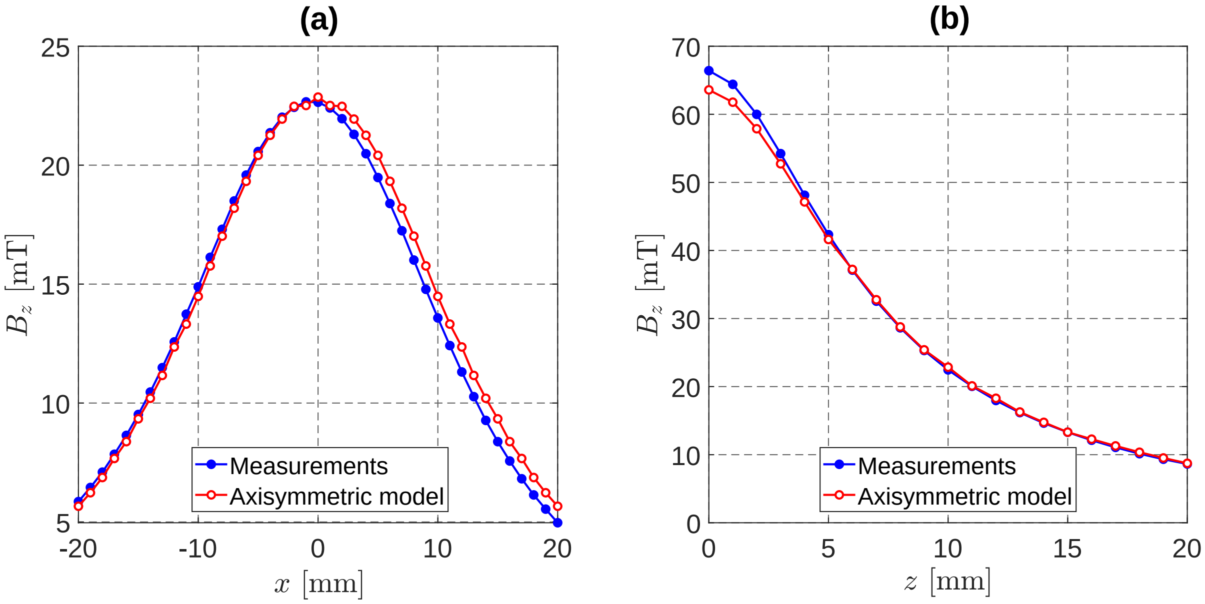

**Figure 6.8:** Magnetic flux density ($z$-component) obtained above the top surface of the magnetic source (without superconducting material). The experimental measurements are compared with the 2D-axisymmetric modeling results. The flux density is plotted over (a) the $x$-coordinate ($y = 0$) at $z = 10$ mm and (b) the $z$-coordinate at the central position ($(x, y) = (0, 0)$). The measurements are performed at a temperature of 77 K for an injected current of 0.5 A.

3S Hall probe (b) described in Section 3.2.1. The measurements were performed in liquid nitrogen and the coil was supplied with a injected current of 0.5 A. Figure 6.8(a) shows the flux density as a function of the $x$-coordinate at $y = 0$ and $z = 10$ mm. Figure 6.8(b) shows the magnetic flux density as a function of the $z$-coordinate at $(x, y) = (0, 0)$. The set of parameters as well as the geometrical dimensions specified in Fig. 6.7 leads to a very good match between measurement data and modeling results.

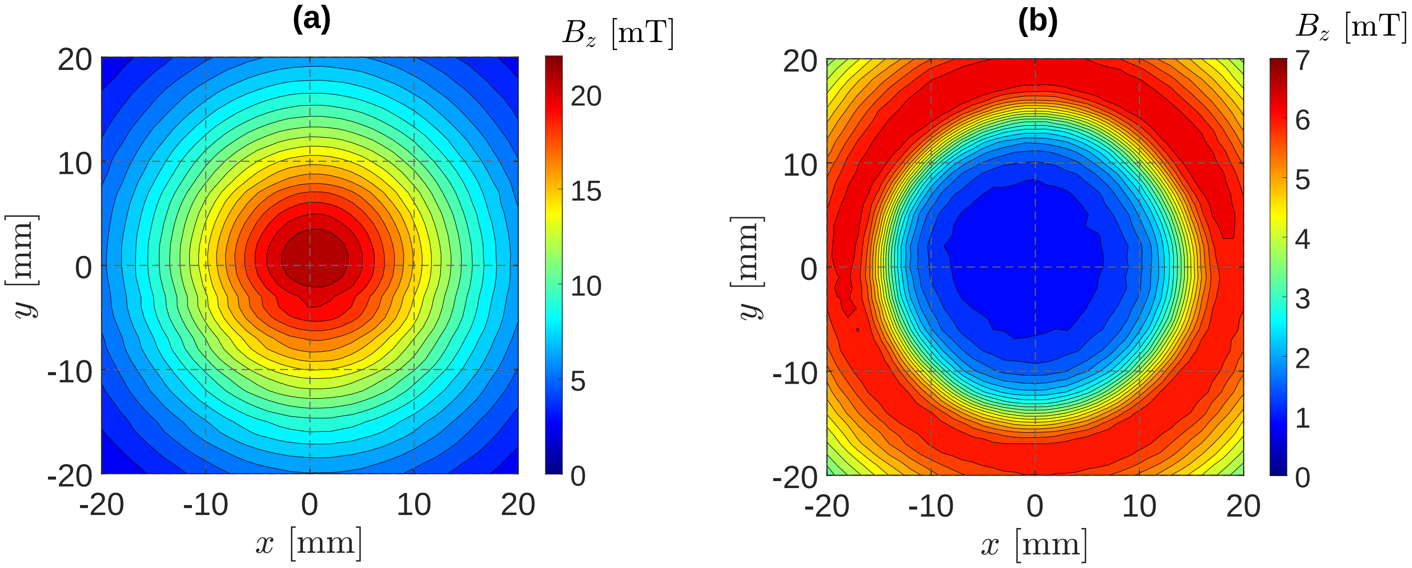

**Figure 6.9:** Mapping of the $z$-component of the magnetic flux density recorded at 3 mm above the bulk top surface area at 77 K. (a) Applied magnetic flux density (measured without superconducting sample) and (b) flux density measured with the presence of bulk HTS cylinder. The coil is fed with an injected current of 0.5 A.

Now that the source parameters and dimensions are properly set, the 2D-axisymmetric model can be used to estimate the screening efficiency of a plain bulk cylinder (sample C001) and compare the results with experimental measurements. Figure 6.9 shows mappings of the $z$-component of the magnetic flux density recorded at approximately 3 mm above the bulk sample. Figure 6.9(a) displays a mapping of the applied flux density recorded without bulk superconductor and Fig. 6.9(b) shows a mapping of the flux density recorded in the presence of the plain bulk cylinder. The mappings were obtained in liquid nitrogen for an injected current of 0.5 A in the source coil. As a reminder, the trapped field characterization of the bulk cylinder C001 presented in Section 4.1.2 showed the strongly inhomogeneous superconducting properties of this sample. Moreover, these mappings highlighted a structural defect impeding the current flow in the cylinder. The results presented in Fig. 6.9 show that such a structural defect does not seem to affect

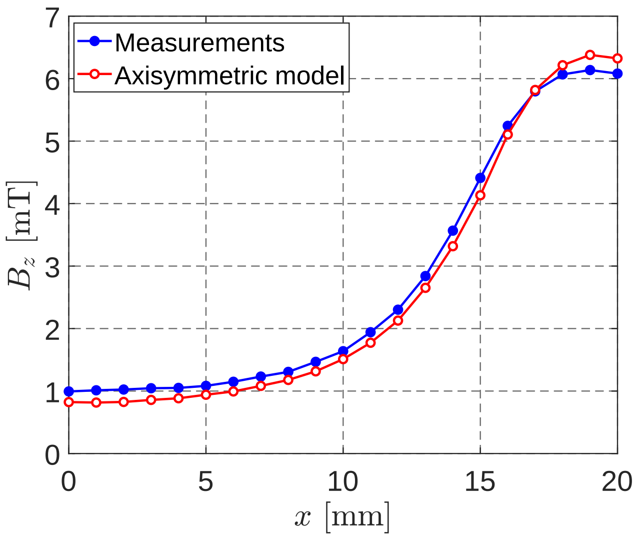

**Figure 6.10:** Magnetic flux density ($z$-component) measured at 3 mm above the bulk surface area as a function of $x$ ($y = 0$) compared to the axisymmetric modeling results. The source coil is supplied with an injected current of 0.5 A. The results are obtained at 77 K.

the homogeneity of the screened flux density measured over the sample. The screened flux density recorded as a function of $x$ at $y = 0$ is plotted in Fig. 6.10. The figure compares the measurement results with those obtained with the 2D-axisymmetric model. The bulk sample is modeled considering field-independent superconducting properties ($J_c = 1.99 \times 10^8$ A/m$^2$ and $n = 36$). The modeling results are in a good agreement with the experimental results.

### 6.2.2 3D model

The whole problem geometry consisting of two half bulk cylinders, the 'eye-shaped' stack of tapes and the magnetic field source should be tackled using a 3D model. The model is implemented using the 'Life-HTS' toolkit[1]. In this model, the layered structure of the stack of CC tapes is replaced by a homogeneous superconducting material characterized by an engineering current density $J_e$. A schematic illustration of the 3D model geometry can be seen in Fig. 6.11. In order to increase the symmetry and decrease the computation time, the model neglects the offset between the two legs of the tapes and suppose a symmetrical structure with respect to the $x$-axis. Moreover, the model assumes the tapes as being centered with respect to the bulk samples. Finally, only a quarter of the structure is modeled. The two half bulk cylinders are separated by a gap of 1 mm. The stack of tapes is characterized by an opening radius $R = 17.5$ mm as well as the values $X_{\text{slit}}$ and

---

[1] Life-HTS: Liege university finite element models for high-temperature superconductors (available at https://www.life-hts.uliege.be/)

$X_{\text{tape}} = X_{\text{slit}} + 10$ mm as illustrated in Fig. 6.11. We have,

$$X_{\text{slit}} = 2R \sin \pi/3 = \sqrt{3}\ R. \tag{6.4}$$

As described in Section 4.1.1, the bulk samples are characterized by a critical current density $J_c \approx 1.99 \times 10^8$ A/m$^2$. The stack of the tapes is characterized by the engineering current density given by Eq. (6.2). Both $J_c$ and $J_e$ are assumed to be field-independent.

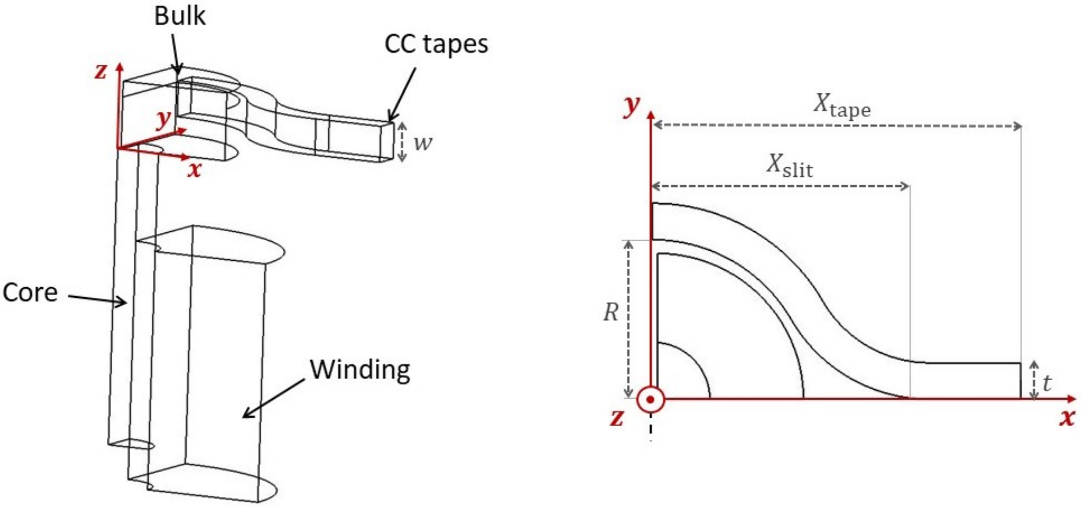

**Figure 6.11:** Illustration of the 3D model which consists of the magnetic source, the cut bulk HTS cylinder (sample C001) and the stack of CC tapes. The figure displays a 3D view of the model (left) and a view from the top (right).

In order to model the applied flux density, the parameters (i.e. the permeability as well as the diameters of the core and the coil) for the source estimated in the previous section from the 2D-axisymmetric model are used in the 3D model. The 3D model is solved using a $H$-$\phi$-formulation. In order to validate this set of parameters used for the 3D model, the applied field computed using this model should coincide with the results obtained using the axisymmetric model. A comparison of the $z$-component of the applied flux density obtained using the 3D model and the axisymmetric model is shown in Fig. 6.12. The results are obtained in the absence of superconducting material. In Fig. 6.12(a), the applied flux density evaluated at 10 mm from the core top surface is plotted as a function of $x$ ($y = 0$). The applied flux density evaluated at the central position ($(x, y) = (0, 0)$) is plotted as a function of the $z$-coordinate in Fig. 6.12(b). The results show a very good agreement between the 2D-axisymmetric model ($A$-formulation) and the 3D model ($H$-$\phi$-formulation).

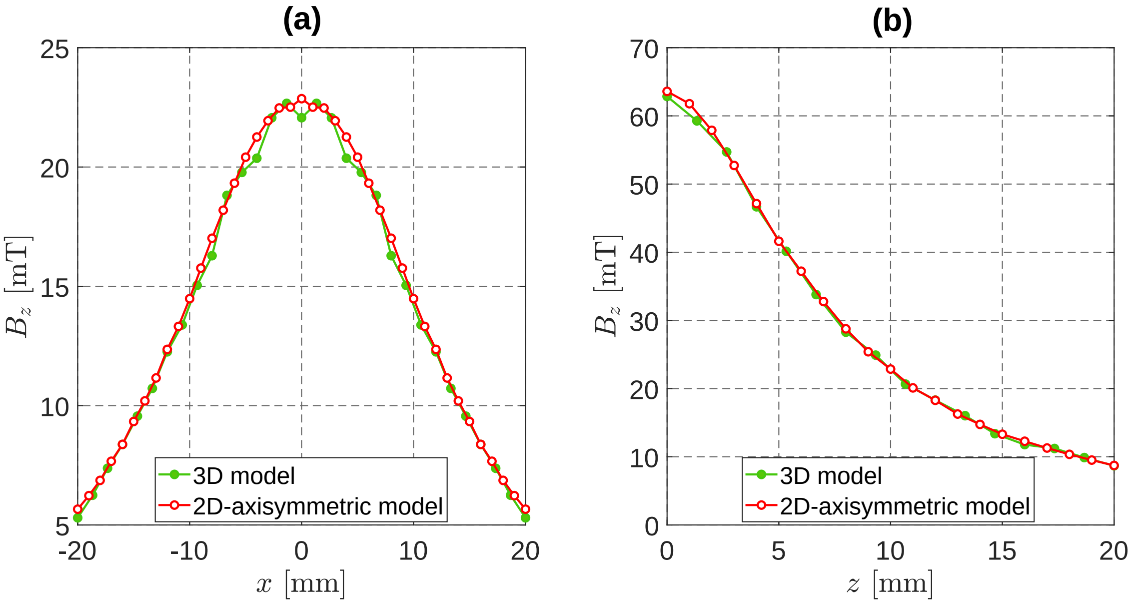

**Figure 6.12:** Magnetic flux density ($z$-component) obtained above the top surface of the magnetic source (without superconducting material). The results obtained with the 3D model are compared to those obtained with the axisymmetric model. The same parameters and dimensions are used for both models. The flux density is plotted over (a) the $x$-coordinate ($y = 0$) at $z = 10$ mm and (b) the $z$-coordinate at the central position ($(x, y) = (0, 0)$). The results are obtained for an injected current of 0.5 A.

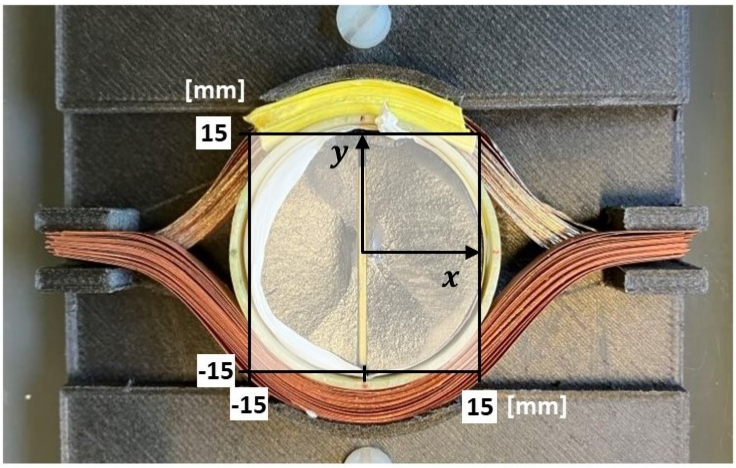

**Figure 6.13:** Photograph of the hybrid screen together with the reference axis system. The white square represents the surface area over which the 2D mappings are recorded.

## 6.3 Results and discussion

In this section, we present and discuss the screening behavior results of the hybrid (bulks + tapes) structure, in particular 2D mappings of the magnetic flux density over a surface of $30 \times 30$ mm$^2$. The measurements are obtained at approximately 3 mm above the bulk samples top surface (corresponding to $\approx 12.4$ mm above the core top surface) using the homemade 3-axis Hall probe set-up described in Section 3.2.1. Figure 6.13 shows a picture of the hybrid screen together with the axis system $(x, y)$ which serves as reference for all the results presented in this section. The figure also shows the surface area (white square) over which the mappings are recorded. These experimental results will be compared with the 3D model previously introduced.

### 6.3.1 Efficiency of a hybrid screen

In order to investigate the screening efficiency, the measurement procedure is based on two steps. The first step consists in measuring the applied flux density: the current is injected in the source coil and the flux density is measured without the screen. The second step consists in measuring the flux density screened by the superconductors: when the injected current is zero, the screen is placed next to the source. Then, the current is injected in the coil at a given sweep rate $dI/dt$. The flux density measurement is then carried out at the exact same location as during the first step. In order to avoid any movement or deformation of the sample holders between step one and step two, the operating temperature is kept constant for the entire measurement procedure.

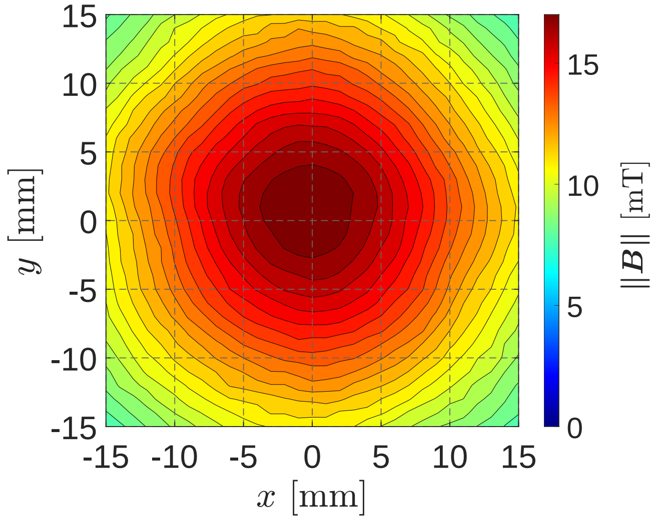

**Figure 6.14:** Mapping of the norm of the magnetic flux density without superconducting screen. The mapping is recorded at 12.4 mm above the core top surface. The coil is supplied with an injected current of 0.5 A and the operating temperature is 77 K.

We first examine the screening efficiency when the source coil is supplied with a constant injected current of 0.5 A. A mapping of the applied flux density is displayed in Fig. 6.14. For this injected current, the applied applied flux density can reach a magnitude up to 17.5 mT at the center of the screen. Figure 6.15 shows mappings of the flux density magnitude under the presence of the superconducting screen. The mapping shown at the left of this figure is recorded when the screen consists of two bulk half cylinders only. The mapping at the right is recorded for the hybrid screen (two bulks + stack of tapes).

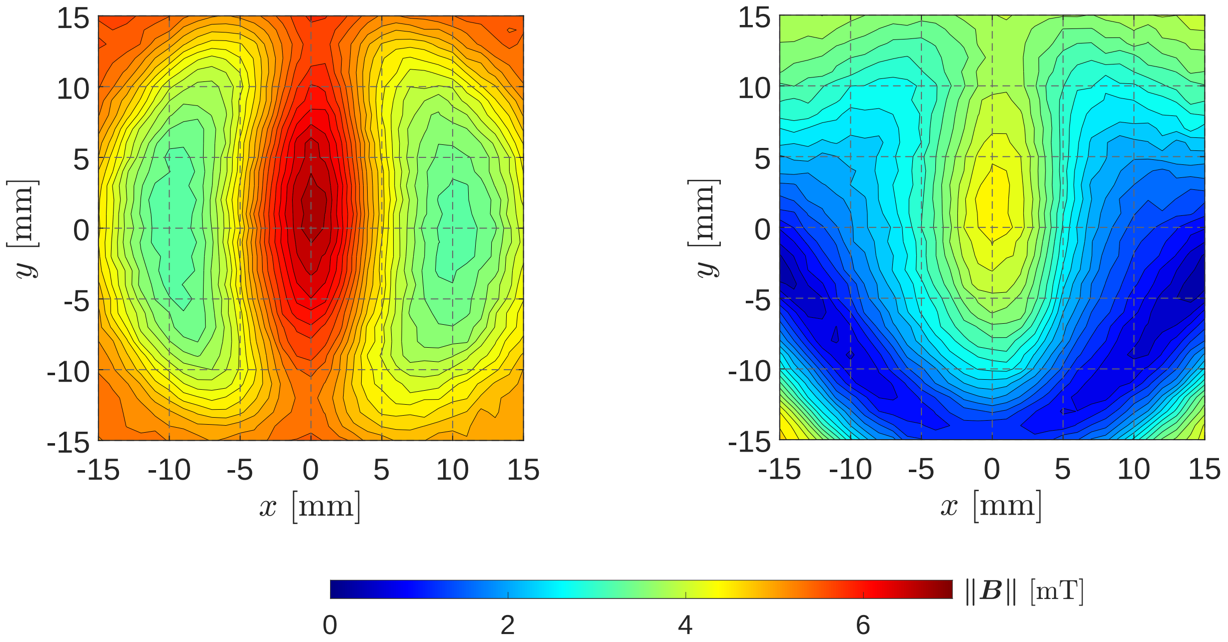

**Figure 6.15:** Mapping of the norm of the magnetic flux density when the screen consists of two bulks only (left) or two bulks with the tapes (right). The mapping is recorded at 12.4 mm above the core top surface area, corresponding to approximately 3 mm above the top surface of the bulk samples. The coil is supplied with an injected current of 0.5 A ($dI/dt \approx 50$ mA/s) and the operating temperature is 77 K.

The first observation is that in both cases, the magnitude of the flux density is globally reduced which is an evident consequence of a finite screening effect. In the case of a magnetic screen based on two bulks only, the flux density concentrates in the central region, showing an important flux leakage through the gap between the two half cylinders. The effect of the gap is also clearly visible for the hybrid screen but the magnitude of the flux leakage is nevertheless significantly reduced. Another conclusion that can be drawn from Fig. 6.15 is the asymmetry in the screening ability of the hybrid screen. The screening is much more efficient in the zone of negative $y$ than in the zone of positive $y$. Indeed, in the case of a hybrid screen, the screening effect is enhanced due to the additional screening currents flowing in the ‘eye-shaped’ loops characterized by an effect between the two legs of tapes. If we compare the right mapping of Fig. 6.15 to the picture in Fig. 6.13, the zone of negative $y$ corresponds to the upper leg region of the slitted tapes. This leg being closer to the measurement surface area, the screening currents result in a more attenuated flux density.

In order to compare measurements data to the results obtained by the 3D model introduced in Section 6.2.2, the screening factor is examined along two specific lines. Figure 6.16 compares the screening factor values in the case of a hybrid screen or a screen

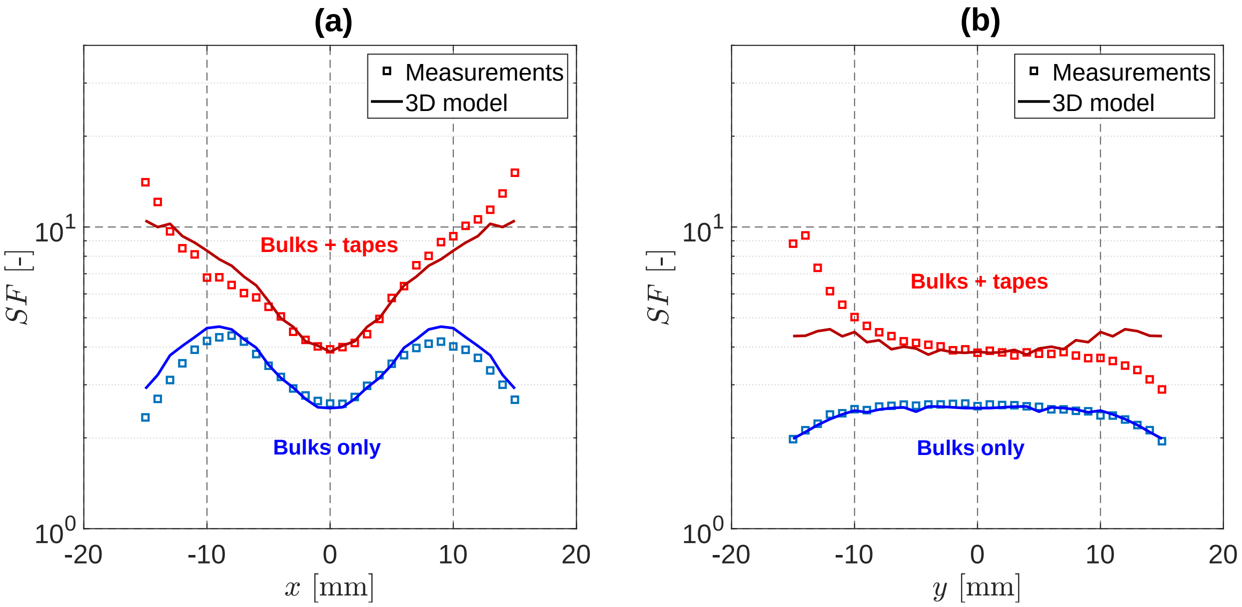

**Figure 6.16:** (a) Screening factor as a function of $x$ at $y = 0$ and (b) as a function of $y$ at $x = 0$. The screen is either hybrid (red) or made of two bulks only (blue). The measurement results are compared to the 3D model results. The injected current is 0.5 A ($dI/dt \approx 50$ mA/s) and the operating temperature is 77 K.

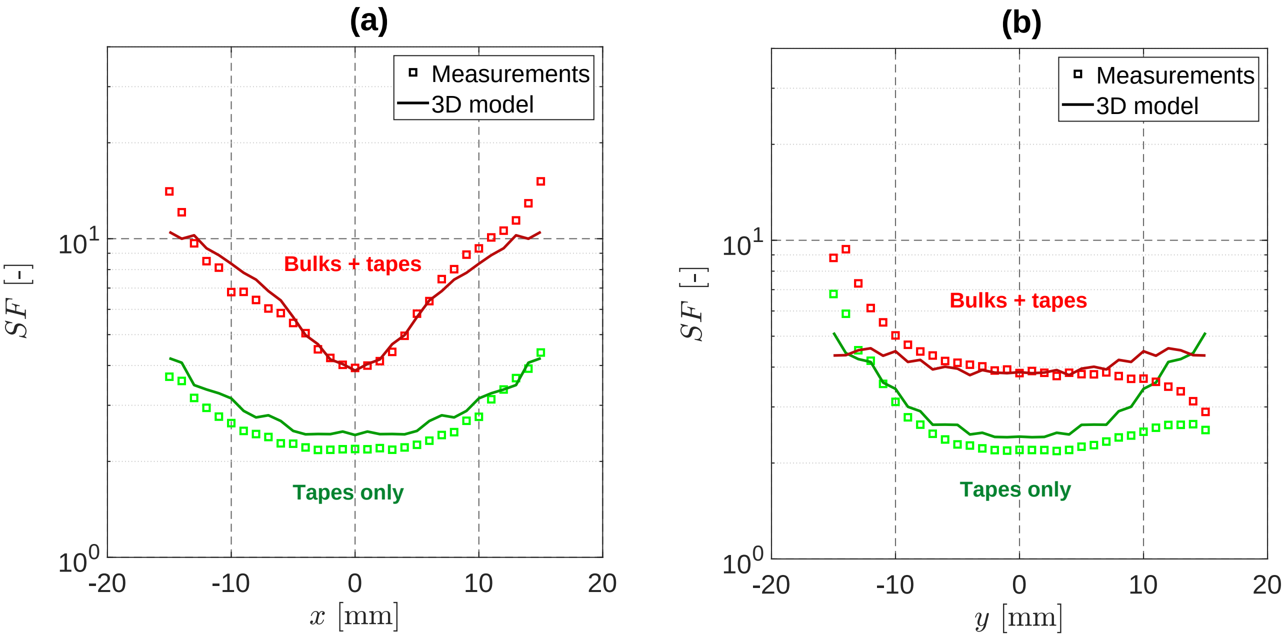

**Figure 6.17:** (a) Screening factor as a function of $x$ at $y = 0$ and (b) as a function of $y$ at $x = 0$. The screen is either hybrid (red) or made of CC tapes only (green). The measurement results are compared to the 3D model results. The injected current is 0.5 A ($dI/dt \approx 50$ mA/s) and the operating temperature is 77 K.

made of two bulks only. Figure 6.16(a) plots the $x$-dependence of $SF$ along the $y = 0$ line and Fig. 6.16(b) plots the $y$-dependence of $SF$ along the $x = 0$ line (along the gap between the two bulk samples). When looking at the blue curves in Fig. 6.16(a), the flux leakage through the gap clearly appears as a drop in the screening factor when approaching $x = 0$. The red curves show that the hybrid screen exhibits a similar behavior but with increased values of screening factor. For instance, at the central position, the screening factor value is $SF \approx 2.6$ for the bulk samples only and $SF \approx 3.93$ for the hybrid screen which represents an approximate increase of 51 %. Another interesting observation, is the fact that the screen made of bulks only exhibits a maximum in $SF$ curve around $x = \pm 8$ mm before following a rapid drop when approaching the extremities of the bulk samples. This was expected as $x = \pm 8$ mm correspond to the centers of the two half cylindrical bulks. The hybrid screen exhibits a minimum in the $SF$ curve at the location of the gap and then increases monotonously towards the extremities. Figure 6.16(a) also shows a good agreement between the modeling and experimental results. The 3D model nicely reproduces the screening behavior along the $x$-axis in both cases. Figure 6.16(b) shows that the agreement is still very good along the $y$-axis for the screen made of bulks only. For the hybrid structure, the 3D model properly reproduces the $SF$ value around $y = 0$ but the modeled results progressively differ from the measurement data as we move away from the center. This is because the model neglects the offset between the two legs of the tapes and assumes a perfectly symmetric geometry with respect to the $x$-axis. The region $y < 0$, corresponds the the top leg side and the measured screening factor is bigger than that predicted by the model. The opposite behavior is observed for the region $y > 0$. In order to distinguish the influence of the bulk materials from the tapes, Fig. 6.17 shows the same measurement than Fig. 6.16 but comparing the hybrid screen to the screen based on 'eye-shaped' tapes only. Again, the model reproduces properly the behavior along the $x$-axis. Along the $y$-axis the model differs from the experimental measurements as it neglects the offset between the legs. The experimental results plotted in Fig. 6.17(b) shows that when approaching the extremities of the gap, the influence of the bulk samples is limited and the behavior of the hybrid screen tends to that of a screen only made of CC tapes.

### 6.3.2 Field dependence of the screening factor

The results presented in the previous section consider the screening efficiency when the current injected in the coil (and so the applied field) is kept constant. It is of interest to analyze the field dependence of the screening factor of the hybrid structure. To do so, we perform measurements at four points of interest above the screen. The measurements are recorded for both the hybrid structure and a screen made of bulks only. Figure 6.18 shows the screening factor as a function of the applied flux density at the 4 points of coordinates $(x, y)$. We stress here that the applied flux density $\|\boldsymbol{B}_{\mathbf{app}}\|$ is the one measured in the absence of superconducting screen. The coordinates system is the one described in Fig. 6.13. The source coil is fed with a current increasing from 0 up 0.8 A. We allow a maximal current value higher than in the previous section as the measurement time is

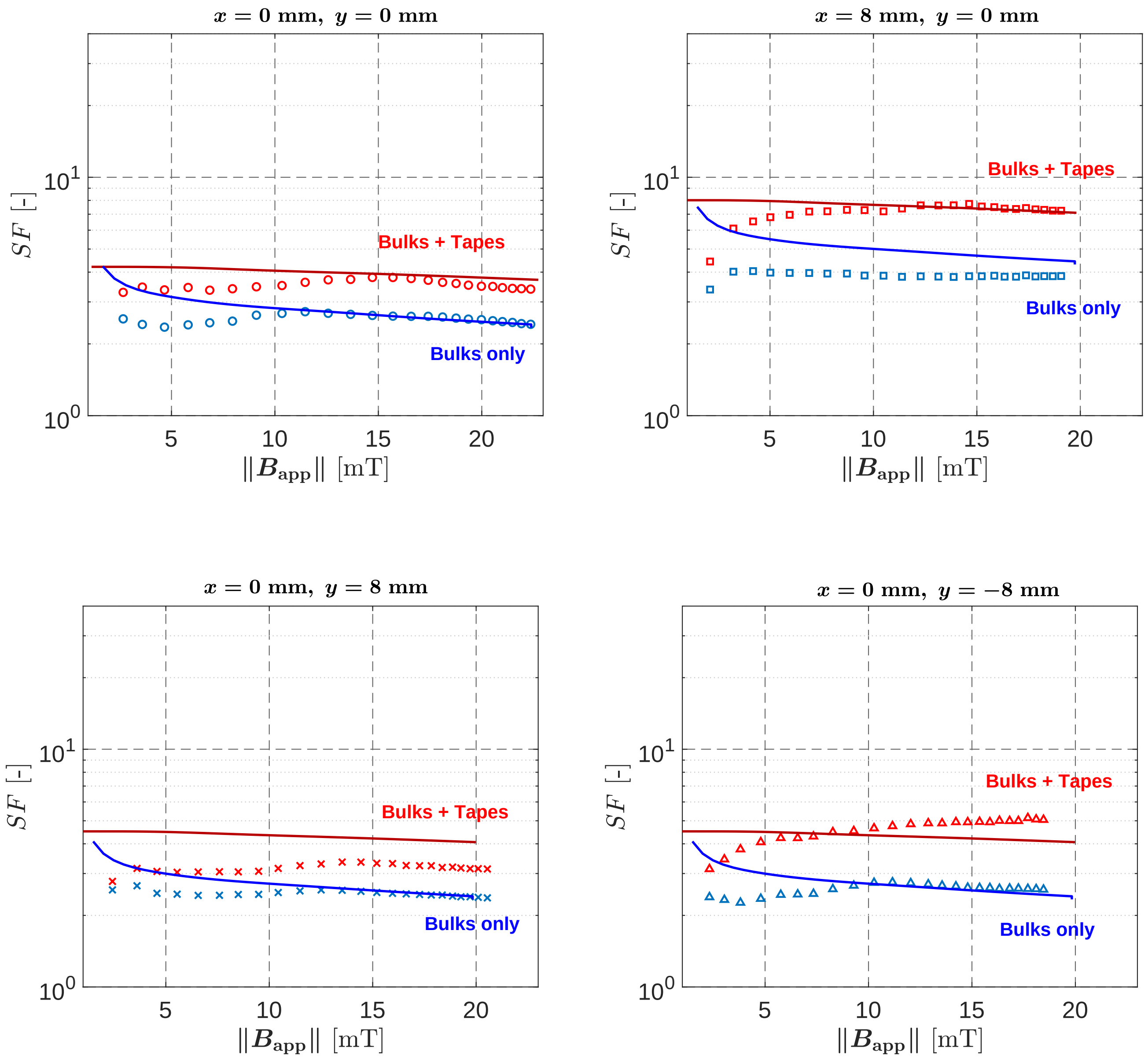

**Figure 6.18:** Field dependence of the screening factor evaluated at different locations of the screen. The measurements are obtained at approximately 3 mm above the bulks top surface. The hybrid screen is compared to the screen made of bulk samples only. The $(x, y)$-coordinates system is displayed in Fig. 6.13. The operating temperature is 77 K. The experimental data (symbols) are compared to the modeling results (solid lines).

much lower than recording a whole $x - y$ mapping. The main conclusion that can be draw from the graphs displayed in Fig. 6.18 is that the screening factor is weakly field-dependent in the range $0 - 20$ mT. When comparing the experimental results to the 3D model for the screen made of bulk samples, the $SF$ values are correctly reproduced except in the very low field region ($\|\boldsymbol{B}_{\text{app}}\| < 5$ mT) where the model systematically overestimates the experimental $SF$. Globally, for the bulks only, the 3D model predicts a short drop up to 5 mT and then a monotonic decrease up to 20 mT. Experimentally, this decreasing behavior is not observed. Overall, the graphs show that the model globally overestimates the $SF$ values in the full range of flux density. This is possibly due to the fact that the critical current density used for the bulk samples in the 3D model overestimates the actual one. Indeed, the value of $J_\mathrm{c}$ may have been degraded during the cutting process. Except for the range $\|\boldsymbol{B}_\mathbf{app}\| < 5$ mT, the $SF$ values obtained by the 3D model in the case of a hybrid screen are in a good agreement with the experimental measurements along the $y = 0$ line. The two bottom graphs show that when $y \neq 0$, the modeling results differ from the experimental observations for the reasons already mentioned in the previous section.

### 6.3.3 Influence of $J_\mathrm{c}$ and the number of tapes on the screening efficiency

The improvement of the screening effect following the combination of bulk HTS samples with closed loops CC tapes is due to the additional screening current flowing in the tapes under an external applied field. Basically, the stack of tapes is characterized by two parameters: the critical current density of the individual tapes and the number of tapes constituting the stack. In this section, we investigate numerically the influence of both parameters on the screening efficiency using the 3D model introduced and validated in Section 6.2.2. As was concluded in the previous sections, we focus here on the screening factor predicted along the $x$-axis ($y = 0$) for which the model reproduces properly the experimental data displayed in Fig. 6.13. The screening efficiency is evaluated in terms of the engineering current density $J_\mathrm{e}$. The influence of the number of tapes is examined in terms of the thickness $t$ of the stack of tapes. The screening factor is plotted as a function of $x$ in Fig. 6.19 for different values of engineering current densities keeping the geometry unchanged (Fig. 6.19(a)) and for different values of stack of tapes thickness $t$ with a constant engineering current density of $J_\mathrm{e} = 3.33 \times 10^8$ A/m$^2$ (Fig. 6.19(b)).

The results plotted in Fig. 6.19(a) are obtained for an injected current in the source coil of 0.5 A. Under these conditions, the value of the engineering current density of the stack of tapes has a very weak influence on the screening factor in the range $J_\mathrm{e} = 0.5 \times 10^8$ A/m$^2$ to $J_\mathrm{e} = 4.5 \times 10^8$ A/m$^2$. The screening factor starts to decrease very slightly and mainly at the extremities of the screen for $J_\mathrm{e} = 0.5 \times 10^8$ A/m$^2$. The results plotted in Fig. 6.19(b) show that considering a constant critical current density, the thickness of the stack of tapes and thus the number tapes may affect the screening efficiency of the hybrid screen. In particular, we observe that decreasing the thickness $t$ from 4 mm to 2 mm significantly reduces the screening effect at the extremities of the screen. In order to explain the very low influence of the engineering current density on the screening effect observed in Fig. 6.19(a), we can look at the induced current in the stack of tapes for each $J_\mathrm{e}$

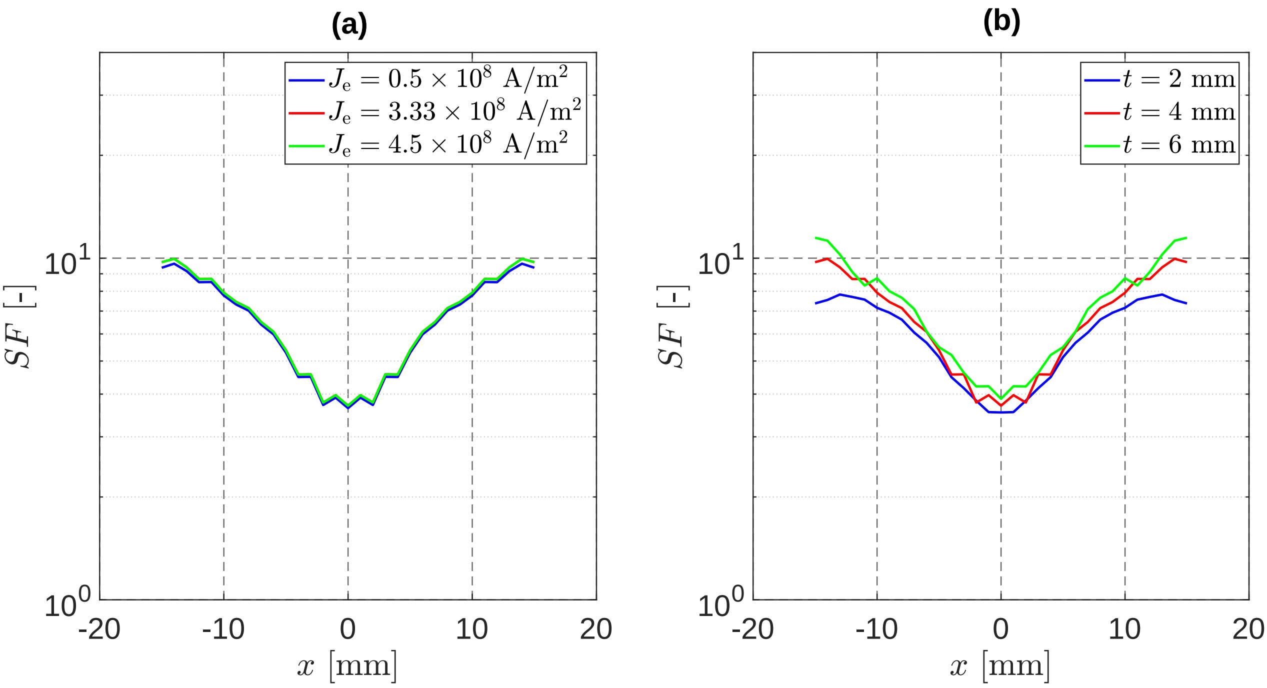

**Figure 6.19:** Modeling results of the screening factor as a function of $x$ ($y = 0$). The $SF$ is plotted (a) for different values of engineering current density and (b) for different thickness of stack of tapes. The results are shown for an injected current of 0.5 A in the source coil. The results plotted in the figure (a) are obtained for a thickness $t = 4$ mm. The results plotted in the figure (b) are obtained for $J_e = 3.33 \times 10^8$ A/m$^2$.

value. Figure 6.20 shows the current density distribution in the stack of tapes for the three investigated $J_e$. From this figure, we can conclude that for $J_e = 4.5 \times 10^8$ A/m$^2$ and $J_e = 3.33 \times 10^8$ A/m$^2$, the screening current density distribution is the same and exhibits a maximum magnitude of $\|\boldsymbol{J}\| \approx 1.4 \times 10^8$ A/m$^2$. However, when the value of $J_e$ is reduced to $0.5 \times 10^8$ A/m$^2$, the maximal value of the screening current is $\|\boldsymbol{J}\| \approx 4.1 \times 10^7$ A/m$^2$. Interestingly, the maximum screening current induced in the superconducting material seems mainly related to the geometry investigated and the applied flux density considered; this maximal screening current density is lower than the engineering current density. Under these conditions, using tapes with a better critical current density will not enhance the screening efficiency. However, when $J_e$ is reduced to $0.5 \times 10^8$ A/m$^2$, the magnitude of screening current is now limited by the low $J_e$ value and the screening effect will be degraded.

As a conclusion, in the range of applied field values considered in this chapter, the screening efficiency of the hybrid structure combining bulk HTS samples with a stack of CC tapes appears to be very weakly affected by the critical current density of the coated conductors. The screening effect seems to be mainly dependent on the geometrical parameters of the tapes. In the geometry investigated, it is worth mentioning that most of the screening effect comes from the bulk HTS samples.

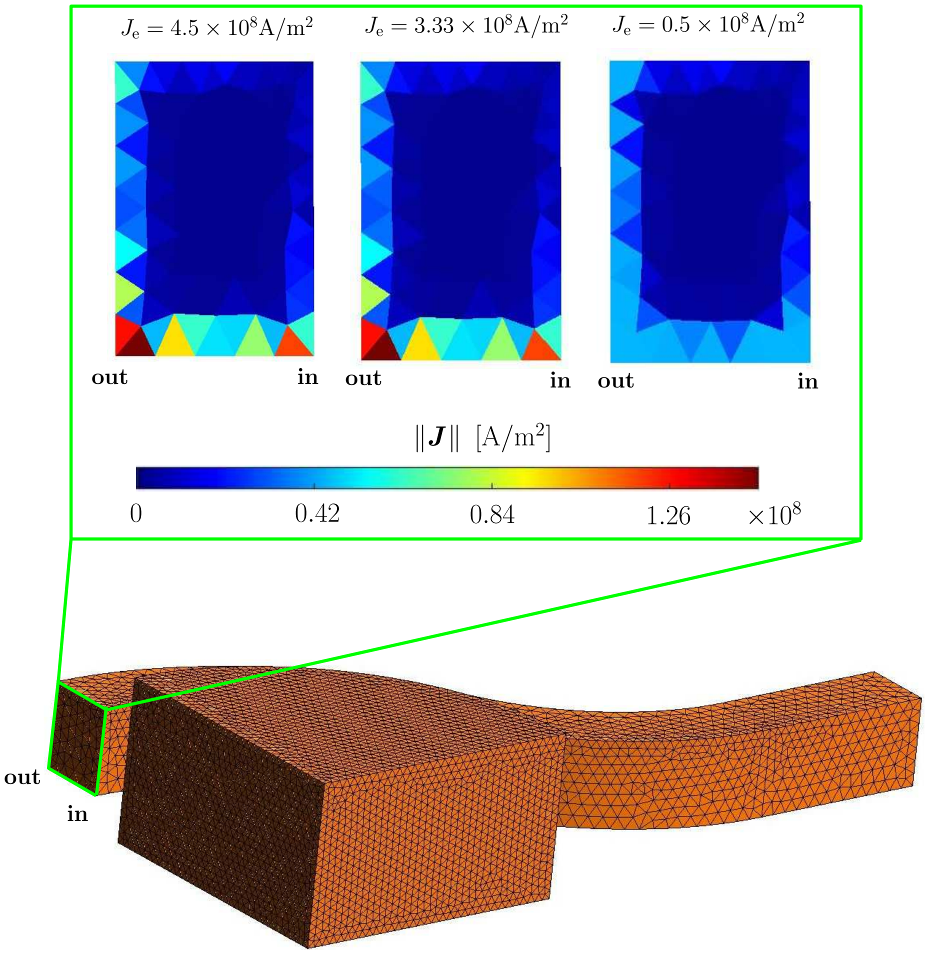

**Figure 6.20:** Screening currents distribution in the stack of tapes for different values of $J_e$. The screening currents distribution are displayed in the plane delimited by the green frame.

## 6.4 Chapter summary

In this chapter, we investigated the possibility to screen a non-uniform magnetic flux density by a hybrid structure combining bulk HTS and CC tapes. The magnetic screen was based on two single grain bulk GdBCO half cylinders surrounded by a stack of CC tapes in 'eye-shaped' loops configuration. The screening efficiency was estimated in terms of the screening factor $SF$ defined as the ratio between the norm of the applied flux density (measured in the absence of superconducting screen) and the norm of the flux density measured under the presence of the magnetic screen.

Experimentally, we observed a finite screening effect ($SF > 1$) in the case of a screen based on bulk HTS samples. A significant flux leakage through the non-superconducting gap between the bulk samples was also evidenced. The screening efficiency was shown to be significantly enhanced by using a hybrid structure (bulks + stack of tapes). This screening improvement can be explained by the additional screening currents flowing in the closed superconducting path provided by the 'eye-shaped' structure of the tapes. In particular, at the central location of the gap, combining the bulk samples with the stack of CC tapes could increase the value of $SF$ by approximately 51 %.

In order to reproduce the experimental results and predict the behavior of such a hybrid screen, a 3D numerical model involving the bulk HTS samples, the stack of CC tapes and the magnetic field source was implemented using a $H$-$\phi$ formulation. The layered structure of the stack of tapes was replaced by a homogeneous material with a field-independent engineering current density. The model neglected the offset between the two legs of the tapes in order to increase the number of symmetries and reduce the computation time. The parameters of the magnetic source were estimated using a 2D-axisymmetric model ($A$-formulation). The results obtained by the 3D model were shown to be in a good agreement with the experimental measurements. The model was then used to estimate the influence of the critical current density of the tapes as well as the number of tapes stacked together on the screening factor values.

Finally let us mention a few limitations and ways of improvement related to the results presented in this chapter. First, the experimental results were obtained using a homemade 3-axis Hall set-up with a noise level ranging between 100 and 200 $\mu$T. This level can affect the accuracy of high screening factor values obtained under low applied flux densities (< 5 mT). Concerning the 3D model, results could be improved by considering the offset between the two legs of the tapes, at the expense of a much higher computational cost. The model could also be improved by considering a stack of tapes with an anisotropic resistivity, to prevent the current to flow in the direction normal to the tapes. The mesh could be optimized for instance by using structured mesh elements which has been shown in previous works to address more efficiently structures with anisotropic properties [244]. Finally, field-dependent superconducting properties ($J_c(B)$ and $n(B)$) could be considered for both bulk materials and CC tapes. Regardless of these possible improvements, the results of this chapter give evidence that coated conductors can be beneficial to arrays of bulk materials. Coated conductors in closed 'eye-shaped' loops configuration were shown to significantly decrease the influence of the non-superconducting gap, resulting in an overall enhanced screening ability.

# Chapter 7

# Screening of the stray magnetic field in the vicinity of a superconducting magnet

In Chapter 6, we investigated the possibility to screen a non-uniform stray magnetic field using a structure combining bulk high-temperature superconducting samples with coated conductor tapes. We demonstrated that the effect of the non-superconducting gap between the bulk samples could be significantly mitigated using CC tapes in closed loops configuration. In this chapter, we investigate experimentally the same kind of structure combining bulk HTS and CC tapes to screen the stray magnetic field in the vicinity of a large field magnet. This work was carried out in the Department of Applied Science and Technology (DISAT) at Politecnico di Torino (Italy), in the framework of a collaboration with Prof. L. Gozzelino.

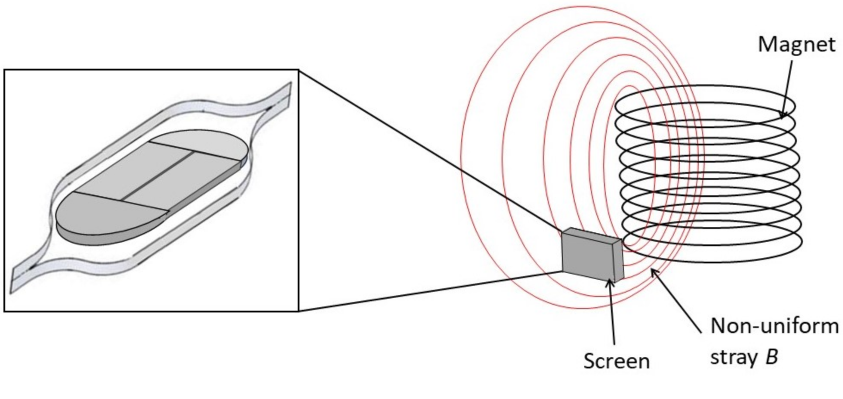

**Figure 7.1:** Schematic illustration of the screen configuration in the vicinity of a large field magnet.

The screening configuration investigated in this chapter is illustrated in Fig. 7.1. The magnet is the source of a significant stray magnetic field. The screen is placed at a specific location next to the magnet so that the magnitude of the flux density measured behind is reduced. The study is performed for multiple orientations of the screen. The superconducting screen is made of CC tapes arranged in 'eye-shaped' loops surrounding an array of 4 bulk HTS samples, as illustrated in Fig. 7.1. The screening efficiency is characterized in terms of the screening factor $SF$ defined by Eq. (6.1), as already introduced in Chapter 6.

This chapter is organized as follows. First, the experimental set-up developed to characterize the screening efficiency is introduced. The section details the source of stray magnetic field as well as the homemade displacement system placed next to the source, holding the Hall probe together with the superconducting screen. The superconducting screen is described as well, in particular, we introduce the array of bulk HTS samples and the characteristics of the coated conductor tapes arranged in closed 'eye-shaped' loops configuration. Finally, we present the experimental results characterizing the screening efficiency.

## 7.1 Experimental set-up

### 7.1.1 Source of stray magnetic field and measurement system

In the previous chapter, we analyzed the efficiency of a hybrid screen under a non-uniform magnetic field with a quite limited magnitude ($\|\boldsymbol{B}\| < 20$ mT). In this chapter, we are interested in investigating the performance of such a hybrid screen under a larger field and over a broader volume. To do so, we used the large bore superconducting magnet shown in the top of Fig. 7.2. This magnet is localized in the Department of Applied Science and Technology at Politecnico di Torino (Italy). The specifications of the magnet have already been described in Section 3.1.2. As a reminder, the magnet consists of 14 735 turns of NbTi wire wound in a total of 36 layers. The magnet is placed in a cryostat and can generate up to 4 T at the center of the bore.

In order to perform flux density measurements over several positions, a homemade displacement system has been realized and placed next to the magnet. This system is shown on the two bottom pictures in Fig. 7.2. It allows to hold the screen in a fixed position as well as the Hall sensor and to move them with respect to each other. The Hall probe shown in the figure is the Arepoc® Axis-3S Hall probe (a) described in Section 3.2.1 (Fig. 3.7). The screen and the Hall sensor are both immersed in a polystyrene tray filled with liquid nitrogen.

In order to determine the magnitude of the stray flux density, a first set of measurements was performed without superconducting screen. A schematic illustration of the magnet inside the cryostat as well as the coordinates system is shown in Fig. 7.3 (right side). The measurements are performed in the median plane ($x = 0$) along the $z$-axis.

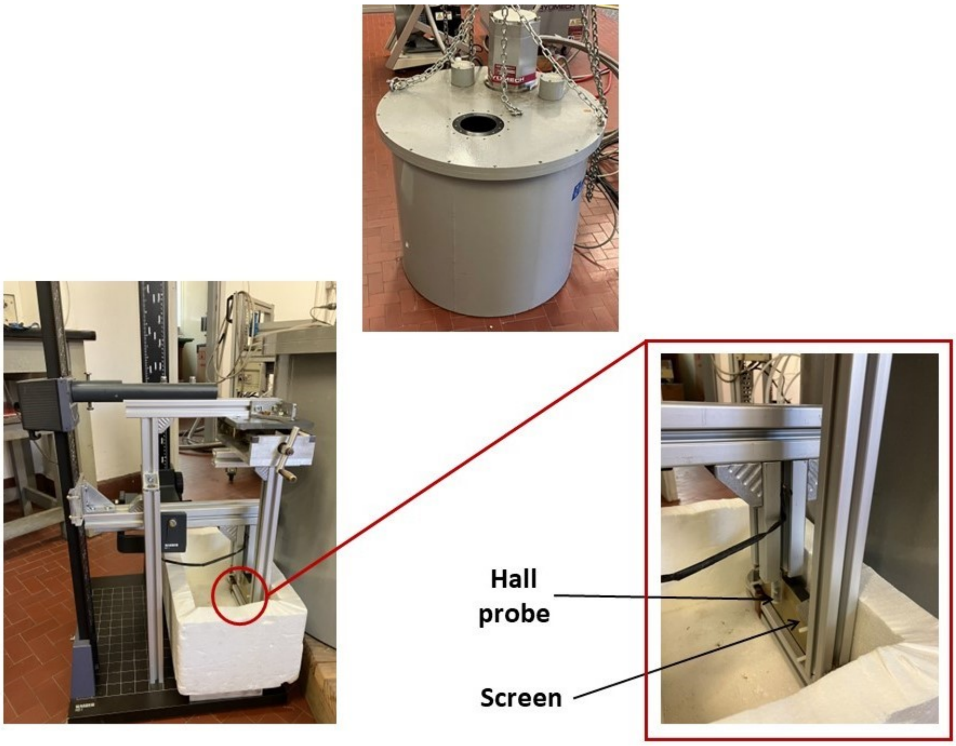

**Figure 7.2:** Pictures of the source of stray magnetic field as well as the homemade displacement system. The top picture shows the cryostat based on closed-cycle gaseous He and a cryocooler. The cryostat contains the superconducting magnet. The two bottom pictures show the homemade displacement system including the magnetic screen and the Hall probe.

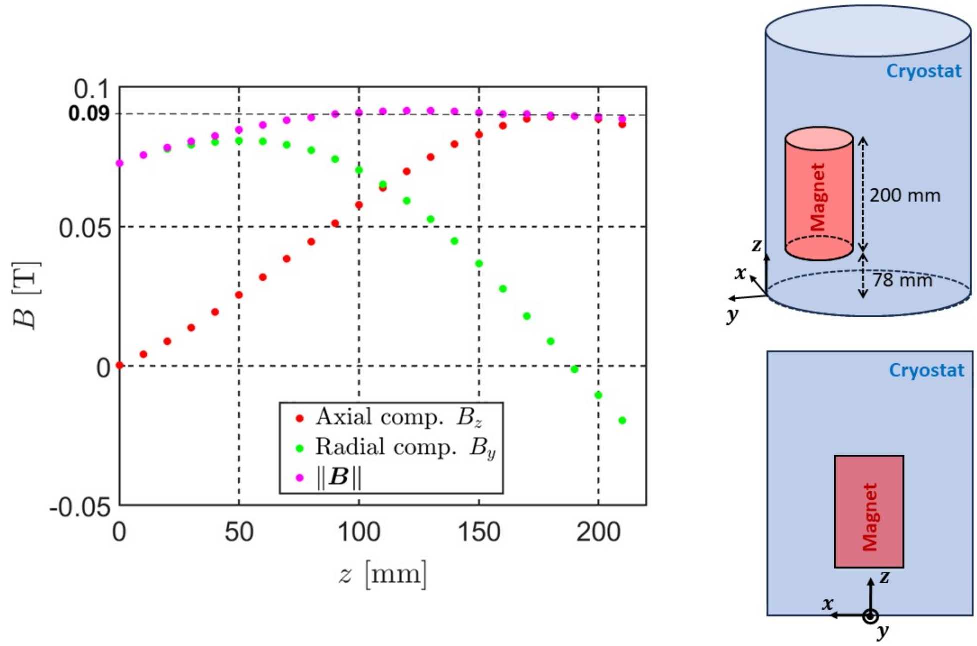

**Figure 7.3:** Measurement of the stray magnetic flux density along the axial axis $z$ in the absence of superconducting screen. The magnet system with the coordinates system are illustrated on the right side of the figure. The measurements are recorded at the central position $x = 0$ at an approximate distance from the cryostat $y \approx 70$ mm.

The probe is placed at approximately 70 mm from the cryostat surface ($y = 70$ mm). The results are plotted on the left side of Fig. 7.3. The graph shows the axial component of the flux density $B_z$, the radial component $B_y$ and the total magnitude $\|\boldsymbol{B}\|$. Here, and in all the results presented in this chapter, the azimuthal component of the flux density is neglected. The results plotted in Fig. 7.3 show that at this distance from the magnet, the stray flux density can reach a magnitude exceeding 90 mT.

### 7.1.2 Superconducting magnetic screen

The goal of this chapter is to investigate the capabilities of a hybrid structure (bulk HTS + CC tapes) to screen a significant stray field over a larger volume than reported in Chapter 6. As a result, the magnetic screen considered here consists of 4 bulk HTS samples arrayed together and surrounded by a stack of 20 CC tapes. The superconducting samples are held together using a carbon fiber reinforced polyamide holder. A picture of the whole magnetic screen is shown in Fig. 7.4.

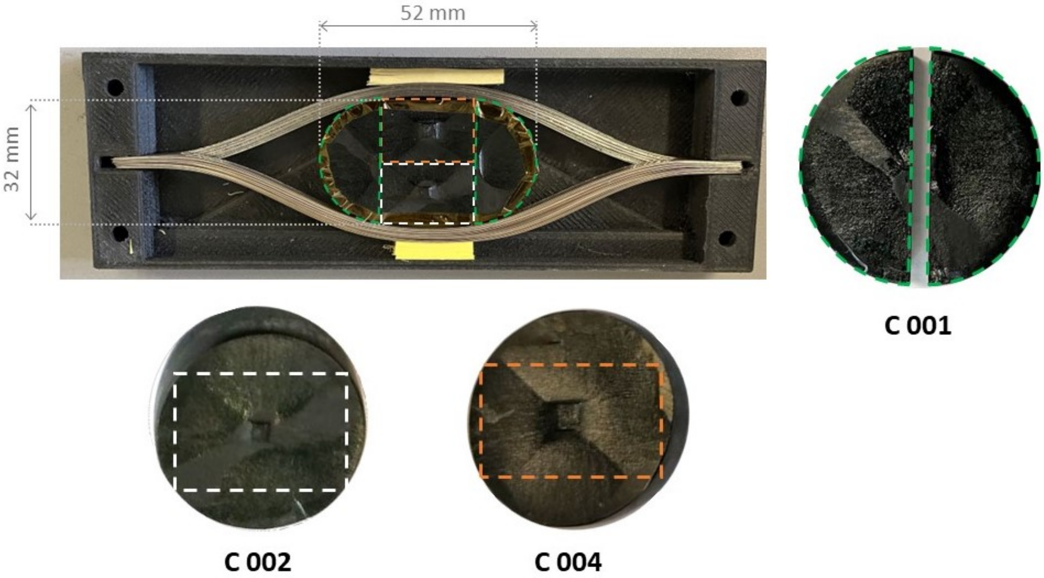

**C 001**

**C 002**

**C 004**

**Figure 7.4:** Picture of the hybrid superconducting screen including the individual bulk samples as well as the coated conductor tapes.

The array of bulk HTS is composed of two half cylindrical samples and two rectangular samples as shown in Fig. 7.4. The two half cylinders were obtained from the GdBCO bulk sample C 001. The process to extract the two half cylinders from the sample C 001 has already been described in the previous chapter. Two rectangular bulk samples of 16 mm × 20 mm were extracted from the samples C 002 and C 004 for which the superconducting properties have been presented in details in Section 4.1. The samples were cut using a diamond wire saw symmetrically with respect to the facet lines as illustrated in Fig. 7.4.

From this process, we obtained two bulk GdBCO rectangular samples whose diagonals approximately coincide with the facet lines of the original samples.

The tape samples are commercial second generation (2G) YBCO coated conductors (CC) from SuperPower®. These tapes have already been used and characterized in a previous work [60]. Each tape has a length of 154 mm and a width of 12 mm. They are based on a Hastelloy® substrate, the HTS layer is 1-1.5 $\mu$m thick and their total thickness is approximately 100 $\mu$m. In order to obtain closed superconducting loops, a central slit (1 mm wide and 126 mm long) was milled along the centerline of each of them. Finally, the tapes are characterized by an approximate critical current density of $J_\mathrm{c} \sim 2 \times 10^6$ A/cm$^2$. This critical current density is an averaged value over a large number of samples characterized in [60] by measuring the persistent current is the 'eye-shaped' tapes after ZFC magnetization.

## 7.2 Results and discussion

In this section, we present and discuss the experimental results on the screening capabilities of the hybrid structure introduced in Section 7.1.2. In particular, we compare the efficiency of a magnetic screen based on bulk HTS samples only with the hybrid magnetic screen (bulks + CC tapes). In the first part, the applied stray magnetic field is kept constant and the screening factor is measured at several locations behind the screen. In the second part, the field dependence of the screening factor is investigated when the screen is arranged in different configurations with respect to the magnet.

### 7.2.1 Efficiency of the hybrid screen

In order to characterize the efficiency of the magnetic screen, both the screen and the Hall probe are fixed on the homemade displacement system presented in Section 7.1 (Fig. 7.2). Once the screen and the probe have been cooled down to 77 K and the current is injected into the magnet, the magnetic flux density is measured at several positions with respect to the screen. For the sake of clarity, a new axis system $(x', z')$ attached to the screen itself is introduced. The screening efficiency is thus characterized by moving the probe along these axes $x'$ and $z'$. A picture of the screen as well as the attached axis system is shown at the top of Fig. 7.5. The graph at the bottom of Fig. 7.5 shows the applied magnetic flux density with respect to the $z'$-coordinate at 3 different positions $x'$ which are illustrated on the picture at the top of Fig. 7.5. These measurement data were obtained when the center of the screen $(x', z') = (0, 0)$ was placed at a height $z = 50$ mm with respect to the base of the cryostat and at a distance $y \approx 60$ mm from the cryostat surface (at $x = 0$), using the $(x, y, z)$-axis system shown in Fig. 7.3. The flux density is measured at approximately 10 mm from the surface of the bulk samples. This specific location was chosen as it corresponds to the highest value of the radial component of the magnetic flux density $B_y$. Figure 7.5 shows that at this location, we observe a stray flux density with a magnitude around 80 mT.

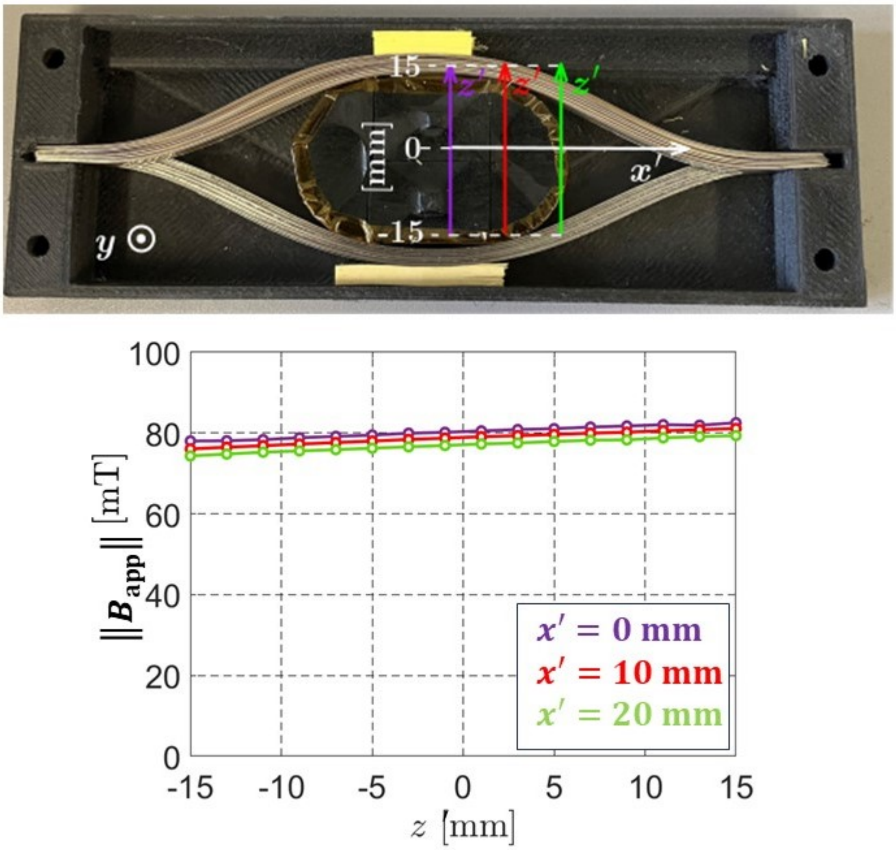

**Figure 7.5:** Top: picture of the hybrid superconducting screen together with the new axis system $(x', z')$. Bottom: Applied magnetic flux density measured along the axis $z'$ at different locations $x'$. These data are obtained when the center of the screen surface $(x', z') = (0, 0)$ is placed at a height $z = 50$ mm with respect to the base of the cryostat and at a distance $y \approx 60$ mm from the cryostat surface (at $x = 0$). See Fig. 7.3 for the $(x, y, z)$-axis system description. The flux density is measured at approximately 10 mm from the surface of the bulk samples.

The screening factor at 77 K and $\|\boldsymbol{B}_{\mathbf{app}}\| \approx 80$ mT is determined at different locations of the screen. Figure 7.6 plots the $SF$ values along the $z'$ axis at 3 different values of $x'$ as illustrated in Fig. 7.5. The measurements are carried out in liquid nitrogen in the exact same conditions than for the applied flux density measurements plotted at the bottom of Fig. 7.5. The graph in Fig. 7.6 compares the screening factor for a screen based on bulk samples only (dashed lines) with the hybrid screen (solid lines). Both cases display a common behavior: a finite magnetic screening effect ($SF > 1$) is observed over a surface of approximately $30 \times 40$ mm$^2$ and the maximum value of the screening factor is slightly shifted from the $z' = 0$ plane. One could think that this shift is due to the inhomogeneity of $J_c$ along the $z'$ axis. However, as described in Section 4.1.1, the bulk samples C 002 and C 004 exhibit very similar $J_c$ values. It is more likely that this shift with respect to $z' = 0$ originates from the non-symmetrical contributions of the axial and radial flux density components along the $z'$ axis. Indeed, for $z'$ between -15 mm and 15 mm, the radial component of the measured flux density under the presence of the screen ($B_y$) exhibits a rather symmetrical behavior with respect to $z'$. However, the flux lines curvature in the presence of the magnetic screen results in a quite asymmetrical axial field component ($B_z$). Indeed, $B_z$ is shown to decrease along $z'$ even if the applied field $B_{\mathrm{app,z}}$ slightly increases as a function of $z'$. Consequently, the norm of the measured flux density (when the superconducting screen is effective) $\|\boldsymbol{B}\|$ exhibits a non-symmetrical behavior along the $z'$ axis resulting in a slightly off-centered maximum in the $SF$ values. In the case of a screen made of bulk HTS only, we note a maximum value of $SF \approx 1.73$. For the hybrid screen, the maximum screening factor is around $SF \approx 2.3$ which represents an increase of approximately 33 %.

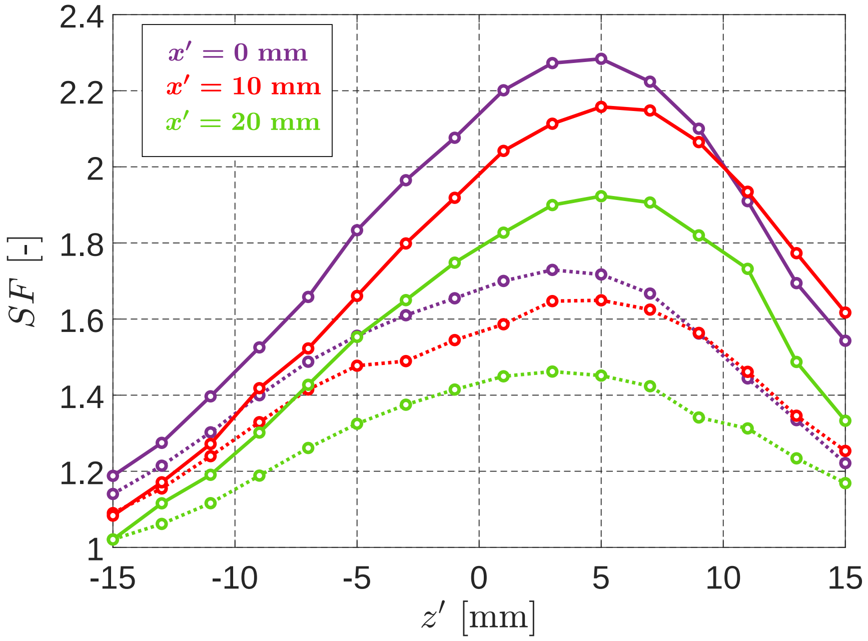

**Figure 7.6:** Screening factor plotted along the axis $z'$ at 3 different locations $x'$. The center of the screen surface $(x', z') = (0, 0)$ is placed at a height $z = 50$ mm with respect to the base of the cryostat and at a distance $y \approx 60$ mm from the cryostat surface (at $x = 0$). The flux density is measured at approximately 10 mm from the surface of the bulk samples. The dashed lines stand for a screen made of bulks only and the solid lines stand for the hybrid (bulks + tapes) screen. The operating temperature is 77 K.

### 7.2.2 Field dependence of the screening factor

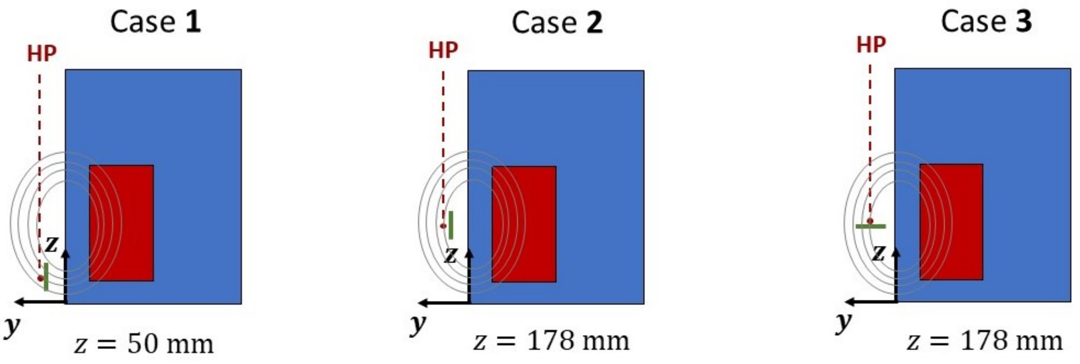

**Figure 7.7:** Schematic illustration of the screen configuration in three cases. The magnet is represented in red and the cryostat in blue. The $z$ coordinate indicated in each case refers to the position of the center of the Hall probe with respect to the cryostat base. In each case, the center of the active region of the Hall probe (HP) is placed at $y = 80$ mm and $x = 0$ ($x$-axis not shown in the figure) and at approximately 10 mm from the center of the screen surface.

Finally, we investigate the evolution of the screening factor with the applied flux density. To do so, three configurations are studied, as illustrated schematically in Fig. 7.7. In the case 1, the screen is placed in the same configuration as in Section 7.2.1. The only difference is that distance from the cryostat (illustrated in blue in Fig. 7.7) is slightly higher, for practical reasons. In the second configuration (case 2), the screen is placed vertically in such a way that the center of its surface is located at half the height of the magnet (illustrated in red in Fig. 7.7) i.e. the center of the screen is aligned horizontally with the center of the magnet. In the third configuration (case 3), the center of the screen surface is still located at half of the magnet height but this time, the screen is placed horizontally. As in Section 7.2.1, the Hall probe is placed facing the center of the screen approximately 10 mm away from its surface.

The screening factor $SF$ measured as a function of the applied flux density $\|\boldsymbol{B}_{\mathbf{app}}\|$ is shown in Fig. 7.8. The $SF(\|\boldsymbol{B}_{\mathbf{app}}\|)$ dependence is plotted for the three cases described in Fig. 7.7. The results were obtained at 77 K for a stray field applied at a sweep rate of $\sim 0.016$ mT/s. First, we observe that the field dependence of the screening effect is very weak in the case 1: the screening factor value evolves from $SF \approx 2.4$ for $\|\boldsymbol{B}_{\mathbf{app}}\| < 20$ mT to approximately 2.15 at $\|\boldsymbol{B}_{\mathbf{app}}\| \approx 80$ mT. In this configuration, the screen is placed at the location where the magnetic field is essentially directed in the radial direction ($\boldsymbol{y}$). When the screen is placed in the vertical configuration, the superconducting screening currents are mainly induced by the radial component of the field ($B_y$). As a result, the screening is effective as the main contribution to the stray field magnitude comes from $B_y$. In case 2, we do not observe any screening at all. The reason is that this configuration

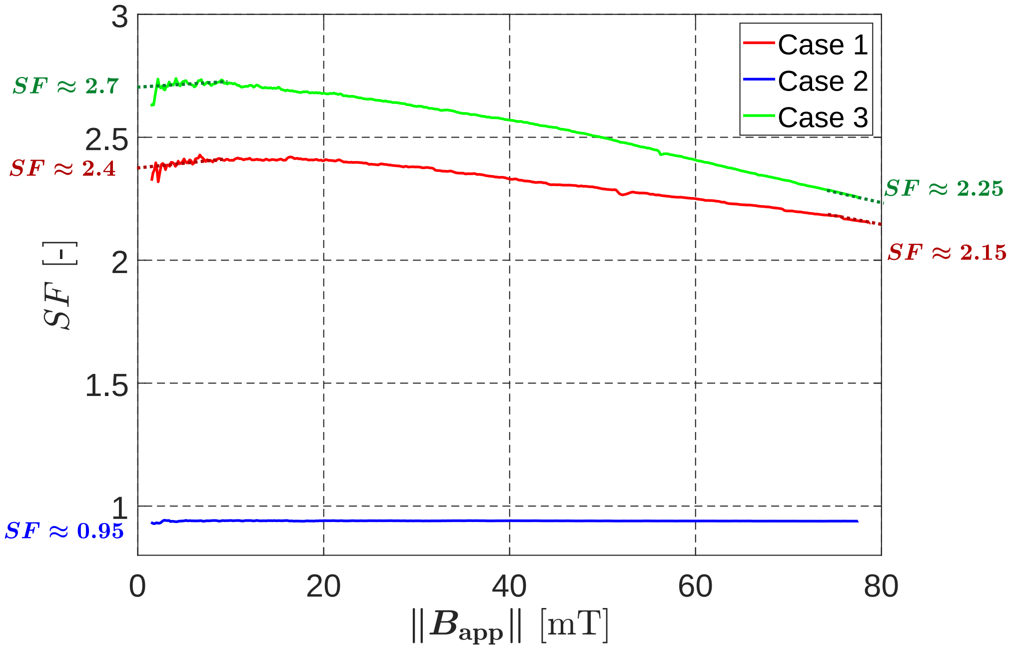

**Figure 7.8:** Field dependence of the screening factor in the three cases described in Fig. 7.7. The field is applied at a sweep rate of approximately 0.016 mT/s. The measurements are performed with the Hall probe facing the center of the screen and placed at approximately 10 mm from the screen surface. The operating temperature is 77 K.

is characterized by a stray field directed mainly along the axial direction ($\boldsymbol{z}$). When the screen is placed vertically, almost no screening current is induced by the axial field component ($B_z$). This is the reason why configuration 3 is studied: when the main contribution to the field magnitude comes from $B_z$, placing the screen in the horizontal orientation allows screening currents to be induced by the axial field component. The screening factor plotted for case 3 in Fig. 7.8 gives evidence of a significant screening effect. Again in this case, a moderate field dependence of the screening factor is observed between 0 and 80 mT.

## 7.3 Chapter summary

In this chapter, we introduced an experimental prototype of superconducting screen combining bulk high-temperature superconducting (HTS) samples with second generation coated conductor (2G CC) tapes. In particular, the structure consists of 4 bulk GdBCO samples arrayed together and surrounded by a stack of 20 YBCO CC tapes arranged in closed 'eye-shape' loops configuration. The efficiency of this screen has been characterized in the vicinity of a magnetic source involving a high stray flux density. The source is a superconducting NbTi magnet placed in a liquid He cryostat and able to generate a flux density up to 4 T at the center of its bore. The magnet is characterized by a stray flux density of $\sim$ 80 mT at a distance of $\sim$ 7 cm from the cryostat outer surface. In order to characterize the screening efficiency of the hybrid (bulks + tapes) structure, a homemade displacement system was placed next to the source magnet.

The magnetic screen has been shown to provide a finite screening effect ($SF > 1$) over a surface of $\sim 30 \times 40$ mm$^2$. Moreover a significant improvement of the screening efficiency was observed by combining the array of bulk HTS with the stack of CC tapes. In practice, an increase of approximately 33 % was measured under a stray field of 80 mT at an operating temperature of 77 K. Finally, the field dependence of the screening factor has also been investigated. Globally, the results showed a moderate field dependence of the screening effect in the range 0-80 mT.

The results presented in this chapter constitute a step forward in the context of magnetic screening of non-uniform stray magnetic field over large volumes, i.e. close to operating conditions encountered in large scale engineering applications. These results can indeed be used to validate 3D numerical models and they can be extrapolated to screens of much larger size.

# Conclusions and perspectives

This thesis was devoted to the investigation of methods to combine efficiently bulk high-temperature superconductors (HTS) and second generation (2G) coated conductors (CC) in order to shield magnetic flux densities over significant volumes. Bulk materials are known to shield large values of magnetic fields but are difficult to manufacture over large size. Coated conductors can be manufactured over hundreds of meters but require a closed superconducting path to shield magnetic fields in quasi-DC regime. In order to investigate the properties of shields combining both bulks and coated conductors, the study was organized into three axes of research.

First, the electrical and magnetic properties of both bulk superconductors and coated conductors used in this thesis were characterized precisely. In the first part of this work, bulk HTS samples were characterized both in terms of critical current density $J_\mathrm{c}$ and flux trapping ability. Two kinds of bulk samples were investigated: four GdBCO HTS cylinders [44,45] and a YBCO HTS rectangular prism. The average $J_\mathrm{c}$ of the bulk cylinders were estimated using a flux extraction magnetometer. The field dependence of $J_\mathrm{c}$ for the rectangular prism was estimated using a Physical Properties Measurement System (PPMS). The trapped flux density distributions measured over the top and bottom surfaces of the YBCO cylinders showed evidence of a quite inhomogeneous critical current density due to the presence of macroscopic defects impeding the proper flow of the current and to an inhomogeneous distribution of pinning centers between the facet lines and the growth sector regions. In the second part, we studied ferromagnetic properties of the Ni-5at.%W substrate of coated conductors at different temperatures based on Rolling Assisted Biaxially Textured Substrates (RABiTS). The study was conducted on a toroidal stack of coated conductors, a configuration that naturally forms a closed magnetic circuit characterized by the absence of demagnetizing effect. Magnetic hysteresis loops were obtained at four different temperatures between 77 and 293 K (room temperature). On one hand, the hysteresis losses were shown to be consistent with the Rayleigh model. On the other hand, the hysteresis cycles could be successfully reproduced using the phenomenological Jiles-Atherton model. Consequently, the results introduced in this study can be used to obtain, by interpolation, the magnetic properties of the Ni-5at.%W alloy at any temperature between 77 and 293 K for a maximum magnetizing field of 2000 A/m.

Regarding the characterizations summarized above, let us mention the lines for further studies. The work could be completed with a more detailed study of asymmetric minor hysteresis loops. The field-dependent properties like the coercive field, the remnant field or the hysteresis losses could be used to obtain scaling laws as introduced in [239]. Doing so, it could be possible to compare the magnetic behavior of the ferromagnetic substrates under different values of bias DC offset superimposed to the AC magnetizing field. In addition, to extend the characterization of magnetic substrate at other temperatures (in particular, at $T < 77$ K), the fitting of the experimental data using the Jiles-Atherton model could be improved using an iterative procedure [185]. The number of fitting parameters could also be reduced by using the experimental data obtained on short samples to estimate the saturation magnetization independently.

As a second research axis, we investigated the efficiency of a magnetic shield based on stacks of coated conductors annuli whose magnetic properties have been previously characterized. The shielding performance was characterized under a uniform external field applied either in the axial direction (parallel to the axis of the shield) or in the transverse direction (perpendicular to the axis of the shield). The study was carried out on three samples with different heights at both room temperature and 77 K. We showed experimentally that the ferromagnetic substrate allows for a shielding factor $> 1$ for both directions of applied field as well as at temperatures $> T_\mathrm{c}$. Numerical models including a field-dependent permeability (measured on the same coated conductors) could reproduce quite successfully the experimental results. We showed that such stacks of CC annuli could be able to shield axial flux densities up to 0.67 T with a shielding factor $> 3$. Numerical models showed that, by tripling the size of the higher investigated stack, we could reach a shielding factor $> 10$ up to an axial flux density of 0.93 T at 77 K. As illustrated in Fig. 8.1, the maximal threshold flux density in the literature is $\backsim$ 400 mT at 77 K and over a volume $\gtrsim 1$ cm$^3$. These shielding performances were observed using (RE)BCO tubes. The results obtained in this thesis demonstrated that larger values of $B_\mathrm{lim}$ could be obtained at 77 K.

Then, we investigated numerically the influence of the critical current density and the magnetic permeability. We observed that $J_\mathrm{c}$ has a very weak effect on the transverse shielding factor whereas it strongly affects the axial shielding. An increasing permeability was shown to have a detrimental effect on the axial magnetic shielding and to improve the transverse shielding. The comparison between the numerical and experimental results stressed the importance of taking into account the field dependence of $\mu_\mathrm{r}$ and $J_\mathrm{c}$ in the numerical models. We also introduced ways of improving the shielding of the stack of CC annuli. Under an axial applied field, the shielding was enhanced by covering one of the extremities of the stack with a superconducting cap. The cap consisted of either a bulk YBCO sample or a stack of HTS tapes. In both cases, the results showed a significant

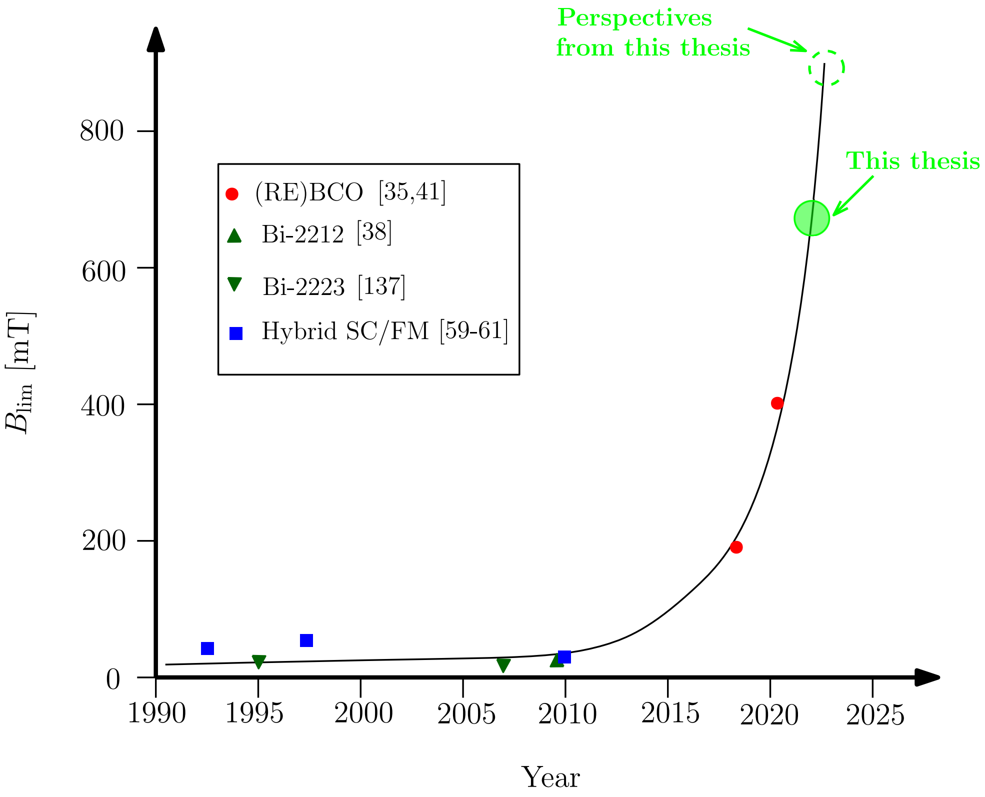

**Figure 8.1:** Threshold magnetic flux density $B_{\rm lim}$ (defined for $SF = 10$) over the years at 77 K and for a shielded volume $\gtrsim 1$ cm$^3$.

increase in the shielding factor compared to a fully open configuration. The experimental results could be quite successfully reproduced using a 2D-axisymmetric model considering a field-dependent critical current density. Finally, we demonstrated the possibility to wrap the stack of annuli with large-width CC tapes to improve the shielding efficiency under a transverse applied field.

Regarding the shields based on a stack of CC annuli, several elements could be investigated in future works. First, the shielding efficiency in axial configuration could only be measured on a sample of limited height due to the small air gap of the source electromagnet. Using a large bore high field magnet to characterize the shielding efficiency of higher samples would allow to confirm experimentally the ability to shield flux densities around 1 T at 77 K over the large volumes investigated. Moreover, the shielding efficiency could possibly be further improved, e.g. by using a second cap to close the second extremity of the cylinder (with a possible gap) to increase the axial shielding and wrapping the cylinder with a large-width CC tape in a 'swiss roll' configuration [251, 252]. The agreement between modeling and experimental results in the 3D transverse case could be also improved by using a detailed layered model instead of a homogenized model [244].

Finally, we investigated another possibility to screen a non-uniform stray magnetic flux density by a hybrid structure combining bulk HTS and 2G CC tapes. In order to enlarge the screened region in the vicinity of the source electromagnet, we used an array of bulk samples surrounded by short-circuited CC tapes. Doing so, the screening effect was enhanced due to the additional screening currents flowing in the closed superconducting path provided by the tapes. The study was performed in two steps. First, we examined an elementary 'unit block' magnetic screen based on two single grain bulk GdBCO half-cylinders surrounded by CC tapes in 'eye-shaped' loops configuration. The screen was placed above the top surface of a coil generating a non-uniform external magnetic field of significant value in a rather small volume, of average size comparable to the size of the hybrid screen. Experimental measurements demonstrated a significant improvement of the screening efficiency by using a hybrid structure (bulks + CC tapes) compared to a screen made of HTS bulks only. More precisely, combining the bulk samples to CC tapes in closed loops configuration could reduce the flux leakage through the non-superconducting joints by approximately 51 % at 77 K. It was also shown that the experimental results could be nicely reproduced with a 3D numerical model using a $H$-$\phi$-formulation in which the layered structure of the stack of tapes is replaced by a homogeneous material considering a field-independent critical current density. In the second step, such a hybrid screen structure was used to screen the stray flux density in the vicinity of a NbTi superconducting magnet. The non-uniform stray magnetic field generated by the magnet exhibits significant values over a volume that is much larger than the investigated screen. This part of the work was carried out in the Department of Applied Science and Technology at Politecnico di Torino (Italy). The screen was based on four single grain GdBCO samples arrayed together and surrounded by a stack of 20 CC tapes arranged in closed 'eye-shape' loops configuration. In practice, a finite screening effect was observed over a surface of $\sim 30 \times 40$ mm$^2$. Moreover, the screening efficiency could be significantly improved by using a hybrid structure compared to an array of bulk HTS only. In practice an increase of approximately 33 % was observed by combining the array of bulk samples to CC tapes at 77 K under an applied flux density of 80 mT. The experimental results obtained in the scope of this study can be used to validate 3D numerical models and can be extrapolated to magnetic screens of larger size.

Only passive hybrid magnetic screens are investigated in this work. Moreover, 3D numerical models showed that increasing the critical current density of the tapes or the number of stacked tapes would not increase significantly the screening efficiency in this geometry and in the range of applied field considered here ($<$ 20 mT). One perspective of future work would be to investigate hybrid screens in different geometries, e.g. where the eye-shaped loops have a shape or a spatial extension that differs from those investigated in this work. Also, it would be relevant to consider an active contribution from the tapes. Another perspective would be to extend the screening characterization to an AC stray field ($<$ 100 Hz) and estimate the effect of AC losses arising in the tapes on the screening efficiency. The array of bulk HTS could be improved by fabricating superconducting joints between the bulk samples to reduce the flux leakage through the joints [75, 76]. Similarly, a wider variety of screen configurations could be investigated by using superconducting joints between coated conductor tapes [78, 80]. The 3D numerical models could possibly be improved by considering a homogenized stack of tapes with an anisotropic resistivity. Alternative homogenized models based on the $T$-$A$-formulation could also be a promising approach for structures based on stacked tapes [104, 254].

As a conclusion, four major objectives have been fulfilled in this thesis. In addition to the precise characterization of electrical and magnetic properties of bulk superconductors and superconducting tapes independently, we investigated experimentally sizeable magnetic shields combining bulk HTS samples and CC tapes. These investigations were performed in configurations of increasing complexity both in terms of symmetry in the shield structure and in terms of applied field uniformity. The results have demonstrated a significant improvement in the shielding efficiency by using a hybrid structure combining bulk HTS and CC tapes. Next, an experimental prototype was successfully tested in the vicinity of a high field magnet characterized by a significant stray flux density. Finally, most of the experimental results obtained in this thesis could be reproduced by numerical models either in 2D or 3D configuration. This thesis constitutes a step forward in the study of magnetic shielding in environments involving large magnetic fields in quasi-DC regime encountered in current and future large scale engineering applications.

# Publications

## Papers in international journals

### Published

- **Brialmont S.**, Fagnard J.-F. and Vanderbemden P., "A simple torque magnetometer for magnetic moment measurement of large samples: Application to permanent magnets and bulk superconductors", *Rev. Sci. Instrum.*, vol. 90, 085101, 2019.
- **Brialmont S.**, Fagnard J.-F., Vanderheyden B., Mazaleyrat F., Hahn S., Patel A. and Vanderbemden P., "Measurement of magnetic hysteresis loops of the Ni-5at.%W alloy substrate as a function of temperature in a stack of 2G HTS-coated conductor annuli", *IEEE Trans. Appl. Supercond.*, vol. 32, 6602710, 2022.
- **Brialmont S.**, Dular J., Wéra L., Fagnard J.-F., Vanderheyden B., Geuzaine C., Hahn S., Patel A. and Vanderbemden P., "Magnetic shielding up to 0.67 T at 77 K using a stack of high temperature superconducting annuli of 26 mm bore", *Supercond. Sci. Technol.*, vol. 36, 054004, 2023.

### Submitted

- Dular J., **Brialmont S.**, Vanderbemden P., Geuzaine C. and Vanderheyden B., "Finite element models for magnetic shields made of stacked superconducting tape annuli", submitted in *IEEE Trans. Appl. Supercond.*, September 2023.
- Rotheudt N., **Brialmont S.**, Fagnard J.-F., Hlasek T., Plechacek J. and Vanderbemden P., "Improving the screening ability of high-temperature superconductors by combining disk-shaped bulks and closed-loop coated conductors", submitted in *Supercond. Sci. Technol.*, February 2024.

## Presentations during international conferences

- **Brialmont S.**, Fagnard J.-F. and Vanderbemden P. *Non-destructive measurement of the magnetic moment of bulk GdBCO samples using a torque magnetometer designed for large size samples.* Oral communication. 11th International Workshop on Processing and Applications of Superconducting Bulk Materials, 2019 Aug. 29-30, Prague, Czech Republic.
- **Brialmont S.**, Fagnard J.-F. and Vanderbemden P. *Design and construction of a torque magnetometer for large size superconductors.* Invited poster communication. 14th European Conference on Applied Superconductivity (EUCAS), 2019 Sept. 1-5, Glasgow, UK.

- **Brialmont S.**, Fagnard J.-F. and Vanderbemden P. *Use of metallic strain gauges for torque magnetometry: application to the contactless characterization of large magnetized superconducting samples*. Oral communication. 19th International Conference on Experimental Mechanics ICEM. 2022 July 17-21, Krakow, Poland.

- **Brialmont S.**, Fagnard J.-F., Vanderheyden B., Hahn S., Park S. H., Patel A. and Vanderbemden P. *Measurement of major and minor magnetic hysteresis loops of the Ni-alloy substrate in a stack of 2G coated conductor tapes as a function of temperature*. Poster communication (virtual). 15th European Conference on Applied Superconductivity (EUCAS), 2021 Sept. 5-9, Moscow, Russia.

- **Brialmont S.**, Dular J., Vanderheyden B., Geuzaine C., Patel A., Hahn S. and Vanderbemden P., *Annuli of coated conductors with a ferromagnetic substrate: magnetic shielding properties at 77 K and at room temperature*. Invited oral communication. 8th International Workshop on Numerical Modelling of High Temperature Superconductors, 2022 June 14-16, Nancy, France.

- **Brialmont S.**, Fagnard J.-F., Fracasso M., Gozzelino L., Yang P., Yang W. and Vanderbemden P., *Screening of the stray magnetic field of a large bore superconducting magnet*. Oral communication. 16th European Conference on Applied Superconductivity (EUCAS), 2023 Sept. 4-7, Bologna, Italy.

- Dular J., **Brialmont S.**, Vanderbemden P., Geuzaine C., Vanderheyden B., *3D Finite Element Models of Stacked Tapes Magnetic Shields*. Oral communication. 8th International Workshop on Numerical Modelling of High Temperature Superconductors, 2022 June 14-16, Nancy, France.

# Bibliography

[1] Jiang Y., Pei R., Xian W., Hong Z. and Coombs T. A., “The design, magnetization and control of a superconducting permanent magnet synchronous motor”, *Supercond. Sci Technol.*, vol. 21, 065011, 2008.

[2] Haran K. S., Loder D., Deppen T. O. and Zeng L., “Actively shielded high-field air-core superconducting machines”, *IEEE Trans. Appl. Supercond.*, vol. 26, 5202508, 2016.

[3] Haran K. S. *et al.*, “High power density superconducting rotating machines - development status and technology roadmap”, *Supercond. Sci. Technol.*, vol. 30, 123002, 2017.

[4] Song X. *et al.*, “A pole pair segment of a 2-MW high-temperature superconducting wind turbine generator”, *IEEE Trans. Appl. Supercond.*, vol. 27, 5201205, 2017.

[5] Sugouchi R. *et al.*, “Conceptual design and electromagnetic analysis of 2 MW fully superconducting synchronous motors with superconducting magnetic shields for turbo-electric propulsion system”, *IEEE Trans. Appl. Supercond.*, vol. 30, 3601905, 2020.

[6] Douine B., Berger K. and Ivanov N., “Characterization of high-temperature superconductor bulks for electrical machine application”, *Materials*, vol. 14, 1636, 2021.

[7] Dorget R. *et al.*, “Review on the use of superconducting bulks for magnetic screening in electrical machines for aircraft applications”, *Materials*, vol. 14, 2847, 2021.

[8] Wang Q., Zhang H., Hao L., Hu J., Wei H., Patel I., Shah A. and Coombs T., “Magnetisation and demagnetisation of trapped field stacks in a superconducting machine for electric aircraft”, *Supercond. Sci. Technol.*, vol. 36, 115023, 2023.

[9] Campbell A. M., “Superconducting and conventional machines”, *Supercond. Sci. Technol.*, vol. 27, 124012, 2014.

[10] Minervini J., Parizh M. and Schippers M., “Recent advances in superconducting magnets for MRI and hadron radiotherapy: an introduction to ‘Focus on superconducting magnets for hadron therapy and MRI’”, *Supercond. Sci Technol.*, vol. 31, 030301, 2018.

[11] Manso Jimeno M., Vaughan J. T. and Geethanath S., “Superconducting magnet designs and MRI accessibility: A review”, *NMR in Biomedicine*, vol. 36(9), e4921, 2023.

[12] Hofman M. B. M., Kuijer J. P. A., de Ridder J. W., Perk L. R. and Verdaasdonk R. M., “Technical Note: Building a combined cyclotron and MRI facility: Implications for interference”, *Med. Phys.*, vol. 40, 012303, 2013.

[13] Amemiya N., Sogabe Y., Sakashita M., Iwata Y., Noda K., Ogitsu T., Ishii Y. and Kurusu T., “Magnetization and field quality of a cosine-theta dipole magnet wound with coated conductors for rotating gantry for hadron cancer therapy”, *Supercond. Sci. Technol.*, vol. 29, 024006, 2016.

[14] Pearson E., Kleeven W., Nuttens V., Zaremba S., Van de Walle J., Forton E., Choo R. and Jongen Y., “Development of Cyclotrons for Proton and Particle Therapy” In: “Rath, A., Sahoo, N. (eds) Particle Radiotherapy”, *Springer*, New Delhi, 2016.

[15] Barna D., “High field septum magnet using a superconducting shield for the Future Circular Collider”, *Phys. Rev. Accel. Beams*, vol. 20, 041002, 2017.

[16] Capobianco-Hogan K. G. *et al.*, “A magnetic field cloak for charged particle beams”, *Nucl. Instrum. Methods Phys. Res. A*, vol. 877, pp. 149-156, 2018.

[17] Statera M., Balossino I., Barion L., Ciullo G., Contalbrigo M., Lenisa P., Lowry M. M., Sandorfi A. M. and Tagliente G., “A bulk superconducting $\mathrm{MgB_2}$ cylinder for holding transversely polarized targets”, *Nucl. Instrum. Methods Phys. Res. A*, vol. 882, pp. 17-21, 2018.

[18] Kahn Y., Safdi B. R. and Thaler J. “Broadband and resonant approaches to axion dark matter detection”, *Phys. Rev. Lett.*, vol. 117, 141801, 2016.

[19] Janů Z. and Soukup F., “Continuous reading SQUID magnetometer and its applications”, *Rev. Sci. Instrum.*, vol. 88, 065104, 2017.

[20] Foner S., “Review of magnetometry”, *IEEE Trans. Magn.*, vol. MAG-17, pp. 3358-3363, 1981.

[21] Robbes D., “Highly sensitive magnetometers - a review”, *Sens. Actuators A*, vol. 129, pp. 86-93, 2006.

[22] Arpaia P., Ballarino A., Giunchi G. and Montenero G., “$\mathrm{MgB_2}$ cylindrical superconducting shielding for cryogenic measurement applications: a case study on DC current transformers”, *JINST*, vol. 9, P04020, 2014.

[23] Pizzella V., Della Penna S., Del Gratta C. and Romani G. L., “SQUID systems for biomagnetic imaging”, vol. 14, R79-R114, 2001.

[24] Ohta H., Matsui T. and Uchikawa Y., “A whole-head SQUID system in a superconducting magnetic shield”, *IEEE Trans. Appl. Supercond.*, vol. 17, pp. 730-733, 2007.

[25] Gu C., Chen S., Pang T. and Qu T.-M., “Experimental realization of open magnetic shielding”, *Appl. Phys. Lett.*, vol. 110, 193505, 2017.

[26] Bergen A., van Weers H. J., Bruineman C., Dhallé M. M. J., Krooshoop H. J. G., ter Brake H. J. M., Ravensberg K., Jackson B. D. and Wafelbakker C. K., “Design and validation of a large-format transition edge sensor array magnetic shielding system for space application”, *Rev. Sci. Instrum.*, vol. 87, 105109, 2016.

[27] Calvelli V., Musenich R., Tunesi F. and Battiston R., “A novel configuration for superconducting space radiation shields”, *IEEE Trans. Appl. Supercond.*, vol. 27, 0500604, 2017.

[28] Kobayashi K., Kon A., Yoshizawa M. and Uchikawa Y., “Active magnetic shielding using symmetric magnetic field sensor method”, *IEEE Trans. Magn.*, vol. 48, pp. 4554-4557, 2012.

[29] Xu X., Liu W., Huang Y., Li W. and Che S., “Magnetic shielding mechanism and structure design of composites at low frequency: A review”, *J. Magn. Magn. Mater.*, vol. 570, 170509, 2023.

[30] Sun J., Ren J., Li J. and Huang Y., “Measurement and analysis of magnetic properties of permalloy for magnetic shielding devices under different temperature environments”, *Materials*, vol. 16, 3253, 2023.

[31] Jiles D., “Introduction to magnetism and magnetic materials, 3rd edition”, Boca Raton, FL, USA: CRC Press, Taylor and Francis, 2015.

[32] Hinterberger A., Gerber S. and Doser M., “Superconducting shielding with Pb and Nb tubes for momentum sensitive measurements of neutral antimatter”, *JINST*, vol. 12, T09002, 2017.

[33] VantHull L. L. and Mercereau J. E., “Magnetic shielding by a superconducting cylinder”, *Rev. Sci. Instrum.*, vol. 34, pp. 1238-1242, 1963.

[34] Claycomb J. R. and Miller J. H., “Superconducting magnetic shields for SQUID applications”, *Rev. Sci. Instrum.*, vol. 70, pp. 4562-4568, 1999.

[35] Pavese F., “Handbook of Applied Superconductivity”, Bristol, UK: Institute of Physics Publishing, pp. 1461-1483, 1998.

[36] Takahata K., Nishijima S., Ohgami M., Okada T., Nakagawa S. and Yoshiwa M., “Magnetic shielding by a tubular superconducting winding in parallel and transverse fields”, *IEEE Trans. Magn.*, vol. 25, pp. 1889-1892, 1989.

[37] Sasaki T. and Itoh I., “Magnetic shielding by Nb-Ti multilayer cylinder”, *Cryogenics*, vol. 36, pp. 497-506, 1996.

[38] Wéra L., Fagnard J.-F., Namburi D. K., Shi Y., Vanderheyden B. and Vanderbemden P., “Magnetic shielding above 1 T at 20 K with bulk, large grain YBCO tubes made by buffer-aided top seeded melt growth”, *IEEE Trans. Appl. Supercond.*, vol. 27, 6800305, 2017.

[39] Gozzelino L. *et al.* “Passive magnetic shielding by machinable $MgB_2$ bulks: measurements and numerical simulations”, *Supercond. Sci. Technol.*, vol. 32, 034004, 2019.

[40] Gozzelino L. *et al.*, “High magnetic shielding properties of an $MgB_2$ cup obtained by machining a spark-plasma-sintered bulk cylinder”, *Supercond. Sci. Technol.*, vol. 33, 044018, 2020.

[41] Rabbers J. J., Oomen M. P., Bassani E., Ripamonti G. and Giunchi G., “Magnetic shielding capability of $MgB_2$ cylinders”, *Supercond. Sci. Technol.*, vol. 23, 125003, 2010.

[42] Fagnard J.-F., Elschner S., Bock J., Dirickx M., Vanderheyden B. and Vanderbemden P., "Shielding efficiency and $E(J)$ characteristics measured on large melt cast Bi-2212 hollow cylinders in axial magnetic fields", *Supercond. Sci. Technol.*, vol. 23, 095012, 2010.

[43] Sasaki T., Tanaka M., Morita M., Miyamoto M. and Hashimoto M., "Magnetic shielding by superconducting Y-Ba-Cu-O prepared by the modified quench and melt growth (QMG) process", *Jpn. J. Appl. Phys.*, vol. 31, pp. 1026-1032, 1992.

[44] Yang P. T., Yang W. M. and Chen J. L., "Fabrication and properties of single grain GdBCO superconducting rings by a buffer aided Gd+011 TSIG method", *Supercond. Sci. Technol.*, vol. 30, 085003, 2017.

[45] Yang P. T., Fagnard J. F., Vanderbemden P. and Yang W., "Magnetic shielding of a short thick GdBCO tube fabricated by the buffer aided top seeded infiltration and growth method", *Supercond. Sci. Technol.*, vol. 32, 115015, 2019.

[46] Zhang Z. Y., Matsumoto S., Teranishi R. and Kiyoshi T., "Magnetic shielding properties of GdBCO bulks with different crystal orientation", *Phys. Proc.*, vol. 27, pp. 180-183, 2012.

[47] Hogan K., Fagnard J.-F., Wéra L., Vanderheyden B. and Vanderbemden P., "Magnetic shielding of an inhomogeneous magnetic field source by a bulk superconducting tube", *Supercond. Sci. Technol.*, vol. 28, 035011, 2015.

[48] Hogan K., Fagnard J.-F., Wéra L., Vanderheyden B. and Vanderbemden P., "Bulk superconducting tube subjected to the stray magnetic field of a solenoid", *Supercond. Sci. Technol.*, vol. 31, 015001, 2018.

[49] Hogan K., "Passive magnetic shielding with bulk high temperature superconductors under a non-uniform magnetic field", PhD thesis, University of Liège, 2018.

[50] Takahashi K., Fujishiro H. and Ainslie M. D., "A new concept of a hybrid trapped field magnet lens", *Supercond. Sci. Technol.*, vol. 31, 044005, 2018.

[51] Prigozhin L. and Sokolovsky V., "3D simulation of superconducting magnetic shields and lenses using the fast Fourier transform", *J. Appl. Phys.*, vol. 123, 233901, 2018.

[52] Kvitkovic J., Pamidi S. and Voccio J., "Shielding AC magnetic fields using commercial $YBa_2Cu_3O_7$-coated conductor tapes", *Supercond. Sci. Technol.*, vol. 22, 125009, 2009.

[53] Kvitkovic J., Patil P., Pamidi S. V. and Voccio J., "Characterization of 2G Superconductor Magnetic Shields at 40-77 K", *IEEE Trans. Appl. Supercond.*, vol. 21, pp. 1477-1480, 2011.

[54] Kvitkovic J., Davis D., Zhang M. and Pamidi S., "Magnetic shielding characteristics of second generation high temperature superconductors at variable temperatures obtained by cryogenic helium gas circulation", *IEEE Trans. Appl. Supercond.*, vol. 25, 8800304, 2015.

[55] Kvitkovic J., Patel S., Zhang M., Zhang Z., Peetz J., Marney A. and Pamidi S., "Enhanced magnetic field sensing using planar high-temperature superconductor shields", *IEEE Trans. Appl. Supercond.* , vol. 28, 9001705, 2018.

[56] Nagasaki Y., Solovyov M. and Gömöry F., "Experimental and numerical investigation of shielding performance of superconducting magnetic shields using coated conductor tapes", *IEEE Trans. Appl. Supercond.*, vol. 28, 6601905, 2018.

[57] Fagnard J.-F., Dirickx M., Levin G. A., Barnes P. N., Vanderheyden B. and Vanderbemden P., "Use of second generation coated conductors for efficient shielding of dc magnetic fields", *J. Appl. Phys.*, vol. 108, 013910, 2010.

[58] Wéra L., Fagnard J. F., Levin G. A., Vanderheyden B. and Vanderbemden P., "Magnetic shielding with YBCO coated conductors: influence of the geometry on its performances", *IEEE Trans. Appl. Supercond.*, vol. 23, 8200504, 2013.

[59] Wéra L., Fagnard J.-F., Levin G. A., Vanderheyden B. and Vanderbemden P., "A comparative study of triaxial and uniaxial magnetic shields made out of YBCO coated conductors", *Supercond. Sci. Technol.*, vol. 28, 074001, 2015.

[60] Wéra L., "Experimental study of methods to increase the shielded volume in passive superconducting magnetic screens", PhD thesis, University of Liège, 2017.

[61] Tomków Ł., Kulikov E., Kozłowski K. and Drobin V., "Improvement of the homogeneity of magnetic field by the attenuation of a selected component with an open superconducting shield made of commercial tapes", *J. Appl. Phys.*, vol. 126, 083903, 2019.

[62] Bortot L. *et al.*, "High-temperature superconducting screens for magnetic field-error cancellation in accelerator magnets", *Supercond. Sci. Technol.*, vol. 34, 105001, 2021.

[63] Itoh M., Ohyama T., Hoshino K., Ishigaki H. and Minemoto T., "Improvement in magnetic shielding by the superposition of a magnetic cylinder over a copper-oxide superconducting cylinder", *IEEE Trans. Appl. Supercond.*, vol. 3, pp. 181-184, 1993.

[64] Mori K. and Minemoto T., "Magnetic shielding of the superposition of a hybrid ferromagnetic cylinder over a BPSCCO Cylinder", *IEEE Trans. Appl. Supercond.*, vol. 7, pp. 378-381, 1997.

[65] Lousberg G. P., Fagnard J.-F., Ausloos M., Vanderbemden P. and Vanderheyden B., "Numerical study of the shielding properties of macroscopic hybrid ferromagnetic/superconductor hollow cylinders", *IEEE Trans. Appl. Supercond.*, vol. 20, pp. 33-41, 2010.

[66] Gozzelino L., Gerbaldo R., Ghigo G., Laviano F., Truccato M. and Agostino A., "Superconducting and hybrid systems for magnetic field shielding", *Supercond. Sci. Technol.*, vol. 29, 034004, 2016.

[67] Fracasso M., Gömöry F., Solovyov M., Gerbaldo R., Ghigo G., Laviano F., Napolitano A., Torsello D. and Gozzelino L., "Modelling and performance analysis of $MgB_2$ and hybrid magnetic shields", *Materials*, vol. 15, 667, 2022.

[68] Gömöry F., Solovyov M., Šouc J., Navau C., Prat-Camps J. and Sanchez A., "Experimental realization of a magnetic cloak", *Science*, vol. 335, pp. 1466-1468, 2012.

[69] Solovyov M., Šouc J., Gömöry F., Rikel M. O., Mikulášová E., Ušáková M. and Ušák E., "Bulk and CC-tape based superconducting shields for magnetic cloaks, *IEEE Trans. Appl. Supercond.*, vol. 27, 8800204, 2017.

[70] Prat-Camps J., Sanchez A. and Navau C., "Superconductor-ferromagnetic metamaterials for magnetic cloaking and concentration", *Supercond. Sci. Technol.*, vol. 26, 074001, 2013.

[71] Zhou P.-B., Ma G.-T., Wang Z.-T., Gong T.-Y., Ye C.-Q. and Zhang H., "Cloaking the static magnetic fields by alternate superconductor-ferromagnet heterostructure", *IEEE Trans. Appl. Supercond.*, vol. 26, 0601805, 2016.

[72] Terao Y., Sekino M., Ohsaki H., Teshima H. and Morita M., "Magnetic shielding characteristics of multiple bulk superconductors for higher field applications", *IEEE Trans. Appl. Supercond.*, vol. 21, pp. 1584-1587, 2011.

[73] Douine B., Malé G., Lubin T., Mezani S., Lévêque J. and Berger K., "Improvement of YBCO superconductor magnetic shielding by using multiple bulks", *J. Supercond. Nov. Magn.*, vol. 27(4), pp. 903-907, 2014.

[74] Wu Y., Zhang G., Wu Y., Zhang D. and Jing L., "Research on improving the shielding effect of stacked superconducting bulks based on increasing the gap reluctance", *IEEE Trans. Appl. Supercond.*, vol. 33, 8800205, 2023.

[75] Congreve J. V. J., Dennis A. R., Shi Y., Bumby C. W., Druiff H., Cardwell D. A. and Durrell J. H., "A reliable technique to fabricate superconducting joints between single grain, Y-Ba-Cu-O bulk superconductors", *Supercond. Sci. Technol.*, vol. 34, 094003, 2021.

[76] Tutt N., Congreve J., Shi Y., Namburi D., Dennis A., Druiff H. and Durrell J., "Fabrication of high-quality joints between Gd-Ba-Cu-O bulk superconductors", *Supercond. Sci. Technol.*, vol. 36, 085004, 2023.

[77] Hatwar R., Kvitkovic J., Herman C. and Pamidi S., "Effect of discontinuities and penetrations on the shielding efficacy of high temperature superconducting magnetic shields", *IOP Conf. Ser. Mat. Sci. Eng.*, vol. 102, 012012, 2015.

[78] Lu J., Han K., Sheppard W. R., Viouchkov Y. L., Pickard K. W. and Markiewicz W. D., "Lap joint resistance of YBCO coated conductors", *IEEE Trans. Appl. Supercond.*, vol. 21, pp. 3009-3012, 2011.

[79] Jin X., Yanagisawa Y., Maeda H. and Takano Y., "Development of a superconducting joint between a $GdBa_2Cu_2O_{7-\delta}$-coated conductor and $GdBa_2Cu_2O_{7-\delta}$ bulk: towards a superconducting joint between RE (Rare Earth) $Ba_2Cu_2O_{7-\delta}$-coated conductors", *Supercond. Sci. Technol.*, vol. 28, 075010, 2015.

[80] Huang D., Shang H., Xie B., Zou Q., Dong H., Wang K., Zhang L., Gu H. and Ding F., "An efficient approach for superconducting joint of YBCO coated conductors", *Supercond. Sci. Technol.*, vol. 35, 075004, 2022.

[81] Tomków Ł., Ciszek M. and Chorowski M., "Combined magnetic screen made of Bi-2223 bulk cylinder and YBCO tape rings - Modeling and experiments", *J. Appl. Phys.*, vol. 117, 043901, 2015.

[82] Tomków Ł., Ciszek M. and Chorowski M., "Frequency effect on shielding quality of closed superconducting magnetic shields made of superconducting tapes", *IEEE Trans. Appl. Supercond.*, vol. 26, 0602204, 2016.

[83] Wang S. Y., Wang S. S., Yu X., Xu H., Li Y. Y., Jiang H. Y. and Sun K. Y., "Design and analysis of a hybrid magnetic shielding system: application for the magnetic non-destructive testing of circuits", *Supercond. Sci. Technol.*, vol. 36, 035001, 2023.

[84] Ashcroft N. W. and Mermin N. D., "Solid State Physics", Philadelphia, PA, USA: HRW International Editions, 1987.

[85] Brandt E. H., Indenbom M. V. and Forkl A., "Type-II superconducting strip in perpendicular magnetic field", *Europhys. Lett.*, vol. 22(9), pp. 735-740, 1993.

[86] Ciszek M., Campbell A. M., Ashworth S. P. and Glowacki B. A., "Energy dissipation in high temperature ceramic superconductors", *J. Appl. Phys.*, vol. 96, 4, 1995.

[87] Grilli F., Ashworth S. P. and Stavrev S., "Magnetization AC losses of stacks of YBCO coated conductors", *Physica C*, vol. 434, pp. 185-190, 2006.

[88] Maievskyi E., "Comparative study of energy dissipation minimum in BSCCO-2223 and YBCO-123 HTS tapes", PhD thesis, Institute of Low Temperature and Structure Research (PAN), 2017.

[89] Meissner W. and Ochsenfeld R., "Ein neuer effekt eintritt der supraleitfähigkeit", *Natrurwiss.*, vol. 21, 787, 1933.

[90] London F. and London H., "The electromagnetic equations of the supraconductor", *Proc. R. Soc. London, A*, vol. 149, pp. 71-88, 1935.

[91] Vanderbemden P., "Determination of critical current in bulk high-temperature superconductors by magnetic flux profile measuring methods", PhD thesis, University of Liège, 1999.

[92] Harshmann D. R. and Mills Jr. A. P., "Concerning the nature of high-$T_c$ superconductivity: survey of experimental properties and implications for interlayer coupling", *Phys. Rev. B*, vol. 45, pp. 10684-10712, 1992.

[93] Orlando T. P. and Delin K. A., "Foundations of Applied Superconductivity", Reading, MA, USA: Addison-Wesley, 1991.

[94] Bardeen J., Cooper L. N. and Schrieffer J. R., "Theory of Superconductivity", *Phys. Rev.*, vol. 108, pp. 1175-1204, 1957.

[95] Bean C. P., "Magnetization of High-Field Superconductors", *Rev. Mod. Phys.*, vol. 36, pp. 31-39, 1964.

[96] Fagnard J.-F., "Experimental and numerical study of the factors influencing the performances of magnetic screens made of high temperature superconductors", PhD thesis, University of Liège, 2011.

[97] Anderson P. W., "Theory of flux creep in hard superconductors", *Phys. Rev. Lett.*, vol. 9, pp. 309-311, 1962.

[98] Anderson P. W. and Kim Y. B., "Hard superconductivity: theory of the motion of Abrikosov flux lines", *Rev. Mod. Phys.*, vol. 36, pp. 39-43, 1964.

[99] Feigel'man M. V., Geshkenbein V. B., Larkin A. I. and Vinokur V. M., "Theory of collective flux creep", *Phys. Rev. Lett.*, vol. 63, pp. 2303-2306, 1989.

[100] Zeldov E., Amer N. M., Koren G., Gupta A., McElfresh M.W. and Gambino R.J., “Flux creep characteristics in high-temperature superconductors”, *Appl. Phys. Lett.*, vol. 56, pp. 680-682, 1990.

[101] Gurevich A. and Küpfer H., “Time scales of the flux creep in superconductors” , *Phys. Rev. B*, vol. 48, pp. 6477-6487, 1993.

[102] Rhyner J., “Magnetic properties and AC-losses of superconductors with power law current-voltage characteristics”, vol. 212, pp. 292-300, 1993.

[103] Sirois F., Grilli F. and Morandi A., “Comparison of constitutive laws for modeling high-temperature superconductors”, *IEEE Trans. Appl. Supercond.*, vol. 29, 8000110, 2019.

[104] Dular J., “Standard and mixed finite element formulations for systems with type-II superconductors”, PhD thesis, University of Liège, 2023.

[105] Ghosh A. K., “$V-I$ transition and $n$-value of multifilamentary LTS and HTS wires and cables”, *Physica C*, vol. 401, pp. 15-21, 2004.

[106] Kim Y. B., Hempstead C. F. and Strnad A. R., “Critical persistent currents in hard superconductors”, *Phys. Rev. Lett.*, vol. 9, pp. 306-309, 1962.

[107] Cardwell D. A., Larbalestier D. C. and Braginski A. (Eds.), “Handbook of Superconductivity: Fundamentals and Materials, Volume I”, Boca Raton, FL, USA: CRC Press, 2022.

[108] Seidel P., “Applied Superconductivity: Handbook on Devices and Applications”, vol. 1, New York, NY, USA: Wiley, 2015.

[109] Zhang P., Li J., Guo Q., Zhu Y., Yan K., Wang R., Zhang K., Liu X. and Feng Y., “NbTi superconducting wires and applications”, in *Titanium for Consumer Applications*, pp. 279-296, Elsevier, 2019.

[110] Lee P. J., “Abridged metallurgy of ductile alloy superconductors”, in *Wiley Encyclopedia of Electrical and Electronics Engineering*, New York, USA: Wiley, 1999.

[111] Matthias B. T., Geballe T. H., Geller S. and Corenzwit E., “Superconductivity of $Nb_3Sn$”, *Phys. Rev.*, vol. 95, p. 1435, 1954.

[112] Godeke A., ten Haken B., ten Kate H. H. J., Larbalestier D. C., “A general scalign relation for the critical current density in $Nb_3Sn$”, *Supercond. Sci. Technol.*, vol. 19, pp. R100-R116 (Topical Review), 2006.

[113] Wesche R., “High-temperature superconductors: Materials, Properties and Applications”, Dordrecht: Kluwer, 1998.

[114] Bednorz J. G. and Müller K. A., “Possible high $T_c$ superconductivity in the Ba-La-Cu-O system”, *Z. Phys. B - Condens. Matter*, vol. 64, pp. 189-193, 1986.

[115] Shen T. *et al.*, “Design, fabrication, and characterization of a high-field high-temperature superconducting Bi-2212 accelerator dipole magnet”, *Phys. Rev. Accel. Beams*, vol. 25, 122401, 2022.

[116] Larbalestier D. C., “The road to conductors of high temperature superconductors: 10 years do make a difference!”, *IEEE Trans. Appl. Supercond.*, vol. 7, pp. 90-97, 1997.

[117] Moodera J. S., Meservey R., Tkaczyk J. E., Hao C. X., Gibson G. A. and Tedrow P. M., “Critical-magnetic-field anisotropy in single-crystal $YBa_2Cu_3O_7$”, *Phys. Rev. B*, vol. 37, pp. 619-622, 1988.

[118] Sato K., Shibuta N., Mukai H., Hikata T., Ueyama M., Kato T. and Fujikami J., “Bismuth superconducting wires and their applications”, *Cryogenics*, vol. 33, pp. 243-246, 1993.

[119] Nagamatsu J., Nakagawa N., Muranaka T., Zenitani Y. and Akimitsu J., “Superconductivity at 39 K in magnesium diboride”, *Nature*, vol. 410, pp. 63-64, 2001.

[120] Hull J. R., “Applications of high-temperature superconductors on power technology”, *Rep. Prog. Phys.*, vol. 66, pp. 1865-1886, 2003.

[121] Tarantini C. *et al.*, “Effects of neutron irradiation on polucristalline $Mg^{11}B_2$”, *Phys. Rev. B*, vol. 73, 134518, 2006.

[122] Campbell A. M. and Cardwell D. A., “Bulk high temperature superconductors for magnet applications”, *Cryogenics*, vol. 37, pp. 567-575, 1997.

[123] Deng Z., Wang J., Zheng J., Zhang Y. and Wang S., “An efficient and economical way to enhance the performance of present HTS Maglev systems by utilizing the anisotropy property of bulk superconductors”, *Supercond. Sci. Technol.*, vol. 26, 025001, 2013.

[124] Hull J. R. and Murakami M., “Applications of bulk high-temperature superconductors”, *Proceedings of the IEEE*, vol. 92, pp. 1705-1718, 2004.

[125] Cardwell D. and Hari Babu N., “Processing and properties of single grain (RE)-Ba-Cu-O bulk superconductors”, *Physica C*, vol. 445-448, pp. 1-7, 2006.

[126] Kim C.-J. and Hong G.-W., “Defect formation, distribution and size reduction of $Y_2BaCuO_5$ in melt-processed YBCO superconductors”, *Supercond. Sci. Technol.*, vol. 12, pp. R27-R41, 1999.

[127] Cloots R., Koutzarova T., Mathieu J.-P. and Ausloos M., “From RE-211 to RE-123. How to control the final microstructure of superconducting single-domains”, *Supercond. Sci. Technol.*, vol. 18, pp. R9-R23, 2005.

[128] Devendra Kumar N., Rajasekharan T. and Seshubai V., “Preform optimization in infiltration growth process: An efficient method to improve the superconducting properties of $YBa_2Cu_3O_{7-\delta}$”, *Physica C*, vol. 495, pp. 55-65, 2013.

[129] Namburi D. K., Shi Y., Palmer K. G., Dennis A.R., Durrell J. H. and Cardwell D. A., “A novel, two-step top seeded infiltration and growth process for the fabrication of single grain, bulk (RE)BCO superconductors”, *Supercond. Sci. Technol.*, vol. 29, 095010, 2016.

[130] Yang P., Yang W., Zhang L. and Chen L., "Novel configurations for the fabrication of high quality REBCO bulk superconductors by a modified RE+011 top-seeded infiltration and growth process", *Supercond. Sci. Technol.*, vol. 31, 085005, 2018.

[131] Devendra Kumar N., Rajasekharan T. and Seshubai V., "YBCO/Ag composites through a preform optimized infiltration and growth process yield high current densities", *Supercond. Sci. Technol.*, vol. 24, 085005, 2011.

[132] Muralidhar M., Ide N., Koblischka M. R., Diko P., Inoue K. and Murakami M., "Microstructure, critical current density and trapped field experiments in IG-processed Y-123", *Supercond. Sci. Technol.*, vol. 29, 054003, 2016.

[133] Namburi D. K., Shi Y. and Cardwell D. A., "The processing and properties of bulk (RE)BCO high temperature superconductors: current status and future perspectives", *Supercond. Sci. Technol.*, vol. 34, 053002, 2021.

[134] Feng Z. L., Yang W. M., Li J. W., Wang M., Yang Y. X., Gao Z. B. and Huang X. N., "A practical processing method for the fabrication of NdBCO seed crystals and high-performance single-domain GdBCO bulk superconductors", *J. Supercond. Nov. Magn.*, vol. 33, pp. 1559-1568, 2020.

[135] Supreeth D. K., Bekinal S. I., Chandranna S. R. and Doddamani M., " A review of superconducting magnetic bearings and their application", *IEEE Trans. Appl. Supercond.*, vol. 32, 3800215, 2022.

[136] Murakami M., "Processing and applications of bulk RE-Ba-Cu-O superconductors", *Int. J. Appl. Ceram. Technol.*, vol. 4, pp. 225-241, 2007.

[137] Coombs T., Campbell A. M., Storey R. and Weller R., "Superconducting magnetic bearings for energy storage flywheels", *IEEE Trans. Appl. Supercond.*, vol. 9, pp. 968-971, 1999.

[138] Miyazaki Y. *et al.*, "Development of superconducting magnetic bearing for flywheel energy storage system", *Cryogenics*, vol. 80, pp. 234-237, 2016.

[139] Coombs T., Hong Z., Yan Y. and Rawlings C. D., "The next generation of superconducting permanent magnets: the flux pumping method", *IEEE Trans. Appl. Supercond.*, vol. 19, pp. 2169-2173, 2009.

[140] Tomita M. and Murakami M., "High-temperature superconductor bulk magnets that can trap magnetic fields of over 17 tesla at 29 K", *Nature*, vol. 421, pp. 517-520, 2003.

[141] Durrell J. H. *et al.*, "A trapped field of 17.6 T in melt-processed, bulk Gd-Ba-Cu-O reinforced with shrink-fit steel", *Supercond. Sci. Technol.*, vol. 27, 082001, 2014.

[142] Miki M. *et al.*, "Development of a synchronous motor with Gd-Ba-Cu-O bulk superconductors as pole-field magnets for propulsion system", *Supercond. Sci. Technol.*, vol. 19, pp. S494-S499, 2006.

[143] Plecháček V., Hejtmánek J. and Šíma V., "The use of the Bi-2223 superconducting tubes", *IEEE Trans. Appl. Supercond.*, vol. 7, pp. 703-706, 1997.

[144] Bock J., Bestgen H., Elschner S. and Preisler E., "Large shaped parts of melt cast BSCCO for application in electrical engineering", *IEEE Trans. Appl. Supercond.*, vol. 3, pp. 1659-1662, 1993.

[145] Plecháček V., Pollert E., Hejtmánek J., Sedmidubský D. and Knížek K., "Improvement of the magnetic shielding and trapping properties of BiPbSrCaCuO superconducting tubes by the use of multiple thermomechanical processing", *Physica C*, vol. 225, pp. 361-368, 1994.

[146] Larbalestier *et al.*, "Strongly linked current flow in polycrystalline forms of the superconductor $MgB_2$", *Nature*, vol. 410, pp. 186-189, 2001.

[147] Fuchs G., Häßler W., Nenkov K., Scheiter J., Perner O., Handstein A., Kanai T., Schultz L. and Holzapfel B., "High trapped fields in bulk $MgB_2$ prepared by hot-pressing of ball-milled precursor powder", *Supercond. Sci. Technol.*, vol. 26, 122002, 2013.

[148] Durrell J. H., Ainslie M. D., Zhou D., Vanderbemden P., Bradshaw T., Speller S., Filipenko M. and Cardwell D. A., "Bulk superconductors: a roadmap to applications", *Supercond. Sci. Technol.*, vol. 31, 103501, 2018.

[149] Giunchi G., Ripamonti G., Cavallin T. and Bassani E., "The reactive Mg liquid infiltration process to produce large superconducting bulk $MgB_2$ manufacts", *Cryogenics*, vol. 46, pp. 237-242, 2006.

[150] Matthews G. A. B., Santra S., Ma R., Grovenor C. R. M., Grant P. S. and Speller S. C., "Effect of the sintering temperature on the microstructure and superconducting properties of $MgB_2$ bulks manufactured by the field assisted sintering technique", *Supercond. Sci. Technol.*, vol. 33, 054003, 2020.

[151] Moseley D. A., Wilkinson D. P., Mousavi T., Dennis A. R., Speller S. and Durrell J. H., "A new $MgB_2$ bulk ring fabrication technique for use in magnetic shielding or bench-top NMR systems", *Supercond. Sci. Technol.*, vol. 35, 085003, 2022.

[152] Naito T., Sasaki T. and Fujishiro H., "Trapped magnetic field and vortex pinning properties of $MgB_2$ superconducting bulk fabricated by a capsule method", *Supercond. Sci. Technol.*, vol. 25, 095012, 2012.

[153] Patel A., Hopkins S. C., Giunchi G., Figini Albisetti A., Shi Y., Palka R., Cardwell D. A. and Glowacki B. A., "The use of an $MgB_2$ hollow cylinder and pulse magnetized (RE)BCO Bulk for magnetic levitation applications", *IEEE Trans. Appl. Supercond.*, vol. 23, 6800604, 2013.

[154] Cavallin T., Quarantiello R., Matrone A. and Giunchi G., "Magnetic shielding of $MgB_2$ tubes in applied DC and AC field", *J. Phys.: Conf. Ser.*, vol. 43, pp. 1015-1018.

[155] Kunzler J. E., Buelher E., Hsu F. S. L. and Wernick J. H., "Superconductivity in $Nb_3Sn$ at high current density in a magnetic field of 88 kgauss", *Phys. Rev. Lett.*, vol. 6, pp. 89-91, 1961.

[156] Segal C. *et al.*, "Evaluation of critical current density and residual resistance ratio limits in powder in tube $Nb_3Sn$ conductors", *Supercond. Sci. Technol.*, vol. 29, 085003, 2016.

[157] Paranthaman M. P. and Izumi T., “High-performance YBCO-coated superconductor wires”, *MRS Bull.*, vol. 29, pp. 533-536.

[158] Heine K., Tenbrink J. and Thoner M., “High-field critical current densities in $Bi_2Sr_2CaCu_2O_{8+x}$/Ag wires”, *Appl. Phys. Lett.*, vol. 55, pp. 2441-2443, 1989.

[159] Tenbrink J., Wilhelm M., Heine K. and Krauth H., “Development of high-$T_c$ superconductor wires for magnet applications”, *IEEE Trans. Magn.*, vol. 27, pp. 1239-1246, 1991.

[160] Motowildo L., Galinski G., Ozeryanski G., Zhang W. and Hellstrom E., “Dependence of critical current density on filament diameter in round multifilament Ag-sheathed $Bi_2Sr_2CaCu_2O_x$ wires processed in $O_2$”, *Appl. Phys. Lett.*, vol. 65, pp. 2731-2733, 1994.

[161] Goyal A., Parans Paranthaman M. and Schoop U., “The RABiTS approach: using rolling-assisted biaxially textured substrates for high-performance YBCO superconductors”, *MRS Bull.*, vol. 29, pp. 552-561, 2004.

[162] Arendt P. N. *et al.*, “High critical current YBCO coated conductors based on IBAD MgO”, *Physica C*, vol. 412-414, pp. 795-800, 2004.

[163] Foltyn S. R., Arendt P. N., Jia Q. X., Wang H., MacManus-Driscoll J. L., Kreiskott S., DePaula R. F., Stan L., Groves J. R. and Dowden P. C., “Strongly coupled critical current density values achieved in $Y_1Ba_2Cu_3O_{7-\delta}$ coated conductors with near-single-crystal texture”, *Appl. Phys. Lett.*, vol. 82, pp. 4519-4521, 2003.

[164] Godeke A. *et al.*, “Development of a wind-and-react Bi-2212 accelerator magnet Technology”, *IEEE Trans. Appl. Supercond.*, vol. 18, pp. 516-519, 2008.

[165] Goldacker W., Grilli F., Pardo E., Kario A., Schlachter S. I. and Vojenčiak M., “Roebel cables from REBCO coated conductors: a one-century-old concept for the superconductivity of the future”, *Supercond. Sci. Technol.*, vol. 27, 093001, 2014.

[166] van der Laan D. C., “$YBa_2Cu_3O_{7-\delta}$ coated conductor cabling for low ac-loss and high-field magnet applications”, *Supercond. Sci. Technol.*, vol. 22, 065013, 2009.

[167] Weiss J. D., Mulder T., ten Kate H. J. and van der Laan D. C., “Introduction of CORC® wires: highly flexible, round high-temperature superconducting wires for magnet and power transmission applications”, *Supercond. Sci. Technol.*, vol. 30, 014002, 2017.

[168] Takayasu M., Mangiarotti F. J., Chiesa L., Bromberg L. and Minervini J. V., “Conductor characterization of YBCO twisted stacked-tape cables”, *IEEE Trans. Appl. Supercond.*, vol. 23, 4800104, 2013.

[169] Celentano G., De Marzi G., Fabbri F., Muzzi L., Tomassetti G., Anemona A., Chiarelli S., Seri M., Bragagni A. and della Corte A., “Design of an industrially feasible twisted-stack HTS cable-in-conduit conductor for fusion application”, *IEEE Trans. Appl. Supercond.*, vol. 24, 4601805, 2014.

[170] Patel A., Baskys A., Mitchell-Williams T., McCaul A., Coniglio W., Hänisch J., Lao M. and Glowacki B. A., “A trapped field of 17.7 T in a stack of high temperature superconducting tape”, *Supercond. Sci. Technol.*, vol. 31, 09LT01, 2018.

[171] Suyama M., Pyon S., Iijima Y., Awaji S. and Tamegai T., "Trapping a magnetic field of 17.89 T in stacked coated conductors by suppression of flux jumps", *Supercond. Sci. Technol.*, vol. 35, 02LT01, 2022.

[172] Zhou W., Staines M., Jiang Z., Badcock R. A., Long N. J., Buckley R. G. and Fang J., "Shielding of perpendicular magnetic fields in metal layers of REBCO superconducting tapes and Roebel cables", *IEEE Trans. Appl. Supercond.*, vol. 28, 8200108, 2018.

[173] Chunguang L., Xu W., Jia W., Liang S., Yusheng H., "Progress on applications of high temperature superconducting microwave filters", *Supercond. Sci. Technol.*, vol. 30, 073001, 2017.

[174] Bian Y. *et al.*, "A miniaturized HTS microwave receiver front-end subsystem for radar and communication applications", *Physica C*, vol. 470, pp. 617-621, 2010.

[175] Holdengreber E., Gao X., Mizrahi M., Schacham S. E. and Farber E., "Superior impedance matching of THz antennas with high temperature superconducting Josephson junctions", *Supercond. Sci. Technol.*, vol. 32, 074006, 2019.

[176] Wördenweber R., "Deposition technologies, growth and properties of high-$T_c$ films", in *High-Temperature Superconductors*, Woodhead Publishing Series in Electronic and Optical Materials, 2011.

[177] D'haeseleer W. D., *et al.*, "Flux Coordinates and Magnetic Field Structure", Heidelberg, Berlin: Springer Berlin Heidelberg, 1991.

[178] Feynman R. P., Leighton R. B. and Sands M. L., "The Feynman Lectures on Physics: Electromagnetism and Matter", vol. 2, Reading, MA, USA: Addison-Wesley Publishing Company, 1964.

[179] Shen L. C. and Kong J. A., "Applied Electromagnetism", *Third ed.*, Stamford, CT, USA: Cengage Learning, 2009.

[180] Bertotti G., "Hysteresis in Magnetism", New York, NY, USA: Academic, 1998.

[181] Jiles D. C. and Atherton D. L., "Theory of ferromagnetic hysteresis", *J. Appl. Phys.*, vol. 55, pp. 2115-2120, 1984.

[182] Jiles D. C. and Thoelke J. B., "Theory of ferromagnetic hysteresis: Determination of model parameters from experimental hysteresis loops", *IEEE Trans. Magn.*, vol. 25, pp. 3928-3930, 1989.

[183] Chwastek K. and Szczygłowski J., "Estimation methods for the Jiles-Atherton model parameters - a review", *Przeglad Elektrotechniczny*, vol. 12, pp. 145-148, 2008

[184] Chwastek K. *et al.*, "Modelling minor hysteresis loops of high silicon steel using the modified Jiles-Atherton approach", *2DM: 10th international workshop on 1&2 dimensional magnetic measurement and testing*, Cardiff (UK), pp. 68-70, 2008.

[185] Pop N. C. and Caltun O. F., "Jiles-Atherton magnetic hysteresis parameters identification", *Acta Phys. Polonica A*, vol. 120, pp. 491-496, 2011.

[186] Weiss P., "L'hypothèse du champ moléculaire et la propriété ferromagnétique", *J. Phys. Theor. Appl.*, vol. 6, pp. 661-690, 1907.

[187] Kobayashi S., Takahashi S., Shishido T., Kamada Y. and Kikuchi H., "Low-field magnetic characterization of ferromagnets using a minor-loop scaling law", *J. Appl. Phys.*, vol. 107, 023908, 2010.

[188] Fiorillo F., "Measurement and Characterization of Magnetic Materials", New York, NY, USA: Elsevier, 2004.

[189] Dular P., Geuzaine C., Henrotte F. and Legros W., "A general environment for the treatment of discrete problems and its application to the finite element method", *IEEE Trans. Magn.*, vol. 34, pp. 3395-3398, 1998.

[190] Geuzaine C. and Remacle J.-F., "Gmsh: A 3D finite element mesh generator with built-in pre-and post-processing facilities", *Int. J. Num. Methods Engineering*, vol. 79, pp. 552-561, 2004.

[191] "Life-HTS: Liège finite element models for high-temperature superconductors", *http://www.life-hts.uliege.be/*.

[192] Dular J., Harutyunyan M., Bortot L., Schöps S., Vanderheyden B. and Geuzaine C., "On the stability of mixed finite-element formulations for high-temperature superconductors", *IEEE Trans. Appl. Supercond.*, vol. 31, 8200412, 2021.

[193] Jackson J. D., "Classical Electrodynamics". College Park, MD, USA: Amer. Assoc. Phys. Teachers, 1999.

[194] Dular J., Geuzaine C. and Vanderheyden B., "Finite-element formulations for systems with high-temperature superconductors", *IEEE Trans. Appl. Supercond.*, vol. 30, 8200113, 2020.

[195] Dular P., Henrotte F., Robert F., Genon A. and Legros W., "A generalized source magnetic field calculation method for inductors of any shapes", *IEEE Trans. Magn.*, vol. 33, pp. 1398-1401, 1997.

[196] Bossavit A., "Computational Electromagnetism. Variational formulation, Complementarity, Edge Elements", San Diego, CA, USA: Academic Press, 1998.

[197] Fair-Rite Products Corp., *https://fair-rite.com/product/rods-4077484611/*, Consultation: 30/06/2023.

[198] TC S.A., "Traité de thermométrie par thermocouple et résistance, version 6.0", Dardilly Cedex, France.

[199] Rotheudt N., Fagnard J.-F., Harmeling P. and Vanderbemden P., "Adapting a commercial integrated circuit 3-axis Hall sensor for measurements at low temperatures: Mapping the three components of B in superconducting applications", *Cryogenics*, vol. 133, 103693, 2023.

[200] Chen I.-G., Liu J., Weinstein R. and Lau K., "Characterization of $YBa_2Cu_3O_7$, including critical current density $J_c$, by trapped magnetic field", *J. Appl. Phys.*, vol. 72, pp. 1013-1020, 1992.

[201] Cardwell D. A., *et al.*, “Round robin tests on large grain melt processed Sm-Ba-Cu-O bulk superconductors”, *Supercond. Sci. Technol.*, vol. 18, pp. S173-S179, 2005.

[202] Kumar N. D., Shi Y., Zhai W., Dennis A. R., Durrell J. H. and Cardwell D. A., “Buffer pellets for high-yield, top-seeded melt growth of large grain Y-Ba-Cu-O superconductors”, *Crys. Growth Des.*, vol. 15, pp. 1472-1480, 2015.

[203] Nariki S., Teshima H. and Morita M., “Performance and applications of quench melt-growth bulk magnets”, *Supercond. Sci. Technol.*, vol. 29, 034002, 2016.

[204] Vakaliuk O., Werfel F., Jaroszynski J. and Halbedel B., “Trapped field potential of commercial Y-Ba-Cu-O bulk superconductors designed for applications”, *Supercond. Sci. Technol.*, vol. 33, 095005, 2020.

[205] Philippe M. P., “Magnetic properties of structures combining bulk high temperature superconductors and soft ferromagnetic alloys”, PhD thesis, University of Liège, 2015.

[206] Patel A., Usoskin A., Baskys A., Hopkins S. C. and Glowacki B. A., “Trapped field profiles for 40-mm wide superconducting tape pieces”, *J. Supercond. Nov. Magn.*, vol. 28, pp. 397-401, 2015.

[207] Mitchell-Williams T. B., Patel A., Baskys A., Hopkins S. C., Kario A., Goldacker W. and Glowacki B. A., “Toward uniform trapped field magnets using a stack of Roebel cable offcuts”, *IEEE Trans. Appl. Supercond.*, vol. 26, 6800404, 2016.

[208] Selva K. and Majkic G., “Trapped magnetic field profiles of arrays of (Gd,Y)$Ba_2Cu_3O_x$ superconductor tape in different stacking configurations”, *Supercond. Sci. Technol.*, vol 26, 115006, 2013.

[209] Houbart M., Fagnard J.-F., Dular J., Dennis A. R., Namburi D. K., Durrell J. H., Geuzaine C., Vanderheyden B. and Vanderbemden P., “Trapped magnetic field distribution above a superconducting linear Halbach array”, *Supercond. Sci. Technol.*, vol. 35, 064005, 2022.

[210] Philippe M. P., Fagnard J. F., Wéra L., Morita M., Nariki S., Teshima H., Caps H., Vanderheyden B. and Vanderbemden P., “Influence of crossed fields in structures combining large grain, bulk (RE)BCO superconductors and soft ferromagnetic discs”, *J. Phys.: Conf. Ser.*, vol. 695, 012003, 2016.

[211] Fagnard J. F., Morita M., Nariki S., Teshima H., Caps H., Vanderheyden B. and Vanderbemden P., “Magnetic moment and local magnetic induction of superconducting/ferromagnetic structures subjected to crossed fields: experiments on GdBCO and modelling”, *Supercond. Sci. Technol.*, vol. 29, 125004, 2016.

[212] Egan R., Philippe M., Wera L., Fagnard J. F., Vanderheyden B., Dennis A., Shi Y., Cardwell D. A. and Vanderbemden P., “A flux extraction device to measure the magnetic moment of large samples; application to bulk superconductors”, *Rev. Sci. Instrum.*, vol. 86, 025107, 2015.

[213] Ausserlechner U., Kasperkovitz P. and Steiner W., “A theoretical discussion of vector pick-up systems for SQUID magnetometers”, *Meas. Sci. Technol.*, vol. 9, pp. 989-1006, 1998.

[214] Quantum Design, “Physical Property Measurement System”, *https://www.qdusa.com/products/ppms.html*, Consultation: 08-06-2023.

[215] Quantum Design, “Physical Property Measurement System: Hardware Manual”, Part number 1070-150, B5, Sixth Ed., 2008.

[216] Quantum Design, “Physical Property Measurement System: ACMS User’s Manual”, 1996.

[217] Hahn S., Voccio J., Park D. K., Kim K. M., Tomita M., Bascuñán J. and Iwasa Y., “A stack of YBCO annuli, thin plate and bulk, for micro-NMR spectroscopy”, *IEEE Trans. Appl. Supercond.*, vol. 22, 4302204, 2012.

[218] Patel A., Hahn S., Voccio J., Baskys A., Hopkins S. C. and Glowacki B. A.,“Magnetic levitation using a stack of high temperature superconducting tape annuli”, *Supercond. Sci Technol.*, vol. 30, 024007, 2017.

[219] Tumanski S., “Handbook of Magnetic Measurements”, Boca Raton, FL, USA: CRC Press, 2011.

[220] Claassen J. H., Willard M. A., Francavilla T. L. and Harris V. G., “Inductive measurements of magnetic properties of ribbon materials”, *Rev. Sci. Instrum.*, vol. 75, 2817, 2004.

[221] Chen D.-X. and Goldfarb R. B., “Kim model for magnetization of type-II superconductors”, *J. Appl. Phys.*, vol. 66, pp. 2489-2500, 1989.

[222] Goldfarb R. B., Cross R. W., Goodrich L. F. and Bergren N. F., “Magnetic measurement of transport critical current density of granular superconductors”, *Cryogenics*, vol. 33, pp. 3-7, 1993.

[223] Calzona V., Cimberle M. R., Ferdeghini C., Putti M. and Siri A. S., “AC susceptibility and magnetization of high-$T_c$ superconductors: critical state model for the intergranular region”, *Physica C*, vol. 157, pp. 425-430, 1989.

[224] Chen D.-X., Pardo E., Sanchez A., “Demagnetizing factors of rectangular prisms and ellipsoids”, *IEEE Trans. Magn.*, vol. 38, pp. 1742-1752, 2002.

[225] Shi Y., Mousavi T., Dennis A. R., Ainslie M. D., Speller S. C., Grovenor C. R. H., Durrell J. H. and Cardwell D. A., “ The effect of facet lines on critical current density and trapped field in bulk RE-Ba-Cu-O single grains”, *Supercond. Sci. Technol.*, vol. 35, 105002, 2022.

[226] Ainslie M. D., Fujishiro H., Ujjie T., Zou J., Dennis A. R., Shi Y.-H. and Cardwell D. A., “Modelling and comparison of trapped fields in (RE)BCO bulk superconductors for activation using pulsed field magnetization”, *Supercond. Sci. Technol.*, vol. 27, 065008, 2014.

[227] Ainslie M. D. and Fujishiro H., “Modelling of bulk superconductor magnetisation”, *Supercond. Sci. Technol.*, vol. 28, 053002, 2015.

[228] de Boer B. *et al.*, “Biaxially textured Ni-alloy tapes as substrates for buffer and YBCO film growth”, *Physica C*, vol. 351, pp. 38-41, 2001.

[229] Verebelyi D. T. *et al.*, “Uniform performance and continuously processed MOD-YBCO-coated conductors using a textured Ni-W substrate”, *Supercond. Sci. Technol.*, vol. 16, pp. L19-L22, 2003.

[230] Ijaduola A. O., Thompson J. R., Goyal A., Thieme C. L. H. and Marken K., “Magnetism and ferromagnetic loss in Ni-W textured substrates for coated conductors”, *Physica C*, vol. 403, pp. 163-171, 2004.

[231] Song K. J., Park Y. M., Yang J. S., Kim S. W., Ko R. K., Kim H. S., Ha H. S., Oh S. S., Park C., Joo J. H. and Kim C. J., “Magnetism in Ni-W textured substrates for coated conductors”, *Journal of the Korea Institute of Applied Superconductivity and Cryogenics*, vol. 7, pp. 7-10, 2005.

[232] Miyagi D., Yunoki Y., Umabuchi M., Takahashi N. and Tsukamoto O., “Measurement of magnetic properties of Ni-alloy substrate of HTS coated conductor in $LN_2$”, *Physica C*, vol. 468, pp. 1743-1746, 2008.

[233] Gömöry F., Vojenčiak M., Pardo E., Solovyov M. and Šouc J., “AC losses in coated conductors”, *Supercond. Sci. Technol.*, vol. 23, 034012, 2010.

[234] Claassen J. H. and Thieme C. L. H., “Magnetic properties of Ni-based substrates for HTS tape”, *Supercond. Sci. Technol.*, vol. 21, 105003, 2008.

[235] Takahashi N., Morishita M., Miyagi D. and Nakano M., “Examination of magnetic properties of magnetic materials at high temperature using a ring specimen”, *IEEE Trans. Magn.*, vol. 46, pp. 548-551, 2010.

[236] Liu G., Zhang G., Jing L., Yu H., Ai L., Yuan W. and Li W., “Influence of substrate magnetism on frequency-dependent transport loss in HTS-coated conductors”, *IEEE Trans. Appl. Supercond.*, vol. 27, 6603807, 2017.

[237] Nguyen D. N., Ashworth S. P., Willis J. O., Sirois F. and Grilli F., “A new finite-element method simulation model for computing AC loss in roll assisted biaxially textured substrate YBCO tapes”, *Supercond. Sci. Technol.*, vol. 23, 025001, 2010.

[238] Lahtinen V., Pardo E., Šouc J., Solovyov M. and Stenvall A., “Ripple field losses in direct current biased superconductors: Simulations and comparison with measurements”, *J. Appl. Phys.*, vol. 115, 113907, 2014.

[239] Takahashi S. and Kobayashi S., “Scaling power-law relations in asymmetrical minor hysteresis loops”, *J. Appl. Phys.*, vol. 107, 063903, 2010.

[240] Dular J., Brialmont S., Vanderbemden P., Geuzaine C. and Vanderheyden B. “Finite element models for magnetic shields made of stacked tapes”, presented at the *8th International Workshop on Numerical Modelling of High Temperature Superconductors*, Nancy, 2022.

[241] Gyselinck J. and Dular P., “A time-domain homogenization technique for laminated iron cores in 3-D finite-element models”, *IEEE Trans. Magn.*, vol. 40, pp. 856-859, 2004.

[242] Wang J., Lin H., Huang Y. and Sun X., “A new formulation of anisotropic equivalent conductivity in laminations”, *IEEE Trans. Magn.*, vol. 47, pp. 1378-1381, 2011.

[243] Zermeño V. M. R. and Grilli F., "3D modelling and simulations of 2G HTS stacks and coils", *Supercond. Sci. Technol.*, vol. 27, 044025, 2014.

[244] Dular J., Brialmont S., Vanderbemden P., Geuzaine C. and Vanderheyden B., "Finite element models for magnetic shields made of stacked superconducting tape annuli", *To be published in IEEE Trans. Appl. Supercond.*, September 2023.

[245] Mager A., "Magnetic shielding efficiencies of cylindrical shells with axis parallel to the field", *J. Appl. Phys.*, vol. 39, pp. 1914-1917, 1968.

[246] Mager A. J., "Magnetic Shields", IEEE Trans. Magn., vol. MAG-6, pp. 67-75, 1970.

[247] Chen D.-X., Pardo E. and Sanchez A., "Fluxmetric and magnetometric demagnetizing factors for cylinders", *J. Magn. Magn. Mater.*, vol. 306, pp. 135-146, 2006.

[248] Cabrera B., "The use of superconducting shields for generating ultra low magnetic field regions and several related experiments", PhD Thesis, Stanford University, 1975.

[249] Navau C., Sanchez A., Pardo E., Chen D. X., Bartholomé E., Granados X., Puig T. and Obradors X., "Critical state in finite type-II superconducting rings", *Phys. Rev. B*, vol. 71, 214507, 2005.

[250] Fagnard J.-F., Vanderheyden B., Pardo E. and Vanderbemden P., "Magnetic shielding of various geometries of bulk semi-closed superconducting cylinders subjected to axial and transverse fields", *Supercond. Sci. Technol.*, vol. 32, 074007, 2019.

[251] Tsuchimoto M., Demachi K. and Itoh I., "Numerical evaluation of uniform magnetic field within superconducting Swiss roll", *Physica C*, vol. 412-414, pp. 719-722, 2004.

[252] Barna D., Novák M., Brunner K., Petrone C., Atanasov M., Feuvrier J. and Pascal M., "NbTi/Nb/Cu multilayer shield for the superconducting shield (SuShi) septum", *IEEE Trans. Appl. Supercond.*, vol. 29, 4900108, 2018.

[253] Rotheudt N., Dular J., Geuzaine C., Fagnard J.-F., Vanderheyden B. and Vanderbemden P., "Measured and modelled vectorial flux density generated by an eye-shaped magnet", presented at *16th European Conference on Applied Superconductivity, EUCAS 2023*, September 2023.

[254] Xu X., Huang Z., Li W., Huang X., Wang M., Hong Z. and Jin Z., "3D finite element modelling on racetrack coils using the homogeneous TA formulation", *Cryogenics*, vol. 119, 103366, 2021.